Acta Pharmacologica Sinica (2011) 32: 1309–1310
 1671-4083/11 $32.00
www.nature.com/aps

Research Highlight

Integrin activation as an alternative treatment approach for inflammatory diseases

Vincent Kam Wai WONG, Liang LIU*

Acta Pharmacologica Sinica (2011) 32: 1309–1310; doi: 10.1038/aps.2011.150; published online 31 Oct 2011

Regulation of immune responses is a complex process that involves many signaling molecules in their specific interactions and interplays. For instance, the leukocytic integrin CD11b/CD18 plays a crucial role in leukocyte infiltration, which is commonly found in most inflammatory diseases.

The highly abundant integrin CD11b/CD18 is a heterodimer of the α_m (CD11b) and β_2 (CD18) subunits. CD11b/CD18 is located in the cell surface of circulating leukocytes and can undergo active conformational change to mediate leukocyte adhesion, migration and accumulation at the sites of inflammation[1]. Current approaches for prevention of leukocyte infiltration focus on inhibiting the adhesion of leukocytic integrins to their respective ligands. For example, the specific integrin antibody M1/70 mAb blocks the binding of integrins to ligands found on the vascular wall, thereby reducing the infiltration of leukocytes into the inflamed tissues (Figure 1)[2, 3]. Despite the intensive research on identifying potent inhibitors for CD11b/CD18, such inhibitors had limited success in treating inflammatory diseases in humans. This may be because of the large intracellular pool of CD11b/CD18 that can be mobilized to leukocyte surface and hinder the complete blockade of CD11b/CD18 with specific antibodies[4], or because it is crucial to have over 90% occupancy of active integrin receptors by inhibitors for suppression of leukocyte recruitment[5]. Moreover, unexpected adverse effects of antibodies against β_2 integrins also prohibited the use of such blocking agent in clinical trials[6]. Recently, Maiguel and colleagues[2] reported a new approach that involves the pharmacological activation, rather than blockade of CD11b/CD18 by small molecules, which has enlightened as promising treatment strategy for inflammatory diseases.

Maiguel and colleagues[2] successfully identified several potent small-molecule agonists (termed as leukadherins), which specifically target and enhance CD11b/CD18-dependent cell adhesion to fibrinogen or inflamed endothelium, leading to reduction of leukocyte migration and recruitment in both *in vitro* and *in vivo* models (Figure 1). Their data provide scientific insight that instead of identification of blocking agents for integrin, discovery of potent integrin CD11b/CD18 agonists could also be another effective strategy in reducing leukocyte infiltration and subsequent inflammation in humans. Through the high-throughput screening (HTS) of a chemical library (>100 000 small molecules), three leukadherin compounds were identified to target the ligand-binding αA domain and allosterically stabilize the active conformation of CD11b/CD18. In addition, leukadherins enhanced CD11b/CD18-dependent cell adhesion and reduced leukocyte motility, which led to a substantial reduction in leukocyte transendothelial migration and recruitment into inflamed tissues. Several clinically relevant diseases models such as thioglycolate-induced peritonitis mice model, arterial balloon injury rat model and zebra-fish tailfin injury model were adopted to demonstrate the physiologically relevant settings for anti-inflammatory effects of leukadherins, The results suggest that leukadherins are therapeutic lead compounds for future optimization. Most importantly, a comparison between M1/70 mAb, a well-characterized CD11b/CD18 antibody[7], and one of these compounds revealed that leukadherin shows better efficacy and well preserves organ function upon inflammatory injury. Collectively, Maiguel's data suggested that integrin-specific, small-molecule agonists represent an effective pharmacological approach for the treatment of inflammatory and autoimmune diseases.

The phenotype of reduced migration and recruitment of inflammatory cells and cellular adhesion due to the increase of constitutively active integrins was firstly demonstrated in knock-in mice expressing constitutively active mutants of the integrins[8]. However, it is not known whether the activation of wild-

State Key Laboratory for Quality Research in Chinese Medicines, Macau University of Science and Technology, Avenida Wai Long, Taipa, Macau, China
* Correspondence: Liang LIU
(lliu@must.edu.mo)

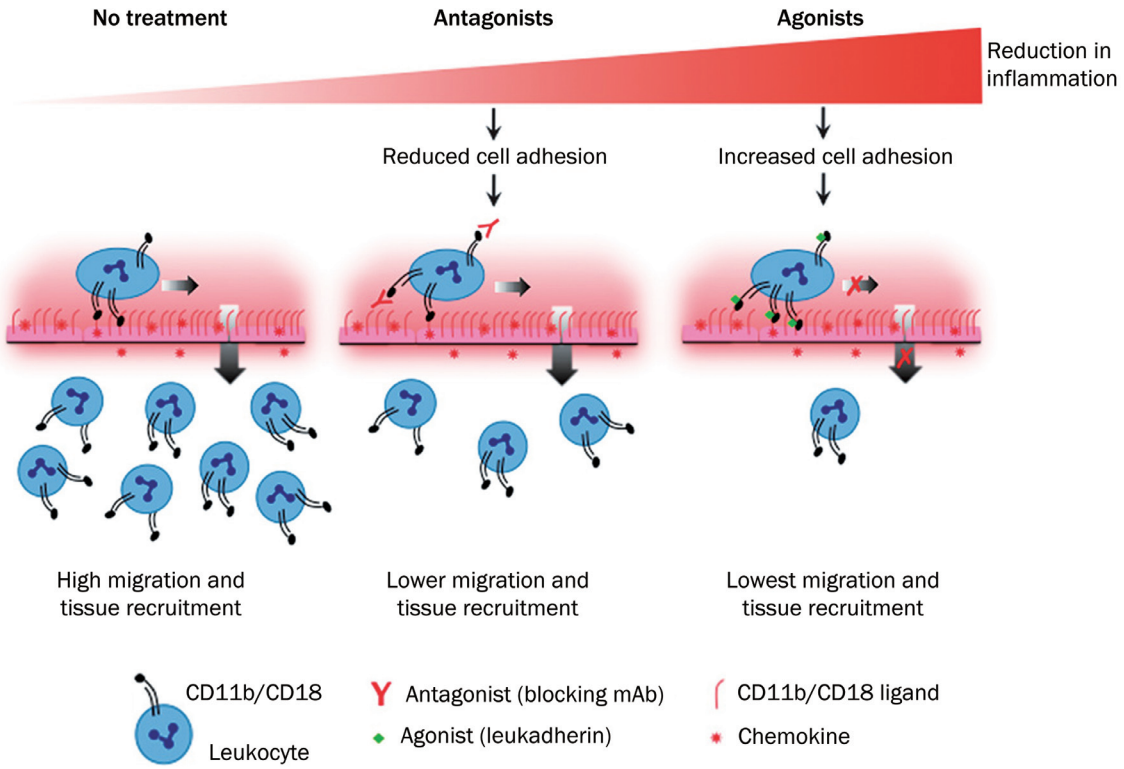

Figure 1. Schematic showing integrin antagonists and agonists differ in their ability to reduce inflammatory disease. Integrin antagonists (central panel), such as blocking mAbs, prevent leukocyte adhesion to the inflamed endothelium, thereby reducing leukocyte migration and tissue recruitment as compared to the untreated situation (left panel). On the other hand, integrin agonists (such as leukadherins), promote the adhesion of leukocytes and reduce their lateral and transendothelial migration, leading to an even greater decrease in the tissue recruitment of leukocytes. Thus, small-molecule integrin agonists (such as leukadherins) represent an alternative strategy for modulating leukocyte recruitment and inflammatory diseases[1]. Reprinted with permission from AAAS: Science Signaling, copyright 2011.

type integrin receptors in normal animals could have a similar phenotype *in vivo* and could reduce inflammation in physiologically relevant disease models. In this respect, Maiguel and colleagues highlighted the use of chemical-biological approach in demonstrating the endogenous, wild-type integrin protein perturbed by a specific small-molecule agonist, and provided an appropriate channel to analyze the effects of integrin activation on cellular functions *in vivo*. On the other hand, treatment of integrin agonists *in vivo* would increase adhesion of inflammatory cells to the vascular endothelium that may lead to vascular damage and leakage. Although Maiguel and colleagues found no systemic signs of vascular injury or leakage from the animals administrated with compounds for more than 3 months, the bio-markers for atherosclerosis can also be monitored in animals treated with integrin agonists for a longer treatment duration[9]. Now, the identification of potent anti-inflammatory compounds has become a hot topic in Chinese herbal drug research[10], therefore, Chinese medicinal herbs may serve as a potential source for the identification of novel integrin agonists in the future.

1 Hynes RO. Integrins: bidirectional, allosteric signaling machines. Cell 2002; 110: 673–87.
2 Maiguel D, Faridi MH, Wei C, Kuwano Y, Balla KM, Hernandez D, *et al*. Small molecule-mediated activation of the integrin CD11b/CD18 reduces inflammatory disease. Sci Signal 2011; 4: ra57.
3 Cox D, Brennan M, Moran N. Integrins as therapeutic targets: lessons and opportunities. Nat Rev Drug Discov 2010; 9: 804–20.
4 Hughes BJ, Hollers JC, Crockett-Torabi E, Smith CW. Recruitment of CD11b/CD18 to the neutrophil surface and adherence-dependent cell locomotion. J Clin Invest 1992; 90: 1687–96.
5 Lum AF, Green CE, Lee GR, Staunton DE, Simon SI. Dynamic regulation of LFA-1 activation and neutrophil arrest on intercellular adhesion molecule 1 (ICAM-1) in shear flow. J Biol Chem 2002; 277: 20660–70.
6 Molloy ES, Calabrese LH. Therapy: Targeted but not trouble-free: efalizumab and PML. Nat Rev Rheumatol 2009; 5: 418–9.
7 Springer T, Galfre G, Secher DS, Milstein C. Mac-1: a macrophage differentiation antigen identified by monoclonal antibody. Eur J Immunol 1979; 9: 301–6.
8 Park EJ, Mora JR, Carman CV, Chen J, Sasaki Y, Cheng G, *et al*. Aberrant activation of integrin alpha4beta7 suppresses lymphocyte migration to the gut. J Clin Invest 2007; 117: 2526–38.
9 Charo IF, Taub R. Anti-inflammatory therapeutics for the treatment of atherosclerosis. Nat Rev Drug Discov 2011; 10: 365–76.
10 Li HY, Cui L, Cui M. Hot topics in Chinese herbal drugs research documented in PubMed/MEDLINE by authors inside China and outside of China in the past 10 years: based on co-word cluster analysis. J Altern Complement Med 2009; 15: 779–85.

Acta Pharmacologica Sinica (2011) 32: 1311–1320
 1671-4083/11 $32.00
www.nature.com/aps

Review

Macro-management of microRNAs in cell cycle progression of tumor cells and its implications in anti-cancer therapy

Lin-hui LIANG, Xiang-huo HE*

State Key Laboratory of Oncogenes and Related Genes, Shanghai Cancer Institute, Renji Hospital, Shanghai Jiao Tong University School of Medicine, Shanghai 200032, China

The cell cycle, which is precisely controlled by a number of regulators, including cyclins and cyclin-dependent kinases (CDKs), is crucial for the life cycle of mammals. Cell cycle dysregulation is implicated in many diseases, including cancer. Recently, compelling evidence has been found that microRNAs play important roles in the regulation of cell cycle progression by modulating the expression of cyclins, CDKs and other cell cycle regulators. Herein, the recent findings on the regulation of the cell cycle by microRNAs are summarized, and the potential implications of miRNAs in anti-cancer therapies are discussed.

Keywords: MicroRNA; cell cycle progression; cancer therapy

Acta Pharmacologica Sinica (2011) 32: 1311–1320; doi: 10.1038/aps.2011.103; published online 12 Sep 2011

Introduction

The cell cycle, which is involved in many cellular processes such as proliferation, development and differentiation, is a crucial process in mammals. In a normal cell, the maintenance of cell cycle fidelity is strictly controlled by surveillance proteins, including cyclins and cyclin-dependent kinases (CDKs). After receiving mitogenic signals, the cells exit from the G_0 phase and enter the G_1 phase. Subsequently, cyclin D binds to CDK4 and CDK6, leading to the partial inactivation of Rb family proteins. Inactivation of Rb proteins results in the transcription of E2F1-related genes. Cyclin E1, which is encoded by an early E2F1 responsive gene, then binds to CDK2 and completely inactivates Rb protein, driving the cells to enter the S phase. When the cells enter the S phase, cyclin A binds to CDK2 and promotes the phosphorylation of many proteins involved in DNA synthesis. Prophase is then initiated after cyclin A binds to CDK1. At the end of interphase, breakdown of the nuclear envelope leads to the interaction of cyclin B with CDK1, which in turn allows the cells to undergo mitosis. In addition to the positive regulation by cyclins/CDKs, the cell cycle is also controlled by negative regulatory proteins, such as CDK inhibitors, which mainly include two families: the INK4 and Cip/Kip families[1]. Additionally, cell cycle regulation is monitored by many checkpoints, such as the ATM/ATR pathway[2]. As summarized above, proper progression through the cell cycle is strictly monitored by various positive and negative surveillance factors. Improper progression through the cell cycle results in many diseases, including cancer. Indeed, the disruption of normal cell cycle progression is a very important event in the initiation and development of cancer. Cancer cells often show genomic instability, which is usually caused by cell cycle dysfunction and leads to unscheduled proliferation[3]. Moreover, genomic instability predisposes cancer cells to acquire more genetic alterations, which contributes to a more aggressive cancer phenotype. Thus, understanding cell cycle dysregulation in cancers will facilitate the development of improved and novel anti-cancer therapies.

MicroRNAs (miRNAs) are small, non-coding RNAs that regulate gene expression mainly by binding to the 3′ untranslated regions (3′-UTRs) of target genes[4]. After miRNAs bind to a target gene, the target protein is down-regulated owing to mRNA degradation or translation termination. Currently, there are 1424 known human microRNAs, and it is predicted that approximately 30% of human protein-coding genes are regulated by miRNAs[5]. In the past five years, compelling studies have demonstrated that miRNAs are involved in many physiological and pathological processes, such as cancer. In 2005, He L and co-workers found that expression of the miR-17-92 cluster was increased in B-cell lymphoma and cooperated with c-myc to accelerate tumor formation *in vivo*[6].

* To whom correspondence should be addressed.
E-mail xhhe@shsci.org
Received 2011-04-09 Accepted 2011-07-05

Additionally, Cimmino A *et al* demonstrated that miR-15 and miR-16 induced apoptosis by targeting BCL-2[7]. These studies indicated that microRNAs can act as potent oncogenes or tumor suppressors and can regulate the progression of cancer. Since then, an increasing number of studies have clarified the role of miRNAs in cell cycle control, proliferation and tumor metastasis. In this review, we will focus on the regulation of tumor cell cycle progression by miRNAs, how miRNAs alter cell cycle regulatory networks and the implications of this regulation in anti-cancer therapy.

The macro-management of miRNAs in cell cycle progression

Evidence for the importance of miRNAs in regulating the cell cycle originated in studies of the miRNA target gene lin-4[8], which acts to modify latent reiterative cell lineages and cell division in *C elegans*. In the past five years, increasing evidence has indicated that miRNAs directly control cell cycle progression by targeting cell cycle regulators. Additionally, miRNAs indirectly control cell cycle progression by targeting signal transduction pathways. Therefore, miRNAs affect cell cycle progression by targeting various genes that span the cell cycle regulatory network.

Let-7 family

The let-7 miRNA was first discovered to be essential for development in *C elegans*, possibly by targeting the lin-41 gene[8]. It was reported that let-7 is downregulated in human lung cancer, and enforced expression of let-7 in lung cancer cells inhibits proliferation[9]. A subsequent study indicated that let-7 not only inhibits proliferation but also alters the cell cycle progression of cancer cells[10]. In that study, Johnson *et al* demonstrated that let-7 overexpression retains cells in the G_1 phase and alters cell cycle-related pathways. CDK6, CDC25A, and cyclin D2 have been validated as direct downstream targets of let-7 in lung cancer cells. Schultz *et al* found reduced expression of let-7b in melanoma cells, and let-7b also delays the G_1/S transition by down-regulating cyclin D1, cyclin D3, cyclin A, and CDK4[11]. Another let-7 family member, let-7a, is down-regulated in prostate cancer and induces G_1 arrest by reducing the levels of the downstream targets E2F2 and cyclin D2[12]. In addition to regulating the G_1/S transition, the let-7 family also affects the G_2/M phase. In human primary fibroblasts, let-7 expression is reduced in the dividing cells. Ectopic expression of let-7 in fibroblast cells decreases proliferation and increases the cell fraction in the G_2/M phase. Let-7 induces G_2/M arrest by down-regulating the CDC34 protein, which then increases wee1 protein levels and subsequently increases the inhibitory phosphorylation of CDC2[13]. In summary, the let-7 family members negatively control cell cycle regulators, which results in reduced proliferation and other cell-type specific phenotypes.

miR-17-92 and miR-106b/25 clusters

Another versatile miRNA family that controls the cell cycle includes the miR-17-92 and miR-106b/25 clusters. This miRNA family is composed of three miRNA clusters located on three different chromosomes. The miRNAs include miR-17, miR-18a, miR-19a, miR-20a, miR-19b-1, and miR-92a-1, which are encoded on chromosome 13; miR-106b, miR-93, and miR-25, encoded on chromosome 7; and miR-106a, miR-18b, miR-20b, miR-19b-2, miR-92a-2, and miR-363, encoded on the X chromosome. The miR-17-92 cluster is amplified in B-cell lymphoma, and enforced expression of miR-17-92 antagonizes c-myc-induced apoptosis and acts with c-myc to increase tumor development in a B-cell lymphoma animal model. These results indicate that the miR-17-92 cluster functions as an oncogene[6]. Expression of the miR-17-92 cluster is also elevated in lung cancer and promotes the proliferation of lung cancer cells[14]. Recently, miR-17-92 was found to be induced by c-myc and to promote tumor angiogenesis[15]. In addition to c-myc, miR-17-92 is induced by E2F transcription factors and forms a negative regulatory loop by directly targeting E2Fs[16, 17]. As a potential mechanism of cancer cell cycle regulation by miR-17-92, it was reported that c-myc-induced miR-17 and miR-20a cooperate with the RB/E2F signaling pathway to control the accurate timing of the G_1/S transition[18]. Cloonan *et al* reported that miR-17-5p regulates more than 20 G_1/S transition-related genes[19], and RBL2 was identified as a functional downstream gene of miR-17-5p[20, 21]. It should be noted that the targets of miR-17-92 depended on the cellular context, which results in diverse functions of the miR-17-92 cluster in different cells. For example, in c-myc-overexpressing Raji cells, miR-17-19b-1 reduces the expression of Bim. In BCL-2-overexpressing SUDHL4 cells, miR-17-19b-1 decreases the expression of CDKN1A/p21 and facilitates the G_1/S transition[22]. In contrast to the function of miR-17-19b-1 in SUDHL4 cells, miR-17/20a inhibits the G_1/S transition in breast cancer cells by reducing the expression of cyclin D1[23]. It has been reported that miR-17-92 regulates a set of G_1/S transition-related genes, including pro-proliferation genes, such as cyclin D1 and E2F1, and anti-proliferation genes, such as CDKN1A (p21), PTEN, RB1, RBL1 (p107), and RBL2 (p130)[24]. The dual regulation of pro-proliferation and anti-proliferation target genes by miR-17-92 may explain the variation in the reported functions of miR-17-92.

In addition to the miR-17-92 cluster, E2F1 also regulates the expression of the miR-106b/25 cluster and is suppressed by the miR-106b/25 cluster, thereby forming a negative regulatory loop[25]. Moreover, up-regulation of the miR-106b/25 cluster impairs the transforming growth factor (TGF)-β tumor suppressor pathway by targeting CDKN1A (p21 Waf1/Cip1) and BCL-2L11 (Bim), which in turn reverses G_1 arrest induced by the TGF-beta signal[25]. Therefore, up-regulation of the miR-106b/25 cluster negatively modulates the TGF-beta tumor suppressor pathway and facilitates the development of tumors.

miR-34 family

The miR-34 family includes important p53-responsive miRNAs, and when upregulated, the miRNAs induce p53-mediated processes, such as cell cycle arrest and apoptosis[26, 27].

In human A549 cells, miR-34a induces G_1 arrest by targeting cyclin D1 and CDK6, which in turn affects the phosphorylation of Rb protein[28]. In neuroblastoma, miR-34a reduces the expression of BCL-2 and MYCN to block the G_1/S transition[29]. E2F3 is also a target of miR-34a in neuroblastoma[30]. However, in human glioma and medulloblastoma cells, miR-34a induces G_1 arrest by reducing c-MET, Notch1, Notch2, and CDK6[31]; in human astrocytes, however, overexpression of miR-34a does not alter cell cycle progression[31]. Another member of the miR-34 family, mir-34b, also regulates cell cycle regulators. In acute myeloid leukemia, miR-34b targets the CREB protein and decreases various CREB downstream proteins, such as BCL-2, cyclin A1, cyclin B1, cyclin D, nuclear factor-kappa B, Janus-activated kinase 1 and signal transducer and activator of transcription 3[32]. miR-34 also regulates cell cycle progression independent of the p53 signal. In p53-null K562 cells, phorbol esters induce miR-34a expression by activating an alternative phorbol ester-responsive promoter to produce a longer pri-miR-34a transcript. Additionally, enforced expression of miR-34a in K562 cells inhibits proliferation and G_1/S transition by targeting CDK4 and CDK6[33]. Another p53 family member, p63 positively regulates cell cycle progression by repressing the expression of miR34a and miR34c[34]. In the absence of p63, miR-34a and miR-34c are increased in primary keratinocytes and embryonic skin, with concomitant G_1 arrest and inhibition of the cell cycle regulators cyclin D1 and CDK4[34]. Taken together, these data indicate that the miR-34 family modulates the expression of various cell cycle-related genes and is therefore important in the cell cycle progression of numerous cell types.

Other miRNAs regulating cell cycle progression

Cell cycle regulators are also modulated by many other miRNAs. One example is cyclin D1, which is regulated by miR-449a[35], miR-193b[36], miR-15/16[37–39], miR-19a[40], miR-195[41], and miR-302a[42]. The cyclin D1 binding proteins CDK4 and CDK6 are also regulated by a number of miRNAs, including miR-107[43], miR-449a[44], miR-129[45], miR-125b[46], miR-15/16[39], miR-24[47], miR-195[41], and miR-124a[48]. Another important G_1/S regulator cyclin E, is down-regulated by miR-16[37] and miR-195[49]. In addition to the positive G_1/S regulators, negative G_1/S regulators are also targeted by various miRNAs. The CDK inhibitor p21 is targeted by miR-17-92 and miR-106b/93[22, 25] in addition to many other miRNAs[50, 51]. The p27 and p57 proteins are regulated by miR-221/222[52, 53] and miR-92b[54]. The INK family member p16 is regulated by miR-24[55]. The number of miRNAs regulating the entry and progression through G_2/M is much fewer than those regulating the G_1/S transition. The G_2/M-related cyclin A is targeted by let-7[11]. miR-132/212 reduces the expression of RB1, which leads to an increase in E2F1 levels and G_2/M arrest[56]. Dihydrofolate reductase (DHFR), an enzyme regulating the S phase, is also regulated by miR-24[57] and miR-192[58]. In addition, PLK1, a critical regulator of many stages of mitosis, is targeted by miR-100[59] and miR-593* [60]. Ectopic expression of miR-100 and miR-593* causes G_2/M arrest and reduces proliferation. Wee 1 kinase, a nuclear protein that delays mitosis by negatively regulating the cyclinB-CDK1 complex, has been identified as a target of miR-128a, miR-155, and miR-516a-3p[61]. A summary of the miRNAs regulating the cell cycle is given in Table 1 and Figure 1.

MicroRNAs add to the complexity of the cell cycle regulatory network

As mentioned above, the cell cycle is monitored by an intricate network of positive and negative regulatory signaling pathways. An imbalance between the positive and negative regulatory pathways is common in cancers. With the addition of miRNAs as cell cycle regulators, new pathways have been discovered, and the context of the network has been remarkably enriched. Additionally, crosstalk between miRNAs and signaling pathways essential to cell cycle progression adds complexity to the cell cycle regulatory network.

RAS/Raf/MEK/Erk signaling pathway

When cells receive exogenous mitogenic signals, such as growth factor stimulation, the receptor tyrosine kinases (RTKs) will activate RAS and its downstream signaling pathways. One important signaling pathway induced by RAS activation is the Raf/MEK/Erk pathway, which leads to the activation of many cyclin/CDK complexes related to the G_1/S transition. The hyperactivation of RAS is common in many tumors. In addition to mutation and constitutive mitogenic stimulation, many studies have indicated that tumor suppressor miRNAs targeting RAS are down-regulated in many cancers, which may contribute to the abnormal RAS activation. Let-7 family miRNAs[62, 63], miR-18* [64], miR-143[65], miR-181[66, 67], miR-96[68], and miR-214[69] directly target RAS and inhibit the proliferation and cell cycle progression of cancer cells, which are down-regulated in various cancers. The down-regulation of these miRNAs may be caused in part by the activation of the RAS signaling pathway, which forms a positive feedback loop. In pancreatic cancer cell lines, the expression of the miR-143/145 cluster is frequently lost. Molecular analysis indicated that RREB1, a transcriptional factor downstream of RAS, can directly bind to the promoter of miR-143/145 and repress their expression[70]. Interestingly, RAS and RREB1 were found to be targets of miR-143 and miR-145, respectively. Thus, in pancreatic cancer, activation of RAS activates RREB1, which in turn represses the expression of the miR-143/145 cluster. The repression of miR-143/145 in turn potentiates RAS signaling, which forms a feed forward circuit. Moreover, some molecules downstream of RAS/MAPK/Erk, such as c-myc, cyclin D2, and CDK6, are also repressed by the miR-143/145 cluster[71]. In addition to tumor suppressive miRNAs, RAS signaling also controls the expression of tumor-promoting miRNAs to facilitate its biological functions. miR-21 is a direct target of AP-1, a transcription factor downstream of the RAS/MAPK/Erk pathway. miR-21 inhibits the expression of several molecules that negatively regulate the RAS/MAPK/Erk pathway, such as Btg2, Spry1, and spry2[72].

In addition to the regulation of specific miRNAs, the RAS/

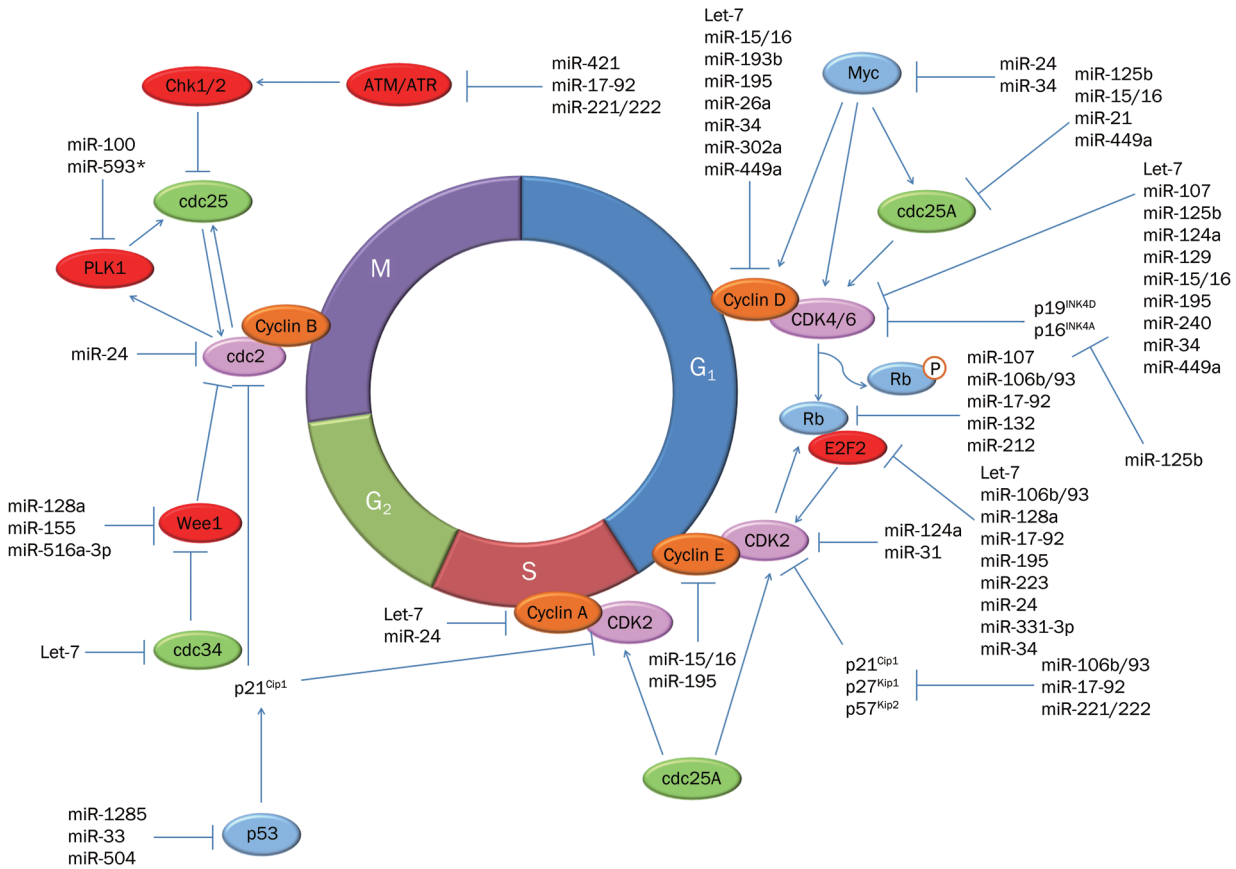

Figure 1. MicroRNAs in the control of cell cycle progression.

MAPK/Erk pathway also can control the expression of all miRNAs through phosphorylation of the HIV TAR RNA binding protein (TRBP), a critical protein of the miRNA generating complex[73]. The phosphorylation of TRBP by MAPK/Erk signaling enhances the expression of proliferation-promoting miRNAs and represses the expression of the let-7 tumor suppressor family. Together, these studies suggest that the RAS pathway can interact with the miRNA network to exert its biological functions.

PI3K/AKT pathway

The PI3K/AKT pathway is another important signaling cascade induced in response to mitogenic stimulation. PI3K/AKT can transduce multiple extracellular signals during G_1 and induce the cell to commit to DNA replication and division. In cancers, the aberrant activation of the PI3K/AKT pathway results in the up-regulation of cyclin D1, activation of the CDK2/cyclin E complex and down-regulation of p21 and p27, coordinately promoting cell cycle progression and the uncontrolled proliferation of cancer cells. PTEN and SHIP are negative regulators of the PI3K/AKT pathway. Many members of the PI3K/AKT pathway are regulated by miRNAs. miR-29a and miR-126 target the p85α and p85β subunits of PI3K[74, 75], respectively. The down-regulation of miR-126 in colon cancer is associated with the up-regulation of the p85β subunit, which induces the phosphorylation of AKT and promotes the proliferation of colon cancer cells[75]. The AKT family is also regulated by miRNAs. For example, AKT1 is suppressed by miR-149* [76], AKT2 is suppressed by miR-184 and miR-150[77, 78], and AKT3 is suppressed by the miR-15/16 cluster[79]. PTEN is an important tumor suppressor that antagonizes PI3K activity by inhibiting the transformation of PIP2 to PIP3. In cancers, the expression of PTEN is repressed by many oncogenic miRNAs, including miR-21[80, 81], miR-221/2[82], miR-301[83], miR-144[84], miR-136[84], and miR-19[85]. SHIP is another lipid phosphatase that inhibits the generation of PIP3. The expression of SHIP can be suppressed by miR-155 in leukemia and lymphoma[86]. The down-regulation of SHIP and up-regulation of miR-155 initiates a series of events that lead to leukemia/lymphoma in a transgenic mouse model. Furthermore, the reduction of SHIP by miR-155 activates PI3K/AKT activation[87]. mTOR is a direct target of PI3K/AKT activation, which is activated by AKT phosphorylation. The activation of mTOR promotes the translation of cell cycle-related proteins, such as c-myc, and represses the expression of p21 and p27. In src-transformed tumor cells, miR-99a is down-regulated, which results in the up-regulation of mTOR[88]. Moreover, the expression of miR-99a is inversely correlated with mTOR expression in lung cancer, and the re-expression of miR-99a in cancer cells inhibited the growth of tumors. Two other miRNAs that target mTOR

Table 1. MicroRNAs and targeted cell cycle regulators.

MicroRNAs	Cell cycle regulators	Reference
miR-124a	CDK2, CDK6	48
miR-132/212	RB1	56
miR-107	CDK6, RBL2	43
miR-137	CDC42	121
miR-26a	Cyclin D1, Cyclin D2	112
miR-593*	PLK1	60
miR-410/650	CDK1	122
miR-449a	Cyclin D1, CDK6, CDC25A	35, 44
miR-33	p53	123
miR-193b	Cyclin D1	36
miR-221/2	p27, p57, PTEN	52, 53
miR-331–3p	E2F1	124
miR-29	CDC42	125
Let-7	E2F2, CyclinD1, Cyclin D2, Cyclin D3, Cyclin A, CDK4, CDC34	9–13
miR-17-92, miR-106b/93	p21, p63, p57, E2F1, E2F2, E2F3, RBL2	15–17, 19–25, 54
miR-129	CDK6	45
miR-125b	CDKN2A, CDK6, CDC25A	46
miR-34	c-myc, Cyclin D1, CDK4, CDK6, E2F3, MYCN	28–34
miR-421	ATM	126
miR-223	E2F1	94
miR-15/16	Cyclin E1, Cyclin D1, Cyclin D2, Cyclin D3, CDC25A, c-myb, CDK6	37–39
miR-21	CDC25A	127
miR-24	E2F2, MYC, CCNA2, CDC2, CDK4	47, 57
miR-100	PLK1	59
miR-195	CDK6, Cyclin D1, E2F3, Cyclin E1	41
miR-128a	E2F3a, Wee 1	61, 128
miR-302a	Cyclin D1	42
miR-1285	p53	129
miR-504	p53	130
miR-155, miR-516a-3p	Wee 1	61

are miR-101 and miR-199a-3p, which suppress the expression of mTOR in lymphoma[89] and hepatocarcinoma[90], respectively.

Myc and E2F family

Myc is a transcription factor that integrates various extracellular signals and initiates transcriptional events to control proliferation, apoptosis and cell cycle progression. The dysregulation of myc is a common event in cancer development. In recent years, studies on miRNAs in the myc regulatory network have contributed to the understanding of the mechanism of myc activities. As a transcription factor, myc regulates the expression of many miRNAs[91]. It has been determined that myc-induced miRNAs directly participate in the down-regulation of myc-repressed genes. For instance, myc activation induces the expression of miR-221 and miR-222, which target p27 and p57. p27 and p57 are known to be repressed by myc. Thus, myc-induced miRNAs can interact with myc target genes to regulate cell cycle progression. In addition to regulating the miRNAs, myc is also directly targeted by miRNAs. In neuroblastoma, let-7e and miR-101 directly target the 3′-UTR, repress the expression of myc and inhibit the growth of tumor cells[92]. In non-small cell lung cancer, miR-145 inhibits proliferation and the G_1/S transition by directly targeting c-myc[93].

The E2F family members are direct targets of myc and regulate the expression of many genes controlling cell cycle progression. As mentioned above, the expression of the E2F family members is tightly controlled by the miR-17-92 family. The interaction between the miR-17-92 and E2F family members is complex. E2F1, E2F2, and E2F3 directly bind to the promoter of miR-20a and activate its transcription; however, miR-20a modulates the translation of E2F2 and E2F3, which suggests an autoregulatory feedback loop between the E2F family members and miR-20a[16]. The rest of the members of the miR-17-92 and miR-106b/93 clusters also interact with the E2F family members and form autoregulatory feedback loops[17, 25]. In addition to the miR-17-92 family members, E2F1 also binds to the promoter of miR-223 and represses its transcription, and E2F1 is also targeted by miR-223[94].

p53 network

p53 is one of the central players in the response to DNA dam-

age and other cellular stresses. p53 is a tumor suppressor that is frequently deleted and/or mutated in tumors. When cells encounter genotoxic insults, p53 controls the transcription of many target genes, among which p21 is the major response molecule that induces cell cycle arrest. The miR-34 family members are direct targets of p53[26, 27] and coordinate with p53 to suppress cell cycle progression and tumor growth. miR-107 is another target of p53[95]. p53 can bind to the promoter of PANK1, the host gene of miR-107, and activate the transcription of PANK1 and miR-107. Interestingly, miR-107 suppresses the expression of two important G_1/S regulators, CDK6 and RBL2. These studies show that miRNAs act as important players in the p53 network.

Implications of cell cycle-related miRNAs in anti-cancer therapies

Cell cycle-related miRNAs can act as oncogenes or tumor suppressors

Cell cycle deregulation and the resulting uncontrolled proliferation is one of the hallmarks of cancer. miRNAs have been shown to be crucial regulators of cell cycle progression, and aberrant expression of miRNAs is universal in human cancer. The first evidence of an aberrantly expressed miRNA was the miR-15/16 cluster, which is frequently deleted and/or down-regulated in chronic lymphocytic leukemia (CLL)[96]. Through microarray technology, the miRNA expression profiles of lung[97], liver[98, 99], breast[100], colon[101, 102] and gastric cancer[103] have been reported, and the results indicate that miRNAs are abnormally expressed in various cancers. Many cell cycle-related miRNAs are specifically deregulated in cancer and function as oncogenes or tumor suppressors. It has been reported that the miR-17-92 cluster is frequently amplified[14, 15], and let-7 is frequently down-regulated[9, 104] in various cancers. miR-17-92 exerts oncogenic functions through positively regulating cell cycle-related proteins, including p21, p63, p57, and RBL2[18–21], whereas let-7 exerts its tumor suppressive function by down-regulating RAS, cyclins and CDK4[8–11]. miR-21 is activated by RAS signaling and suppressed by several negative regulators of RAS signaling and the PI3K/AKT pathway, which in turn potentiates RAS activation and PI3K/AKT activities[72]. The crosstalk between miR-21 and cell cycle regulation contributes to the development of a cancer phenotype. In summary, the cell cycle-related miRNAs can act as oncogenes or tumor suppressors by affecting cell cycle progression, which causes uncontrolled proliferation and more aggressive cancer phenotypes.

miRNAs may serve as therapeutic targets/candidates in cancer

As oncogenes or tumor suppressors, cell cycle-related miRNAs may serve as therapeutic targets in cancers. By specific inhibition or selective re-introduction of miRNAs in cancers, miRNAs may have therapeutic effects. Approaches to the delivery of miRNAs *in vivo* include anti-miRNA oligonucleotides, antagomiRs, locked nucleic acid (LNA), miRNA sponges and nanoparticles, which each have their advantages and disadvantages that have been elegantly reviewed elsewhere[105]. Importantly, some miRNAs have been shown to suppress tumor growth *in vitro* and *in vivo*. Let-7 inhibits the proliferation of hepatocellular carcinoma cells (HCC)[106], prostate cancer cells[12], lung cancer cells[107] and melanoma cells[11] *in vitro* and the tumor growth of lung cancer[108] and breast cancer[109] *in vivo*. Therapeutic studies on miRNAs *in vivo* have revealed promising results. miR-21 is up-regulated by RAS *in vitro* and *in vivo* and is frequently overexpressed in human cancers. LNA directed against miR-21 reduced tumor growth *in vivo*[110], which suggests a therapeutic role for anti-miR-21 in treating cancers. In addition, miR-16, which is frequently deleted and/or down-regulated in human cancers, significantly inhibits prostate tumor growth *in vivo* when delivered by atelocollagen via tail vein injection[111]. These results indicate that the delivery of miR-16 could be used to treat patients with advanced prostate cancer. Notably, miR-26a is down-regulated in HCC, and the restoration of miR-26a *in vitro* induces cell cycle arrest by targeting cyclin D2 and cyclin E2. Intriguingly, the delivery of miR-26a using adeno-associated virus (AAV) inhibits the proliferation of cancer cells, induces tumor-specific apoptosis and results in dramatic protection from disease progression without toxicity[112]. Together, these *in vitro* and *in vivo* studies suggest that miRNAs can be targeted or directly delivered *in vivo* to suppress tumor growth, which may provide new strategies for developing next-generation anti-cancer therapeutics.

miRNAs are also associated with chemosensitivity and radiation sensitivity. miR-221/222 are overexpressed in fulvestrant-resistant breast cancer cells and are associated with the acquisition of fulvestrant resistance[113]. Furthermore, up-regulation of miR-221/222 in breast cancer cells also causes tamoxifen resistance by targeting p27[114]. miR-221/222 is a promising candidate for breast cancer with chemoresistance. Another miRNA that has been shown to be involved in chemoresistance is miR-21. miR-21-transfected HCC cells are resistant to 5-fluorouracil/interferon-α[115], which suggests that anti-miR-21 may increase the chemosensitivity of cancer cells. Indeed, anti-miR-21 improves the cytotoxicity induced by 5-FU in glioblastoma cells[116]. Anti-miR-21 also increases the chemosensitivity of cells to arsenic trioxide[117] and taxol[118]. These findings suggest that anti-miR-21 could be used in combination with chemical reagents to increase the cytotoxic effects of cancer therapeutics.

miRNAs are also involved in the radiation sensitivity of cancers. In prostate cancer, multiple miRNAs, including miR-106b, have demonstrated altered expression in response to radiation[119]. The up-regulation of miR-106b in prostate cancer overrides p21-activated cell cycle arrest and growth inhibition induced by radiation[119], providing a potential target for radiation-resistant prostate cancer. In contrast to miR-106b, miR-101 sensitizes tumor cells to radiation in vitro and in vivo by targeting DNA-PKCs and ATM[120]. Collectively, studies on the involvement of miRNAs in chemo- and radio resistance and sensitivity provide new targets and candidates for cancer treatment.

Conclusion

Herein, we summarized the current understanding of miRNAs in regulating cell cycle progression. Many cell cycle regulatory proteins are regulated by miRNAs, and these proteins also control the expression of miRNAs, which display a complex interaction network. The deregulation of this network is tightly associated with the progression of human cancers. The discovery and thorough understanding of this complicated network will open an avenue for developing novel, promising therapeutics for the treatment of cancer.

Acknowledgements

This work was partially supported by the National Natural Science Foundation of China (No 91029728 and 81071637), the Science & Technology Commission of Shanghai Municipality (10JC1414200) and the Shanghai Rising-Star Program Funds (11QA1406200). We thank Jie Ding for artwork preparation and Jian Yao for manuscript editing. We apologize to those colleagues who have contributed to this exciting field but whose work could not be cited because of space limitations.

References

1 CJ Sherr, JM Roberts. CDK inhibitors: positive and negative regulators of G1-phase progression. Genes Dev 1999; 13: 1501–12.
2 Yang J, Xu ZP, Huang Y, Hamrick HE, Duerksen-Hughes PJ, Yu YN. ATM and ATR: sensing DNA damage. World J Gastroenterol 2004; 10: 155–60.
3 Malumbres M, Barbacid M. Cell cycle, CDKs and cancer: a changing paradigm. Nat Rev Cancer 2009; 9: 153–66.
4 L He, GJ Hannon, MicroRNAs: small RNAs with a big role in gene regulation. Nat Rev Genet 2004; 5: 522–31.
5 Friedman RC, Farh KK, Burge CB, Bartel DP. Most mammalian mRNAs are conserved targets of microRNAs. Genome Res 2009; 19: 92–105.
6 He L, Thomson JM, Hemann MT, Hernando-Monge E, Mu D, Goodson S, *et al*. A microRNA polycistron as a potential human oncogene. Nature 2005; 435: 828–33.
7 Cimmino A, Calin GA, Fabbri M, Iorio MV, Ferracin M, Shimizu M, *et al*. miR-15 and miR-16 induce apoptosis by targeting BCL2. Proc Natl Acad Sci U S A 2005; 102: 13944–9.
8 Reinhart BJ, Slack FJ, Basson M, Pasquinelli AE, Bettinger JC, Rougvie AE, *et al*. The 21-nucleotide let-7 RNA regulates developmental timing in *Caenorhabditis elegans*. Nature 2000; 403: 901–6.
9 Takamizawa J, Konishi H, Yanagisawa K, Tomida S, Osada H, Endoh H, *et al*. Reduced expression of the let-7 microRNAs in human lung cancers in association with shortened postoperative survival. Cancer Res 2004; 64: 3753–6.
10 Johnson CD, Esquela-Kerscher A, Stefani G, Byrom M, Kelnar K, Ovcharenko D, *et al*. The let-7 microRNA represses cell proliferation pathways in human cells. Cancer Res 2007; 67: 7713–22.
11 Schultz J, Lorenz P, Gross G, Ibrahim S, Kunz M. MicroRNA let-7b targets important cell cycle molecules in malignant melanoma cells and interferes with anchorage-independent growth. Cell Res 2008; 18: 549–57.
12 Dong Q, Meng P, Wang T, Qin W, Qin W, Wang F, *et al*. MicroRNA let-7a inhibits proliferation of human prostate cancer cells *in vitro* and *in vivo* by targeting E2F2 and CCND2. PLoS One 2010; 5: e10147.
13 Legesse-Miller A, Elemento O, Pfau SJ, Forman JJ, Tavazoie S, Coller HA. Let-7 overexpression leads to an increased fraction of cells in G_2/M, direct down–regulation of Cdc34, and stabilization of Wee1 kinase in primary fibroblasts. J Biol Chem 2009; 284: 6605–9.
14 Hayashita Y, Osada H, Tatematsu Y, Yamada H, Yanagisawa K, Tomida S, *et al*. A polycistronic microRNA cluster, miR-17-92, is overexpressed in human lung cancers and enhances cell proliferation. Cancer Res 2005 ; 65: 9628–32.
15 Dews M, Homayouni A, Yu D, Murphy D, Sevignani C, Wentzel E, *et al*. Augmentation of tumor angiogenesis by a Myc-activated microRNA cluster. Nat Genet 2006; 38: 1060–5.
16 Sylvestre Y, De Guire V, Querido E, Mukhopadhyay UK, Bourdeau V, Major F, *et al*. An E2F/miR-20a autoregulatory feedback loop. J Biol Chem 2007; 282: 2135–43.
17 Woods K, Thomson JM, Hammond SM. Direct regulation of an oncogenic micro-RNA cluster by E2F transcription factors. J Biol Chem 2007; 282: 2130–4.
18 Pickering MT, Stadler BM, Kowalik TF. miR-17 and miR-20a temper an E2F1-induced G_1 checkpoint to regulate cell cycle progression. Oncogene 2009; 28: 140–5.
19 Cloonan N, Brown MK, Steptoe AL, Wani S, Chan WL, Forrest AR, *et al*. The miR-17-5p microRNA is a key regulator of the G_1/S phase cell cycle transition. Genome Biol 2008; 9: R127.
20 Lu Y, Thomson JM, Wong HY, Hammond SM, Hogan BL. Transgenic over-expression of the microRNA miR-17-92 cluster promotes proliferation and inhibits differentiation of lung epithelial progenitor cells. Dev Biol 2007; 310: 442–53.
21 Wang Q, Li YC, Wang J, Kong J, Qi Y, Quigg RJ, *et al*. miR-17-92 cluster accelerates adipocyte differentiation by negatively regulating tumor-suppressor Rb2/p130. Proc Natl Acad Sci U S A 2008; 105: 2889–94.
22 Inomata M, Tagawa H, Guo YM, Kameoka Y, Takahashi N, Sawada K. MicroRNA-17-92 down-regulates expression of distinct targets in different B-cell lymphoma subtypes. Blood 2009; 113: 396–402.
23 Yu Z, Wang C, Wang M, Li Z, Casimiro MC, Liu M, *et al*. A cyclin D1/microRNA 17/20 regulatory feedback loop in control of breast cancer cell proliferation. J Cell Biol 2008; 182: 509–17.
24 Trompeter HI, Abbad H, Iwaniuk KM, Hafner M, Renwick N, Tuschl T, *et al*. MicroRNAs MiR-17, MiR-20a, and MiR-106b act in concert to modulate E2F activity on cell cycle arrest during neuronal lineage differentiation of USSC. PLoS One 2011; 6: e16138.
25 Petrocca F, Visone R, Onelli MR, Shah MH, Nicoloso MS, de Martino I, *et al*. E2F1-regulated microRNAs impair TGFbeta-dependent cell-cycle arrest and apoptosis in gastric cancer. Cancer Cell 2008; 13: 272–86.
26 He L, He X, Lim LP, de Stanchina E, Xuan Z, Liang Y, *et al*. A microRNA component of the p53 tumour suppressor network. Nature 2007; 447: 1130–4.
27 Chang TC, Wentzel EA, Kent OA, Ramachandran K, Mullendore M, Lee KH, *et al*. Transactivation of miR-34a by p53 broadly influences gene expression and promotes apoptosis. Mol Cell 2007; 26: 745–52.
28 Sun F, Fu H, Liu Q, Tie Y, Zhu J, Xing R, *et al*. Downregulation of CCND1 and CDK6 by miR-34a induces cell cycle arrest. FEBS Lett 2008; 582: 1564–8.
29 Cole KA, Attiyeh EF, Mosse YP, Laquaglia MJ, Diskin SJ, Brodeur GM, *et al*. A functional screen identifies miR-34a as a candidate neuroblastoma tumor suppressor gene. Mol Cancer Res 2008; 6: 735–42.
30 Welch C, Chen Y, Stallings RL. MicroRNA-34a functions as a potential tumor suppressor by inducing apoptosis in neuroblastoma cells. Oncogene 2007; 26: 5017–22.
31 Li Y, Guessous F, Zhang Y, Dipierro C, Kefas B, Johnson E, *et al*.

MicroRNA-34a inhibits glioblastoma growth by targeting multiple oncogenes. Cancer Res 2009; 69: 7569–76.
32 Pigazzi M, Manara E, Baron E, Basso G. miR-34b targets cyclic AMP-responsive element binding protein in acute myeloid leukemia. Cancer Res 2009; 69: 2471–8.
33 Navarro F, Gutman D, Meire E, Cáceres M, Rigoutsos I, Bentwich Z, *et al*. miR-34a contributes to megakaryocytic differentiation of K562 cells independently of p53. Blood 2009; 114: 2181–92.
34 Antonini D, Russo MT, De Rosa L, Gorrese M, Del Vecchio L, Missero C. Transcriptional repression of miR-34 family contributes to p63-mediated cell cycle progression in epidermal cells. J Invest Dermatol 2010; 130: 1249–57.
35 Noonan EJ, Place RF, Basak S, Pookot D, Li LC. miR-449a causes Rb-dependent cell cycle arrest and senescence in prostate cancer cells. Oncotarget 2010; 1: 349–58.
36 Xu C, Liu S, Fu H, Li S, Tie Y, Zhu J, *et al*. MicroRNA-193b regulates proliferation, migration and invasion in human hepatocellular carcinoma cells. Eur J Cancer 2010; 46: 2828–36.
37 Balakrishnan A, Stearns AT, Park PJ, Dreyfuss JM, Ashley SW, Rhoads DB, *et al*. MicroRNA miR-16 is anti-proliferative in enterocytes and exhibits diurnal rhythmicity in intestinal crypts. Exp Cell Res 2010; 316: 3512–21.
38 Bandi N, Zbinden S, Gugger M, Arnold M, Kocher V, Hasan L, *et al*. miR-15a and miR-16 are implicated in cell cycle regulation in a Rb-dependent manner and are frequently deleted or down-regulated in non-small cell lung cancer. Cancer Res 2009; 69: 5553–9.
39 Liu Q, Fu H, Sun F, Zhang H, Tie Y, Zhu J, *et al*. miR-16 family induces cell cycle arrest by regulating multiple cell cycle genes. Nucleic Acids Res 2008; 36: 5391–404.
40 Qin X, Wang X, Wang Y, Tang Z, Cui Q, Xi J, *et al*. MicroRNA-19a mediates the suppressive effect of laminar flow on cyclin D1 expression in human umbilical vein endothelial cells. Proc Natl Acad Sci U S A 2010; 107: 3240–4.
41 Xu T, Zhu Y, Xiong Y, Ge YY, Yun JP, Zhuang SM. MicroRNA-195 suppresses tumorigenicity and regulates G_1/S transition of human hepatocellular carcinoma cells. Hepatology 2009; 50: 113–21.
42 Card DA, Hebbar PB, Li L, Trotter KW, Komatsu Y, Mishina Y, *et al*. Oct4/Sox2-regulated miR-302 targets cyclin D1 in human embryonic stem cells. Mol Cell Biol 2008; 28: 6426–38.
43 Feng L, Xie Y, Zhang H, Wu Y. miR-107 targets cyclin–dependent kinase 6 expression, induces cell cycle G_1 arrest and inhibits invasion in gastric cancer cells. Med Oncol 2011. DOI: 10.1007/s12032-011-9823-1.
44 Yang X, Feng M, Jiang X, Wu Z, Li Z, Aau M, *et al*. miR-449a and miR-449b are direct transcriptional targets of E2F1 and negatively regulate pRb-E2F1 activity through a feedback loop by targeting CDK6 and CDC25A. Genes Dev 2009; 23: 2388–93.
45 Wu J, Qian J, Li C, Kwok L, Cheng F, Liu P. miR-129 regulates cell proliferation by downregulating Cdk6 expression. Cell Cycle 2010; 9: 1809–18.
46 Shi L, Zhang J, Pan T, Zhou J, Gong W, Liu N, *et al*. MiR-125b is critical for the suppression of human U251 glioma stem cell proliferation. Brain Res 2010; 1312: 120–6.
47 Lal A, Navarro F, Maher CA, Maliszewski LE, Yan N, O'Day E, *et al*. MiR-24 inhibits cell proliferation by targeting E2F2, MYC, and other cell-cycle genes via binding to "seedless" 3′UTR microRNA recognition elements. Mol Cell 2009; 35: 610–25.
48 Agirre X, Vilas-Zornoza A, Jiménez-Velasco A, Martin-Subero JI, Cordeu L, Gárate L, *et al*. Epigenetic silencing of the tumor suppressor microRNA Hsa-miR-124a regulates CDK6 expression and confers a poor prognosis in acute lymphoblastic leukemia. Cancer Res 2009; 69: 4443–53.
49 Sekiya Y, Ogawa T, Iizuka M, Yoshizato K, Ikeda K, Kawada N. Down-regulation of cyclin E1 expression by microRNA-195 accounts for interferon-β-induced inhibition of hepatic stellate cell proliferation. J Cell Physiol 2011; 226: 2535–42.
50 Borgdorff V, Lleonart ME, Bishop CL, Fessart D, Bergin AH, Overhoff MG, *et al*. Multiple microRNAs rescue from Ras-induced senescence by inhibiting $p21^{Waf1/Cip1}$. Oncogene 2010; 29: 2262–71.
51 Wu S, Huang S, Ding J, Zhao Y, Liang L, Liu T, *et al*. Multiple microRNAs modulate $p21^{Cip1/Waf1}$ expression by directly targeting its 3′ untranslated region. Oncogene 2010; 29: 2302–8.
52 Dai R, Li J, Liu Y, Yan D, Chen S, Duan C, *et al*. miR-221/222 suppression protects against endoplasmic reticulum stress-induced apoptosis via p27(Kip1)- and MEK/ERK-mediated cell cycle regulation. Biol Chem 2010; 391: 791–801.
53 Qian K, Hu L, Chen H, Li H, Liu N, Li Y, *et al*. Hsa-miR-222 is involved in differentiation of endometrial stromal cells *in vitro*. Endocrinology 2009; 150: 4734–43.
54 Sengupta S, Nie J, Wagner RJ, Yang C, Stewart R, Thomson JA. MicroRNA 92b controls the G_1/S checkpoint gene p57 in human embryonic stem cells. Stem Cells 2009; 27: 1524–8.
55 Lal A, Kim HH, Abdelmohsen K, Kuwano Y, Pullmann R Jr, Srikantan S, *et al*. p16(INK4a) translation suppressed by miR-24. PLoS One 2008; 3: e1864.
56 Park JK, Henry JC, Jiang J, Esau C, Gusev Y, Lerner MR, *et al*. miR-132 and miR-212 are increased in pancreatic cancer and target the retinoblastoma tumor suppressor. Biochem Biophys Res Commun 2011; 406: 518–23.
57 Mishra PJ, Song B, Mishra PJ, Wang Y, Humeniuk R, Banerjee D, *et al*. MiR-24 tumor suppressor activity is regulated independent of p53 and through a target site polymorphism. PLoS One 2009; 4: e8445.
58 Song B, Wang Y, Kudo K, Gavin EJ, Xi Y, Ju J. miR-192 Regulates dihydrofolate reductase and cellular proliferation through the p53-microRNA circuit. Clin Cancer Res 2008; 14: 8080–6.
59 Shi W, Alajez NM, Bastianutto C, Hui AB, Mocanu JD, Ito E, *et al*. Significance of Plk1 regulation by miR-100 in human nasopharyngeal cancer. Int J Cancer 2010; 126: 2036–48.
60 Ito T, Sato F, Kan T, Cheng Y, David S, Agarwal R, *et al*. Polo-like kinase 1 regulates cell proliferation and is targeted by miR-593* in esophageal cancer. Int J Cancer 2011; 129: 2134–46.
61 Butz H, Likó I, Czirják S, Igaz P, Khan MM, Zivkovic V, *et al*. Down–regulation of Wee1 kinase by a specific subset of microRNA in human sporadic pituitary adenomas. J Clin Endocrinol Metab 2010; 95: E181–91.
62 Lee ST, Chu K, Oh HJ, Im WS, Lim JY, Kim SK, *et al*. Let-7 microRNA inhibits the proliferation of human glioblastoma cells. J Neurooncol 2011; 102: 19–24.
63 Kumar MS, Erkeland SJ, Pester RE, Chen CY, Ebert MS, Sharp PA, *et al*. Suppression of non-small cell lung tumor development by the let-7 microRNA family. Proc Natl Acad Sci U S A 2008; 105: 3903–8.
64 Tsang WP, Kwok TT. The miR-18a* microRNA functions as a potential tumor suppressor by targeting on K-Ras. Carcinogenesis 2009; 30: 953–9.
65 Chen X, Guo X, Zhang H, Xiang Y, Chen J, Yin Y, *et al*. Role of miR-143 targeting KRAS in colorectal tumorigenesis. Oncogene 2009; 28: 1385–92.
66 Hashimoto Y, Akiyama Y, Otsubo T, Shimada S, Yuasa Y. Involvement of epigenetically silenced microRNA-181c in gastric carcinogenesis. Carcinogenesis 2010; 31: 777–84.
67 Shin KH, Bae SD, Hong HS, Kim RH, Kang MK, Park NH. miR-181a shows tumor suppressive effect against oral squamous cell

carcinoma cells by downregulating K-ras. Biochem Biophys Res Commun 2011; 404: 896–902.
68 Yu S, Lu Z, Liu C, Meng Y, Ma Y, Zhao W, *et al*. miRNA-96 suppresses KRAS and functions as a tumor suppressor gene in pancreatic cancer. Cancer Res 2010; 70: 6015–25.
69 Liu J, Luo XJ, Xiong AW, Zhang ZD, Yue S, Zhu MS, MicroRNA-214 promotes myogenic differentiation by facilitating exit from mitosis via down–regulation of proto-oncogene N-ras. J Biol Chem 2010; 285: 26599–607.
70 Kent OA, Chivukula RR, Mullendore M, Wentzel EA, Feldmann G, Lee KH, *et al*. Repression of the miR-143/145 cluster by oncogenic Ras initiates a tumor-promoting feed-forward pathway. Genes Dev 2010; 24: 2754–9.
71 Zhu H, Dougherty U, Robinson V, Mustafi R, Pekow J, Kupfer S, *et al*. EGFR signals down-regulate tumor suppressors miR-143 and miR-145 in Western diet-promoted murine colon cancer: role of G_1 regulators. Mol Cancer Res 2011; 9: 960–75.
72 Hatley ME, Patrick DM, Garcia MR, Richardson JA, Bassel-Duby R, van Rooij E, *et al*. Modulation of K-Ras-dependent lung tumorigenesis by MicroRNA-21. Cancer Cell 2010; 18: 282–93.
73 Paroo Z, Ye X, Chen S, Liu Q. Phosphorylation of the human microRNA-generating complex mediates MAPK/Erk signaling. Cell 2009; 139: 112–22.
74 Pandey AK, Verma G, Vig S, Srivastava S, Srivastava AK, Datta M. miR-29a levels are elevated in the *db/db* mice liver and its overexpression leads to attenuation of insulin action on PEPCK gene expression in HepG2 cells. Mol Cell Endocrinol 2011; 332: 125–33.
75 Guo C, Sah JF, Beard L, Willson JK, Markowitz SD, Guda K. The noncoding RNA, miR-126, suppresses the growth of neoplastic cells by targeting phosphatidylinositol 3-kinase signaling and is frequently lost in colon cancers. Genes Chromosomes Cancer 2008; 47: 939–46.
76 Lin RJ, Lin YC, Yu AL. miR-149* induces apoptosis by inhibiting Akt1 and E2F1 in human cancer cells. Mol Carcinog 2010; 49: 719–27.
77 Watanabe A, Tagawa H, Yamashita J, Teshima K, Nara M, Iwamoto K, *et al*. The role of microRNA-150 as a tumor suppressor in malignant lymphoma. Leukemia 2011; 25: 1324–34.
78 Foley NH, Bray IM, Tivnan A, Bryan K, Murphy DM, Buckley PG. MicroRNA-184 inhibits neuroblastoma cell survival through targeting the serine/threonine kinase AKT2. Mol Cancer 2010; 9: 83.
79 Roccaro AM, Sacco A, Thompson B, Leleu X, Azab AK, Azab F, *et al*. MicroRNAs 15a and 16 regulate tumor proliferation in multiple myeloma. Blood 2009; 113: 6669–80.
80 Liu C, Yu J, Yu S, Lavker RM, Cai L, Liu W, *et al*. MicroRNA-21 acts as an oncomir through multiple targets in human hepatocellular carcinoma. J Hepatol 2010; 53: 98–107.
81 Yamanaka Y, Tagawa H, Takahashi N, Watanabe A, Guo YM, Iwamoto K, *et al*. Aberrant overexpression of microRNAs activate AKT signaling via down-regulation of tumor suppressors in natural killer-cell lymphoma/leukemia. Blood 2009; 114: 3265–75.
82 Chun-Zhi Z, Lei H, An-Ling Z, Yan-Chao F, Xiao Y, Guang-Xiu W, *et al*. MicroRNA-221 and microRNA-222 regulate gastric carcinoma cell proliferation and radioresistance by targeting PTEN. BMC Cancer 2010; 10: 367.
83 Shi W, Gerster K, Alajez NM, Tsang J, Waldron L, Pintilie M, *et al*. MicroRNA-301 mediates proliferation and invasion in human breast cancer. Cancer Res 2011; 71: 2926–37.
84 Lee DY, Jeyapalan Z, Fang L, Yang J, Zhang Y, Yee AY, *et al*. Expression of versican 3′-untranslated region modulates endogenous microRNA functions. PLoS One 2010; 5: e13599.
85 Doghman M, El Wakil A, Cardinaud B, Thomas E, Wang J, Zhao W, *et al*. Regulation of insulin-like growth factor-mammalian target of rapamycin signaling by microRNA in childhood adrenocortical tumors. Cancer Res 2010; 70: 4666–75.
86 Costinean S, Sandhu SK, Pedersen IM, Tili E, Trotta R, Perrotti D, *et al*. Src homology 2 domain-containing inositol-5-phosphatase and CCAAT enhancer-binding protein beta are targeted by miR-155 in B cells of Emicro-MiR-155 transgenic mice. Blood 2009; 114: 1374–82.
87 Bhattacharyya S, Balakathiresan NS, Dalgard C, Gutti U, Armistead D, Jozwik C, *et al*. Elevated miR-155 promotes inflammation in cystic fibrosis by driving hyperexpression of interleukin-8. J Biol Chem 2011; 286: 11604–15.
88 Oneyama C, Ikeda J, Okuzaki D, Suzuki K, Kanou T, Shintani Y, *et al*. MicroRNA-mediated downregulation of mTOR/FGFR3 controls tumor growth induced by Src-related oncogenic pathways. Oncogene 2011; 30: 3489–501.
89 Merkel O, Hamacher F, Laimer D, Sifft E, Trajanoski Z, Scheideler M. Identification of differential and functionally active miRNAs in both anaplastic lymphoma kinase (ALK)+ and ALK– anaplastic large-cell lymphoma. Proc Natl Acad Sci U S A 2010; 107: 16228–33.
90 Bhatia S, Kaul D, Varma N. Functional genomics of tumor suppressor miR-196b in T-cell acute lymphoblastic leukemia. Mol Cell Biochem 2011; 346: 103–16.
91 Kim JW, Mori S, Nevins JR. Myc-induced microRNAs integrate Myc-mediated cell proliferation and cell fate. Cancer Res 2010; 70: 4820–8.
92 Buechner J, Tømte E, Haug BH, Henriksen JR, Løkke C, Flægstad T, *et al*. Tumour-suppressor microRNAs let-7 and mir-101 target the proto-oncogene MYCN and inhibit cell proliferation in MYCN-amplified neuroblastoma. Br J Cancer 2011; 105: 296–303.
93 Chen Z, Zeng H, Guo Y, Liu P, Pan H, Deng A, *et al*. miRNA-145 inhibits non-small cell lung cancer cell proliferation by targeting c-Myc. J Exp Clin Cancer Res 2010; 29: 151.
94 Pulikkan JA, Dengler V, Peramangalam PS, Peer Zada AA, Müller-Tidow C, Bohlander SK, *et al*. Cell-cycle regulator E2F1 and microRNA-223 comprise an autoregulatory negative feedback loop in acute myeloid leukemia. Blood 2010; 115: 1768–78.
95 Böhlig L, Friedrich M, Engeland K. p53 activates the PANK1/miRNA-107 gene leading to downregulation of CDK6 and p130 cell cycle proteins. Nucleic Acids Res 2011; 39: 440–53.
96 Calin GA, Dumitru CD, Shimizu M, Bichi R, Zupo S, Noch E, *et al*. Frequent deletions and down-regulation of micro-RNA genes miR-15 and miR-16 at 13q14 in chronic lymphocytic leukemia. Proc Natl Acad Sci U S A 2002; 99: 15524–9.
97 Yanaihara N, Caplen N, Bowman E, Seike M, Kumamoto K, Yi M, *et al*. Unique microRNA molecular profiles in lung cancer diagnosis and prognosis. Cancer Cell 2006; 9: 189–98.
98 Murakami Y, Yasuda T, Saigo K, Urashima T, Toyoda H, Okanoue T, *et al*. Comprehensive analysis of microRNA expression patterns in hepatocellular carcinoma and non-tumorous tissues. Oncogene 2006; 25: 2537–45.
99 Li W, Xie L, He X, Li J, Tu K, Wei L, *et al*. Diagnostic and prognostic implications of microRNAs in human hepatocellular carcinoma. Int J Cancer 2008; 123: 1616–22.
100 Iorio MV, Ferracin M, Liu CG, Veronese A, Spizzo R, Sabbioni S, *et al*. MicroRNA gene expression deregulation in human breast cancer. Cancer Res 2005; 65: 7065–70.
101 Michael MZ, SM OC, van Holst Pellekaan NG, Young GP, James RJ. Reduced accumulation of specific microRNAs in colorectal neoplasia. Mol Cancer Res 2003; 1: 882–91.
102 Schetter AJ, Leung SY, Sohn JJ, Zanetti KA, Bowman ED, Yanaihara

N, *et al*. MicroRNA expression profiles associated with prognosis and therapeutic outcome in colon adenocarcinoma. JAMA 2008; 299: 425–36.

103 Petrocca F, Visone R, Onelli MR, Shah MH, Nicoloso MS, de Martino I, *et al*. E2F1-regulated microRNAs impair TGFbeta-dependent cell-cycle arrest and apoptosis in gastric cancer. Cancer Cell 2008; 13: 272–86.

104 Sempere LF, Christensen M, Silahtaroglu A, Bak M, Heath CV, Schwartz G, *et al*. Altered microRNA expression confined to specific epithelial cell sub-populations in breast cancer. Cancer Res 2007; 67: 11612–20.

105 Nana-Sinkam SP, Croce CM. MicroRNAs as therapeutic targets in cancer. Transl Res 2011; 157: 216–25.

106 Lan FF, Wang H, Chen YC, Chan CY, Ng SS, Li K, *et al*. Hsa-let-7g inhibits proliferation of hepatocellular carcinoma cells by down-regulation of c-Myc and upregulation of p16(INK4A). Int J Cancer 2011; 128: 319–31.

107 He XY, Chen JX, Zhang Z, Li CL, Peng QL, Peng HM. The let-7a microRNA protects from growth of lung carcinoma by suppression of k-Ras and c-Myc in nude mice. J Cancer Res Clin Oncol 2010; 136: 1023–8.

108 Esquela-Kerscher A, Trang P, Wiggins JF, Patrawala L, Cheng A, Ford L, *et al*. The let-7 microRNA reduces tumor growth in mouse models of lung cancer. Cell Cycle 2008; 7: 759–64.

109 Yu F, Yao H, Zhu P, Zhang X, Pan Q, Gong C, *et al*. let-7 regulates self renewal and tumorigenicity of breast cancer cells. Cell 2007; 131: 1109–23.

110 Frezzetti D, De Menna M, Zoppoli P, Guerra C, Ferraro A, Bello AM, *et al*. Upregulation of miR-21 by Ras *in vivo* and its role in tumor growth. Oncogene 2011; 30: 275–86.

111 Takeshita F, Patrawala L, Osaki M, Takahashi RU, Yamamoto Y, Kosaka N, *et al*. Systemic delivery of synthetic microRNA-16 inhibits the growth of metastatic prostate tumors via downregulation of multiple cell-cycle genes. Mol Ther 2010; 18: 181–7.

112 Kota J, Chivukula RR, O'Donnell KA, Wentzel EA, Montgomery CL, Hwang HW, *et al*. Therapeutic microRNA delivery suppresses tumorigenesis in a murine liver cancer model. Cell 2009; 137: 1005–17.

113 Rao X, Di Leva G, Li M, Fang F, Devlin C, Hartman-Frey C, *et al*. MicroRNA-221/222 confers breast cancer fulvestrant resistance by regulating multiple signaling pathways. Oncogene 2011; 30: 1082–97.

114 Miller TE, Ghoshal K, Ramaswamy B, Roy S, Datta J, Shapiro CL, *et al*. MicroRNA-221/222 confers tamoxifen resistance in breast cancer by targeting $p27^{Kip1}$. J Biol Chem 2008; 283: 29897–903.

115 Tomimaru Y, Eguchi H, Nagano H, Wada H, Tomokuni A, Kobayashi S, *et al*. MicroRNA-21 induces resistance to the anti-tumour effect of interferon-α/5-fluorouracil in hepatocellular carcinoma cells. Br J Cancer 2010; 103: 1617–26.

116 Ren Y, Kang CS, Yuan XB, Zhou X, Xu P, Han L, *et al*. Co-delivery of as-miR-21 and 5-FU by poly(amidoamine) dendrimer attenuates human glioma cell growth *in vitro*. J Biomater Sci Polym Ed 2010; 21: 303–14.

117 Li Y, Zhu X, Gu J, Dong D, Yao J, Lin C, *et al*. Anti-miR-21 oligonucleotide sensitizes leukemic K562 cells to arsenic trioxide by inducing apoptosis. Cancer Sci 2010; 101: 948–54.

118 Mei M, Ren Y, Zhou X, Yuan XB, Han L, Wang GX, *et al*. Down-regulation of miR-21 enhances chemotherapeutic effect of taxol in breast carcinoma cells. Technol Cancer Res Treat 2010; 9: 77–86.

119 Li B, Shi XB, Nori D, Chao CK, Chen AM, Valicenti R, *et al*. Down-regulation of microRNA 106b is involved in p21-mediated cell cycle arrest in response to radiation in prostate cancer cells. Prostate 2011; 71: 567–74.

120 Yan D, Ng WL, Zhang X, Wang P, Zhang Z, Mo YY, *et al*. Targeting DNA-PKCs and ATM with miR-101 sensitizes tumors to radiation. PLoS One 2010; 5: e11397.

121 Chen Q, Chen X, Zhang M, Fan Q, Luo S, Cao X. miR-137 is frequently down-regulated in gastric cancer and is a negative regulator of Cdc42. Dig Dis Sci 2011; 56: 2009–16.

122 Chien WW, Domenech C, Catallo R, Kaddar T, Magaud JP, Salles G, *et al*. Cyclin-dependent kinase 1 expression is inhibited by $p16^{INK4a}$ at the post-transcriptional level through the microRNA pathway. Oncogene 2011; 30: 1880–91.

123 Herrera-Merchan A, Cerrato C, Luengo G, Dominguez O, Piris MA, Serrano M, *et al*. miR-33-mediated downregulation of p53 controls hematopoietic stem cell self-renewal. Cell Cycle 2010; 9: 3277–85.

124 Guo X, Guo L, Ji J, Zhang J, Zhang J, Chen X, *et al*. miRNA-331-3p directly targets E2F1 and induces growth arrest in human gastric cancer. Biochem Biophys Res Commun 2010; 398: 1–6.

125 Lang N, Liu M, Tang QL, Chen X, Liu Z, Bi F. Effects of microRNA-29 family members on proliferation and invasion of gastric cancer cell lines. Chin J Cancer 2010; 29: 603–10.

126 Hu H, Du L, Nagabayashi G, Seeger RC, Gatti RA. ATM is down-regulated by N-Myc-regulated microRNA-421. Proc Natl Acad Sci U S A 2010; 107: 1506–11.

127 Wang P, Zou F, Zhang X, Li H, Dulak A, Tomko RJ Jr, *et al*. microRNA-21 negatively regulates Cdc25A and cell cycle progression in colon cancer cells. Cancer Res 2009; 69: 8157–65.

128 Zhang Y, Chao T, Li R, Liu W, Chen Y, Yan X, *et al*. MicroRNA-128 inhibits glioma cells proliferation by targeting transcription factor E2F3a. J Mol Med 2009; 87: 43–51.

129 Tian S, Huang S, Wu S, Guo W, Li J, He X. MicroRNA-1285 inhibits the expression of p53 by directly targeting its 3′untranslated region. Biochem Biophys Res Commun 2010; 396: 435–9.

130 Hu W, Chan CS, Wu R, Zhang C, Sun Y, Song JS, *et al*. Negative regulation of tumor suppressor p53 by microRNA miR-504. Mol Cell 2010; 38: 689–99.

Acta Pharmacologica Sinica (2011) 32: 1321–1326
 1671-4083/11 $32.00
www.nature.com/aps

Original Article

Protective effect of Bu-7, a flavonoid extracted from *Clausena lansium*, against rotenone injury in PC12 cells

Bo-yu LI, Yu-he YUAN, Jin-feng HU, Qing ZHAO, Dong-ming ZHANG, Nai-hong CHEN*

State Key Laboratory of Bioactive Substances and Functions of Natural Medicines, Institute of Materia Medica, Chinese Academy of Medical Sciences and Peking Union Medical College, Beijing 100050, China

Aim: To investigate the protective effect and underlying mechanisms of Bu-7, a flavonoid isolated from the leaves of *Clausena lansium*, against rotenone-induced injury in PC12 cells.
Methods: The cell viability was evaluated using MTT assay. The cell apoptosis rate was analyzed using flow cytometry. JC-1 staining was used to detect the mitochondrial membrane potential (MMP). Western blotting analysis was used to determine the phosphorylation of c-Jun N-terminal kinase (JNK), p38 mitogen-activated protein kinase (p38), tumor protein 53 (p53), Bcl-2–associated X protein (Bax), B-cell lymphoma 2 (Bcl-2), and caspase 3.
Results: Treatment of PC12 cells with rotenone (1–20 μmol/L) significantly reduced the cell viability in a concentration-dependent manner. Pretreatment with Bu-7 (0.1 and 10 μmol/L) prevented PC12 cells from rotenone injury, whereas Bu-7 (1 μmol/L) had no significant effect. Pretreatment with Bu-7 (0.1 and 10 μmol/L) decreased rotenone-induced apoptosis, attenuated rotenone-induced mitochondrial potential reduction and suppressed rotenone-induced protein phosphorylation and expression, whereas Bu-7 (1 μmol/L) did not cause similar effects. Bu-7 showed inverted bell-shaped dose-response relationship in all the effects.
Conclusion: Bu-7 protects PC12 cells against rotenone injury, which may be attributed to MAP kinase cascade (JNK and p38) signaling pathway. Thus, Bu-7 may be a potential bioactive compound for the treatment of Parkinson's disease.

Keywords: Bu-7; *Clausena lansium*; neuroprotection; Parkinson's disease; rotenone; apoptosis; PC12 cells

Acta Pharmacologica Sinica (2011) 32: 1321–1326; doi: 10.1038/aps.2011.119; published online 3 Oct 2011

Introduction

Parkinson's disease (PD) is a major age-related neurodegenerative disorder which is accompanied primarily by motor symptoms, such as resting tremor, rigidity and bradykinesia. It is pathologically characterized by the loss of dopaminergic neurons in the substantia nigra pars compacta (SNpc) and the accumulation of aggregated alpha-synuclein in brain stem, spinal cord, and cortex[1]. Several lines of evidence have converged to suggest that environmental neurotoxins, such as rotenone[2], and mutant proteins, such as DJ-1, PINK1, and LRRK2[3], may be importantly involved in the etiopathogenesis of PD.

Long-term, systemic administration of rotenone, a natural substance which is widely used as a pesticide, produces the selective degeneration of dopaminergic neurons and PD-like locomotor symptoms in rats[2]. Among the various animal models of PD, the rotenone model has its own advantages. Firstly, unlike the other models, it reproduces most of the movement disorder symptoms and the histopathological features of PD, including Lewy bodies[4, 5]. Secondly, rotenone is a powerful inhibitor of complex I in the mitochondrial respiration, and recent epidemiological studies suggest the involvement of these toxic compounds in the higher incidence of sporadic Parkinsonism[6–8]. Observations have shown that a defect in mitochondrial complex I activity may induce the apoptosis of dopaminergic cells, which may contribute to the neurodegenerative process in PD[9]. Administration of rotenone has been used extensively to create PD models to screen for neuroprotective agents both *in vivo*[10, 11] and *in vitro*[12, 13].

Therapeutic efforts aimed at providing protection against apoptosis may be beneficial in PD. In this regard, natural products are attractive sources of chemical structures that could exhibit potent biological activities. *Clausena lansium* is a fruit tree native to the south of China, and a decoction of its dried leaves was used to treat acute and chronic viral hepatitis in local folk medicine[14]. More recently, there has been

* To whom correspondence should be addressed.
E-mail chennh@imm.ac.cn
Received 2011-05-11 Accepted 2011-07-20

renewed interest in the neuroprotective potential of the leaf extracts of *Clausena lansium*; for example, research has been carried out on the effects of clausenamide in enhancing learning and memory[15, 16]. In a previous attempt to detect more information about the biological activities of *Clausena lansium*, we separated the natural chemicals systematically from the leaves[17]. After preliminary screening, we found that one compound, termed Bu-7, was a biologically active substance. This is a known compound[18], and the chemical structure of Bu-7 is shown in Figure 1.

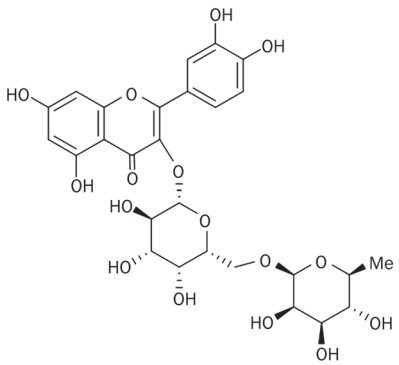

Figure 1. The chemical structure of Bu-7.

PC12 cells, a cell line established from a rat pheochromocytoma, have many properties in common with primary sympathetic neurons and chromaffin cell cultures, and these cells have been used primarily as neuron models[19]. In this article, we report the protective effect of Bu-7 in PC12 cells against rotenone injury.

Materials and methods

Drugs and reagents

Bu-7 was provided by the Department of Medicinal Chemistry, Institute of Materia Medica, Chinese Academy of Medical Sciences & Peking Union Medical College (Beijing, China). Rotenone, 6-OHDA and 1-methyl-4-phenylpyridinium (MPP^+) were purchased from Sigma-Aldrich (St Louis, MO, USA). 3-(4,5-Dimethylthiazol-2-yl)-2,5-diphenyl-tetrazolium bromide (MTT) and propidium iodide (PI) were purchased from Sigma Chemical Company (USA). JC-1 and Rhodamine 123 were purchased from Beyotime (China). Primary antibodies and secondary antibodies were purchased from Cell Signaling Technology (USA). All other chemicals were of analytical grade and commercially available.

Compound preparation

The Bu-7 compound was prepared as previously described[17]. Briefly, the air-dried leaves (0.8 kg) of *Clausena lansium* were extracted with 70% ethanol for 2 h under reflux conditions, and the 70% ethanol extract was concentrated under reduced pressure. Subsequently, it was partitioned with petroleum ether (60–90 °C), ethyl acetate and butyl alcohol, respectively. The butyl alcohol portion (50 g) was chromatographed over a silica gel column using ethyl acetate-methanol as the gradient eluent (50:1–1:1, *v/v*) to produce 32 fractions. Fractions 20–27 were subjected to RP-18 column chromatography and eluted using a gradient of methanol-H_2O (30%–70%, *v/v*) to 20 fractions. Fraction 11 (1.1 g) was subjected to column chromatography on silica gel and eluted with $CHCl_3$-methanol-H_2O (8:2.5:0.3, *v/v/v*) to yield several fractions. Fractions 6–8 (502 mg) were again subjected to RP-18 column chromatography and eluted using a gradient of methanol-H_2O (20%–50%, *v/v*) to yield fractions A and B. Fraction A was subjected to a Sephadex LH-20 column using 70% methanol-H_2O and purified using high-pressure liquid chromatography (HPLC) (YMC-Pack ODS-A column [20 mm×250 mm, 5 μm]) with 13% acetonitrile-H_2O (0.05% TFA) to yield Bu-7 (17 mg).

Cell culture

PC12 cells were purchased from the American Type Culture Collection (ATCC). The cells were cultured in Dulbecco's modified Eagle's medium (Invitrogen, Gibco, USA) supplemented with 5% heat-inactivated fetal bovine serum (Invitrogen, Gibco, USA), 5% equine serum (Thermo Scientific, Hyclone, USA), 100 U/mL penicillin and 100 μg/mL streptomycin. The cultures were maintained in a humidified incubator at 37 °C in an atmosphere of 95% air and 5% CO_2. The media were changed every two or three days.

Drug treatments

Rotenone and Bu-7 were reconstituted fresh in dimethyl sulfoxide and distilled water, respectively, prior to each experiment. Bu-7 (0.1, 1, 10 μmol/L) was added 0.5 h prior to the rotenone treatment in the cell cultures to evaluate its protective effect.

Cell viability assay

Cell viability was determined using the MTT assay. After incubation with MTT solution for 4 h, the cells were exposed to an MTT-formazan dissolving solution for 8–12 h. The optical density (*OD*) was then determined using an absorbance microplate reader (Molecular Devices, Toronto, Canada) at a wavelength of 570 nm. The cell viability was expressed as a percentage of the *OD* value of the control cultures.

Analysis of apoptosis by flow cytometry

The apoptosis rate was measured by flow cytometry, as reported previously[20]. Briefly, PC12 cells were washed with PBS (pH 7.4), fixed in cold 70% (*v/v*) ethanol, and incubated at -20 °C for at least 2 h. The fixed cells were harvested by centrifugation at 250×*g* for 5 min. The cell pellets were resuspended in PBS at room temperature for 10 min, and after another centrifugation, the cell pellets were resuspended in PBS containing 0.2 g/L RNase A and incubated at 37 °C for 30 min. The cells were then stained with propidium iodide (PI) at a final concentration of 100 μg/mL at 4 °C for 30 min. The suspensions were analyzed using a FACS scan flow cytometer (Becton Dickinson).

Measurement of mitochondrial membrane potential (MMP)

Changes in the inner MMP were determined by incubating with 10 μg/mL of Rhodamine 123 for 30 min at 37 °C in the dark. The cells were then washed with PBS three times, and the fluorescence intensity was determined using flow cytometry. JC-1 was also used to measure the change of the inner MMP. PC12 cells were incubated with 10 μg/mL JC-1 at 37 °C. JC-1 accumulates in the mitochondria, forming red fluorescent aggregates at high membrane potentials; at a low membrane potential, JC-1 exists mainly in the green fluorescent, monomeric form. After incubating for 20 min, the cells were washed with PBS for 3 times and submitted to fluorescence microscopy analysis. The JC-1-loaded cells were excited at 488 nm, and the emission was detected at 590 nm (JC-1 aggregates) and 525 nm (JC-1 monomers). Mitochondrial depolarization was indicated by an increase in the green/red fluorescence intensity ratio, which was calculated with Image J software.

Western blot analysis

After treatment, the cells were washed with PBS and lysed in lysis buffer (50 mmol/L Tris-HCl, 150 mmol/L NaCl, 1% NP-40, 1 mmol/L PMSF, 50 μg/mL leupeptin, 1 μg/mL pepstatin A, 20 μg/mL aprotinin, 1 mmol/L EDTA, 1 mmol/L EGTA, 1 mmol/L DTT, 1 mmol/L Na_3VO_4, 50 mmol/L NaF, and 20 mmol/L β-glycerophosphate Na_2, pH 8.0). The protein concentrations were measured with a BCA kit (Pierce). The cell lysates were solubilized in SDS sample buffer, separated by SDS-PAGE and transferred to a PVDF membrane (Millipore). The membrane was blocked with 3% BSA and incubated with the primary antibody, anti-JNK/p-JNK MAPK, anti-p38/p-p38 MAPK, anti-p53, anti-Bax, anti-Bcl-2, or anti-caspase 3, followed by a horseradish peroxidase (HRP)-conjugated secondary antibody. The proteins were detected using the enhanced chemiluminescence plus detection system (Molecular Device, Lmax) and analyzed with Science Lab 2005 Image Gauge software. β-Actin served as an internal control.

Statistical analysis

All of the data obtained in the experiments were represented as the mean±standard deviation (SD). The statistical analysis was performed using the SPSS 13.0 software package. Differences were determined using one-way analysis of variance (ANOVA), and *P* values of less than 0.05 and 0.01 were regarded as statistically significant.

Results

Bu-7 protects against rotenone-induced PC12 cell death

To investigate how rotenone influences neuronal cytotoxicity, PC12 cells were treated with various concentrations of rotenone (0, 0.1, 1, 5, 10, or 20 μmol/L) for 24 h. As shown in Figure 2A, rotenone induced a dose-dependent cytotoxicity in the PC12 cells. The cells were then treated for 24 h with various concentrations of Bu-7 with or without rotenone (1 μmol/L) to determine the effect of Bu-7 on the rotenone-induced cytotoxicity. The cells treated with rotenone demonstrated a viability of 69.2%±3.0%. We found that Bu-7 had a dose-dependent

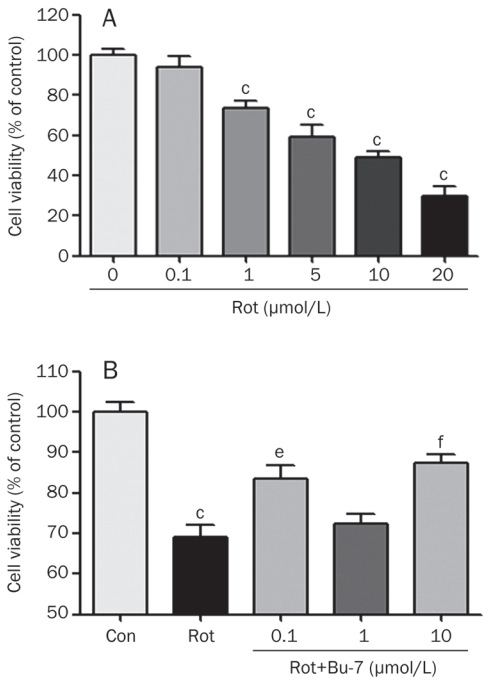

Figure 2. Bu-7 reduces rotenone (Rot)-induced cell death. (A) PC12 cells were treated with various concentrations of Rot for 24 h. (B) The effect of Bu-7 was examined on PC12 cells treated with 1 μmol/L Rot for 24 h. PC12 cells were exposed to different concentrations (0.1, 1, and 10 μmol/L) of Bu-7 and Rot. The cell viability was evaluated by MTT assay. n=6. Mean±SD. ^{c}P<0.01 *vs* control. ^{e}P<0.05, ^{f}P<0.01 *vs* Rot-treated group.

effect on cell viability after the rotenone treatment (Figure 2B), increasing the viability of the PC12 cells to 83.6%±3.2%, 72.3%±2.4%, and 87.3%±2.3% at a concentration of 0.1, 1 and 10 μmol/L, respectively, compared with the control group.

Bu-7 protects against rotenone-induced apoptosis

To determine how Bu-7 protects cells against rotenone, the PC12 cells were stained with propidium iodide (PI) and then analyzed using flow cytometry. The PC12 cells treated with rotenone (1 μmol/L, 24 h) showed an obvious apoptosis rate of 30.0%±1.0%, whereas Bu-7 treatment of the cells (0.1, 1, and 10 μmol/L) significantly attenuated rotenone-induced apoptosis (21.6%±0.2%, 26.2%±1.4%, and 21.2%±0.4%, respectively, Figure 3).

Bu-7 attenuated the rotenone-induced mitochondrial potential reduction in PC12 cells

Normal PC12 cells stained with the JC-1 dye emitted a mitochondrial orange-red fluorescence with a small amount of green fluorescence. These JC-1 aggregates within the normal mitochondria were dispersed to the monomeric form (green fluorescence) after the addition of 1 μmol/L rotenone in the culture medium for 24 h (122.1%±8.2%). However, Bu-7 relieved the rotenone-induced mitochondrial depolarization, as shown by the fluorescent color changes from green to orange-red (87.1%±5.3%, 107.0%±4.7%, and 90.2%±2.6%,

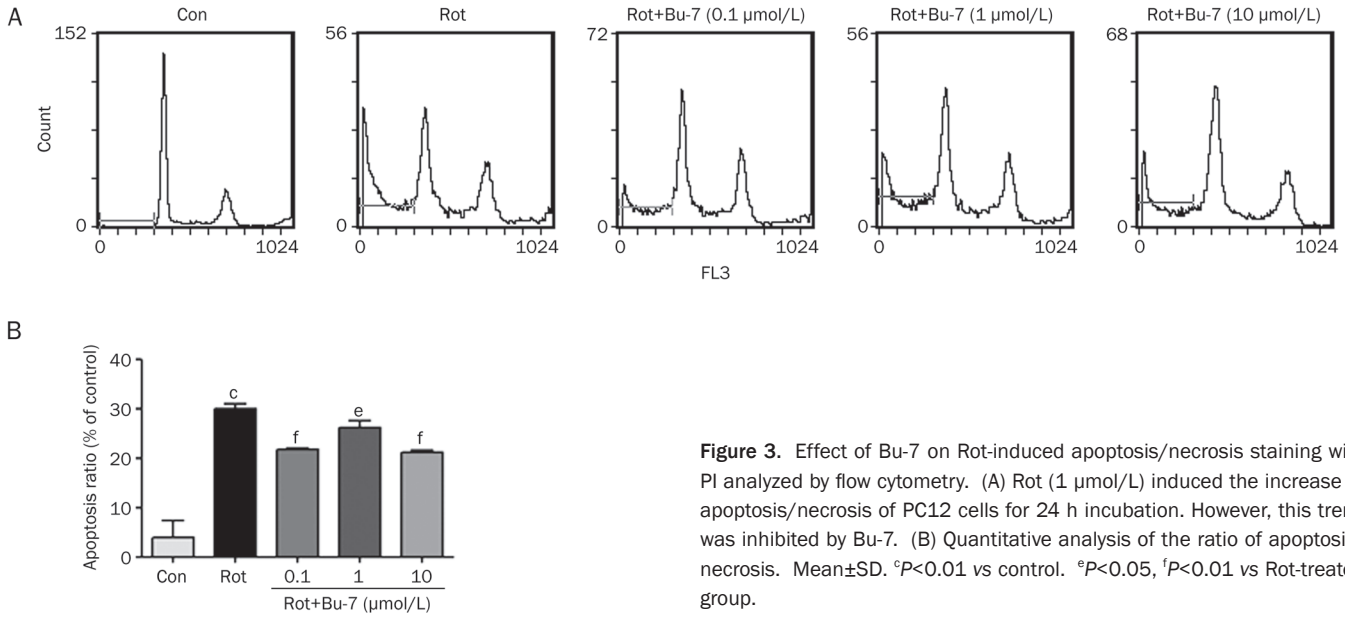

Figure 3. Effect of Bu-7 on Rot-induced apoptosis/necrosis staining with PI analyzed by flow cytometry. (A) Rot (1 μmol/L) induced the increase of apoptosis/necrosis of PC12 cells for 24 h incubation. However, this trend was inhibited by Bu-7. (B) Quantitative analysis of the ratio of apoptosis/necrosis. Mean±SD. $^{c}P<0.01$ *vs* control. $^{e}P<0.05$, $^{f}P<0.01$ *vs* Rot-treated group.

respectively, Figure 4). These data showed that rotenone induced mitochondrial membrane permeabilization and caused collapse of the MMP in PC12 cells, whereas Bu-7 significantly attenuated this response.

Bu-7 suppresses the levels of apoptotic proteins associated with p53 in rotenone injured PC12 cells, which is partly through the MAPK signaling pathway

The MAPK signaling pathway may be involved in the intrinsic mitochondrial apoptosis pathway. The effect of Bu-7 on the expression levels of apoptotic proteins was determined using Western blot analysis in PC12 cells exposed to rotenone. The rotenone treatment (1 μmol/L, 24 h) increased the phosphorylation status of JNK (218.0%±11.1%) and p38 (215.6%±42.0%), increased the expression of p53 (496.1%±10.0%) and the ratio of Bax/Bcl-2 (264.2%±16.1%), and increased the expression levels of cleaved (presumably active) caspase 3 (219.1%±25.0%). The pretreatment with Bu-7 (0.1, 1, or 10 μmol/L) prevented the rotenone-induced increase of the above proteins in the same dose-dependent manner as was observed in the cell viability and apoptosis experiments (Figure 5).

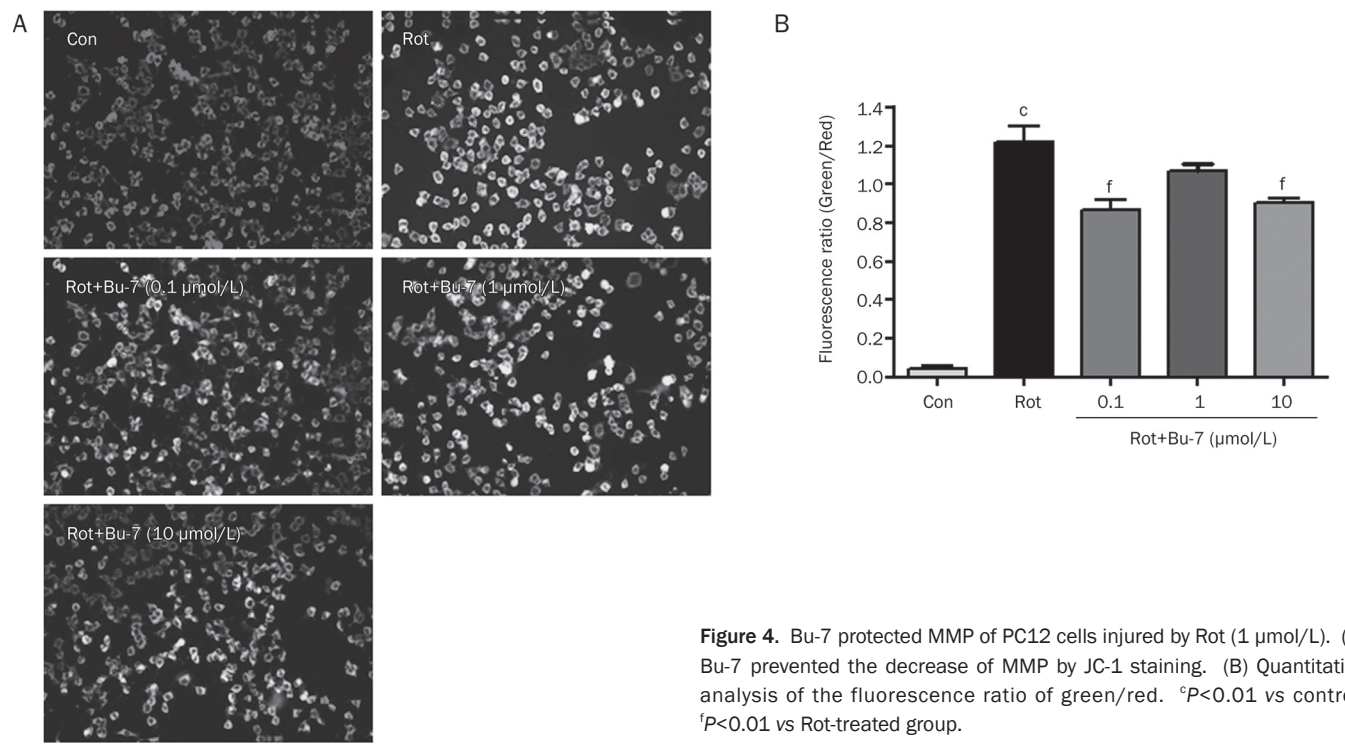

Figure 4. Bu-7 protected MMP of PC12 cells injured by Rot (1 μmol/L). (A) Bu-7 prevented the decrease of MMP by JC-1 staining. (B) Quantitative analysis of the fluorescence ratio of green/red. $^{c}P<0.01$ *vs* control, $^{f}P<0.01$ *vs* Rot-treated group.

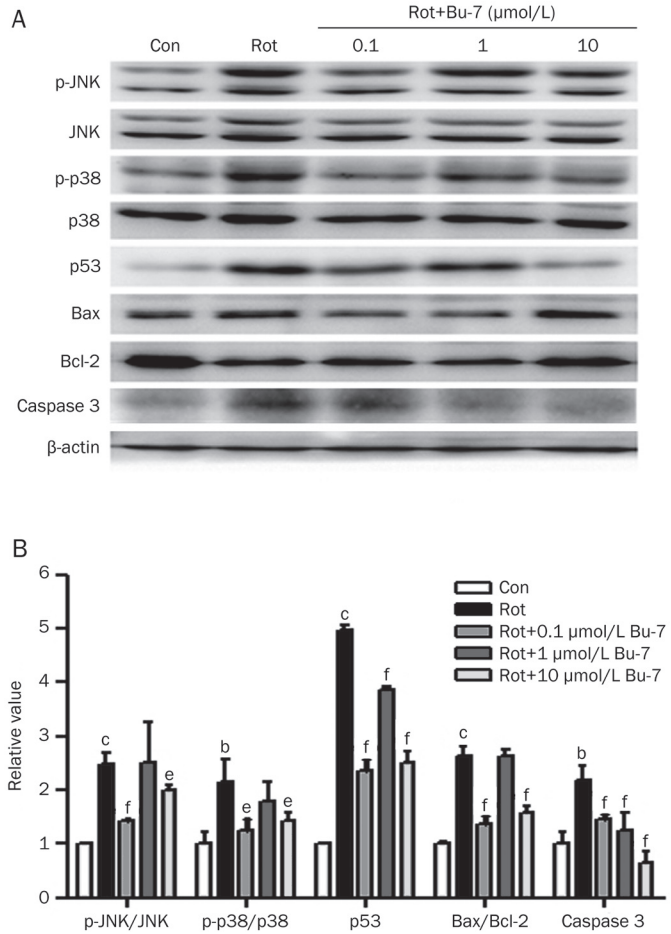

Figure 5. Effect of Bu-7 on the phosphorylation of JNK/p38 MAPK, the expression of p53, Bax, Bcl-2, and caspase 3 in PC12 cells exposed to Rot. (A) PC12 cells were lysed after treatment with Bu-7 and Rot (1 μmol/L). Protein expressions were detected by Western blotting. (B) Quantitative analysis of the phosphorylation of JNK/p38 MAPK, the expression of p53, Bax, Bcl-2, and caspase 3 by Science Lab 2005 Image Gauge software. n=3. Mean±SD. ^{b}P<0.05, ^{c}P<0.01 *vs* control. ^{e}P<0.05, ^{f}P<0.01 *vs* Rot-treated group.

Discussion

In our previous study, we found that Bu-7 increased the cell viability of PC12 cells injured by rotenone, 6-OHDA, and MPP^+ by MTT assay (unpublished observations). It is well known that rotenone, 6-OHDA, and MPP^+ cause neurotoxicity in cells *in vitro*[21, 22]; thus, our previous data suggested that Bu-7 may have a positive effect on anti-apoptosis and mitochondrial protection. Therefore, in our present study, we utilized rotenone to create an *in vitro* cell model to study the protective effects of Bu-7 in PC12 cells and tried to find the possible underlying mechanisms.

Mitochondria are involved in cell survival and play a central role in apoptotic cell death signaling through the control of cellular energy metabolism, the generation of reactive oxygen species (ROS), and the release of apoptotic factors into the cytosol. Evidence showed that ROS are involved in the apoptotic mechanism of rotenone-mediated neurotoxicity[23]. The mitochondrial membrane permeability transition induces the formation of ROS by the inhibition of the respiratory chain and vice versa[24]. Our data showed that Bu-7 protected PC12 cell viability, decreased the apoptosis rate and attenuated the collapse of the MMP induced by rotenone in a manner that resembled an inverted bell-shaped curve. The results demonstrated that Bu-7 had a protective effect against rotenone injury in PC12 cells.

We then further investigated the protective mechanisms of Bu-7 against rotenone-induced apoptosis. Previous evidence from both postmortem PD brain tissues and cellular and animal models suggested that pathways involving p53/Bcl-2-family members may represent suitable targets in apoptosis in PD[25–29]. The activation of JNK and p38 were reported to be responsible for p53-dependent apoptosis including the inhibition of the anti-apoptotic Bcl-2 protein, which further promoted the caspase process, which had a general role in rotenone-induced apoptosis in neuronal cells[30]. It was observed in SH-SY5Y cells that rotenone induced apoptosis through the activation of the JNK and p38 signaling pathways, which indicated their role in neuronal apoptosis[31–34]. Our results showed that rotenone (1 μmol/L) induced the phosphorylation of JNK and p38 after treatment for 24 h. Bu-7 pretreatment inhibited the rotenone-induced phosphorylation of both JNK and p38 and decreased the p53 level that was increased by rotenone. Bu-7 also prevented the increase of the Bax/Bcl-2 ratio and the increase of caspase 3 activity in the rotenone-treated PC12 cells. These results indicated that Bu-7 prevented the rotenone-induced apoptosis that is associated with the p53 pathway, which might occur through the inhibition of JNK and p38 activities.

Our experiments showed that the dose-response relationship of Bu-7 resembled an inverted bell-shaped curve. This kind of dose-response relationship has been reported previously[21, 35, 36]. It is common that a chemical binds to two or more targets/receptors with different affinities. At different doses, the compound may activate different receptors and produce different effects, even opposite ones, in which case, the dose-response relationship is irregular. Further research is required to identify the receptors in an effort to explain the inverted bell-shaped dose-response relationship for Bu-7.

In conclusion, we isolated Bu-7 from extracts of *Clausena lansium* leaves[17] and our present observations identified a beneficial role of Bu-7 against rotenone-induced apoptosis in PC12 cells that may operate via an inhibition of the p38/JNK pathway. Epidemiological studies revealed a correlation between general pesticide (*ie*, rotenone) exposure and an increased risk of PD; therefore, our findings suggested that Bu-7 could be used as a leading compound that might be useful for the treatment of PD. Because our research demonstrated the utility of the bioactive substances in *Clausena lansium*, we are systematically extracting and separating additional compounds from *Clausena lansium* leaves to find out chemicals which have higher bioactivities than Bu-7; at the same time, we are attempting to chemically modify Bu-7 to obtain an increased

bioactivity.

Acknowledgements

This work was supported by the National Natural Science Foundation of China (No 30973887, 81073078, 81073130, Key Program No U832008 and 90713045), National Sci-Tech Major Special Item for New Drug Development (No 2008ZX09101, 2009ZX09303, 2009ZX09303-003, and 2009ZX09301-003-11-1) and Doctoral Fund of Ministry of Education of China (No 20070023037).

Author contribution

Bo-yu LI designed the study, performed the research, and wrote the paper; Yu-he YUAN and Jin-feng HU provided assistance in experimental methods; Dong-ming ZHANG and Qing ZHAO extracted Bu-7; and Nai-hong CHEN designed the research and revised the paper.

References

1 Forno LS. Neuropathology of Parkinson's disease. J Neuropathol Exp Neurol 1996; 55: 259–72.
2 Betarbet R, Sherer TB, MacKenzie G, Garcia-Osuna M, Panov AV, Greenamyre JT. Chronic systemic pesticide exposure reproduces features of Parkinson's disease. Nat Neurosci 2000; 3: 1301–6.
3 Lees AJ, Hardy J, Revesz T. Parkinson's disease. Lancet 2009; 373: 2055–66.
4 Betarbet R, Sherer TB, Greenamyre JT. Animal models of Parkinson's disease. Bioessays 2002; 24: 308–18.
5 Uversky VN. Neurotoxicant-induced animal models of Parkinson's disease: understanding the role of rotenone, maneb and paraquat in neurodegeneration. Cell Tissue Res 2004; 318: 225–41.
6 Priyadarshi A, Khuder SA, Schaub EA, Priyadarshi SS. Environmental risk factors and Parkinson's disease: a metaanalysis. Environ Res 2001; 86: 122–7.
7 Vanacore N, Nappo A, Gentile M, Brustolin A, Palange S, Liberati A, *et al*. Evaluation of risk of Parkinson's disease in a cohort of licensed pesticide users. Neurol Sci 2002; 23: S119–20.
8 Chance B, Williams GR, Hollunger G. Inhibition of electron and energy transfer in mitochondria. I. Effects of Amytal, thiopental, rotenone, progesterone, and methylene glycol. J Biol Chem 1963; 238: 418–31.
9 Hartley A, Stone JM, Heron C, Cooper JM, Schapira AH. Complex I inhibitors induce dose-dependent apoptosis in PC12 cells: relevance to Parkinson's disease. J Neurochem 1994; 63: 1987–90.
10 Tapias V, Cannon JR, Greenamyre JT. Melatonin treatment potentiates neurodegeneration in a rat rotenone Parkinson's disease model. J Neurosci Res 2010; 88: 420–7.
11 Monti B, Gatta V, Piretti F, Raffaelli SS, Virgili M, Contestabile A. Valproic acid is neuroprotective in the rotenone rat model of Parkinson's disease: involvement of alpha-synuclein. Neurotox Res 2010; 17: 130–41.
12 Valverde G De Andrade D, Madureira de Oliveria D, Barreto G, Bertolino LA, Saraceno E, Capani F, *et al*. Effects of the extract of *Anemopaegma mirandum* (Catuaba) on Rotenone-induced apoptosis in human neuroblastomas SH-SY5Y cells. Brain Res 2008; 1198: 188–96.
13 Kim HJ, Park HJ, Park HK, Chung JH. Tranexamic acid protects against rotenone-induced apoptosis in human neuroblastoma SH-SY5Y cells. Toxicology 2009; 262: 171–4.
14 Liu GT, Li WX, Chen YY, Wei HL. Hepatoprotective action of nine constituents isolated from the leaves of *Clausena lansium* in mice. Drug Dev Res 1996; 39: 174–8.
15 Zhang J, Cheng Y, Zhang JT. Protective effect of (–)clausenamide against neurotoxicity induced by okadaic acid and beta-amyloid peptide25–35. Yao Xue Xue Bao 2007; 42: 935–42.
16 Qian W, Wang LN, Song M, Zheng XW, Hang TJ, Zhang ZX. Excretion of (–)-clausenamide in rats. Yao Xue Xue Bao 2006; 41: 789–92.
17 Zhao Q, Li C, Yang J, Zhang D. Chemical constituents of *Clausena lansium*. Zhongguo Zhong Yao Za Zhi 2010; 35: 997–1000.
18 Guzhva N, Luk'yanchikov M, Ushakov V, Sarkisov L. Flavonoids of *Astragalus captiosus*. Chem Nat Compd 1986; 22: 729.
19 Greene LA, Tischler AS. Establishment of a noradrenergic clonal line of rat adrenal pheochromocytoma cells which respond to nerve growth factor. Proc Natl Acad Sci U S A 1976; 73: 2424–8.
20 Nicoletti I, Migliorati G, Pagliacci MC, Grignani F, Riccardi C. A rapid and simple method for measuring thymocyte apoptosis by propidium iodide staining and flow cytometry. J Immunol Methods 1991; 139: 271–9.
21 Zhang ZT, Cao XB, Xiong N, Wang HC, Huang JS, Sun SG, *et al*. Morin exerts neuroprotective actions in Parkinson disease models *in vitro* and *in vivo*. Acta Pharmacol Sin 2010; 31: 900–6.
22 Lin CM, Lin RD, Chen ST, Lin YP, Chiu WT, Lin JW, *et al*. Neurocytoprotective effects of the bioactive constituents of *Pueraria thomsonii* in 6-hydroxydopamine (6-OHDA)-treated nerve growth factor (NGF)-differentiated PC12 cells. Phytochemistry 2010; 71: 2147–56.
23 Tan S, Sagara Y, Liu Y, Maher P, Schubert D. The regulation of reactive oxygen species production during programmed cell death. J Cell Biol 1998; 141: 1423–32.
24 Polster BM, Fiskum G. Mitochondrial mechanisms of neural cell apoptosis. J Neurochem 2004; 90: 1281–9.
25 Mattson MP. Apoptosis in neurodegenerative disorders. Nat Rev Mol Cell Biol 2000; 1: 120–9.
26 Waldmeier PC. Prospects for antiapoptotic drug therapy of neurodegenerative diseases. Prog Neuropsychopharmacol Biol Psychiatry 2003; 27: 303–21.
27 Reed JC. Apoptosis-based therapies. Nat Rev Drug Discov 2002; 1: 111–21.
28 Ferri KF, Kroemer G. Organelle-specific initiation of cell death pathways. Nat Cell Biol 2001; 3: E255–63.
29 Zimmermann KC, Bonzon C, Green DR. The machinery of programmed cell death. Pharmacol Ther 2001; 92: 57–70.
30 Pei W, Liou AK, Chen J. Two caspase-mediated apoptotic pathways induced by rotenone toxicity in cortical neuronal cells. FASEB J 2003; 17: 520–2.
31 Caughlan A, Newhouse K, Namgung U, Xia Z. Chlorpyrifos induces apoptosis in rat cortical neurons that is regulated by a balance between p38 and ERK/JNK MAP kinases. Toxicol Sci 2004; 78: 125–34.
32 Newhouse K, Hsuan SL, Chang SH, Cai B, Wang Y, Xia Z. Rotenone-induced apoptosis is mediated by p38 and JNK MAP kinases in human dopaminergic SH-SY5Y cells. Toxicol Sci 2004; 79: 137–46.
33 Junn E, Mouradian MM. Apoptotic signaling in dopamine-induced cell death: the role of oxidative stress, p38 mitogen-activated protein kinase, cytochrome c and caspases. J Neurochem 2001; 78: 374–83.
34 Davis RJ. Signal transduction by the JNK group of MAP kinases. Cell 2000; 103: 239–52.
35 Dai G, Huang C, Li Y, Pi YH, Wang BH. Inhibitory effects of AcSDKP on proliferation of human bone marrow mesenchymal stem cells *in vitro*. Sheng Li Xue Bao 2006; 58: 110–5.
36 Gao M, Liu R, Zhu SY, Du GH. Acute neurovascular unit protective action of pinocembrin against permanent cerebral ischemia in rats. J Asian Nat Prod Res 2008; 10: 551–8.

Acta Pharmacologica Sinica (2011) 32: 1327–1336
 1671-4083/11 $32.00
www.nature.com/aps

Original Article

Over-expression of Slit2 induces vessel formation and changes blood vessel permeability in mouse brain

Hai-xiong HAN, Jian-guo GENG*

Laboratory of Molecular Cell Biology, Institute of Biochemistry and Cell Biology, Shanghai Institutes for Biological Sciences, Chinese Academy of Sciences, Shanghai 200031, China

Aim: To investigate the effect of the axon guidance cue Slit2 on the density of blood vessels and permeability of the blood-brain barrier in mouse brain.
Methods: hSlit2 transgenic mouse line was constructed, and the phenotypes of the mice were compared with wild-type mice in respect to the lateral ventricle (LV), ventricle pressure, and the choroids plexus. An *in vivo* Miles permeability assay and an amyloid-β permeability assay were used to assess the permeability of brain blood vessels. Brain vessel casting and intracerebral hemorrhage models were built to investigate vessel density in the transgenic mice. An *in vitro* permeability assay was used to test whether Slit2 could change the permeability and tight junctions of blood vessel endothelial cells.
Results: Hydrocephalus occurred in some transgenic mice, and a significantly larger lateral ventricle area and significantly higher ventricle pressure were observed in the transgenic mice. The transgenic mice displayed changed construction of the choroids plexus, which had more micro vessels, dilated vessels, gaps between epithelial cells and endothelial cells than wild-type mice. Slit2 significantly increased brain vessel density and the permeability of brain vessels to large molecules. These blood vessels were more sensitive to cues that induce brain hemorrhage. At the cellular level, Slit2 disturbed the integrity of tight junctions in blood vessel endothelial cells and improved the permeability of the endothelial cell layer. Thus, it promoted the entry of amyloid-β peptides from the serum into the central nervous system, where they bound to neurons.
Conclusion: Slit2 increases vessel density and permeability in the brains of transgenic mice. Thus, Slit2 induces numerous changes in brain vessels and the barrier system.

Keywords: Slit2; blood-brain barrier; permeability; vessel endothelial cell; tight junction

Acta Pharmacologica Sinica (2011) 32: 1327–1336; doi: 10.1038/aps.2011.106; published online 10 Oct 2011

Introduction

Vasogenic brain edema, which is defined as the translocation of proteins and fluid from the vascular space across the blood-brain barrier (BBB)[1], is a major life-threatening complication of various injuries to the central nervous system (CNS)[2, 3]. Endothelial cells of the brain vasculature form the BBB and maintain the homeostasis of the central nervous system (CNS). Pathological conditions such as brain tumors and head injuries increase the permeability of the brain microvasculature and destroy the BBB[4]. Vascular endothelial growth factor (VEGF) is well known as the major inducer of angiogenesis, and it also increases the permeability of the microvasculature and stimulates endothelial cell growth[5–8]. Increased VEGF expression may cause vascular leakage in the CNS *in vivo*[9]. However, the underlying molecular and pathogenic mechanisms behind edema and blood-brain vessel leakage are poorly understood.

The Slit family of guidance cues interacts with the Roundabout (Robo) family of transmembrane receptors in physiological and pathological processes requiring cell migration[10–13]. During development of the nervous system, Slit-Robo signaling regulates the repulsion or attraction of projecting axons and migrating neurons[14, 15]. Vascular endothelial cells secrete Slit2, which binds to Robo1 on leukocytes and acts as an endogenous inhibitor of leukocyte chemotaxis[16–21]. Additionally, Slit2 mediates directional migration of malignant cells[22–24]. We and others have previously reported that Slit proteins secreted by solid tumors bind to Robo1, which is expressed on vascular and lymphatic endothelial cells, to

* To whom correspondence should be addressed.
E-mail genglaboratory@gmail.com
Received 2011-03-31 Accepted 2011-06-29

stimulate angiogenesis and lymph angiogenesis[25–31]. Slit2 is expressed in the CNS while Robo1 is expressed in blood vessel endothelial cells. However, whether expression of these proteins can change the permeability of blood vessels and whether abnormal expression can induce vessel leakage and edema remain to be determined.

In this study, we constructed a transgenic mouse line that over-expresses human Slit2 and observed that hydrocephalous occurs in some of these transgenic mice. The transgenic mice also had larger lateral ventricles and higher ventricle pressure than wild-type mice. Comparison of the choroids plexus, where cerebrospinal fluid (CSF) is secreted, revealed that there was a change in the construction of the choroids plexus, with the transgenic mice having more microvessels, dilated vessels, gaps between epithelial cells and endothelial cells. We also found that Slit2 could improve brain vessel density and promote the permeability of brain vessels to large molecules. These blood vessels were also more sensitive to cues that induced brain hemorrhage. At the cellular level, Slit2 disturbed the integrity of tight junctions in blood vessel endothelial cells and increased the permeability of the endothelial cell layer. The ability of Slit2 to increase the permeability of the BBB resulted in an increase in the transfer of amyloid-β peptides from the serum to the CNS, where they bound to neurons.

Material and methods

Generation of hSlit2 transgenic mice and detection of hSlit2 over-expression

hSlit2 transgenic mice were generated according to standard procedures. The transgene was constructed by cloning cDNA encoding full-length human Slit2 between the *Bam*H I and *Xbo* I restriction sites of the MCS (multi clone site) of pCEP4F. Genotypes were confirmed by Southern blot and PCR analysis. PCR screening of hSlit2 heterozygotes was performed on standard tail genomic DNA preparations using a pair of primers specific for human Slit2 cDNA (forward: 5′-GGTGACGGATCCCATATCGCGGTAGAACTC-3′; reverse: 5′-GGACACCTCGAGCGTACAGCCGCACTTCAC-3′). PCR cycles were as follows: 95 °C, 4 min (1 cycle); 94 °C, 45 s; 55 °C, 45 s; and 72 °C, 1 min (63 cycles); and 72 °C, 10 min (2 cycles). PCR products were analyzed on 1% agarose gels. Slit2 homozygosity was confirmed by genetic methods based on the principle that the progeny of Slit2 homozygotes mated to wild-type C57 mice should all be heterozygotes. The brains from C57 control littermate mice and hSlit2 transgenic mice from founder #9 were snap frozen in liquid N_2 and pulverized. The brain powder was homogenized in 1 mL RIPA lysis buffer [50 mmol/L Tris-HCl, pH 7.4, 150 mmol/L NaCl, 1% Nonidet P-40, 0.5% deoxycholid acid, 0.1% sodium dodecyl sulfate (SDS), 5 mmol/L EDTA, 2 mmol/L phenylmethylsulfonyl fluoride (PMSF), 20 μg/mL aprotinin, 20 μg/mL leupeptin, 10 μg/mL pepstatin A, and 150 mmol/L benzamidine] in a Dounce tissue homogenizer. After homogenization, the samples were centrifuged at 12 000×*g* for 10 min to remove tissue debris and boiled in SDS sample buffer for 5 min. They were then subjected to 7% SDS-PAGE electrophoresis, transferred to blotting membranes, probed with 1 μg/mL anti-Slit2 monoclonal antibody (5A5) and detected with the horseradish peroxidase-conjugated goat anti-mIgG Ab using a chemiluminescent detection system.

Comparison of the LV area and the choroid plexus

The mouse brains were fixed in 4% PFA (Sigma) and cut into consecutive longitudinal sections. A photo was taken of every longitudinal sections from each brain with an Olympus MVX10. Then the area of the lateral ventricle was calculated by Image Tool 3 (UTHSCSA), and the average area of consecutive sections from each mouse was calculated. The data represent the means for groups of six mice. For histological examination of the choroid plexus, brains were isolated from age-matched C57 and Slit2 adult mice, cut into small coronal blocks, fixed in 4% formaldehyde, embedded in paraffin, and cut into 0.5-mm sections following standard procedures. Tissue sections were counterstained with hematoxylin. The same regions of the choroid plexus in all mouse brains were photographed.

Electron microscopy

The choroid plexuses used for TEM were fixed in 2% glutaraldehyde and 1% sucrose in 0.1 mol/L cacodylate buffer for 3 h. The samples were washed in 0.1 mol/L cacodylate buffer and then post-fixed in 1% osmium tetraoxide in 0.1 mol/L cacodylate buffer for 2 h, all at pH 7.0 and 25 °C. The choroid plexuses were embedded in epon after dehydration in a graded series of ethanol. Epon was polymerized at 60 °C for 48 h. Serial sections of 80 nm were cut on a Leica Super Nova ultramicrotome with a diamond knife and collected on formvar-coated nickel grids. Sections were contrasted with uranylacetate and stained with 1% toluidine blue. The sample grids were observed using a Hitachi 600 TEM.

In vivo Miles permeability assay and amyloid-β permeability assay

To investigate the effects of over-expression of hSlit2 in the brain on vascular permeability, a Miles assay was performed. Mice received an iv injection of sterile 0.5% Evans blue dye (200 μL) via the tail vein. Mice were killed 20 min after the injections by cervical dislocation after anesthesia. The brains (weighted) were cut into small pieces and incubated in 500 mL of formamide at 37 °C for 48 h to extract the Evans blue dye. The absorbance of the extracts was read at 630 nm in a spectrophotometer (Beckman DU 640). For the amyloid-β permeability assay, mice received an iv injection of 6.9 μmol/L FITC-Aβ (100 μL) via the tail vein. Mice were killed 48 h after the injections by cervical dislocation after anesthesia. The brains of the mice were prepared on crystal slides, and the nuclei were stained with DAPI.

LV pressure assay

Mice (12 weeks of age) were anesthetized by ip injection of sodium pentobarbital (70 mg/kg). A small hole 0.5 mm posterior and 1.0 mm lateral of the bregma was drilled to perfo-

rate the skull. A pressure transducer linked to a monitor was injected into the brain at a depth of 2.3 mm unilaterally. Then the LV pressure was read on a computer that was linked to the monitor (Powerlab 4/30). The pressure was measured as mmH_2O.

Immunohistochemical staining

Antibodies against vWF (Antibody Diagnostica Inc; a 1:200 dilution for paraffin-embedding), Slit2 (5 μg/mL for paraffin-embedding sections), and Robo1 (20 μg/mL for paraffin-embedding sections) were used for immunohistochemical staining as described previously.

Brain vessel casting

After systemic heparinization with 750 IU/kg intravenous heparin, the common carotid arteries were cannulated and perfused with approximately 100 mL of 27 °C saline, followed by a 2.5% buffered glutaraldehyde solution (Sigma) at pH 7.4.

The casts were made by perfusion of the arteries with 100 mL of Mercox (SPI, West Chester, PA, USA) diluted with 20% methyl methacrylate monomers (Aldrich Chemical, Milwaukee, WI, USA). After complete polymerization, the brains were harvested and macerated in 5% potassium hydroxide, followed by drying and mounting for scanning electron microscopy. The microvascular corrosion casts were imaged after being coated with gold with a Hitachi S-450 scanning electron microscope.

Intracerebral hemorrhage (ICH) model

Mice (12 weeks of age) were prepared for surgery and anesthetized by ip injection of sodium pentobarbital (70 mg/kg)[32]. A small hole 1.0 mm posterior and 3.0 mm lateral of the bregma was drilled to perforate the skull. A 1-μL Hamilton syringe was used to deliver 500 nL of collagenase/saline (150 U/μL) to the caudate/putamen at a depth of 4.0 mm unilaterally. After the injection of collagenase/saline (~30 s), the needle remained in place for another 2 min to prevent reflux of fluid. Then the scalp skin was closed using 4.0 nylon sutures. Twenty-four hours later, the mice were perfused with PBS, the brains were harvested, and 14-μm sections were prepared using a cryostat and mounted on glass slides. An Olympus BX100 upright systems microscope with a digital camera was used to capture images. The hemorrhage volume was measured using the Stereologer software system.

In vitro permeability assay

We coated transwell inserts (Corning, 48-well, 3-mm pore) with collagen and seeded HUVEC cells at a density of 30 000 cells per well. Cells were then cultured for another 24 h. One hour later, Slit2, VEGF, R5, and FITC-DEXTRAN (25 mg/mL, Sigma) were added to the top of the inserts. The absorbance of the solution in each well was measured at 492 nm (n=6 wells each).

Statistical analysis

Statistical significance was determined by Student's t-test. P-values of 0.05 and 0.01 were considered statistically significant and very significant, respectively.

Results

Generation of hSlit2 transgenic mice and over-expression of hSlit2 in mouse brains

To study the function of Slit2 in the whole blood vessel system, we constructed a Slit2 over-expressing mouse transgenic plasmid, for which a schematic display is shown in Figure 1A. The full-length human Slit2 cDNA, which is 4689 bases, was inserted between the *Bam*H I/*Xbo* I restriction sites of the MCS of the pCEP4F vector, which has a pCMV promoter and an N-terminal flag-tag. The plasmid was linearized with restriction enzymes, injected into the pronuclei of fertilized C57×CBA F1 oocytes and transplanted into the mother mouse. The offspring mice were analyzed by dot blot (Figure

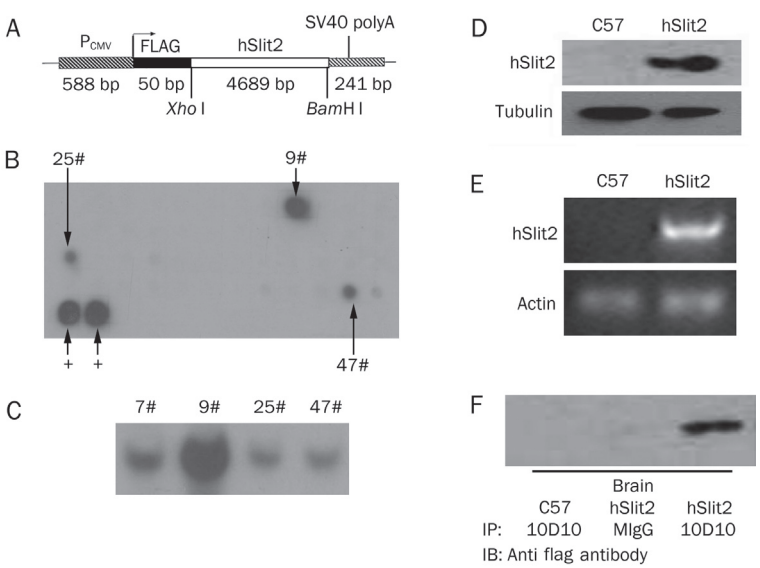

Figure 1. Generation of hSlit2 transgenic mice and over-expression of hSlit2 in hSlit2 mouse brains. (A) Schematic display of the human Slit2 (hSlit2) transgene. The transgene was constructed by cloning cDNA encoding full length human Slit2 between the *Bam*H I/*Xbo* I restriction sites of the MCS of pCEP4F. (B) Dot blotting of DNA isolated from hSlit2 transgenic mice. The presence of the transgene in mice was verified by dot blotting using a [^{32}P]-labeled fragment of the hSlit2 plasmid. (C) Southern blotting of hSlit2 transgenic mice. The presence of the transgene was further confirmed by Southern blotting of DNA isolated from mice that were shown to be positive for the transgene based on the dot blot analysis with a [^{32}P]-labeled fragment of the hSlit2 plasmid. (D) Expression of the hSlit2 protein in the hSlit2 transgenic mice compared with C57 mice. The expression of Slit2 (~200 kDa) in the brains of C57 and Slit2 mice was detected with anti-Slit2 IgG 5A5. (E) RT-PCR of hSlit2 in mRNA extracts from C57 and hSlit2 mouse brains. (F) Western blot analysis of flag-tagged proteins. Brain lysates from C57 and hSlit2 mice that were ip injected with an anti-Slit2 antibody, 10D10, and probed with an anti-flag tag antibody.

1B). Mouse lines 9, 25, and 47 were shown to express human Slit2. The presence of the human Slit2 transgene was also confirmed by Southern blot analysis (Figure 1C). Among the three transgenic strains, we found that strain 9 had the strongest signal in dot blot and Southern blot assays, so we focused our research on strain 9. We observed that the transgenic mice expressed more Slit2 in the brain compared with C57 mice at the transcriptional and translational levels (Figure 1D, 1E). We used the Slit2 antibody 10D10 to immune-precipitate the mouse brain lysate and detected the precipitate with anti-flag antibody, and we found that flag-Slit2 was expressed in the transgenic mouse brain (Figure 1F).

The phenotype of Slit2 mice and comparison of the LV area

Most of the transgenic mice initially appeared normal (Figure 2A), but about 5% of the transgenic mice had an intumescent head (Figure 2B). This phenotype appeared at the age of 4–6 weeks in all three of the transgenic mouse lines, line 9, line 25, and line 47. Mice with an intumescent head died within 2 weeks, at the age of 6–8 weeks. Anatomical analysis of these mice revealed high levels of encephalopathic edema. In mice where this brain phenotype was observed, the brain edema was serious and the brain tissue was destroyed to such a degree that the structure of the brain could not be recognized. Thus, we focused our research on the transgenic mice that did not have this phenotype. Brain edema is linked to the CSF system, including the production, circulation and absorption of CSF. We therefore examined brain structures related to the CSF system. In the brain, CSF is produced in the lateral ventricle, so we compared the lateral ventricle of transgenic mice and non-transgenic mice. We found that the lateral ventricle area was larger in the brains of transgenic mice (Figure 2C, 2D) than in control mice (Figure 2E, 2F). For this study, the mice were all 8 weeks old, and the same result was seen in male and female mice. Figure 2G shows a schematic display of the mouse brain. The arrow indicates the lateral ventricle. We calculated the entire area of the LV in slides created from the brains of each mouse with Image Tool 3 (UTHSCSA) and found that the LV area was larger in transgenic mice (n=6, P<0.01) (Figure 2H). LV pressure was also detected in the lateral ventricles of the mouse brains. In transgenic mice, the pressure was 128 mmH_2O, and in control mice, it was 81 mmH_2O (Figure 2I) (n=7, P<0.01). Thus, the LV pressure was higher in the brains of transgenic mice compared with control mice.

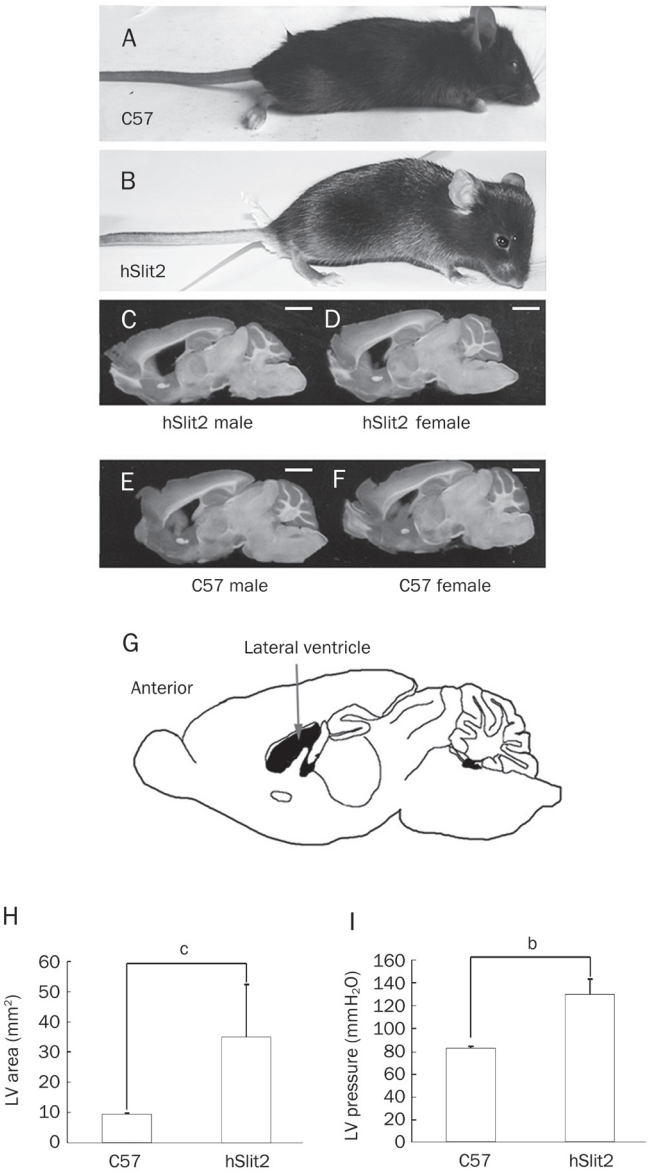

Figure 2. The phenotype of hSlit2 mice and comparison of the LV area. (A and B) Comparison of a C57 mouse (A) with a hSlit2 mouse (B) with a megahead. The forebrain of the hSlit2 mouse is much larger than that of the C57 mouse. (C, D and E, F) Slides of longitudinal sections of brains from hSlit2 mice (C, male; D, female) and C57 mice (E, male; F, female). The lateral ventricle area was larger in hSlit2 mice than in C57 mice. Scale bar: 2 mm. (G) Schematic diagram of the mouse brain. The arrow indicates the lateral ventricle (black). (H) Measurement of the lateral ventricle area in brain longitudinal section slides of C57 and hSlit2 mice. The data represent the mean results from groups of six mice; bars, SEM. ^cP<0.01. (I) LV pressure in C57 and hSlit2 mice. The data represent the mean results from groups of seven mice; bars, SEM. ^bP<0.05.

Changes in the structure and function of the choroid plexus

In mouse brains, the choroid plexus produces CSF. The structure of the choroids plexus was obviously different between transgenic and control mice. In control mice, it was a tight, mono-cell layer covered with microvessels (Figure 3A); however, in transgenic mice, there were gaps between the epithelial cell layer and the vessels (Figure 3B, 3C), the vessels were enlarged and had gaps, and the epithelial cells were crenated (Figure 3C). The mice used in these experiments were all 10 weeks old. Examination under an electron microscope revealed gaps between the epithelial tight junctions in transgenic mice (Figure 3E); such gaps were not observed in control mice (Figure 3D). ZO-1 is an important component of cell-cell tight junctions and can be used as a marker for the completeness and density of tight junctions. We used fluorescence

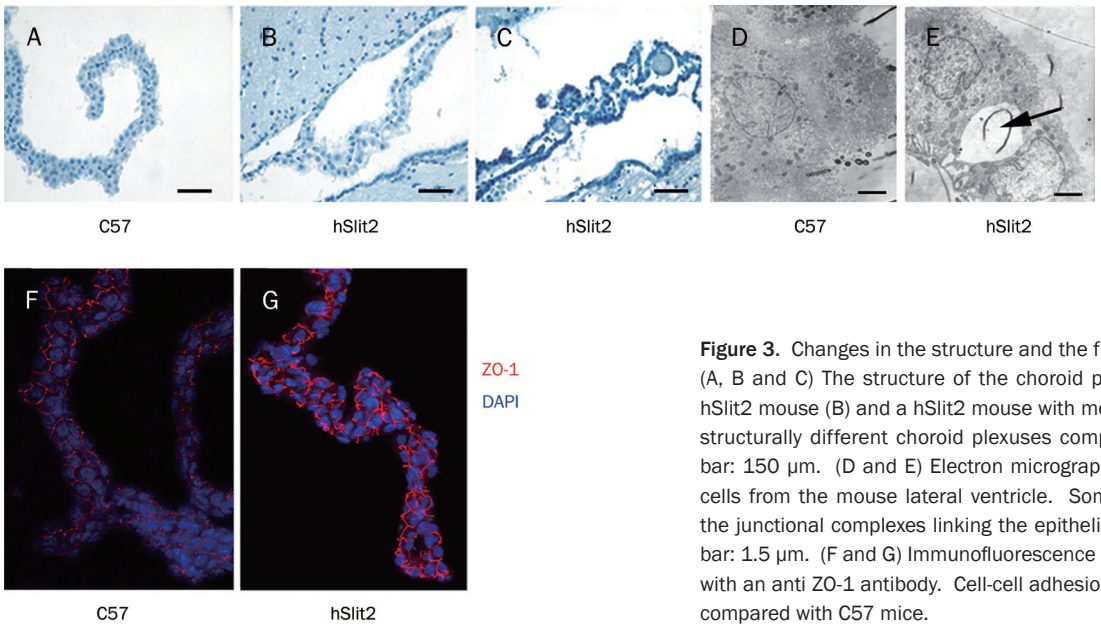

Figure 3. Changes in the structure and the function of the choroid plexus. (A, B and C) The structure of the choroid plexus of a C57 mouse (A), a hSlit2 mouse (B) and a hSlit2 mouse with megahead (C). hSlit2 mice had structurally different choroid plexuses compared with C57 mice. Scale bar: 150 μm. (D and E) Electron micrograph of choroid plexus epithelial cells from the mouse lateral ventricle. Some vacuoles appear between the junctional complexes linking the epithelial cells in hSlit2 mice. Scale bar: 1.5 μm. (F and G) Immunofluorescence of the choroids plexus probed with an anti ZO-1 antibody. Cell-cell adhesion was different in hSlit2 mice compared with C57 mice.

immunostaining to detect ZO-1 in the choroid plexus. In control mice, ZO-1 had an equal and continuous distribution (Figure 3F), while in transgenic mice, the distribution of ZO-1 was disturbed (Figure 3G) and the tight junctions were destroyed.

More vessels are present in the choroid plexus and the brain of transgenic mice

Staining of slides of the brain cortex with anti-CD31 antibody showed that more micro-blood vessels were present in the brains of hSlit2 transgenic mice (Figure 4B) compared with C57 mice (Figure 4A). The gray density was 1.7% in C57 mice and 4.6% in hSlit2 transgenic mice ($P<0.01$, Figure 4C). We also stained the brain cortex slides with anti-vWF antibody and found that hSlit2 transgenic mice had an increased number of vessels (Figure 4E) compared with C57 mice (Figure 4D). Calculating the numbers of vessels present on the slides revealed that C57 mice had about 200 micro-vessels/mm^2, while hSlit2 transgenic mice had about 450 micro-vessels/mm^2 (Figure 4F), and most of these brain micro-vessels consisted of only one endothelial cell. Furthermore, we performed brain vessel casting, which also showed that hSlit2 transgenic mice had more brain vessels (Figure 4H) compared with C57 mice (Figure 4G).

Slit2 changes the permeability of cell-cell adhesions

To evaluate whether Slit2 improves the permeability of blood vessels, we performed a Miles assay on hSlit2 transgenic mice. An increased amount of Evans blue dye was detected in the brain tissue of transgenic mice compared with C57 mice (Figure 5A), which indicates that the blood vessels in the brains of transgenic mice are more permeable, allowing the entry of Evans blue dye into the tissue. Previous research has indicated that hyperplastic vessels are incomplete, more permeable, and more sensitive to destructive mechanism compared with normal vessels. Thus, we induced intracerebral hemorrhaging in the transgenic mice. This was accomplished by injecting collagenase into the mouse brains, which destroys blood vessels in the brain and causes intracerebral hemorrhaging. Examination of brain slides from mice in which intracerebral hemorrhaging was induced showed that transgenic mice have a larger hemorrhage area compared with the control mice (Figure 5C, 5D). Next, we measured the hemorrhage volume using the Stereologer software system and found that the hemorrhage volume also was increased in the transgenic mice (Figure 5B). These results indicate that the blood vessels in the brains of the transgenic mice are more permeable and much more sensitive to collagenase, which destroys the vessel structure. Thus, Slit2 may not only promote angiogenesis but could also increase the permeability of blood vessel endothelial cells, which are the most important component of blood vessels. VE-cadherin is a member of the cadherin family, which is expressed specifically in endothelial cells and plays important roles in endothelial cell cell-cell adhesion. Immunofluorescent detection of HUVECs using an anti-VE-Cadherin antibody revealed that, without incubation with Slit2, VE-Cadherin expression was equal, continuous and mostly localized to the conjunction sites of cell-cell adhesions (Figure 5E), while HUVECs incubated with the Slit2 protein had a disturbed distribution and lacked continuous expression of VE-Cadherin (Figure 5F). To verify that Slit2 can affect the permeability of blood vessels, we performed an *in vitro* permeability assay. We coated transwell inserts (Corning, 48-well, 3-mm pore) with collagen and seeded HUVECs at a density of 30 000 cells per well. Once these cells formed a monolayer, we added Slit2 protein and other stimulating factors to the upper well. FITC-dextran was added 1 h later, and fluorescence was detected in the bottom wells. Our results show that VEGF-A can improve the permeability of HUVECs and Slit2 by 1.5 fold and 2 fold, respectively, and that a blocking antibody against the Slit2-Robo signal, R5, can block the effect of Slit2 on cell

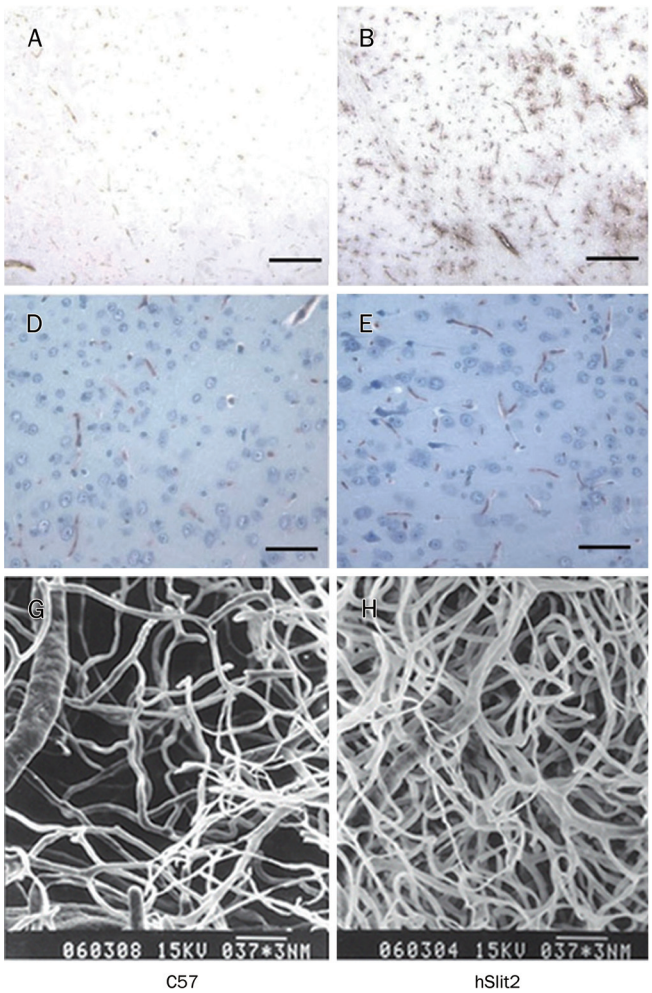

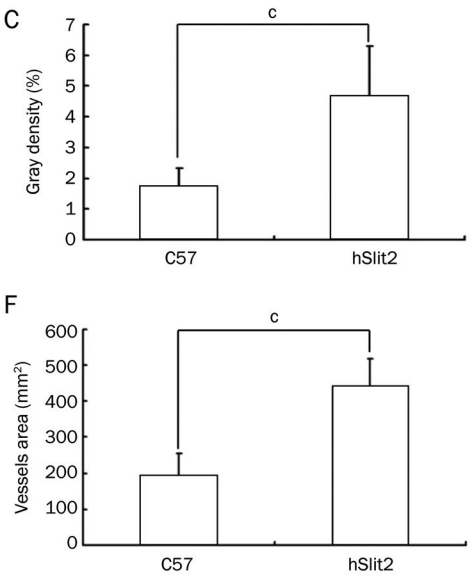

Figure 4. More vessels are present in the choroid plexus and the brain of transgenic mice. (A, B and C) ICH of CD31 in C57 (A) and hSlit2 mice (B). Gray density statistics of CD31 staining (C), $^{c}P<0.01$. Scale bar: 150 μm. (D, E and F) ICH of vWF in C57 (D) and hSlit2 mice (E). The difference in the number of stained vessels in the same area was statistically significant (F), $^{c}P<0.01$. Scale bar: 50 μm. (G and H) Scanning electron microscopy of corrosion casts of the brain vessel of C57 (G) and hSlit2 mice (H).

permeability, returning it to basal levels (Figure 5G).

The presence of amyloid-β peptide in the brains of Slit2 mice

Amyloid-β 40 peptides were detected on slides of the transgenic mouse brains (Figure 6A) but not slides of C57 mouse brains (Figure 6D). In the cortex and hippocampus, amyloid-β 42 was detected in granual and pyramid cells in transgenic mice (Figure 6B, 6C) but not in C57 mice of the same age (Figure 6E, 6F). Furthermore, we injected FITC-Amyloid-β40 into the circulation by ip to see if the circulating peptides could enter the CNS. Florescence was observed on brain cortex slides prepared from the transgenic mice 1 h (Figure 6G), 24 h (Figure 6H), and 48 h (Figure 6I) after injection. The florescence was higher with increasing time, but even 48 h after injection, no florescence was detected on brain cortex slides prepared from C57 mice (Figure 6J, 6K).

hSlit2 transgenic mice have normal aqueduct and subarachnoid space, and Slit2 over-expression does not alter VEGF expression levels

To determine the course of the enlarged lateral ventricles observed in Slit2 transgenic mice, we compared the aqueduct and the subarachnoid space of transgenic and C57 mice. However, there were no obvious differences in these two areas between transgenic and C57 mice. The aqueduct was smooth and clear, and the aqueduct tube had the same inside diameter and did not contain any clogs (Figure 7A–7D). The SAS also had a complete and clear structure with no clogs or signs of collapse in the transgenic mice (Figure 7E–7H). We also found that Slit2 over-expression did not alter VEGF expression at either the protein or mRNA level (Figure 7I, 7J). These results show that the structures linked to circulation and absorption of CSF were complete and normal in the transgenic mice and that the enlargement of the lateral ventricle is caused by the abnormal production of CSF in the choroid plexus. On the other hand, the normal circulation and absorption of CSF could compensate for the abnormal production of cerebrospinal fluid, which could explain why edema was only observed in a small percentage of the transgenic mice.

Discussion

The brain barriers, including the blood-brain barrier, the blood-CSF barrier and the ventricular wall, provide a stable micro-environment for the proper functioning of the central nervous system. At the bases of the barrier structures are the junction structures, such as adherence junctions and tight junc-

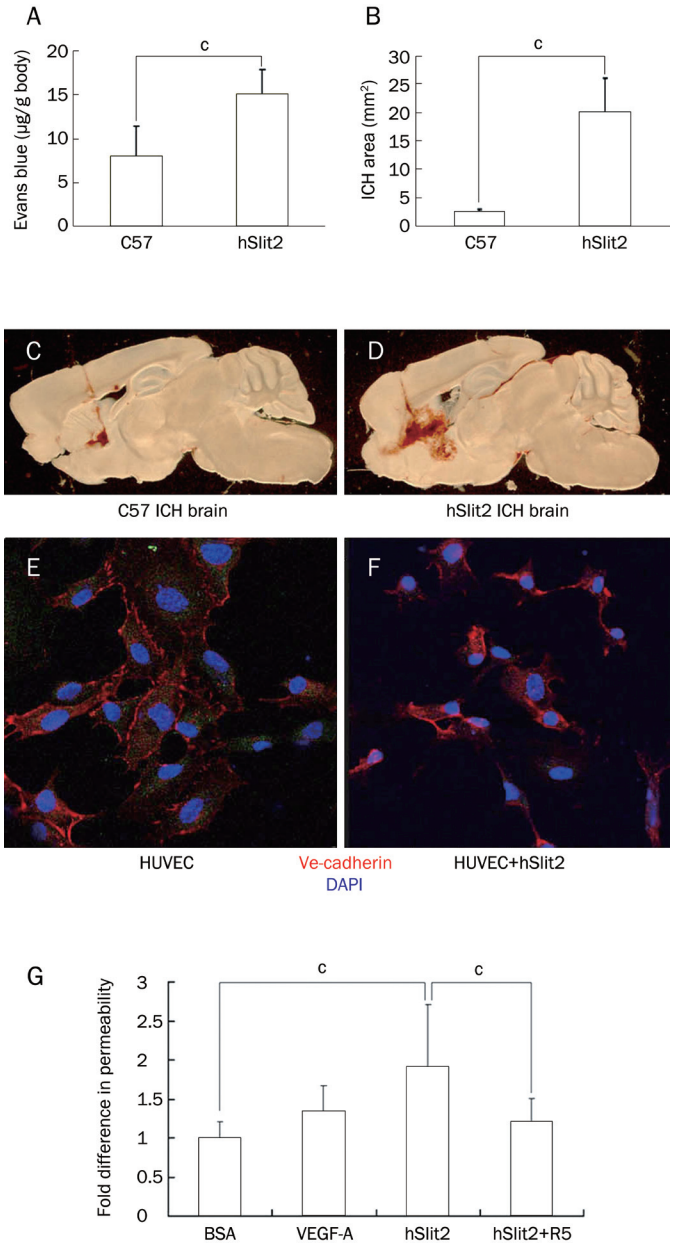

Figure 5. hSlit2 expression changes blood vessel permeability at sites of cell-cell adhesion. (A) Permeability of C57 and hSlit2 mouse brains. The data represent the mean results from seven mice; bars, SEM. $^{c}P<0.01$. (B) Measurement of the ICH area in brain longitudinal section slides from C57 and hSlit2 mice. The data represent the mean results from six mice; bars, SEM. $^{c}P<0.01$. (C and D) Longitudinal section slides of mouse brains in which ICH was induced. The ICH area was bigger in Slit2 mice (D) than in C57 mice (C). (E and F) Immunoflorescence of HUVECs with anti VE-cadherin antibody. Cell-cell adhesion was different in hSlit2 stimulated HUVECs (F) compared with cells not stimulated with hSlit2 (E). (G) hSlit2 increases the permeability of HUVECs in *in vitro* permeability assays. The Robo blocking antibody R5 could block this effect.

tions between endothelial cells, epithelial cells and pericytes[33]. These junction structures are dynamic structures that consist of transmembrane proteins, cytoplasmic accessory proteins and scaffold proteins. Under different physiological and pathological conditions, changes occur in the expression, distribution, modification and interaction of these proteins[34]. These changes are regulated by several cell signaling pathways, and to date, the calcium channel pathway, the phosphorylation signaling pathway and the G-protein signaling pathway have been shown to change the expression and distribution of junction proteins, further affecting the function of barrier structure[35]. The brain blood vessel system is the structural basis of the blood-brain barrier, and the junctions between vessel endothelial cells have the most important effect on the permeability of the BBB. Many molecules, such as small chemical molecules, signaling proteins and inflammatory factors, can change the permeability of blood vessels. VEGF is an important angiogenic cue, and some reports have shown that VEGF improves the permeability of blood vessels and the BBB. VEGF binds to its receptor on blood vessel endothelial cells and triggers signaling pathways in the cell cytoplasm. This, in turn, alters the expression, phosphorylation and distribution of VE-cadherin and thus changes the permeability of blood vessels by disturbing the junction structures[36]. However, barrier structures are very complex and have many components. Therefore, whether other cues that induce angiogenesis have some effect on the permeability of the blood-brain barrier should be investigated.

The guidance cue Slit2 has been reported to regulate a number of physiological processes, mostly in the central nervous system, by controlling cell migration. Previous research from our lab indicated that Slit2 promotes tumor angiogenesis in a manner similar to VEGF[25]. In this paper, we found that Slit2 improved blood vessel density in the brain and promoted the permeability of brain blood vessels to large molecules. In addition, these blood vessels were more sensitive to cues that can induce brain hemorrhage. At the cellular level, Slit2 disturbed the integrity of blood vessel endothelial cell tight junctions and improved the permeability of the endothelial cell layer, thus promoting the entry of amyloid-β peptides from the serum into the central nervous system, where they bind to neurons. We also found that hydrocephalous occurred in some of the hSlit2 transgenic mice. In addition, we observed a larger lateral ventricle area and higher ventricle pressure in the transgenic mice. A comparison of the choroids plexus, where CSF is secreted, revealed that transgenic mice have changes in the structure of the choroids plexus, including more microvessels, dilated vessels, and gaps between epithelial cells and endothelial cells. Thus, Slit2 could bind to its receptor Robo1 on endothelial cells and affect the junction through signaling in the cytoplasm. It has been reported that Slit2 modifies the activity of cytoplasmic GTP enzymes, which affect tight junction structures by regulating adherence proteins and cell scaffold proteins[37]. However, the signaling pathway by which Slit2 affects cell-cell adhesion structures requires further investigation. Because adherent structures consist of a large number of proteins, it is unclear which proteins are affected by Slit2. For example, which changes in protein expression or function are the direct results of Slit2 signaling, and which

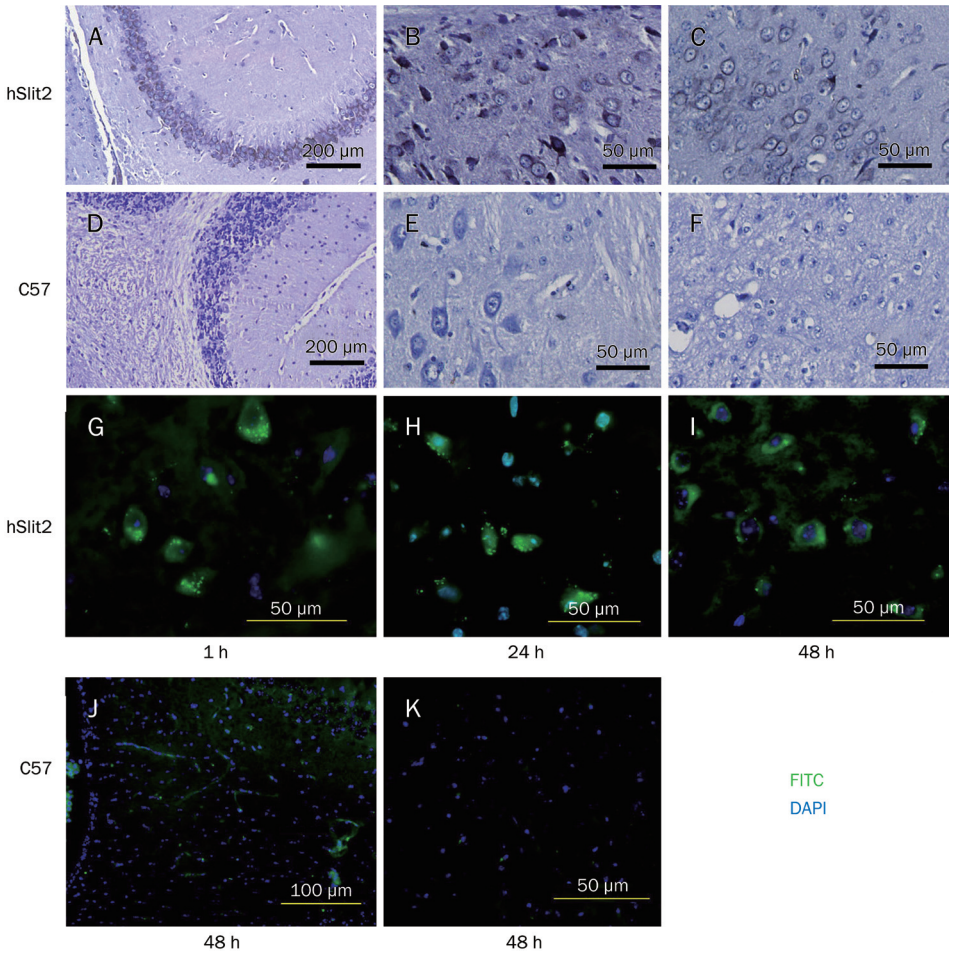

Figure 6. The presence of the Aβ peptide in the brain of Slit2 mice. (A and D) Detection of Aβ 40 in Slit2 and C57 mouse brains. IHC of Slit2 mouse brain slides (A) stained with Aβ 40 antibody. No staining was observed in slides prepared from C57 mouse brains (D). (B, C and E, F) Detection of Aβ 42 in Slit2 and C67 mouse brains. IHC of Slit2 mouse brain slides (B, C) stained with Aβ 42 antibody. No staining was observed in slides prepared from C57 mouse brains (E, F). (G, H, I and J, K) Blood-borne FITC-labeled Aβ42 crosses the blood-brain barrier, enters into the brain tissue and binds selectively to neurons in Slit2 mice (G). Within 1 h post-injection, FITC-labeled Aβ42 leaked from local vessels and bound to the surfaces of neurons (H, I). At 24 and 48 h post-injection, neurons bound with FITC-labeled Aβ42 were abundant in the indicated brain regions. NO FITC-labeled Aβ42 bound to neurons in C57 mice (J, K).

protein changes are the result of subsequent disturbances of junction structures? These are all important questions that need to be answered to understand the molecular mechanism by which Slit2 alters the permeability of barriers.

In the brains of transgenic mice of 6-week-old, we observed binding of the amyloid-β peptide to neurons. This suggested that Slit2 promotes the entry of amyloid-β peptides from the serum into the central nervous system, where they then bind to neurons. The binding of amyloid-β peptides to neurons is a phenotype of the early stage of Alzheimer's disease. However, whether Slit2 is over-expressed in patients with Alzheimer's disease and the relationship between Slit2 and Alzheimer's disease need to be further investigated and will be the focus of future work in our lab.

Slit2 improves the permeability of the blood-brain barrier and thus may have some medical application for the delivery of drugs to the central nervous system, a problem that has puzzled many researchers because drugs targeting the central nervous system often cannot penetrate the blood-brain barrier at sufficient therapeutic doses[38]. In our study, we found that Slit2 promotes the entry of a fluorescent-labeled peptide into the central nervous system. This result suggests that Slit2 may promote the penetration of large-molecule drugs from the peripheral circulation into the central nervous system by increasing the permeability of the blood-brain barrier. Whether manipulation of Slit2 levels or activity can be applied to the field of central nervous system drug delivery requires further investigation, which we plan on pursuing in the future.

Acknowledgements

We thank Dr Biao WANG for the construction of the pCMV-hSlit2 expression plasmid. This work was supported by grants from the National Natural Science Foundation of China (30811120438, 30721065, 30700409, and 30630036), the Ministry of Science and Technology of China (2007CB914501, 2007CB947102, 2009ZX09103-685, and 2010CB529700), Shanghai Municipal Commission for Science and Technology (08JC1421400), and the National Institute of Health (RO1AI064743 and RO1CA126897).

Author contribution

Hai-xiong HAN and Jian-guo GENG designed the research. Hai-xiong HAN performed the research, analyzed the data, and wrote the paper.

References

1 Hackett PH. High altitude cerebral edema and acute mountain sickness: a pathophysiology update. Adv Exp Med Biol 1999; 474:

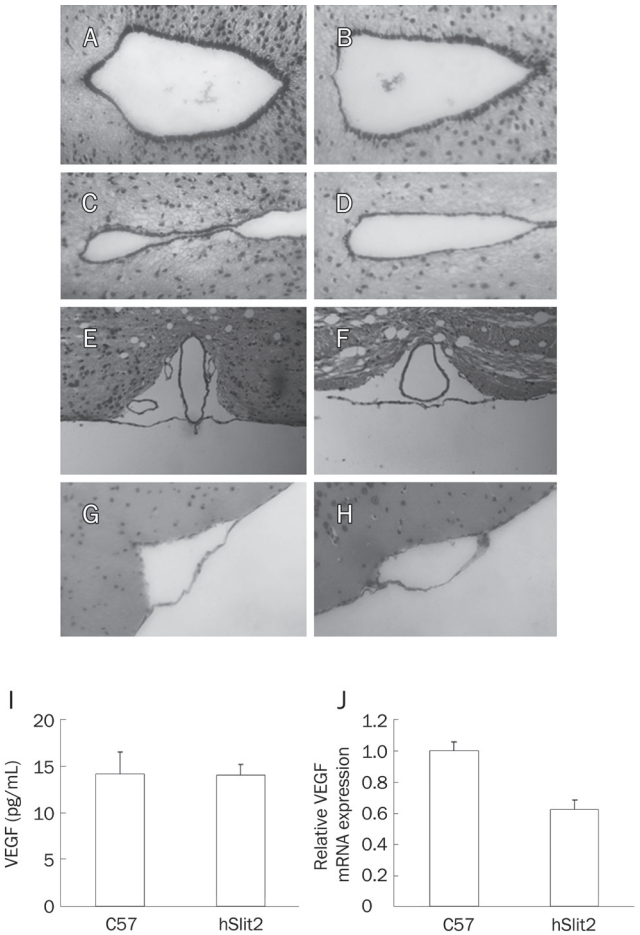

Figure 7. Structure of the aqueduct and SAS and expression of VEGF in transgenic and C57 mice. (A, B and C, D) Structure of the aqueduct in Slit2 mice (A, C) and C57 mice (B, D). No difference was observed in the aqueduct between Slit2 and C57 mice. (E, F and G, H) Structure of the SAS in Slit2 mice (E, G) and C57 mice (F, H). No difference was observed in the SAS between Slit2 and C57 mice. (I) VEGF concentrations in the blood of C57 and Slit2 mice. Serum VEGF levels of C57 and Slit2 mice were detected with a VEGF ELISA kit (Quantikine Immunoassay Lot: 234711). The data represent the mean results for groups of eight mice; bars, SEM. (J) Q-PCR analysis of VEGF mRNA extracted from C57 and hSlit2 mice. VEGF expression was not increased by hSlit2 in mouse brains.

23–45.
2 Murakami K, Kondo T, Yang G, Chen SF, Morita-Fujimura Y, Chan PH. Cold injury in mice: a model to study mechanisms of brain edema and neuronal apoptosis. Prog Neurobiol 1999; 57: 289–99.
3 Pilitsis JG, Rengachary SS. Complications of head injury. Neurol Res 2001; 23: 227–36.
4 Wang W, Dentler WL, Borchardt RT. VEGF increases BMEC monolayer permeability by affecting occludin expression and tight junction assembly. Am J Physiol Heart Circ Physiol 2001; 280: H434–40.
5 Ferrara N. The role of vascular endothelial growth factors in pathological angiogenesis. Breast Cancer Res Treat 1995; 36: 127–37.
6 Senger DR, Van de Water L, Brown LF, Nagy JA, Yeo KT, Yeo TK, *et al*. Vascular permeability factor (VPF, VEGF) in tumor biology. Cancer Metastasis Rev 1993; 12: 303–24.
7 Stephan CC, Brock TA. Vascular endothelial growth factor, a multifunctional polypeptide. P R Health Sci J 1996; 15: 169–78.
8 Thomas KA. Vascular endothelial growth factor, a potent and selective angiogenic agent. J Biol Chem 1996; 271: 603–6.
9 Schoch HJ, Fischer S, Marti HH. Hypoxia-induced vascular endothelial growth factor expression causes vascular leakage in the brain. Brain 2002; 125: 2549–57.
10 Kidd T, Brose K, Mitchell KJ, Fetter RD, Tessier-Lavigne M, Goodman CS, *et al*. Roundabout controls axon crossing of the CNS midline and defines a novel subfamily of evolutionarily conserved guidance receptors. Cell 1998; 92: 205–15.
11 Brose K, Bland KS, Wang KH, Arnott D, Henzel W, Goodman CS, *et al*. Slit proteins bind Robo receptors and have an evolutionarily conserved role in repulsive axon guidance. Cell 1999; 96: 795–806.
12 Li HS, Chen JH, Wu W, Fagaly T, Zhou L, Yuan W, *et al*. Vertebrate Slit, a secreted ligand or the transmembrane protein Roundabout, is a repellent or olfactory bulb axons. Cell 1999; 96: 807–18.
13 Plachez C, Andrews W, Liapi A, Knoell B, Drescher U, Mankoo B, *et al*. Slit1 and Slit2 cooperate o prevent premature midline crossing of retinal axons in the mouse visual system. Neuron 2002; 33: 219–32.
14 Bashaw GJ, Kidd T, Murray D, Pawson T, Goodman CS. Repulsive axon guidance: Abelson and Enabled play opposing roles downstream of the roundabout receptor. Cell 2000; 101: 703–15.
15 Dickson BJ, Gilestro GF. Regulation of commissural axon path finding by Slit and its Robo receptors. Annu Rev Cell Dev Biol 2006; 22: 651–75.
16 Wu JY, Feng L, Park HT, Havlioglu N, Wen L, Tang H, *et al*. The neuronal repellent Slit inhibits leukocyte chemotaxis induced by chemotactic factors. Nature 2001; 410: 948–52.
17 Guan H, Zu G, Xie Y, Tang H, Jonhson M, Xu X, *et al*. Neuronal repellent Slit2 inhibits dendritic cell migration and the development of immune responses. J Immunol 2003; 171: 6519–26.
18 Kanellis J, Garcia GE, Li P, Parra G, Wilson CB, Rao Y, *et al*. Modulation of inflammation by Slit protein *in vivo* in experimental crescentic glomerulonephritis. Am J Pathol 2004; 165: 341–52.
19 Prasad A, Qamri Z, Wu J, Ganju RK. Slit2/Robo1 modulates the CXCL12/CXCR4-induced chemotaxis of T cells. J Leukoc Biol 2007; 82: 465–76.
20 Altay T, McLaughlin B, Wu JY, Park TS, Gidday JM. Slit modulates cerebrovascular inflammation and mediates neuroprotection against global cerebral ischemia. Exp Neurol 2007; 207: 186–94.
21 Tole S, Mukovozov IM, Huang YW, Magalhaes MA, Yan M, Crow MR, *et al*. The axonal repellent, Slit2, inhibits directional migration of circulating neutrophils. J Leukoc Biol 2009; 86: 1403–15.
22 Schmid BC, Rezniczek GA, Fabjani G, Yoneda T, Leodolter S, Zeillinger R. The neuronal guidance cue Slit2 induces targeted migration and may play a role in brain metastasis of breast cancer cells. Breast Cancer Res Treat 2007; 106: 333–42.
23 Mertsch S, Schmitz N, Jeibmann A, Geng JG, Paulus W, Senner V. Slit2 involvement in glioma cell migration is mediated by Robo1 receptor. J Neurooncol 2008; 87: 1–7.
24 Yuasa-Kawada J, Kinoshita-Kawada M, Rao Y, Wu JY. Deubiquitinating enzyme USP33/VDU1 is required for Slit signaling in inhibiting breast cancer cell migration. Proc Natl Acad Sci U S A 2009; 106: 14530–5.
25 Wang B, Xiao Y, Ding BB, Zhang N, Yuan X, Gui L, *et al*. Induction of tumor angiogenesis by Slit-Robo signaling and inhibition of cancer growth by blocking Robo activity. Cancer Cell 2003; 4: 19–29.
26 Wang LJ, Zhao Y, Han B, Ma YG, Zhang J, Yang DM, *et al*. Targeting Slit–Roundabout signaling inhibits tumor angiogenesis in chemical-induced squamous cell carcinogenesis. Cancer Sci 2008; 99: 510–7.
27 Urbich C, Rössig L, Kaluza D, Potente M, Boeckel JN, Knau A, *et al*.

HDAC5 is a repressor of angiogenesis and determines the angiogenic gene expression pattern of endothelial cells. Blood 2009; 113: 5669–79.

28 Shen F, Liu X, Geng JG, Guo SW. Increased immunoreactivity to Slit/Robo1 in ovarian endometriomas. Am J Pathol 2009; 175: 479–88.

29 Zhang B, Dietrich UM, Geng JG, Bicknell R, Esko JD, Wang L. Repulsive axon guidance molecule Slit3 is a novel angiogenic factor. Blood 2009; 114: 4300–9.

30 Ma S, Liu X, Geng JG, Guo SW. Increased SLIT immunoreactivity as a biomarker for recurrence in endometrial carcinoma. Am J Obstet Gynecol 2010; 202: 68.e1–68.e11.

31 Yang XM, Han HX, Sui F, Dai YM, Chen M, Geng JG. Slit-Robo signaling mediates lymphangiogenesis and promotes tumor lymphatic metastasis. Biochem Biophys Res Commun 2010; 396: 571–7.

32 Xu F, Previti ML, Nieman MT, Davis J, Schmaier AH, Van Nostrand WE. AbetaPP/APLP2 family of Kunitz serine proteinase inhibitors regulate cerebral thrombosis. J Neurosci 2009; 29: 5666–70.

33 Engelhardt B, Sorokin L. The blood-brain and the blood-cerebrospinal fluid barriers: function and dysfunction. Semin Immunopathol 2009; 31: 497–511.

34 Pottiez G, Flahaut C, Cecchelli R, Karamanos Y. Understanding the blood-brain barrier using gene and protein expression profiling technologies. Brain Res Rev 2009; 62: 83–98.

35 Terry S, Nie M, Matter K, Balda MS. Rho signaling and tight junction functions. Physiology (Bethesda) 2010; 25: 16–26.

36 Argaw AT, Gurfein BT, Zhang Y, Zameer A, John GR. VEGF-mediated disruption of endothelial CLN-5 promotes blood-brain barrier breakdown. Proc Natl Acad Sci U S A 2009; 106: 1977–82.

37 Liu D, Hou J, Hu X, Wang X, Xiao Y, Mou Y, *et al*. Neuronal chemorepellent Slit2 inhibits vascular smooth muscle cell migration by suppressing small GTPase Rac1 activation. Circ Res 2006; 98; 480–9.

38 Alam MI, Beg S, Samad A, Baboota S, Kohli K, Ali J, *et al*. Strategy for effective brain drug delivery. Eur J Pharm Sci 2010; 40: 385–403.

Acta Pharmacologica Sinica (2011) 32: 1337–1344
 1671-4083/11 $32.00
www.nature.com/aps

Original Article

Platonin inhibited PDGF-BB-induced proliferation of rat vascular smooth muscle cells via JNK1/2-dependent signaling

Yi CHANG[1, 2, #], Yih-Huei UEN[3, #], Chang-Chih CHEN[4], Song-Chow LIN[2], Shiao-Yun TSENG[2], Yi-Hsuan WANG[2], Joen-Rong SHEU[2, *], Cheng-Ying HSIEH[2, *]

[1]Department of Anesthesiology, Shin Kong Wu Ho-Su Memorial Hospital, Taipei, Taiwan, China and School of Medicine, Fu-Jen Catholic University, Taipei, Taiwan, China; [2]Department of Pharmacology, Taipei Medical University, Taipei, Taiwan, China; [3]Department of Surgery, Chi-Mei Medical Center, Tainan, Taiwan, China; [4]Department of Surgery, Mackay Memorial Hospital, Taipei, Taiwan, China and School of Dentistry, Taipei Medical University, Taipei, Taiwan, China

Aim: To examine the inhibitory actions of the immunoregulator platonin against proliferation of rat vascular smooth muscle cells (VSMCs).
Methods: VSMCs were prepared from the thoracic aortas of male Wistar rats. Cell proliferation was examined using MTT assays. Cell cycles were analyzed using flow cytometry. c-Jun N-terminal kinase (JNK)1/2, extracellular signal-regulated kinase (ERK)1/2, AKT, and c-Jun phosphorylation or p27 expression were detected using immunoblotting.
Results: Pretreatment with platonin (1–5 μmol/L) significantly suppressed VSMC proliferation stimulated by PDGF-BB (10 ng/mL) or 10% fetal bovine serum (FBS), and arrested cell cycle progression in the S and G_2/M phases. The same concentrations of platonin significantly inhibited the phosphorylation of JNK1/2 but not ERK1/2 or AKT in VSMCs stimulated by PDGF-BB. Furthermore, platonin also attenuated c-Jun phosphorylation and markedly reversed the down-regulation of p27 expression after PDGF-BB stimulation.
Conclusion: Platonin inhibited VSMC proliferation, possibly via inhibiting phosphorylation of JNK1/2 and c-Jun, and reversal of p27 down-regulation, thereby leading to cell cycle arrest at the S and G_2/M phases. Thus, platonin may represent a novel approach for lowering the risk of abnormal VSMC proliferation and related vascular diseases.

Keywords: platonin; cell cycle; JNK1/2; PDGF-BB; p27; vascular smooth muscle cells

Acta Pharmacologica Sinica (2011) 32: 1337–1344; doi: 10.1038/aps.2011.105; published online 5 Sep 2011

Introduction

Abnormal proliferation of vascular smooth muscle cells (VSMCs) is implicated in the pathogenesis of several diseases, including atherosclerosis, restenosis after angioplasty, transplant vasculopathy, and failure of vein graft bypasses[1]. Numerous growth factors and cytokines are reported to be released in human vascular lesions by dysfunctional endothelial cells, inflammatory cells, platelets, and VSMCs, and these mediate chemoattraction, cell migration, proliferation, apoptosis, and matrix modulation[2]. Basic fibroblast growth factor initiates medial proliferation of VSMCs, whereas platelet-derived growth factor (PDGF) induces subsequent migration of VSMCs toward the intima. Intimal proliferation and matrix accumulation have been reported to occur under the influence of PDGF, transforming growth factor-β, angiotensin II, epidermal growth factor, and insulin-like growth factor 1[3]. Although all of these factors may play roles in driving cellular events that lead to vascular proliferative diseases, PDGF is considered to be the main cause[4].

PDGF is a peptide growth factor that provides signals for the proliferation of target cells. PDGF isoforms consist of different combinations of two polypeptide chains (the A- and B-chains), including PDGF-AA, -AB, and -BB. α- and β-receptors of PDGF have specific affinities for their isoforms, a preference of the β-receptor for the PDGF-B chain, for example[5]. PDGF receptor (PDGFR)-β expression increases in atherosclerotic lesions and is primarily limited to VSMCs[6]. PDGF-BB propagates mitogenic signals through the autophosphorylation of the PDGFR-β tyrosine residues. Tyrosine-phosphorylated PDGFR-β interacts with several other cytoplasmic proteins

# These authors contributed equally to this work.
* To whom correspondence should be addressed.
E-mail sheujr@tmu.edu.tw (Joen-Rong SHEU);
d102093001@tmu.edu.tw (Cheng-Ying HSIEH)
Received 2011-03-17 Accepted 2011-07-05

that constitute Src homology 2 (SH2) domains, including phospholipase Cγ (PLCγ), ras guanine 5′-triphosphatase-activating protein, phosphatidyl-inositol 3-kinase (PI-3K), and tyrosine phosphatase SHP-2. These signaling molecules mediate cellular activities, including proliferation, migration, and differentiation in response to PDGF in VSMCs[7]. Furthermore, it is well known that PDGF transmits its signal into the intracellular space through the activation of AKT and mitogen-activated protein kinases (MAPKs)[8].

Platonin (4,4′,4″-thrimethyl-3,3′,3″-triheptyl-7-[2″-thiazolyl]-2,2′-trimethinethiazolocyanine-3-3″-diiodide) (Figure 1), a cyanine photosensitizing dye, is an immunomodulator[9, 10] currently in use as an effective medicine for rheumatoid arthritis[10, 11]. Administration of platonin is known to inhibit the up-regulation of inflammatory molecules, including interleukin (IL)-1β, IL-6, tumor necrosis factor (TNF)-α, and inducible nitric oxide synthase (iNOS) in endotoxin-activated macrophages[12, 13]. Furthermore, platonin also reduces circulatory failure and mortality in septic rats[14]. The anti-inflammatory mechanisms of platonin may be due to the suppression of MAPKs, nuclear factor (NF)-κB, and activator protein (AP)-1[15]. Recently, platonin was also reported to be capable of inhibiting cell growth and inducing extensive autophagy-associated cell death in leukemic cells[16].

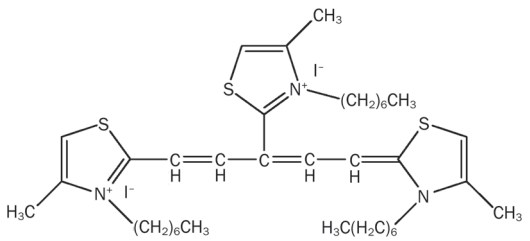

Figure 1. Chemical structure of platonin (4,4′,4″-thrimethyl-3,3′,3″-triheptyl-7-[2″-thia-zolyl]-2,2′-trimethinethiazolocyanine-3-3″-diiodide).

Considering the pivotal roles of VSMC proliferation in the development of atherosclerosis and restenosis, this study was designed to examine the action mechanisms of platonin in inhibiting VSMC proliferation stimulated by PDGF-BB.

Materials and methods

Materials

Platonin was synthesized by Kankohsha (Osaka, Japan) and obtained from Gwo Chyang Pharmaceuticals (Tainan, Taiwan, China). Male Wistar rats were purchased from BioLASCO (Taipei, Taiwan, China). Dulbecco's modified Eagle's medium (DMEM), trypsin (0.25%), *L*-glutamine, penicillin/streptomycin, and fetal bovine serum (FBS) were purchased from Gibco (Gaithersburg, MD, USA). 3-(4,5-Dimethylthiazol-2-yl)-2,5-diphenyltetrazolium bromide (MTT) and sp600125 (an inhibitor of JNK1/2 phosphorylation) were from Sigma-Aldrich (St Louis, MO, USA). Recombinant PDGF-BB was purchased from PeproTech (Rocky Hill, NJ, USA). The anti-phospho-ERK1/2 (Thr^{202}/Tyr^{204}), anti-phospho-AKT (Ser^{473}), and anti-phospho-c-Jun N-terminal kinase (JNK) (Thr^{183}/Tyr^{185}) monoclonal antibodies (mAbs) were purchased from Cell Signaling (Beverly, MA, USA). The phospho-c-Jun mAb was purchased from Santa Cruz Biotechnology (Santa Cruz, CA, USA). The anti-p27 polyclonal antibody (pAb) was purchased from Genetex (Irvine, CA, USA). The anti-α-tubulin mAb was purchased from NeoMarkers (Fremont, CA, USA). The Hybond-P polyvinylidene difluoride (PVDF) membrane, enhanced chemiluminescence (ECL) Western blotting detection reagent and analysis system, horseradish peroxidase (HRP)-conjugated donkey anti-rabbit immunoglobulin G (IgG), and sheep anti-mouse IgG were purchased from Amersham (Buckinghamshire, UK). Platonin was dissolved in phosphate-buffered saline (PBS) and stored at 4 °C until use.

VSMC isolation and culture

All animal experiments were carried out according to the Guide for the Care and Use of Laboratory Animals (National Academy Press, Washington, DC, USA, 1996). VSMCs were enzymatically dispersed from the thoracic aortas of male Wistar rats (250–300 g). The thoracic aorta was removed and stripped of the endothelium and adventitia. VSMCs were obtained using a combination of collagenase and elastase digestion[17]. The cells were grown in DMEM supplemented with 20 mmol/L HEPES, 10% fetal bovine serum (FBS), 1% penicillin/streptomycin, and 2 mmol/L glutamine at 37 °C in a humidified atmosphere of 5% CO_2. VSMCs at passage 4–8 were used in all experiments. Primary cultured rat aortic VSMCs showed the "hills and valleys" pattern, and the expression of α-smooth muscle actin was confirmed (data not shown).

Proliferation assays

VSMCs (2×10^4 cells/well) were seeded on 24-well plates and cultured in DMEM containing 10% FBS for 24 h. The medium was then replaced with serum-free medium for 24 h. Serum-starved VSMCs were pretreated with platonin (1–5 μmol/L), sp600125 (5 and 10 μmol/L) or an isovolumetric solvent control (PBS) for 20 min and then stimulated with PDGF-BB (10 ng/mL) or 10% FBS for 48 h. The cell number was measured using a colorimetric assay based on the ability of mitochondria in viable cells to reduce the MTT as previously described[18]. The cell number index was calculated as the absorbance of treated cells/control cells×100%.

Cell cycle analysis

For cell cycle analysis, starved VSMCs (2×10^5 cells/dish) were pretreated with platonin (2 and 5 μmol/L), sp600125 (5 and 10 μmol/L) or PBS for 20 min and then stimulated with PDGF-BB (10 ng/mL) for 24 h. After 24 h, cells were detached from the plate using trypsin, washed with PBS, and fixed in 70% ethanol for 30 min. Cells were then washed with PBS and resuspended in a solution containing RNase (50 μg/mL), propidium iodide (PI; 80 μg/mL) and Triton-X-100 (0.2%). Samples were incubated for 20 min and subjected to flow cytometric

analysis (Beckman Coulter, Ramsey, MN, USA).

Immunoblotting

Immunoblotting analysis was performed to determine the expression of proteins in VSMCs as described previously[19]. Serum-starved VSMCs (2×10^5 cells/dish) were treated with platonin (1–5 μmol/L) or PBS for 20 min, followed by the addition of PDGF-BB (10 ng/mL) or 10% FBS for the indicated times. After treatment, proteins were extracted with lysis buffer. The lysates were centrifuged, the supernatant protein (50 μg) was collected and subjected to sodium dodecylsulfate polyacrylamide gel electrophoresis (SDS-PAGE), and the separated proteins were electrophoretically transferred onto 0.45-μm polyvinylidene difluoride (PVDF) membranes. The blots were blocked with TBST (10 mmol/L Tris-base, 100 mmol/L NaCl, and 0.01% Tween 20) containing 5% bovine serum albumin (BSA) for 1 h and were then probed with various primary antibodies. The membranes were incubated with HRP-linked anti-mouse IgG or anti-rabbit IgG (diluted 1:3000 in TBST) for 1 h. Immunoreactive bands were detected by an enhanced chemiluminescence (ECL) system. The bar graph depicts the ratios of quantitative results obtained by scanning reactive bands and quantifying the optical density using videodensitometry (Bio-profil; Biolight Windows Application V2000.01; Vilber Lourmat, France).

Confocal microscopy

Confocal microscopy was used to evaluate the expression of phospho-JNK1/2 in VSMCs. VSMCs (1×10^5 cells/cover slip) were placed on cover slips and allowed to adhere in a cell culture incubator overnight and then were starved for 24 h. VSMCs were treated as per the design of the experiment and were then fixed with 4% paraformaldehyde for 30 min and permeabilized with 80% methanol for 15 min. After incubation with 3% skimmed milk in PBS for 60 min, the preparation was incubated for 1 h with a primary Ab (1:80). Cells were then washed three times with PBS and exposed to the secondary Ab [FITC-conjugated anti-rabbit immunoglobin G (IgG) at 1:100, 1% BSA/PBS] for 60 min. The slides were prepared with a mounting buffer (Vector Laboratories, Burlingame, CA, USA) under a glass cover slip on a Leica TCS SP5 Confocal Spectral Microscope Imaging System using an argon/krypton laser (Mannheim, Germany).

Statistical analysis

The experimental results are expressed as mean±SEM and are accompanied by the number of observations. The data were assessed by analysis of variance (ANOVA). If this analysis indicated significant differences among the group means, then each group was compared using the Newman-Keuls method. A P value of <0.05 was considered statistically significant.

Results

Effects of platonin on VSMC proliferation stimulated by PDGF-BB or FBS

Figure 2 (panels A and B) shows that VSMC proliferation induced by PDGF-BB (10 ng/mL) or 10% FBS increased by approximately 89% and 94%, respectively. Furthermore, pretreatment with platonin inhibited cell proliferation after both PDGF-BB (66.3%, 96.6%, and 122.4%, respectively) and FBS (57.4%, 67.3%, and 84.3%, respectively) stimulation in a concentration-dependent (1, 2, and 5 μmol/L) manner, indicating that the inhibitory effects of platonin on VSMC proliferation are not specific to PDGF-BB. Morphological analysis also showed a similar effect as exhibited in the MTT assay of PDGF-BB-stimulated VSMCs (Figure 2C). These results suggest that platonin inhibited both PDGF-BB- and FBS-induced VSMC proliferation in a concentration-dependent manner.

Effects of platonin on cell cycle progression in PDGF-BB-stimulated VSMCs

To investigate the effect of platonin on cell cycle progression in VSMCs, the DNA content was analyzed using PI staining. After stimulation with PDGF-BB (10 ng/mL), the percentage of cells in the S (6.7%±0.2% to 9.3%±0.8%, P<0.05; n=5) and G_2/M phases (19.9%±1.0% to 23.1%±0.8%, P<0.05; n=5) increased, while the proportion of cells in the G_0/G_1 phase was reduced (70.6%±1.3% to 64.4%±1.9%, P<0.05; n=5) (Table 1). Platonin (5 μmol/L) treatment resulted in an accumulation of cells in the S and G_2/M phases, and a reduction was noted in the G_0/G_1 phase compared to the PBS-treated group (S phase, 9.3%±0.8% *vs* 14.2%±0.9%, P<0.01; n=5; G_2/M phase, 23.1%±0.8% *vs* 26.7%±0.9%, P<0.05; n=5; G_0/G_1 phase, 64.4%±1.9% *vs* 56.9%±1.1%, P<0.01; n=5) (Table 1). These results indicate that platonin was effective in arresting the cell cycle in the S and G_2/M phases in PDGF-BB-stimulated VSMCs.

Table 1. Effects of platonin on cell cycle progression in platelet-derived growth factor (PDGF)-BB (10 ng/mL)-stimulated vascular smooth muscle cells (VSMCs).

	Sub-G_1 (%)	G_0/G_1 (%)	S (%)	G_2/M (%)
Resting	1.6±0.5	70.6±1.3	6.7±0.2	19.9±1.0
PBS+PDGF-BB	1.8±0.3	64.4±1.9[b]	9.3±0.8[b]	23.1±0.8[b]
Platonin (2 μmol/L) +PDGF-BB	1.5±0.3	62.6±1.7	9.5±1.0	26.3±1.1
Platonin (5 μmol/L) +PDGF-BB	2.2±0.4	56.9±1.1[f]	14.2±0.9[f]	26.7±0.9[e]

The cell cycle distribution was assessed by flow cytometry as described in "Materials and methods". Data are presented as the mean±SEM. n=5. [b]P<0.05, compared to the resting group. [e]P<0.05, [f]P<0.01, compared to the PBS+PDGF-BB group.

The effects of platonin on AKT, ERK1/2, and JNK1/2 phosphorylation in PDGF-BB-stimulated VSMCs

The PDGF-BB-induced activation of several signaling proteins, including AKT (Figure 3), ERK1/2 (Figure 4A), and JNK1/2 (Figure 4B), was detected to unravel the mechanisms of platonin in VSMC proliferation. In the present study, phospho-

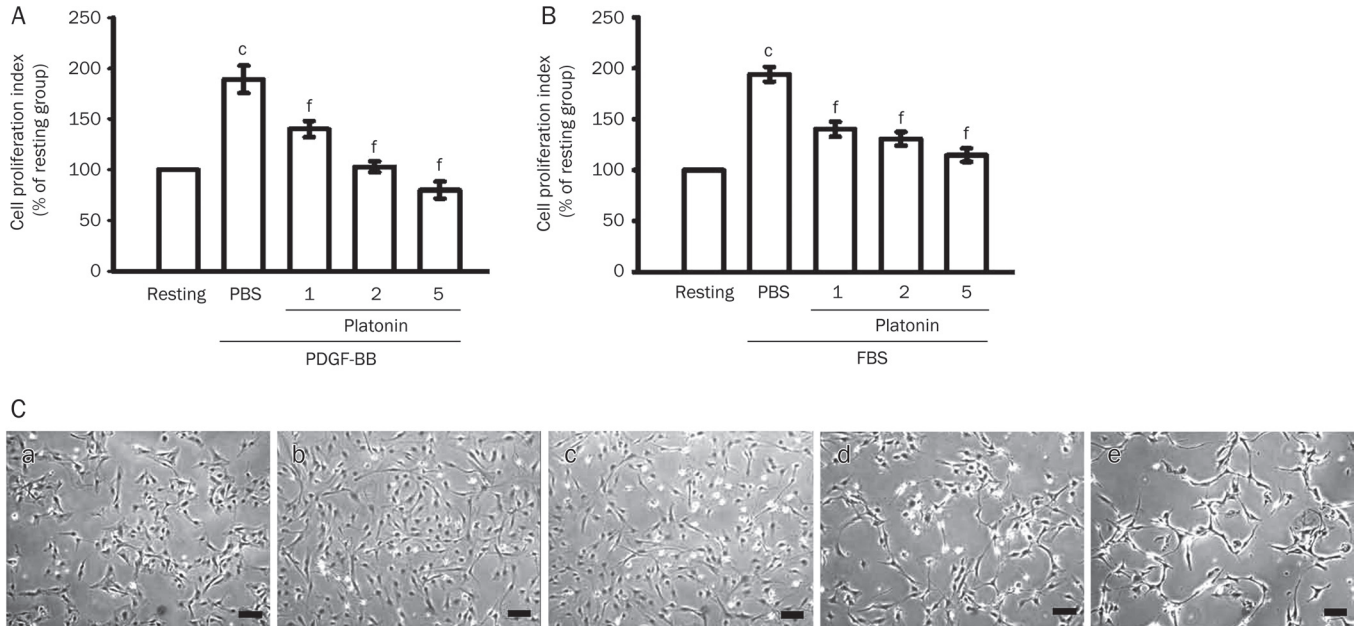

Figure 2. The effects of platonin on cell proliferation in vascular smooth muscle cells (VSMCs) stimulated by platelet-derived growth factor (PDGF)-BB or fetal bovine serum (FBS). VSMCs (2×10^4 cells/well) were treated with only PBS (resting) or were preincubated with PBS and platonin (1, 2, and 5 μmol/L), followed by the addition of PDGF-BB (10 ng/mL) (A) or 10% FBS (B) for 48 h to stimulate cell proliferation. Cell numbers were evaluated by an MTT assay as described in our methods. The data are presented as the mean±SEM. n=5. $^cP<0.01$, compared to the resting group. $^fP<0.01$, compared to the PBS+PDGF-BB (A) or PBS+FBS (B) group. (C) Morphological photographs of VSMC proliferation that show (a) resting cells (treated with only PBS) or cells preincubated with (b) PBS, (c) platonin (1 μmol/L), (d) platonin (2 μmol/L), and (e) platonin (5 μmol/L), followed by the addition of PDGF-BB (10 ng/mL) for 48 h. The black bar represents 50 μm.

rylation of JNK1/2, but not ERK1/2 or AKT, stimulated by PDGF-BB (10 ng/mL) for 10 min was markedly inhibited by platonin (2 and 5 μmol/L) (Figures 3, 4). Confocal microscopy provided further evidence of the inhibitory effect of platonin on JNK1/2 phosphorylation in VSMCs. As shown in Figure 4C, minimal expression of phospho-JNK1/2 was detected in resting cells (Figure 4Ca) and was more pronounced in the PDGF-BB (10 ng/mL)-treated cells (Figure 4Cb). However, pretreatment with platonin (2 μmol/L) resulted in a significantly decreased expression of phospho-JNK1/2 (Figure 4Cc) in PDGF-BB-stimulated cells. These findings are consistent with the results described in Figure 4B. In addition, as shown in Figure 4D, treatment with platonin (2 and 5 μmol/L) significantly inhibited JNK1/2 phosphorylation in 10% FBS-treated cells but not resting cells. This result indicates that platonin may inhibit JNK1/2 phosphorylation in activated VSMCs but not in resting cells. These results suggest that the JNK1/2 signaling pathway may play an important role in platonin-mediated inhibition of PDGF-BB-stimulated VSMC proliferation.

The effects of platonin on c-Jun phosphorylation and p27 expression in PDGF-BB-stimulated VSMCs

Several lines of evidence indicate that the JNK-mediated phosphorylation of c-Jun is necessary for cell proliferation[20, 21]. Zhan *et al*[22] also reported that the pivotal role of c-Jun in PDGF-BB-induced VSMC proliferation is mediated by the down-regulation of p27 expression, an inhibitor of cyclin-dependent kinase (CDK). Based on the above results demonstrating that platonin's inhibition of cell proliferation may interfere with JNK1/2 phosphorylation, we sought to examine

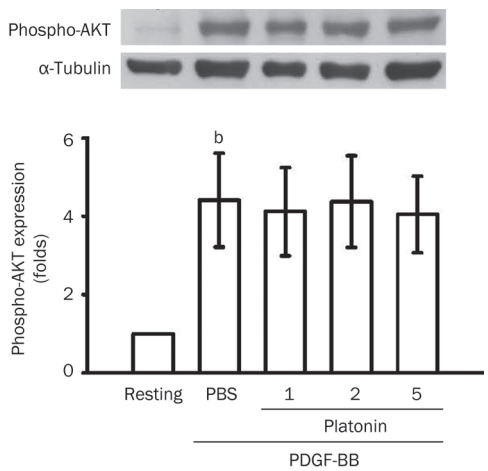

Figure 3. The effect of platonin on AKT phosphorylation in vascular smooth muscle cells (VSMCs) stimulated by platelet-derived growth factor (PDGF)-BB. VSMCs (2×10^5 cells/dish) were treated with only PBS (resting) or were pretreated with PBS and platonin (1, 2, and 5 μmol/L), followed by the addition of PDGF-BB (10 ng/mL) for 10 min to trigger AKT phosphorylation. The data are presented as the mean±SEM. n=3. $^bP<0.05$, compared to the resting group.

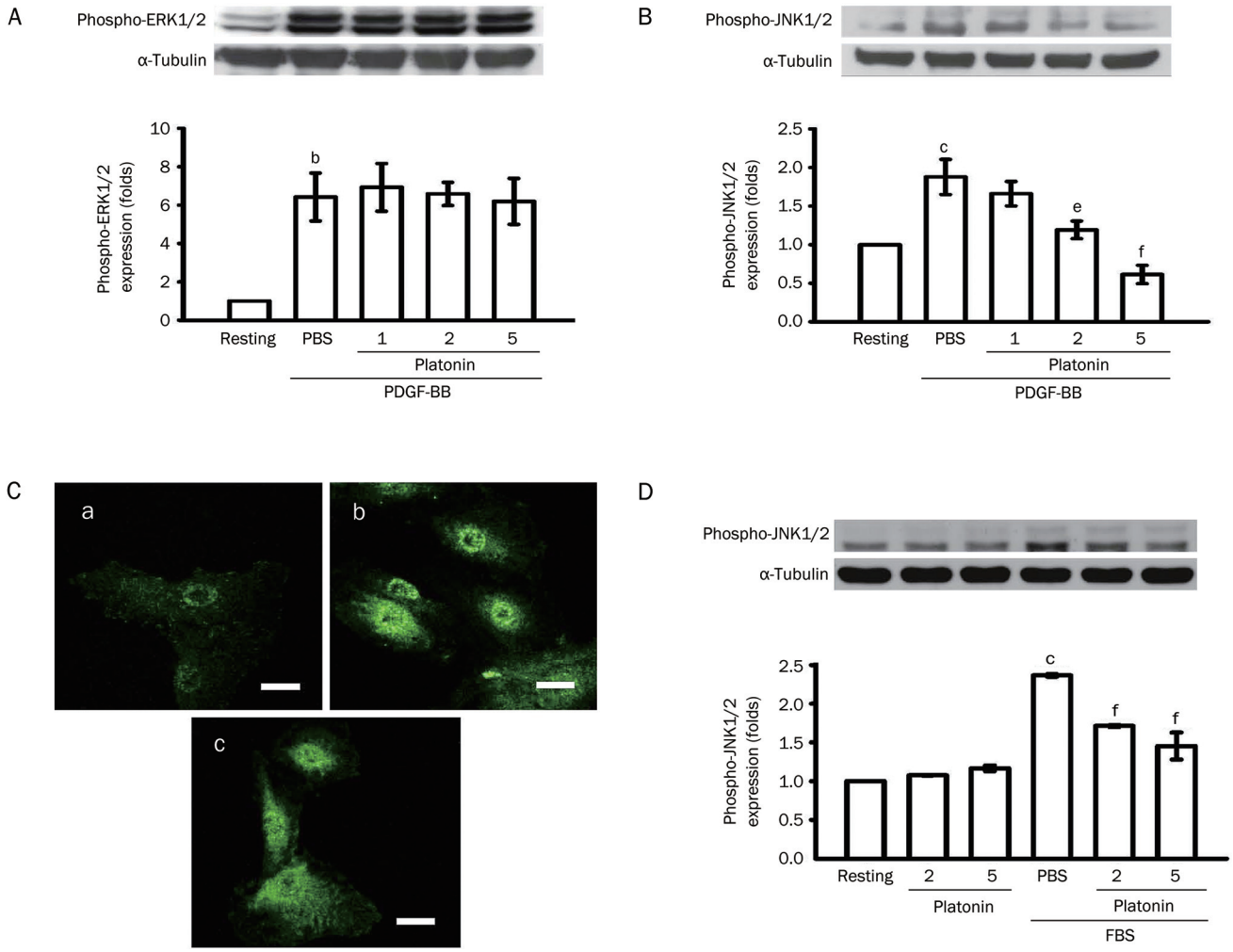

Figure 4. The effects of platonin on ERK1/2 and JNK1/2 phosphorylation in vascular smooth muscle cells (VSMCs) stimulated by platelet-derived growth factor (PDGF)-BB or fetal bovine serum (FBS). (A and B) VSMCs (2×10^5 cells/dish) were treated with only PBS (resting) or preincubated with PBS and platonin (1, 2, and 5 μmol/L), followed by the addition of PDGF-BB (10 ng/mL) for 10 min to stimulate (A) ERK1/2 and (B) JNK1/2 phosphorylation. (C) VSMCs (1×10^5 cells/cover slip) were incubated with (a) PBS only (resting) or were pretreated with (b) PBS and (c) platonin (2 μmol/L), followed by the addition of PDGF-BB (10 ng/mL) for 10 min. Confocal images are representative of those obtained in three separate experiments demonstrating the expression of phospho-JNK1/2 in VSMCs. The white bar indicates 20 μm. (D) VSMCs (2×10^5 cells/dish) were incubated with only PBS (resting) or platonin (2 and 5 μmol/L) or pretreated with PBS and platonin (2 and 5 μmol/L), followed by the addition of FBS (10%) to stimulate JNK1/2 phosphorylation. The data are presented as the mean±SEM. n=3. ^bP<0.05, ^cP<0.01 compared to the resting group. ^eP<0.05, ^fP<0.01 compared to the (B) PBS+PDGF-BB group or (D) PBS+FBS group.

whether platonin interferes with c-Jun phosphorylation and p27 expression. As shown in Figure 5A, PDGF-BB (10 ng/mL) induced expression of phospho-c-Jun in VSMCs after 30 min of stimulation. Figure 5B shows that c-Jun phosphorylation was markedly inhibited by platonin (1–5 μmol/L) in a concentration-dependent manner. p27 protein was robustly expressed in resting cells, whereas PDGF-BB (10 ng/mL) treatment for 24 h caused significant down-regulation of p27 expression. Platonin (2 and 5 μmol/L) markedly reversed this effect (Figure 5C).

The correlation between the JNK1/2 phosphorylation and cell proliferation in activated VSMCs

As shown in Figure 6A, pretreatment with sp600125 (5 and 10 μmol/L) markedly suppressed cell proliferation in PDGF-BB-stimulated VSMCs. In addition, sp600125 (10 μmol/L) treatment in PDGF-BB-stimulated cells resulted in an increase of cells in the G_2/M phase and a reduction in the G_0/G_1 phase compared to the DMSO-treated group (G_2/M phase, 21.7%±0.7% *vs* 32.2%±2.4%, P<0.01, n=3; G_0/G_1 phase, 66.8%±2.9% *vs* 56.6%±1.5%, P<0.05, n=3) (Figure 6B). These results further demonstrate that changes in JNK1/2 phosphorylation status play a pivotal role in the regulation of cell proliferation in activated VSMCs.

Discussion

This study demonstrates that platonin, a trithiazole pentamethine cyanine, inhibits PDGF-BB-stimulated VSMC prolifera-

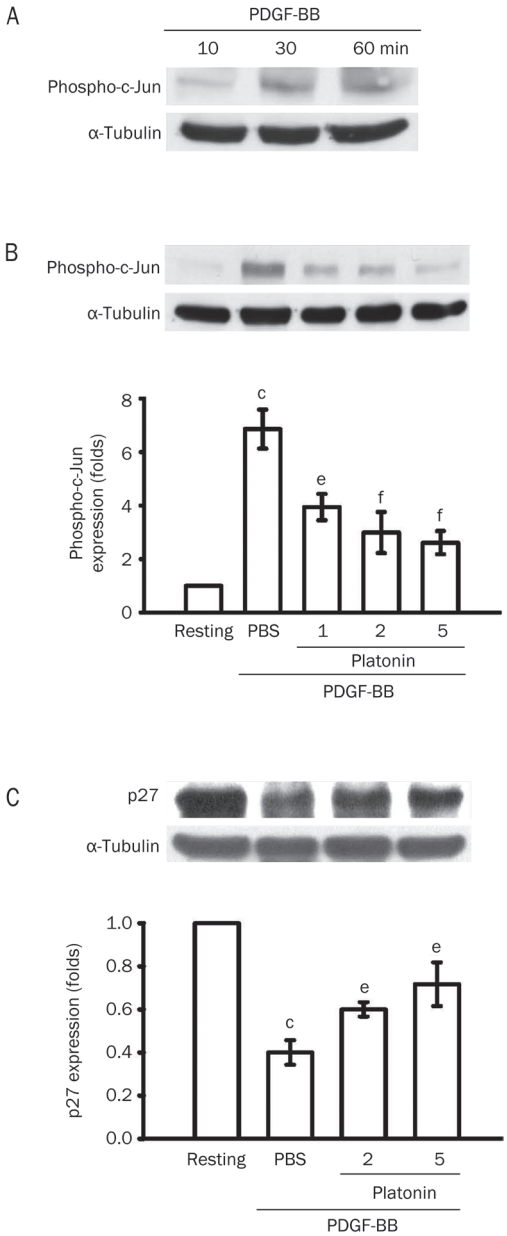

Figure 5. The effects of platonin on c-Jun phosphorylation and p27 expression in vascular smooth muscle cells (VSMCs) stimulated by platelet-derived growth factor (PDGF)-BB. (A) VSMCs (2×10^5 cells/dish) were treated with PDGF-BB (10 ng/mL) for the indicated times (10, 30, and 60 min), were incubated with only PBS (resting), or were pretreated with PBS and various concentrations of platonin, followed by the addition of PDGF-BB (10 ng/mL) to stimulate (B) c-Jun phosphorylation after 30 min. (C) Down-regulation of p27 expression after 24 h. The data are presented as the mean±SEM. n=3. ^cP<0.01 compared to the resting group. ^eP<0.05, ^fP<0.01 compared to the PBS+PDGF-BB group.

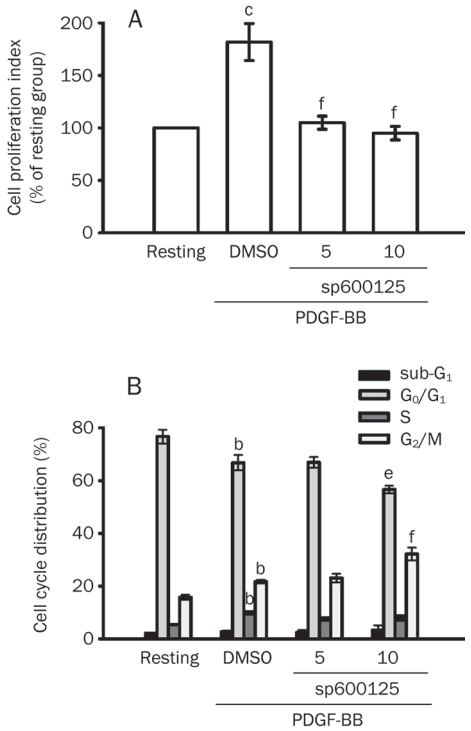

Figure 6. The effects of sp600125 on cell proliferation and cell cycle progression in PDGF-BB-stimulated VSMCs. VSMCs were incubated with PBS (resting) or were pretreated with either sp600125 (5 and 10 μmol/L) or an isovolumetric solvent control (0.1% DMSO), followed by the addition of PDGF-BB (10 ng/mL) to stimulate (A) cell proliferation by MTT assay and (B) cell cycle progression by flow cytometry, as described in our methods. The data are presented as the mean±SEM. n=3. ^bP<0.05, ^cP<0.01 compared to the resting group. ^eP<0.05, ^fP<0.01 compared to the 0.1% DMSO group.

tion by suppressing JNK-dependent signals, resulting in cell cycle arrest in the S and G_2/M phases. VSMC proliferation plays an important role in the pathophysiological course of atherosclerosis and restenosis after balloon angioplasty. Therefore, the modulation of VSMC proliferation has important therapeutic implications[1]. In the present study, we found that platonin inhibited cell proliferation in PDGF-BB-stimulated VSMCs at 1–5 μmol/L. This result suggests that platonin could be a potential agent for treating VSMC proliferation-related diseases. Inflammatory processes followed by the proliferation of vascular components such as VSMCs and the extracellular matrix are associated with neointimal thickening[23]. Furthermore, reactive oxygen species (ROS) are reported to be a key mediator of signaling pathways that underlie vascular inflammation[24]. In past studies, platonin was shown to be a potent antioxidant and exert inhibitory effects against macrophage activation and inflammatory responses[12–14]. The inhibitory effects of platonin can potentially be harnessed and used to treat atherosclerosis or restenosis.

VSMCs proliferate via a mitotic process determined by the progression of the cell cycle. The cell cycle can be divided into two distinct phases: the synthesis (S) phase, in which DNA is replicated, and the mitosis (M) phase, in which cell division occurs. In animal cells, the components required for these phases are regulated by extracellular growth factors, and they are found mainly in the two gap phases, G_1 (between M and

S) and G_2 (between S and M)[25]. Platonin has been reported to induce significant G_0/G_1 arrest of a panel of human leukemic cell lines, including U937, HL-60, K562, NB4, and THP-1[16]. In this study, we also found that the loss of the proliferative capacity of VSMCs that had been treated with platonin is associated with cells that have been arrested in the S and G_2/M phases. This phenomenon indicates that platonin may have different effects on the cell cycle in different cell types.

PDGF-BB is considered to be the most important chemoattractant for VSMCs, and it activates multiple signaling pathways, including PI-3K/AKT and MAPKs[8]. In the present study, we found that platonin inhibited the phosphorylation of JNK1/2, but not AKT or ERK1/2, in PDGF-BB-stimulated VSMCs. The JNK protein kinases include at least three subtypes: JNK1, JNK2, and JNK3. JNK1 and 2 are ubiquitously expressed, and the expression of JNK3 is restricted to the brain, heart, and testes[26]. Extracellular stimuli lead to the activation of MAPK kinase kinases (MAPKKKs) that subsequently activate MAPK kinases 4 and 7 (MKK4 and MKK7), both of which phosphorylate JNKs. Activated JNKs result in the phosphorylation of many transcription factors, including the c-Jun component of the activator protein (AP)-1 transcription family[26, 27]. c-Jun is known to be required for PDGF-induced VSMC migration and proliferation, and JNK knockdown can attenuate cell migration and proliferation in PDGF-stimulated VSMCs[20, 22]. Furthermore, dominant-negative c-Jun lacking the transactivation domain of wild-type c-Jun (Ad-DN-c-Jun), which specifically blocks AP-1 transcriptional activity, significantly inhibited PDGF-BB-induced VSMC proliferation and suppressed PDGF-BB-induced down-regulation of CDK p27[21]. In this study, platonin inhibited JNK1/2 and c-Jun phosphorylation and reversed the down-regulation of p27 expression in VSMCs stimulated by PDGF-BB. These results indicate that JNK1/2-dependent signals may play important roles in the platonin-mediated inhibition of VSMC proliferation. Furthermore, JNK, c-Jun, and p27 activation have also been reported to regulate S and G_2/M phases of cell-cycle progression[28–31]. These studies are consistent with our finding that the platonin treatment arrested cell cycle progression in the S and G_2/M phases, which may have resulted from the suppression of JNK1/2-dependent signals.

In conclusion, this study demonstrates that platonin inhibits VSMC proliferation; this inhibition may involve the inhibition of both JNK1/2 phosphorylation and c-Jun activation and the reversal of down-regulated p27 expression, thereby leading to cell cycle arrest in the S and G_2/M phases. We suggest that platonin may be a potential therapeutic agent for treating diseases related to VSMC proliferation.

Acknowledgements

This work was supported by grants from Shin Kong Wu Ho-Su Memorial Hospital (SKH-8302-98-DR-31) and Chi-Mei Medical Center-Taipei Medical University (97CM-TMU-13).

Author contribution

Yi CHANG and Chang-Chih CHEN performed the research and wrote the manuscript; Yih-Huei UEN designed and performed the research; Song-Chow LIN, Shiao-Yun TSENG, and Yi-Hsuan WANG performed some of the experiments and analyzed data; and Joen-Rong SHEU and Cheng-Ying HSIEH designed the research.

References

1 Hedin U, Roy J, Tran PK. Control of smooth muscle cell proliferation in vascular disease. Curr Opin Lipidol 2004; 15: 559–65.
2 Ross R. Cell biology of atherosclerosis. Annu Rev Physiol 1995; 57: 791–804.
3 Dzau VJ, Braun-Dullaeus RC, Sedding DG. Vascular proliferation and atherosclerosis: new perspectives and therapeutic strategies. Nat Med 2002; 8: 1249–56.
4 Ferns GA, Raines EW, Sprugel KH, Motani AS, Reidy MA, Ross R. Inhibition of neointimal smooth muscle accumulation after angioplasty by an antibody to PDGF. Science 1991; 253: 1129–32.
5 Raines EW. PDGF and cardiovascular disease. Cytokine Growth Factor Rev 2004; 15: 237–54.
6 Wilcox JN, Smith KM, Williams LT, Schwartz SM, Gordon D. Platelet-derived growth factor mRNA detection in human atherosclerotic plaques by *in situ* hybridization. J Clin Invest 1988; 82: 1134–43.
7 Heldin CH, Westermark B. Mechanism of action and *in vivo* role of platelet-derived growth factor. Physiol Rev 1999; 79: 1283–316.
8 Cospedal R, Abedi H, Zachary I. Platelet-derived growth factor-BB (PDGF-BB) regulation of migration and focal adhesion kinase phosphorylation in rabbit aortic vascular smooth muscle cells: roles of phosphatidylinositol 3-kinase and mitogen-activated protein kinases. Cardiovasc Res 1999; 41: 708–21.
9 Mito K. A needle-type immunotherapeutic system incorporating laser light and platonin in combination with ethanol injection in the treatment of cancer growing in deep organs. Front Med Biol Eng 1999; 9: 275–84.
10 Kondo N, Ko H, Motoyoshi F, Orii T. B cell suppressing and $CD8^+$ T cell enhancing effects of photosensitive dye platonin in humans. J Rheumatol 1989; 16: 936–9.
11 Motoyoshi F, Kondo N, Ono H, Orii T. The effect of photosensitive dye platonin on juvenile rheumatoid arthritis. Biotherapy 1991; 3: 241–4.
12 Chen CC, Lee JJ, Tsai PS, Lu YT, Huang CL, Huang CJ. Platonin attenuates LPS-induced CAT-2 and CAT-2B induction in stimulated murine macrophages. Acta Anaesthesiol Scand 2006; 50: 604–12.
13 Lee JJ, Huang WT, Shao DZ, Liao JF, Lin MT. Platonin, a cyanine photosensitizing dye, inhibits pyrogen release and results in antipyresis. J Pharmacol Sci 2003; 93: 376–80.
14 Hsiao G, Lee JJ, Chou DS, Fong TH, Shen MY, Lin CH, *et al*. Platonin, a photosensitizing dye, improves circulatory failure and mortality in rat models of endotoxemia. Biol Pharm Bull 2002; 25: 995–9.
15 Lee JJ, Liu CL, Tsai PS, Yang CL, Lao HC, Huang CJ. Platonin inhibits endotoxin-induced MAPK and AP-1 up-regulation. J Surg Res 2011; 167: e299–305.
16 Chen YJ, Huang WP, Yang YC, Lin CP, Chen SH, Hsu ML, *et al*. Platonin induces autophagy-associated cell death in human leukemia cells. Autophagy 2009; 5: 173–83.
17 Pauly RR, Bilato C, Cheng L, Monticone R, Crow MT. Vascular smooth muscle cell cultures. Methods Cell Biol 1997; 52: 133–54.
18 Hsieh CY, Liu CL, Hsu MJ, Jayakumar T, Chou DS, Wang YH, *et al*. Inhibition of vascular smooth muscle cell proliferation by the vitamin E derivative pentamethylhydroxychromane in an *in vitro* and *in vivo* study: pivotal role of hydroxyl radical-mediated PLCgamma1 and JAK2 phosphorylation. Free Radic Biol Med 2010; 49: 881–93.

19 Hsieh CY, Hsu MJ, Hsiao G, Wang YH, Huang CW, Chen SW, *et al*. Andrographolide enhances NF-{kappa}B subunit p65 Ser536 dephosphorylation through activation of protein phosphatase 2A (PP2A) in vascular smooth muscle cells. J Biol Chem 2011; 286: 5942–55.
20 Ioroi T, Yamamori M, Yagi K, Hirai M, Zhan Y, Kim S, *et al*. Dominant negative c-Jun inhibits platelet-derived growth factor-directed migration by vascular smooth muscle cells. J Pharmacol Sci 2003; 91: 145–8.
21 Zhan Y, Kim S, Yasumoto H, Namba M, Miyazaki H, Iwao H. Effects of dominant-negative c-Jun on platelet-derived growth factor-induced vascular smooth muscle cell proliferation. Arterioscler Thromb Vasc Biol 2002; 22: 82–8.
22 Zhan Y, Kim S, Izumi Y, Izumiya Y, Nakao T, Miyazaki H, *et al*. Role of JNK, p38, and ERK in platelet-derived growth factor-induced vascular proliferation, migration, and gene expression. Arterioscler Thromb Vasc Biol 2003; 23: 795–801.
23 Inoue T, Node K. Molecular basis of restenosis and novel issues of drug-eluting stents. Circ J 2009; 73: 615–21.
24 Brandes RP, Weissmann N, Schröder K. NADPH oxidases in cardiovascular disease. Free Radic Biol Med 2010; 49: 687–706.
25 Björklund M, Taipale M, Varjosalo M, Saharinen J, Lahdenperä J, Taipale J. Identification of pathways regulating cell size and cell-cycle progression by RNAi. Nature 2006; 439: 1009–13.
26 Sumara G, Belwal M, Ricci R. "Jnking" atherosclerosis. Cell Mol Life Sci 2005; 62: 2487–94.
27 Davis RJ. Signal transduction by the JNK group of MAP kinases. Cell 2000; 103: 239–52.
28 Oktay K, Buyuk E, Oktem O, Oktay M, Giancotti FG. The c-Jun N-terminal kinase JNK functions upstream of Aurora B to promote entry into mitosis. Cell Cycle 2008; 7: 533–41.
29 Gutierrez GJ, Tsuji T, Chen M, Jiang W, Ronai ZA. Interplay between Cdh1 and JNK activity during the cell cycle. Nat Cell Biol 2010; 12: 686–95.
30 Hu B, Mitra J, van den Heuvel S, Enders GH. S and G_2 phase roles for Cdk2 revealed by inducible expression of a dominant-negative mutant in human cells. Mol Cell Biol 2001; 21: 2755–66.
31 Servant MJ, Coulombe P, Turgeon B, Meloche S. Differential regulation of p27(Kip1) expression by mitogenic and hypertrophic factors: involvement of transcriptional and posttranscriptional mechanisms. J Cell Biol 2000; 148: 543–56.

Acta Pharmacologica Sinica (2011) 32: 1345–1350
 1671-4083/11 $32.00
www.nature.com/aps

Original Article

Regulation of angiotensin-(1–7) and angiotensin II type 1 receptor by telmisartan and losartan in adriamycin-induced rat heart failure

Wen-na ZONG#, Xiao-hui YANG#, Xiu-mei CHEN, Hong-juan HUANG, Hong-jian ZHENG, Xiao-yi QIN, Yong-hong YONG, Ke-jiang CAO, Jun HUANG, Xin-zheng LU*

Department of Cardiology, First Affiliated Hospital, Nanjing Medical University, Nanjing 210029, China

Aim: To investigate the possible effects of telmisartan and losartan on cardiac function in adriamycin (ADR)-induced heart failure in rats, and to explore the changes in plasma level of angiotensin-(1–7)[Ang-(1–7)] and myocardial expression of angiotensin II type 1/2 receptors (AT_1R / AT_2R) and Mas receptor caused by the two drugs.
Methods: Male Sprague-Dawley rats were randomly divided into 4 groups: the control group, ADR-treated heart failure group (ADR-HF), telmisartan plus ADR-treated group (Tel+ADR) and losartan plus ADR-treated group (Los+ADR). ADR was administrated (2.5 mg/kg, ip, 6 times in 2 weeks). The rats in the Tel+ADR and Los+ADR groups were treated orally with telmisartan (10 mg/kg daily po) and losartan (30 mg/kg daily), respectively, for 6 weeks. The plasma level of Ang-(1–7) was determined using ELISA. The mRNA and protein expression of myocardial Mas receptor, AT_1R and AT_2R were measured using RT-PCR and Western blotting, respectively.
Results: ADR significantly reduced the plasma level of Ang-(1–7) and the expression of myocardial Mas receptor and myocardial AT_2R, while significantly increased the expression of myocardial AT_1R. Treatment with telmisartan and losartan effectively increased the plasma level of Ang-(1–7) and suppressed myocardial AT_1R expression, but did not influence the expression of Mas receptor and AT_2R.
Conclusion: The protective effects of telmisartan and losartan in ADR-induced heart failure may be partially due to regulation of circulating Ang-(1–7) and myocardial AT_1R expression.

Keywords: angiotensin-(1–7); Mas; angiotensin I receptor; angiotensin II receptor; adriamycin; heart failure; telmisartan; losartan

Acta Pharmacologica Sinica (2011) 32: 1345–1350; doi: 10.1038/aps.2011.96; published online 3 Oct 2011

Introduction

Adriamycin (ADR) is an anthracycline antibiotic commonly used in the treatment of a wide range of cancers, including hematological malignancies, many types of carcinomas, and soft tissue sarcomas. Importantly, the use of adriamycin can cause acute and chronic side effects. The chronic side effects are represented by the development of cardiomyopathy and ultimately, irreversible congestive heart failure[1, 2]. Great effort has been expended in preventing or mitigating the cardiotoxic side effects of ADR[3–7]; however, the mechanisms underlying ADR-induced heart failure are not fully understood.

The renin-angiotensin system (RAS) is one of the key regulators of blood pressure and cardiovascular disease[8–10] and involves several enzymes and receptors: renin, angiotensin II (Ang II), the Ang II type 1 receptor (AT_1R), the Ang II type 2 receptor (AT_2R) and the Mas receptor. Many reports have demonstrated the critical roles that these factors have in heart failure[9]. Ang II is an oligopeptide that causes vasoconstriction, increased blood pressure, and release of aldosterone from the adrenal cortex, while AT_1R and AT_2R are the receptors for Ang II. AT_1R mediates the major cardiovascular effects of Ang II, including vasoconstriction, increased vasopressin secretion, cardiac hypertrophy, cardiac contractility and extracellular matrix formation[9]. Conversely, effects mediated by AT_2R include inhibition of cell growth, neuronal regeneration, cellular differentiation and possibly vasodilatation[9]. Angiotensin-(1–7) [Ang-(1–7)] is a peptide formed from either Ang I or Ang II[9]. Ang-(1–7) is considered to be an important peptide fragment of the RAS, and it plays crucial roles that are often opposite from those of Ang II[11]. Ang-(1–7) can induce vasodilatation, diuresis and natriuresis, anti-hypertrophy, anti-proliferation, anti-fibrosis and stimulate bradykinin and NO release via binding to the Mas receptor[12]. The Mas receptor is

# The first two authors contributed equally to this work.

* To whom correspondence should be addressed.
E-mail xzlu@njmu.edu.cn
Received 2010-12-31 Accepted 2011-06-21

an oncogene as well as a receptor for Ang-(1–7)[13]. In a previous work, Mas receptor-deficient mice showed higher blood pressure values, impaired endothelial function, decreased NO production and lower endothelial NO synthetase expression[14], indicating that the Ang-(1–7)/Mas receptor axis plays an important role in cardioprotective and antihypertensive effects. Importantly, Ang-(1–7) can prevent heart failure after myocardial ischemia[15].

Some recent studies have reported that angiotensin converting enzyme inhibitors (ACEIs) and angiotensin receptor blockers (ARBs), two classes of drugs that target RAS, may prevent ADR-induced cardiotoxicity[16–19]. However, the underlying mechanisms are largely unclear. In the present study, we investigated the regulation of two ARBs (telmisartan and losartan) on plasma Ang-(1–7) levels and the mRNA and protein expression of the myocardial AT_1R, AT_2R and Mas receptors in ADR-induced heart failure.

Materials and methods

Animals

A total of 70 male Sprague-Dawley (SD) rats weighing (217±18) g were obtained from Slack Laboratory Animal Co Ltd in Shanghai (SCXK: 2008-0004, China). All experimental procedures were conducted according to the Institutional Animal Care guidelines and approved ethically by the Administration Committee of Experimental Animals, Jiangsu Province, China.

Drugs

ADR, telmisartan and losartan were obtained from Hisun Pharmaceutical Co Ltd (Zhejiang, China), Novartis (Switzerland) and MSD Pharmaceutical Co Ltd (Hangzhou, China), respectively.

Experimental protocol

Rats were randomly divided into four groups: (1) the control group (n=10, intraperitoneally injected an equal volume of normal saline); (2) the ADR-treated heart failure group (ADR-HF, n=20, intraperitoneally injected ADR, a 2.5 mg/kg dose administered 6 times in 2 weeks, resulting in a cumulative dose of 15 mg/kg); (3) the ADR plus telmisartan group (Tel+ADR, n=20, intraperitoneally injected ADR as in the ADR-HF group and administered telmisartan 10 mg/kg per day orally for 6 weeks, for a cumulative dose of 420 mg/kg); and (4) the ADR plus losartan group (Los+ADR, n=20, intraperitoneally injected ADR as in the ADR-HF group and administered Los 30 mg/kg per day orally for 6 weeks, for a cumulative dose of 1260 mg/kg). During the treatment period, body weights of the rats were measured every three days, and the doses of ADR, telmisartan or losartan were adjusted according to the change in body weight. The death of animals was recorded daily.

Echocardiography

Four weeks after the last injection, the cardiac function of the rats was evaluated by transthoracic echocardiography (Vivid 7, General Electric Co) with a 10-MHz linear-array transducer as reported previously[20]. Briefly, rats were weighed and anesthetized using 10% chloral hydrate intraperitoneally (30 mg/kg) and placed on a warm blanket. The cardiac long-axis and short-axis views were obtained in the 2-dimensional mode, and M-mode tracings were recorded. Left ventricular internal dimension systole (LVIDs), left ventricular internal dimension diastole (LVIDd) and left ventricular ejection fraction (LVEF) were recorded in the M-mode tracings by the same expert, and all measurements were performed by an observer blinded to the treatments. We defined heart failure in this rat model according to the cardiac function as assessed by echocardiography.

Plasma Ang-(1–7) assay

After echocardiography, the abdominal aorta was carefully isolated, and 5 mL of arterial blood was collected into tubes containing disodium EDTA. Then, the plasma was obtained and stored at -80°C until use. Plasma Ang-(1–7) was assayed using an ELISA kit (Catalog No: F1763, Xitang Biotechnology Co, Ltd, Shanghai, China) with a microplate reader (Clinibio-128C). The optical density at 450 nm was obtained within 30 min. The standard curve was constructed by plotting the mean absorbance obtained for each reference standard against its concentration[21]. Using the mean absorbance value for each sample, the corresponding concentration was determined from the standard curve.

RNA isolation and RT-PCR

After blood collection, deeply anesthetized rats were sacrificed. Hearts were isolated and rinsed in saline. The cardiac ventricles were separated from the atria, weighed, cut into two segments, frozen in liquid nitrogen and stored at -70°C. Total RNA in the aorta from the four groups of rats was extracted using Trizol reagent (Invitrogen, USA)[22]. The RNA concentration was determined by the absorbance at 260 nm. The mRNA expression of the myocardial Mas receptor, AT_1R and AT_2R was determined by RT-PCR (TaKaRa Biotechnology Co Ltd, Dalian, China). The reaction conditions of RT-PCR were as follows: 30 °C for 10 min, 47 °C for 30 min, 99 °C for 5 min and 5 °C for 5 min. After reverse transcription, the cDNA was denatured at 94 °C for 2 min and subjected to 35 cycles of PCR at 94 °C for 30 s, 60 °C for 30 s and 72 °C for 1 min (Mas receptor) and 35 cycles of PCR at 94 °C for 30 s, 59 °C for 30 s and 72 °C for 1 min (AT_1R, AT_2R, and β-actin), followed by extension at 72 °C for 7 min. The selected primers designed for Mas receptor, AT_1R, AT_2R, and β-actin were as follows: forward: 5′-ACTGCCGGGCGGTCATCATC-3′, reverse: 5′-GGTGGAGAAAAGCAAGGAGC-3′ for Mas receptor (263 bp); forward: 5′-GCCCTGGCTGATTTATGC-3′, reverse: 5′-GGAAAGGGAACACGAAGC-3′ for AT_1R; forward: 5′-TGGCTTGTCTGTC CTCAT-3′, reverse: 5′-AGACTTGGTCACGG GTAA-3′ for AT_2R; forward: 5′-AAGACCTGTACGCCAACACAGT-3′, reverse: 5′-AGAAGCATTTGCGGTGGACGAT-3′ for β-actin.

Western blotting analysis

Western blotting analysis was performed as described previously[23, 24]. Protein (20 μg) extracted from the heart tissues from the four groups was subjected to 10% polyacrylamide gel electrophoresis and then transferred onto PVDF membranes. The membranes were probed using primary antibodies against the Mas receptor, AT_1R and AT_2R (all from Santa Cruz Biotechnology, USA) overnight at 4 °C, followed by horseradish peroxidase-conjugated secondary antibody (Santa Cruz Biotechnology, USA) for 2 h at room temperature. Glyceraldehyde 3-phosphate dehydrogenase (GAPDH) (Kang Chen Bio-Tech, Shanghai, China) was used as the loading control. Antibody binding was visualized using the ECL system (Yuehua Medical Instrument Co Ltd, Guangdong, China), and the amount of Mas receptor, AT_1R and AT_2R were expressed relative to that of GAPDH[22].

Statistical analysis

Results are presented as the mean±standard deviation (SD). Comparisons between two groups were assessed by Student's *t*-test, and comparisons of three or more groups were performed using one-way ANOVA followed by LSD *post-hoc* using SPSS 11.5 software (Chicago, IL, USA). Statistical significance was set at $P<0.05$.

Results

Heart failure model

Body weights were comparable among the four groups at the start of the study. However, after treatment, the weight gain was less in the ADR-HF group than in controls (304.4±19.8 g *vs* 408.6±12.8 g, $P<0.01$, Table 1, Figure 1). The body weights of the Tel+ADR and Los+ADR groups were higher than that of ADR-HF group ($P<0.01$, Table 1, Figure 1), although these were still lower than that of the control ($P<0.01$, Table 1, Figure 1). No significant differences between the weights of the Tel+ADR and Los+ADR groups were observed ($P>0.05$, Table 1, Figure 1). At the end of the treatment (4 weeks after the last injection), the numbers of rats in each group were as follows: Control, $n=10$; ADR-HF, $n=9$; Tel+ADR, $n=12$; and Los+ADR, $n=13$.

Table 1. Weight and cardiac functional parameters at the end of the study (week 6) in four groups. Data are expressed as mean±SD. $^bP<0.05$, $^cP<0.01$ *vs* controls. $^eP<0.05$, $^fP<0.01$ *vs* adriamycin-induced heart failure rats.

	Controls (n=10)	ADR-HF (n=9)	Tel+ADR (n=12)	Los+ADR (n=13)
Weight (g)	408.6±12.8	304.4±19.8^b	343.0±32.16^{cf}	348.5±31.52^{cf}
LVIDs (mm)	3.64±0.33	4.53±0.41^e	3.99±0.52^e	3.79±0.41^e
LVIDd (mm)	5.79±0.48	6.81±0.30^e	6.08±0.33^e	6.14±0.44^e
LVEF (%)	81.5±1.4	63.8±4.4^f	72.5±1.8^{cf}	73.9±2.7^{cf}

Controls=with normal saline injection; ADR-HF=adriamycin-induced heart failure rats; Tel+ADR=telmisartan plus adriamycin-treated rats; Los+ADR=losartan plus adriamycin-treated rats. LVIDs=left ventri-cular internal dimension systole; LVIDd=left ventricular internal dimensi- on diastole; LVEF=left ventricular ejection fraction.

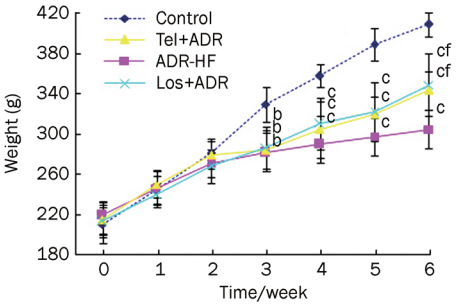

Figure 1. Changes in body weight in each group of rats. Controls=With normal saline injection; ADR-HF=Adriamycin-induced heart failure rats; Tel+ADR=Telmisartan plus Adriamycin-treated rats; Los+ADR=Losartan plus Adriamycin-treated rats. Data are expressed as mean±SD. $^bP<0.05$, $^cP<0.01$ *vs* control group. $^fP<0.01$ *vs* ADR-HF group. Control, $n=10$; ADR-HF, $n=9$; Tel+ADR, $n=12$; and Los+ADR, $n=13$.

The cardiac function of the rats was tested at the end of the treatment (Figure 2). Compared with the control group, LVIDs and LVIDd in ADR-HF group increased significantly, while LVEF decreased significantly (LVIDs: 4.53±0.41 mm *vs* 3.64±0.33 mm, $P<0.05$; LVIDd: 6.81±0.30 mm *vs* 5.79±0.48 mm, $P<0.05$; LVEF: 63.8%±4.4% *vs* 81.5%±1.4%, $P<0.01$, Table 1), indicating that cardiac function was significantly impaired in the ADR-HF group. Interestingly, while the LVEF of the ADR-HF was 63.8%±4.4%, those of the Tel+ADR and Los+ADR groups were 72.5%±1.8% and 73.9%±2.7%, respectively, indicating a significant improvement ($P<0.01$, for both; Table 1). No significant differences in the LVIDs, LVIDd, and LVEF between the Tel+ADR and Los+ADR groups were observed (Table 1).

Plasma levels of Ang-(1–7)

The plasma level of Ang-(1–7) in the ADR-HF group was lower than that in the control group (4.27±2.79 ng/mL *vs* 10.26±2.39 ng/mL, $P<0.01$, Figure 3). Ang-(1-7) plasma levels of the Tel+ADR and Los+ADR groups were higher than that in ADR-HF group (7.16±2.13 ng/mL *vs* 4.27±2.79 ng/mL; 7.08±1.49 ng/mL *vs* 4.27±2.79 ng/mL, both $P<0.05$, Figure 3) but were still lower than that in control group ($P<0.05$, Figure 3). There was no difference in plasma levels of Ang-(1–7) between the Tel+ADR and Los+ADR groups ($P>0.05$, Figure 3).

Expression of the Mas receptor, AT_1R and AT_2R in the heart

The expression levels of the Mas receptor, AT_1R and AT_2R in cardiomyocytes were examined by RT-PCR analysis (Figure 4) and Western blotting (Figure 5). The mRNA and protein expression of the Mas receptor and AT_2R were reduced in the ADR-HF group compared with the control group. Conversely, mRNA and protein expression of AT_1R were increased. Treatment with telmisartan and losartan significantly suppressed the upregulation of AT_1R but did not change the expression of

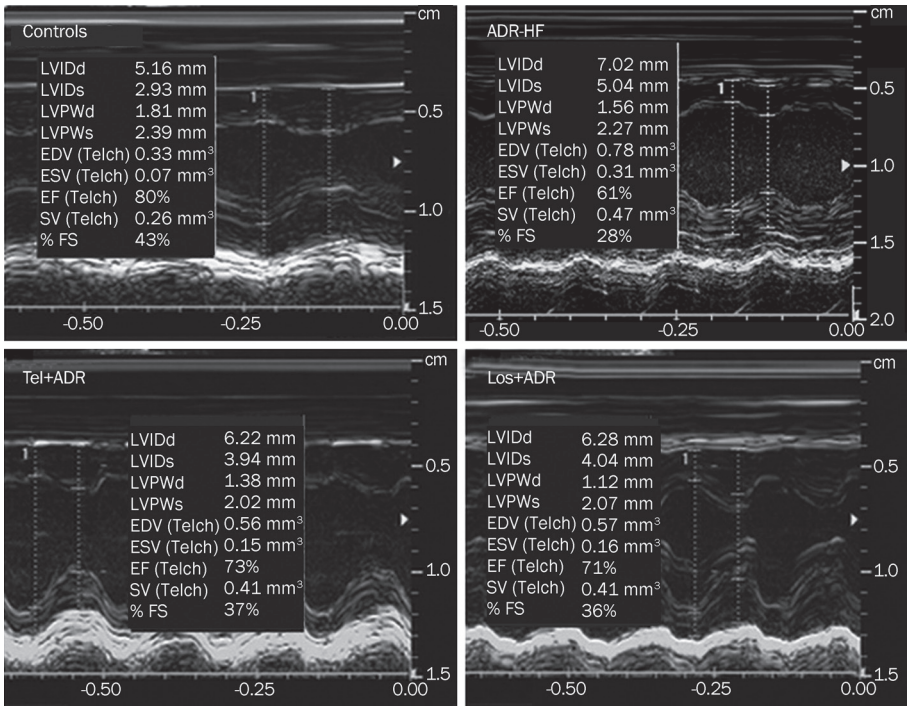

Figure 2. Transthoracic echocardiography to evaluate the cardiac function of rats. Controls=With normal saline injection; ADR-HF=Adriamycin-induced heart failure rats; Tel+ADR=Telmisartan plus Adriamycin-treated rats; Los+ADR=Losartan plus Adriamycin-treated rats.

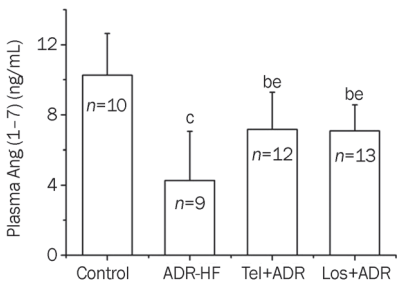

Figure 3. Plasma levels of angiotensin-(1–7) [Ang-(1–7)] were determined by ELISA in rats of the control, ADR-HF, Tel+ADR, and Los+ADR groups at the end of the study. Controls=With normal saline injection; ADR-HF=Adriamycin-induced heart failure rats; Tel+ADR=Telmisartan plus Adriamycin-treated rats; Los+ADR=Losartan plus Adriamycin-treated rats. Mean±SD. $^{b}P<0.05$, $^{c}P<0.01$ *vs* controls. $^{e}P<0.05$ *vs* ADR-HF.

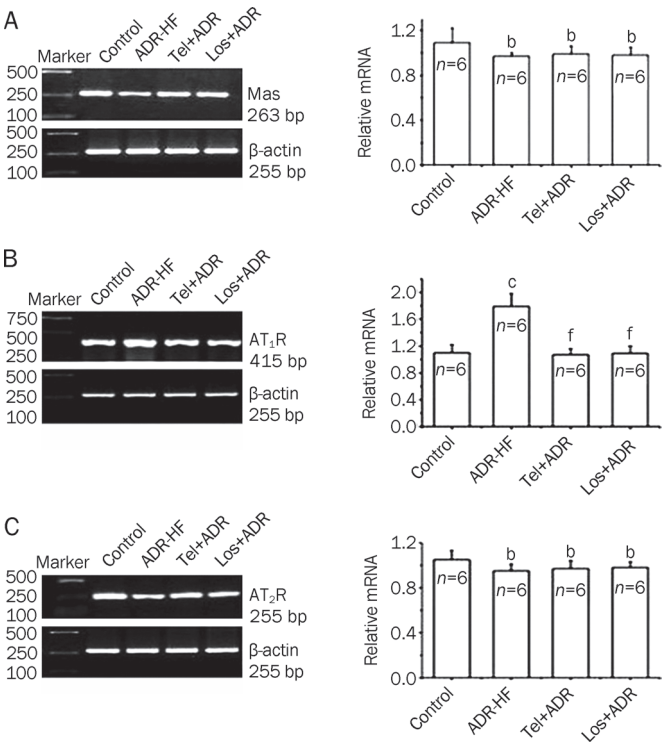

Figure 4. The mRNA expression levels of the Mas receptor (A), AT_1R (B), and AT_2R (C) in cardiac tissues at the end of the study were determined by RT-PCR. The amounts are expressed relative to the amount of β-actin. Controls=With normal saline injection; ADR-HF=Adriamycin-induced heart failure rats; Tel+ADR=Telmisartan plus Adriamycin-treated rats; Los+ADR=Losartan plus Adriamycin-treated rats. *n*=6. Mean±SD. $^{b}P<0.05$, $^{c}P<0.01$ *vs* control groups. $^{f}P<0.01$ *vs* ADR-HF.

the Mas receptor and AT_2R.

Discussion

In this study, we showed that ADR decreased plasma Ang-(1–7) levels and myocardial Mas receptor and AT_2R mRNA and protein expression, whereas it upregulated the myocardial mRNA and protein expression of AT_1R. Two kinds of ARBs, telmisartan and losartan, attenuated the ADR-induced reduction of plasma Ang-(1–7) and suppressed the ADR-induced enhancement of myocardial AT_1R expression. Telmisartan and losartan did not change the expression of the Mas receptor and AT_2R.

Ang-(1–7) is produced from Ang I and Ang II. Under physi-

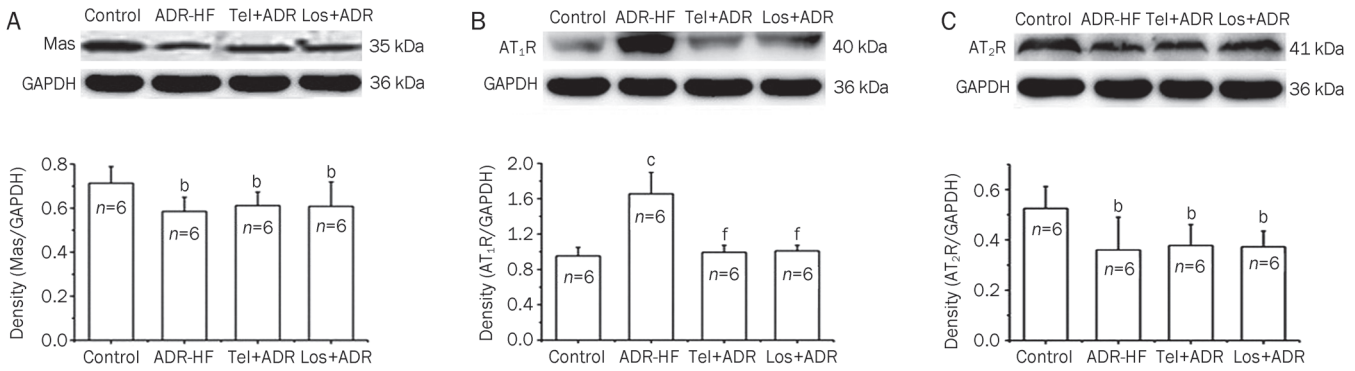

Figure 5. The protein expression levels of the Mas receptor (A), AT_1R (B), and AT_2R (C) in cardiac tissues at the end of the study were determined by Western blotting. Amounts of Mas, AT_1R, and AT_2R were expressed relative to the amount of GAPDH in each sample. Controls=With normal saline injection; ADR-HF=Adriamycin-induced heart failure rats; Tel+ADR=Telmisartan plus Adriamycin-treated rats; Los+ADR=Losartan plus Adriamycin-treated rats. Data are expressed as mean±SD. $^bP<0.05$, $^cP<0.01$ *vs* control group. $^fP<0.01$ *vs* ADR-HF.

ological conditions, plasma concentrations of Ang-(1–7) are similar to the plasma levels of Ang II[25]. Conversely, under some pathological conditions, *eg*, untreated essential hypertensive subjects, the urinary concentrations of Ang-(1–7) is lower than in normotensive controls, but chronic treatment with ARBs increases plasma levels of Ang-(1–7) 5- to 25-fold in both rats and humans[26]. Moreover, previous reports have suggested that Ang-(1–7) is cardioprotective in myocardial ischemia/reperfusion and heart remodeling after heart infarction or heat failure[27, 28]. In our study, the plasma Ang-(1–7) level was significantly lowered by ADR treatment. Surprisingly, treatment with either telmisartan or losartan resulted in increases in plasma Ang-(1–7) compared with the untreated ADR-HF group (both $P<0.05$). Based on the current results, we postulate that endogenous Ang-(1–7) could be a positive physiological protector for the heart, possibly mediating the beneficial effects of ARBs for ADR-induced heart failure.

AT_1R and AT_2R both belong to the family of G protein-coupled receptors, but they share only a 32%–34% identity at the amino acid level[9]. AT_1R is widely distributed in the adrenal glands, kidneys, blood vessels, heart, brain, liver, bronchial tissue and other tissues[9]. After stimulation with Ang II, AT_1R can cause vasoconstriction, Na/H_2O reabsorption, inflammatory response, hypertrophy, hyperplasia, cell proliferation and so on[9]. It has been reported that the increase in oxidative stress coexists with AT_1R upregulation in models of hypertension[29]. The data presented in this study showed that in the ADR-HF group, expression of the AT_1R was upregulated compared with the control group ($P<0.05$). This phenomenon may be due to enhanced oxidative stress and an activated RAS localized to cardiac tissue during heart failure. In addition, in the telmisartan- or losartan-treated rat heart, expression of the AT_1R returned to control values, suggesting that the inhibitory effect of ARBs on the AT_1R contributes critically to their protective effect in ADR-induced heart failure.

The AT_2R is localized in numerous embryonic and neonatal tissues, but its expression declines rapidly after birth and is then restricted to certain organs such as the adrenal glands, ovary, heart, brain, uterus, vascular endothelium, kidney and lung[9]. Stimulation of the AT_2R can cause vasodilation, a reduced inflammatory response, apoptosis, anti-proliferation and anti-oxidative stress[9]. Previous studies demonstrated that the amount of AT_2R was negatively correlated with LVIDd and positively correlated with LVEF, suggesting that left ventricular dysfunction was associated with decreased expression of myocardial AT_2R protein[30]. The Mas receptor is also a G protein-coupled receptor, and it is widely expressed in some tissues[31]. Importantly, it is the receptor for Ang-(1–7)[13]. Recently, new evidence has suggested that Ang-(1–7) acts via NO/cGMP to prevent the Ang II-induced translocation of the nuclear factor of activated T cells in cardiomyocytes[32]. Moreover, in both *in vitro* and *in vivo* conditions, Mas receptor-deficient mice showed impairment of cardiac functions such as hypotonia of myocardial contraction and reduction of cardiac output[13]. Our study showed that in ADR-treated rats, both the mRNA and protein expression of the AT_2R and Mas receptor were downregulated. However, treatment with ARBs did not restore the expression of the AT_2R and Mas, suggesting that although the decreases in the expression level of the AT_2R and Mas receptor may be characteristics of ADR-induced heart failure, the cardio-protection of ARBs is not mediated by the AT_2R and Mas receptor.

In summary, our results confirmed that ARBs are beneficial for ADR-induced heart failure and demonstrated that the influences of ARBs on circulating Ang-(1–7) levels and AT_1R expression in cardiomyocytes may contribute to the cardioprotection of ARBs in this model. Our data may add new evidence to this research field and provide new mechanisms for applications of ARBs to reduce cardiotoxicity in ADR-treated patients.

Acknowledgements

This work was supported by the National Natural Science Foundation of China (No 30770890).

Author contribution

Xin-zheng LU, Ke-jiang CAO and Jun-HUANG designed research; Wen-na ZONG, Xiao-hui YANG, Xiu-mei CHEN, Hong-juan HUANG, Hong-jian ZHENG and Xiao-yi QIN performed research; Yong-hong YONG contributed new analytical tools and reagents; Wen-na ZONG analyzed data; Wen-na ZONG and Xin-zheng LU wrote the paper.

References

1 Singal PK, Li T, Kumar D, Danelisen I, Iliskovic N. Adriamycin-induced heart failure: mechanism and modulation. Mol Cell Biochem 2000; 207: 77–86.
2 Singal PK, Iliskovic N. Doxorubicin–induced cardiomyopathy. N Engl J Med 1998; 339: 900–5.
3 Sia YT, Lapointe N, Parker TG, Tsoporis JN, Deschepper CF, Calderone A, *et al*. Beneficial effects of long-term use of the antioxidant probucol in heart failure in the rat. Circulation 2002; 105: 2549.
4 Ezhilan RA, Rajesh R, Rajaprabhu D, Meena B, Ganesan B, Anandan R. Antioxidant defense of glutamine on myocardial antioxidant status in adriamycin-induced cardiomyopathy in rats. J Cell Animal Biol 2008; 2: 107–11.
5 Dhalla NS, Wang X, Sethi R, Das PK, Beamish RE. Beta-adrenergic linked signal transduction mechanisms in failing hearts. Heart Failure Rev 1997; 2: 55–65.
6 Takeuchi M, Lee JD, Shimizu H, Ueda T. Effects of long-term oral treatment with selective vasopressin V2 receptor antagonist (OPC-31260) on adriamycin-induced heart failure in rats. Int J Cardiol 2006; 108: 231–6.
7 Lu L, Wu W, Yan J, Li X, Yu H, Yu X. Adriamycin-induced autophagic cardiomyocyte death plays a pathogenic role in a rat model of heart failure. Int J Cardiol 2009; 134: 82–90.
8 Schmieder RE, Hilgers KF, Schlaich MP, Schmidt BMW. Renin-angiotensin system and cardiovascular risk. Lancet 2007; 369: 1208–19.
9 Hebert PR, Foody J, Hennekens CH. The renin-angiotensin system: the role of inhibitors, blockers, and genetic polymorphisms in the treatment and prevention of heart failure. Curr Vasc Pharmacol 2003; 1: 33–9.
10 Jickling GC, Xu H, Stamova B, Ander BP, Zhan X, Tian Y, *et al*. Signatures of cardioembolic and large–vessel ischemic stroke. Ann Neurol 2010; 68: 681–92.
11 Santos RA, Ferreira AJ, Simoes ESAC. Recent advances in the angiotensin–converting enzyme 2-angiotensin(1–7)-Mas axis. Exp Physiol 2008; 93: 519–27.
12 Iwai M, Horiuchi M. Devil and angel in the renin–angiotensin system: ACE-angiotensin II-AT1 receptor axis vs. ACE2-angiotensin-(1–7)-Mas receptor axis. Hypertens Res 2009; 32: 533–6.
13 Santos RA, Simoes e Silva AC, Maric C, Silva DM, Machado RP, de Buhr I, *et al*. Angiotensin-(1–7) is an endogenous ligand for the G protein-coupled receptor Mas. Proc Natl Acad Sci U S A 2003; 100: 8258–63.
14 Xu P, Costa–Goncalves AC, Todiras M, Rabelo LA, Sampaio WO, Moura MM, *et al*. Endothelial dysfunction and elevated blood pressure in MAS gene–deleted mice. Hypertension 2008; 51: 574–80.
15 Loot AE, Roks AJ, Henning RH, Tio RA, Suurmeijer AJ, Boomsma F, *et al*. Angiotensin-(1–7) attenuates the development of heart failure after myocardial infarction in rats. Circulation 2002; 105: 1548–50.
16 Iqbal M, Dubey K, Anwer T, Ashish A, Pillai KK. Protective effects of telmisartan against acute doxorubicin-induced cardiotoxicity in rats. Pharmacol Rep 2008; 60: 382–90.
17 Ibrahim MA, Ashour OM, Ibrahim YF, EL-Bitar HI, Gomaa W, Abdel-Rahim SR. Angiotensin-converting enzyme inhibition and angiotensin AT1-receptor antagonism equally improve doxorubicin-induced cardiotoxicity and nephrotoxicity. Pharmacol Res 2009; 60: 373–81.
18 Cadeddu C, Piras A, Mantovani G, Deidda M, Dessi M, Madeddu C, *et al*. Protective effects of the angiotensin II receptor blocker telmisartan on epirubicin-induced inflammation, oxidative stress, and early ventricular impairment. Am Heart J 2010; 160: 487.e1–7.
19 Arozal W, Watanabe K, Veeraveedu PT, Thandavarayan RA, Harima M, Sukumaran V, *et al*. Effect of telmisartan in limiting the cardiotoxic effect of daunorubicin in rats. J Pharm Pharmacol 2010; 62: 1776–83.
20 Xing SS, Bi XP, Tan HW, Zhang Y, Xing QC, Zhang W. Overexpression of interleukin-18 aggravates cardiac fibrosis and diastolic dysfunction in fructose-fed rats. Mol Med 2010; 16: 465–70.
21 Kjaergaard AD, Bojesen SE, Johansen JS, Nordestgaard BG. Elevated plasma YKL-40 levels and ischemic stroke in the general population. Ann Neurol 2010; 68: 672–80.
22 Correale J, Villa A. Role of CD8+ CD25+ Foxp3+ regulatory T cells in multiple sclerosis. Ann Neurol 2010; 67: 625–38.
23 Fan Y, Shen F, Frenzel T, Zhu W, Ye J, Liu J, *et al*. Endothelial progenitor cell transplantation improves long-term stroke outcome in mice. Ann Neurol 2010; 67: 488–97.
24 Kang YJ, Digicaylioglu M, Russo R, Kaul M, Achim CL, Fletcher L, *et al*. Erythropoietin plus insulin–like growth factor-I protects against neuronal damage in a murine model of human immunodeficiency virus-associated neurocognitive disorders. Ann Neurol 2010; 68: 342–52.
25 Joyner J, Neves LA, Granger JP, Alexander BT, Merrill DC, Chappell MC, *et al*. Temporal-spatial expression of ANG-(1–7) and angiotensin-converting enzyme 2 in the kidney of normal and hypertensive pregnant rats. Am J Physiol Regul Integr Comp Physiol 2007; 293: R169–R177.
26 Dilauro M, Burns KD. Angiotensin-(1–7) and its effects in the kidney. ScientificWorldJournal 2009; 9: 522–35.
27 Grobe JL, Mecca AP, Lingis M, Shenoy V, Bolton TA, Machado JM, *et al*. Prevention of angiotensin II-induced cardiac remodeling by angiotensin-(1–7). Am J Physiol-Heart Circ Physiol 2007; 292: H736–H743.
28 Loot AE, Roks AJM, Henning RH, Tio RA, Suurmeijer AJH, Boomsma F, *et al*. Angiotensin-(1–7) attenuates the development of heart failure after myocardial infarction in rats. Circulation 2002; 105: 1548–53.
29 Reja V, Goodchild AK, Phillips JK, Pilowsky PM. Upregulation of angiotensin AT1 receptor and intracellular kinase gene expression in hypertensive rats. Clin Exp Pharmacol Physiol 2006; 33: 690–5.
30 Matsumoto T, Ozono R, Oshima T, Matsuura H, Sueda T, Kajiyama G, *et al*. Type 2 angiotensin II receptor is downregulated in cardiomyocytes of patients with heart failure. Cardiovasc Res 2000; 46: 73–81.
31 Katovich MJ, Grobe JL, Raizada MK. Angiotensin-(1–7) as an antihypertensive, antifibrotic target. Curr Hypertens Reports 2008; 10: 227–32.
32 Gomes ER, Lara AA, Almeida PW, Guimaraes D, Resende RR, Campagnole-Santos MJ, *et al*. Angiotensin-(1–7) prevents cardiomyocyte pathological remodeling through a nitric oxide/guanosine 3′,5′-cyclic monophosphate-dependent pathway. Hypertension 2010; 55: 153–60.

Acta Pharmacologica Sinica (2011) 32: 1351–1356
 1671-4083/11 $32.00
www.nature.com/aps

Original Article

Negative association between free triiodothyronine level and international normalized ratio in euthyroid subjects with acute myocardial infarction

Li LI[1, #], Chang-yan GUO[1, #], Jing YANG[2], En-zhi JIA[1, *], Tie-bing ZHU[1], Lian-sheng WANG[1], Ke-jiang CAO[1], Wen-zhu MA[1], Zhi-jian YANG[1]

[1]*Department of Cardiovascular Medicine, First Affiliated Hospital of Nanjing Medical University, Nanjing 210029, China;* [2]*First Clinical College of Nanjing Medical University, Nanjing 210029, China*

Aim: To investigate the relationship between free triiodothyronine (FT3) and the international normalized ratio (the ratio of the prothrombin time of a patient to the normal sample, INR) in Chinese euthyroid subjects with acute ST-segment elevation myocardial infarction (STEMI).
Methods: A total of 231 consecutive patients (177 males, 54 females) with STEMI were enrolled. Anthropometric and laboratory measurements, including heart rate, respiratory rate, blood pressure, body temperature, platelet count, INR, prothrombin time, activated partial thromboplastin time, FT3, free thyroxine (FT4), and thyroid-stimulating hormone, were collected from all the patients. The levels of FT3 and FT4 were measured with a full-automatic immune analyzer. The INR was determined using a coagulation analyzer.
Results: Patients were classified into 4 groups according to their quartile FT3 and FT4 levels: 0.40–3.09 (*n*=52), 3.10–3.69 (*n*=56), 3.70–4.29 (*n*=64) and 4.30–7.10 (*n*=59) for FT3; 4.9–14.8 (*n*=57), 14.9–16.8 (*n*=58), 16.9–18.7 (*n*=57) and 18.8–29.0 (*n*=59) for FT4. Subjects with a high FT3 level had significantly lower values of INR than those with a low FT3 level (*P*=0.01). Multiple linear regression analysis revealed decreased serum FT3 as an independent risk factor for elevated INR values (β=-0.139, *P*=0.025). The value of INR was similar among the 4 groups according to the quartile FT4 levels (*P*=0.36).
Conclusion: Free triiodothyronine was negatively associated with INR in the patients with acute STEMI and normal thyroid function.

Keywords: free triiodothyronine; free thyroxine; prothrombin time; international normalized ratio; acute ST elevation myocardial infarction; Chinese euthyroid subject

Acta Pharmacologica Sinica (2011) 32: 1351–1356; doi: 10.1038/aps.2011.118; published online 3 Oct 2011

Introduction

In 1878, Greenfield found diffuse atherosclerosis in a 58-year-old woman with myxedema at autopsy[1, 2]. Soon after, Kocher reported that arteriosclerosis commonly occurs after thyroid extirpation and raised the hypothesis of a causal relationship between hypothyroidism and atherosclerosis[3]. This link between the hemostatic system and thyroid disease was finally described in 1913, when an episode of cerebral vein thrombosis in a hyperthyroid patient was reported[4].

It is now well-known that thyroid dysfunction and autoimmunity may modify the physiological processes of primary and secondary hemostasis and lead to bleeding or thrombosis[5]. Following levothyroxine treatment, patients with overt hypothyroidism display decreased bleeding time, prothrombin time (PT), activated partial thromboplastin time (APTT), and clotting time as well as increased factor VIII activity, von Willebrand factor, and platelet count[6]. The occurrence of myocardial infarction (MI) shortly after the initiation of thyroid hormone substitution treatment could reflect an acutely increased risk of thrombosis[7, 8].

The association between the thyroid hormone level and the coagulation system in subjects with acute ST-segment elevation myocardial infarction (STEMI) and normal thyroid function has not been definitely elucidated. In the present study, we prospectively explored this association in Chinese euthyroid subjects with STEMI.

Materials and methods

Study subjects

From 27 July 2010 to 21 March 2011, 231 consecutive euthyroid patients (177 males), aged 30 to 94 years (mean, 63 years) with

# The first two authors contributed equally to this work.
*To whom correspondence should be addressed.
E-mail enzhijia@yahoo.cn
Received 2011-04-08 Accepted 2011-08-02

acute STEMI at the First Affiliated Hospital of Nanjing Medical University, Nanjing, China, were enrolled in the study. The current guidelines for the ECG diagnosis of the ST segment elevation type of acute myocardial infarction require at least 1 mm (0.1 mV) of ST segment elevation in the limb leads, and at least 2 mm elevation in the precordial leads[9]. Because anticoagulation is an integral part of both fibrinolytic therapy and percutaneous intervention (PCI) in the reperfusion treatment of STEMI[10], all patients were given antiplatelet therapy with aspirin and clopidogrel. Exclusion criteria were cardiac shock, severe liver and/or renal dysfunction, hyperthyroidism, hypothyroidism, severe hypovolemia, thyroid disease, and concurrent treatment with diuretics or amiodarone. Complete medical histories, including history of bleeding and smoking habits, were recorded.

Among the 231 patients with STEMI, the types of MI were anteroseptal MI in 35 cases, anterior wall MI in 72 cases, extensive anterior wall MI in 20 cases, inferior wall MI in 98 cases, and lateral wall MI in 6 cases. Patients were divided into 4 groups according to their levels of free triiodothyronine (FT3) and free thyroxine (FT4). The median (quartile range) for FT3 and FT4 were 3.7 pmol/L (3.1–4.3 pmol/L) and 16.9 pmol/L (14.9–18.8 pmol/L), respectively.

This study was approved by the Ethics Committee of the First Affiliated Hospital of Nanjing Medical University, and informed consent was obtained from each patient.

Clinical characteristics

At admission to the coronary care unit, the patients were immediately examined by the attending physician, who performed a complete physical examination, including blood pressure, heart rate, respiratory rate, and body temperature, and recorded demographic and historical data.

Systolic blood pressure (SBP) and diastolic blood pressure (DBP) were measured in the right arm with the participant seated and the arm bared. Three readings were recorded for each individual, and the average was recorded. After a rest of at least 5 min, the heart rate was measured by pulse palpation over a 30-s period and was multiplied by 2 to evaluate the heart rate per minute. The respiratory rate was measured by observing the frequency of thoracic ups and downs over a 60-s interval. The axillary body temperature was measured by placing a thermometer under the armpit, with the arm skin tightening the thermometer. The thermometer was removed and read after 5–10 min.

Thyroid level measurements

The 12-h fasting blood samples were collected from every patient upon admission to the coronary unit. All samples were collected in serum separator tubes and immediately centrifuged (at 3000 r/min for 20 min at room temperature) and analyzed. Thyroid-stimulating hormone (TSH), FT3, and FT4 levels were measured with full-automatic immune analyzer (cobas e601, Roche, Berlin, Germany), with normal reference ranges of 0.3–4.2 mIU/L, 3.10–6.8 pmol/L, and 12.0–22.0 pmol/L, respectively.

Blood coagulation measurements

Two common coagulation tests, PT and APTT, were performed with a computerized blood coagulation analyzer (CA 7000, Sysmex, Kobe, Japan). The reference ranges for PT and APTT were 11.0±3 s and 24.5±10 s, respectively. The international normalized ratio (INR) is the ratio of the PT of the patient to a normal (control) sample. The INR was measured by the coagulation analyzer (CA 7000, Sysmex, Kobe, Japan), with a reference range of 0.8–1.2. The platelet count was obtained with an automated blood analyzer (XE-2100; Sysmex, Kobe, Japan).

Statistical analysis

Significance was defined as a P value of <0.05. Data were analyzed with Statistics Package for Social Sciences (version 16.0; SPSS Inc, Chicago). All variables were checked by the Kolmogorov-Smirnov test.

Patients were classified into 4 groups according to their quartile FT3 and FT4 levels, respectively: 0.40–3.09 (n=52 patients), 3.10–3.69 (n=56), 3.70–4.29 (n=64), and 4.30–7.10 (n=59) for FT3; 4.9–14.8 (n=57 patients), 14.9–16.8 (n=58), 16.9–18.7 (n=57), and 18.8–29.0 (n=59) for FT4. In every group, the DBP, body temperature, heart rate, respiratory rate, PT, APTT, platelet count, and TSH were expressed as median (quartile range), and comparisons between the 4 groups were analyzed by Kruskal-Wallis test (for non-normal distribution). Age, SBP, FT4, FT3, and INR were expressed as the mean±SD, and comparisons were analyzed by analysis of variance (ANOVA)-Sheffe's F test. Categorical variables, including sex, were compared among the groups of patients by chi-squared analysis.

The independent relationship between FT3 or FT4 and other variables was assessed by stepwise or enter multiple regression analysis, respectively. Differences were considered to be significant if the null hypothesis could be rejected with >95% confidence. All reported P values are two-tailed.

Results

Demographic and clinical characteristics and coagulation parameters in patients according to the level of FT3 and FT4

Of the 231 patients with STEMI, 177 (76.6%) were male and 54 (23.4%) were female. Table 1 shows the baseline demographic and clinical characteristics and biochemical and coagulation parameters of the 4 groups. The frequency distribution of sex (P=0.04) differed significantly among the groups. Age (P=0.00), SBP (P=0.02), DBP (P=0.01), INR (P=0.01), PT (P=0.00), and APTT (P=0.00) differed significantly among the groups. However, platelet count (P=0.21), body temperature (P=0.55), heart rate (P=0.21), respiratory rate (P=0.53), FT4 (P=0.23), and TSH (P=0.88) were similar among the 4 groups.

Patients were classified into 4 groups according to their quartile FT4 levels. Sex (P=0.67), age (P=0.85), SBP (P=0.58), DBP (P=0.83), platelet count (P=0.24), INR (P=0.36), body temperature (P=0.86), heart rate (P=0.25), respiratory rate (P=0.12), PT (P=0.39), APTT (P=0.17), and TSH (P=0.26) were similar among the 4 groups (Table 2). FT3 (P=0.04) differed significantly among the groups.

Table 1. Clinical characteristics and biochemical and coagulation parameters in patients according to the level of free triiodothyronine.

Variable	Free triiodothyronine (quartile range)				Chi-square or *F*	*P*
	0.40–3.09 (*n*=52)	3.10–3.69 (*n*=56)	3.70–4.29 (*n*=64)	4.30–7.10 (*n*=59)		
Age (year)	66.9 (54.5–79.5)	69.1 (57.3–81.0)	64.5 (51.9–77.0)	53.5 (43.1–63.8)	20.01	0.00
Male/Female	34/18	41/15	50/14	52/7	8.42	0.04
SBP (mmHg)	123 (99–147)	120 (101–139)	131 (110–152)	124 (106–142)	3.28	0.02
DBP (mmHg)	74 (65–80)	70 (65–79)	78 (70–90)	80 (70–85)	16.9	0.01
Platelet count (10^9/L)	196 (117–275)	187 (131–244)	206 (110–301)	218 (137–299)	1.52	0.21
INR	1.05 (0.88–1.22)	1.00 (0.88–1.12)	0.97 (0.86–1.08)	0.96 (0.78–1.14)	3.84	0.01
BT (°C)	36.8 (36.5–37.0)	36.6 (36.5–36.8)	36.6 (36.5–36.8)	36.7 (36.5–36.8)	2.09	0.55
HR (beat/min)	81.5 (69.5–91.7)	72.0 (64.0–88.5)	74.0 (66.0–80.8)	75.5 (64.3–84.0)	4.53	0.21
RR (time/min)	18.0 (18.0–20.0)	18.0 (17.8–20.0)	18.0 (18.0–20.0)	18.0 (17.0–20.0)	2.19	0.53
PT (s)	11.4 (10.4–14.0)	11.1 (10.2–12.5)	10.6 (9.8–12.7)	10.1 (9.6–11.8)	13.5	0.00
APTT (s)	33.0 (27.0–42.3)	27.7 (24.1–32.9)	28.9 (24.9–37.5)	27.4 (24.7–34.5)	14.5	0.00
FT4 (pmol/L)	16.0 (14.0–18.4)	16.9 (14.5–19.3)	17.1 (15.2–18.3)	17.4 (15.7–19.5)	4.27	0.23
TSH (mIU/L)	1.03 (0.54–2.64)	1.46 (0.83–2.29)	1.30 (0.72–2.51)	1.43 (0.93–2.24)	0.69	0.88

SBP, systolic blood pressure; DBP, diastolic blood pressure; INR, international normalized ratio; BT, body temperature; HR, heart rate; RR, respiratory rate; PT, prothrombin time; APTT, activated partial thromboplastin time; FT4, free thyroxine; TSH, thyroid-stimulating hormone.

Table 2. Clinical characteristics and biochemical and coagulation parameters in patients according to the level of free thyroxine.

Variable	Free thyroxine (quartile range)				Chi-square or *F*	*P*
	4.9–14.8 (*n*=57)	14.9–16.8 (*n*=58)	16.9–18.7 (*n*=57)	18.8–29.0 (*n*=59)		
Age (year)	63.4 (50.6–76.2)	62.1 (46.9–77.3)	63.8 (52.0–75.4)	64.2(50.9–77.4)	0.27	0.85
Male/Female	45/12	47/11	42/15	43/16	1.54	0.67
SBP (mmHg)	123 (108–137)	123 (95–151)	127 (106–148)	126 (107–146)	0.66	0.58
DBP (mmHg)	75 (70–80)	74 (64–80)	75 (68–89)	74 (70–85)	0.88	0.83
Platelet count (10^9/L)	177 (147–222)	180 (143–247)	200 (167–235)	199 (152–237)	4.19	0.24
INR	1.00 (0.87–1.13)	0.98 (0.85–1.10)	0.97 (0.83–1.11)	1.02 (0.81–1.22)	1.08	0.36
BT (°C)	36.6 (36.5–37.1)	36.6 (36.5–36.8)	36.6 (36.5–36.8)	36.7 (36.5–36.8)	0.74	0.86
HR (beat/min)	71.5 (64.0–82.5)	74.0 (64.0–85.0)	78.0 (65.5–84.5)	78.0 (70.0–95.0)	4.08	0.25
RR (time/min)	18.0 (18.0–20.0)	18.0 (18.0–20.0)	18.0 (16.5–19.5)	18.0 (18.0–20.0)	5.76	0.12
PT (s)	11.1 (10.4–12.5)	10.6 (9.8–12.8)	10.5 (9.6–12.9)	11.0 (9.8–13.1)	2.99	0.39
APTT (s)	30.2 (25.9–36.5)	27.8 (24.7–33.7)	27.7 (24.2–34.2)	31.1 (25.1–38.5)	5.08	0.17
FT3 (pmol/L)	3.38 (2.34–4.42)	3.69 (2.92–4.46)	3.83 (3.14–4.52)	3.72 (2.81–4.63)	2.87	0.04
TSH (mIU/L)	1.19 (0.58–2.06)	1.15 (0.89–2.19)	1.62 (0.75–3.59)	1.62 (0.91–2.49)	4.04	0.26

SBP, systolic blood pressure; DBP, diastolic blood pressure; INR, international normalized ratio; BT, body temperature; HR, heart rate; RR, respiratory rate; PT, prothrombin time; APTT, activated partial thromboplastin time; FT3, free triiodothyronine; TSH, thyroid-stimulating hormone.

Multiple linear regression analysis with FT3 and FT4 as the dependent variable

Multiple linear regression analysis was used to examine the independent association between FT3 or FT4 and INR in patients with STEMI. In this model, FT3 or FT4 was employed as the dependent variable, and other variables were considered as the independent variables. Table 3 shows that INR (β=-0.139, *P*=0.025), age (β=-0.344, *P*=0.000), and DBP (β=0.144, *P*=0.020) were significant independent factors associated with the level of FT3 after adjustment. Figure 1 presents the partial regression and shows the relationship between FT3 and INR.

Sex (β=0.063, *P*=0.377), age (β=0.120, *P*=0.097), body temperature (β=-0.020, *P*=0.763), heart rate (β=0.065, *P*=0.336), respiratory rate (β=-0.056, *P*=0.413), SBP (β=-0.028, *P*=0.784), DBP (β=0.126, *P*=0.215), platelet count (β=0.086, *P*=0.218), and INR (β=0.024, *P*=0.725) were not significantly associated with the FT4 levels (Table 4).

Discussion

In the present study, we investigated the association between thyroid hormones and the coagulation system in patients with STEMI and normal thyroid function. Subjects with high FT3

Table 3. Multiple linear regression analysis to identify independent variables associated with serum free triiodothyronine levels.

Variable	Unstandardized coefficients B	Std. Error	Standardized coefficients (Beta)	*T*	*P*
Constant	5.199	0.532 –		9.776	0.000
Age (year)	-0.023	0.004	-0.344	-5.596	0.000
DBP (mmHg)	0.009	0.004	0.144	2.352	0.020
INR	-0.973	0.351	-0.139	-2.261	0.025

DBP, diastolic blood pressure; INR, international normalized ratio. Stepwise multiple linear regression analysis was performed.

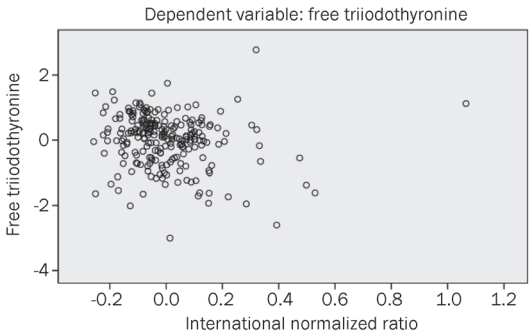

Figure 1. The relationship between free triiodothyronine (FT3) and the international normalized ratio (INR) in Chinese euthyroid subjects.

levels had lower INR values than those with low FT3 (P=0.01). To our knowledge, this is the first study to report that an increased INR is associated with a decreased FT3 level in euthyroid patients.

The strong relationship between thyroid hormones and the coagulation system has been appreciated since the beginning of the past century[11]. For instance, hyperthyroid patients are known to have an increased prevalence of shortened APTT and higher fibrinogen levels than those with normal thyroid function. Because prolonged APTT and PT results indicate a reduced coagulation response and a bleeding tendency, these findings indicate that hyperthyroidism might be associated with hypercoagulability[12]. Previous studies largely have explored patients with clinically overt hypo- or hyperthyroidism who appeared to have an increased risk of bleeding or thrombosis[13].

In contrast, conflicting results have been reported concerning the association between subclinical hyperthyroidism and coagulation. Bucerius *et al* reported that subclinical hyperthyroidism has no significant impact on coagulation metabolism[14], whereas Smallridge reported that subclinical hyperthyroidism is associated with various cardiac effects, particularly atrial fibrillation that increases the thromboembolism risk[15]. Recently, a correlation between thyroid hormone levels and atherosclerosis was suggested in euthyroid patients, in whom the thyroid hormone levels were found to affect the presence and severity of coronary atherosclerosis[11]. Similarly, logistic regression analysis in the present study revealed decreased serum FT3 as an independent risk factor for elevated INR in patients with STEMI and normal thyroid function, after adjustment for confounders. Age was also observed to be an independent risk factor for elevated FT3, consistent with a previous study showing that the FT3 level in old subjects is negatively associated with age[16].

Female gender by itself had a negative and independent

Table 4. Multiple linear regression analysis to identify independent variables associated with serum free thyroxine levels.

Variable	Unstandardized coefficients B	Std. Error	Standardized coefficients (Beta)	*T*	*P*
Constant	18.171	21.557 –		0.843	0.400
Sex	0.489	0.552	0.063	0.885	0.377
Age (year)	0.030	0.018	0.120	1.667	0.097
BT (°C)	-0.175	0.581	-0.020	-0.301	0.763
HR (beat/min)	0.003	0.003	0.065	0.964	0.336
Respiratory rate (time/min)	-0.031	0.037	-0.056	-0.821	0.413
SBP (mmHg)	-0.004	0.016	-0.028	-0.275	0.784
DBP (mmHg)	0.032	0.025	0.126	1.245	0.215
Platelet count (10^9/L)	0.004	0.003	0.086	1.235	0.218
INR	0.528	1.498	0.024	0.353	0.725

BT, body temperature; HR, heart rate; SBP, systolic blood pressure; DBP, diastolic blood pressure; INR, international normalized ratio.

influence on mortality in STEMI patients[17]. However, of the 231 patients with STEMI in our study, 177 (76.6%) were male and 54 (23.4%) were female. Among the subjects with a high serum FT3 level, there were significantly more males than females (P=0.04). A typical pattern of altered thyroid hormone metabolism called nonthyroid illness syndrome (NTI) occurs after acute MI. This syndrome is characterized by low serum and free T3 levels, increased serum reverse T3 levels, and, in the most severe condition, by decreased serum T4 and TSH levels[18]. In present study, among of 231 patients, 23% were lower than the normal reference of FT3 (3.1 pmol/L).

Thyroid hormones exert various effects on the coagulation system[19]. Modulation of the levels of T3 in hyper- and hypothyroidism is extremely important for the capability to increase or decrease the concentrations of fibrinogen and numerous blood clotting factors[20]. In particular, a decrease in active hormone T3 leads to further impairment in cardiac function[21]. Recently, Lymvaios *et al* reported that T3 levels are closely correlated with the cardiac function after AMI[22]. Everts *et al* also reported that T3, and not T4, is transported into the myocyte[23]. However, the exact mechanisms underlying the association between FT3 and cardiac function require further study. Regardless, these previous findings, combined with those of the present study, indicate the importance of assessing the FT3 level of patients. Acute myocardial infarction was the consequence of the acutely increased coronary thrombogenesis and the deficient blood. Whether or not substitution of thyroid hormone should be (routinely) considered as a treatment in patients with STEMI undergoing surgery should be considered.

The findings of the present study are consistent with previous observations that a rise in thyroxine level is associated with increased levels of factors VIII and IX, von Willebrand factor, and fibrinogen[24]. Several biological mechanisms have been proposed to explain this intriguing association, including the effects of thyroid hormones on the synthesis of coagulation factors and the thyroid-related autoimmune processes[13, 19]. However, the exact mechanism underlying the relationship between FT3 and INR remains unclear. Deficiency or excess of thyroid hormone may disturb the production and/or clearance of coagulation factors, such that a patient will bleed or develop thrombosis[20].

Limitations of the present study include a small sample size and the patient selection. Future large clinical and intervention studies are needed to obtain more definitive information on the clinical relevance and the effects of pharmacologic treatment with acute MI. Prophylactic examination of FT3 might be proposed in cases of older people with cardiovascular disease.

In conclusion, free T3 is negatively associated with INR in patients with acute STEMI and normal thyroid function.

Acknowledgements

This study was supported by the National Natural Science Foundation of China (No 30400173 and 30971257).

Author contribution

En-zhi JIA designed research; Li LI and Chang-yan GUO performed research; Tie-bing ZHU, Lian-sheng WANG, Ke-jiang CAO contributed new analytical tools and reagents; Wen-zhu MA, Zhi-jian YANG, and Jing YANG analyzed data; Li LI wrote the paper.

References

1 Greenfield WS. Autopsy findings in a 58 year old woman with myxoedema public hed as an appendix. Ord WM Med Chir Trans 1878; 61: 57
2 Cappola AR, Ladenson PW. Hypothyroidism and atherosclerosis. J Clin Endocr Metab 2003; 88: 2438–44.
3 Kocher T. Ueber Kropfexstirpation und ihre Folgen. Arch Klein Cir 1883; 29: 254–337.
4 Squizzato A, Gerdes VE, Brandjes DP, Büller HR, Stam J. Thyroid diseases and cerebrovascular disease. Stroke 2005; 36: 2302–10.
5 Marongiu F, Cauli C, Mariotti S. Thyroid, hemostasis and thrombosis. J Endocrinol Invest 2004; 27: 1065–71.
6 Gullu S, Sav H, Kamel N. Effects of levothyroxine treatment on biochemical and hemostasis parameters in patients with hypothyroidism. Eur J Endocrinol 2005; 152: 355–61.
7 Smyth CJ. Angina pectoris and myocardial infarctlon as complications of myxedema. Am Heart J 1938: 15: 652–60.
8 Wayne EJ. Clinical and metabolic studies in thyroid disease. Br Med J 1960: 1 : 78–90.
9 2005 American Heart Association Guidelines for Cardiopulmonary Resuscitation and Emergency Cardiovascular Care — Part 8: Stabilization of the Patient With Acute Coronary Syndromes. Circulation 2005; 112: IV-89-IV-110.
10 Wong CK, White HD. Antithrombotic therapy in ST-segment elevation myocardial infarction. Expert Opin Pharmacother 2011; 12: 213–23.
11 Squizzato A, Romualdi E, Büller HR, Gerdes VE. Thyroid dysfunction and effects on coagulation and fibrinolysis: a systematic review. J Clin Endocrinol Metab 2007; 92: 2415–20.
12 Lippi G, Franchini M, Targher G, Montagnana M, Salvagno GL, Guidi GC, *et al*. Hyperthyroidism is associated with shortened APTT and increased fibrinogen values in a general population of unselected outpatients. J Thromb Thrombolysis 2009; 28: 362–5.
13 Franchini, M, Lippi G, Manzato F, Vescovi PP, Target G. Hemostatic abnormalities in endocrine and metabolic disorders. Eur J Endocrinol 2010; 162: 439–51.
14 Bucerius J, Naubereit A, Joe AY, Ezziddin S, Biermann K, Risse J, *et al*. Subclinical hyperthyroidism seems not to have a significant impact on systemic anticoagulation in patients with coumarin therapy. Thromb Haemost 2008; 100: 803–9.
15 Smallridge RC. Disclosing subclinical thyroid disease. An approach to mild laboratory abnormalities and vague or absent symptoms. Postqrad Med 2000; 107: 143–6, 149–52.
16 Corsonello A, Montesanto A, Berardelli M, De Rango F, Dato S, Mari V Mazzei B, *et al*. A cross-section analysis of FT3 age-related changes in a group of old and oldest-old subjects, including centenarians' relatives, shows that a down-regulated thyroid function has a familiar component and is related to longevity. Age Ageing 2010; 39: 723–7.
17 Trigo J, Mimoso J, Gago P, Marques N, Faria R, Santos W, *et al*. Female gender: an independent factor in ST-elevation myocardial infarction. Rev Port Cardiol 2010; 29: 1383–94.
18 Adler SM, Wartofsky L. The non-thyroidal illness syndrome. Endocrinol Metab Clin North Am 2007; 36: 657–72.
19 Franchini M, Montagnana M, Manzato F, Vescovi PP. Thyroid

dysfunction and hemostasis: an issue still unresolved. Semin Thromb Hemost 2009; 35: 288–94.

20 Shih CH, Chen SL, Yen CC, Huang YH, Chen CD, Lee YS, *et al*. Thyroid hormone receptor-dependent transcriptional regulation of fibrinogen and coagulation proteins. Endocrinology 2004; 145: 2804–14.

21 Iervasi G, Pingitore A, Landi P, Ripoli A, Scarlattini M, L'Abbate A, *et al*. Low T3 syndrome: a strong prognostic predictor of death in patients with heart disease. Circulation 2003; 107: 708–13.

22 Lymvaios I, Mourouzis I, Cokkinos DV, Dimopoulos MA, Toumanidis ST, Pantos C. Thyroid hormone and recovery of cardiac function in patients with acute myocardial infarction: A strong association? Eur J Endocrinol 2011; 165: 107–14.

23 Everts ME, Verhoeven FA, Bezstarosti K, Moerings EP, Hennemann G, Visser TJ, *et al*. Uptake of thyroid hormones in neonatal rat cardiac myocytes. Endocrinology 1996; 137: 4235–42.

24 Debeij J, Cannegieter SC, VAN Zaane B, Smit JW, Corssmit EP, Rosendaal FR, *et al*. The effect of changes in thyroxine and thyroid-stimulating hormone levels on the coagulation system. J Thromb Haemost 2010; 8: 2823–6.

Acta Pharmacologica Sinica (2011) 32: 1357–1363
 1671-4083/11 $32.00
www.nature.com/aps

Original Article

Polymorphisms of genes in nitric oxide-forming pathway associated with ischemic stroke in Chinese Han population

Jiang-tao YAN[1, #], Lan ZHANG[1, #], Yu-jun XU[1], Xiao-jing WANG[2], Cong-yi WANG[3], Dao-wen WANG[1, *]

[1]Institute of Hypertension and Department of Internal Medicine, Tongji Hospital, Tongji Medical College, Huazhong University of Science and Technology, Wuhan 430030, China; [2]Department of Oral Biology, School of Dental Medicine, University of Pittsburgh, Pittsburgh, PA 15219, USA; [3]Center for Biotechnology and Genomic Medicine, Medical College of Georgia, Augusta, GA 30912, USA

Aim: To investigate the association of polymorphisms in four critical genes implicated in the NO-forming pathway with ischemic stroke (IS) in a Chinese Han population.
Methods: DNA samples of 558 IS patients and 557 healthy controls from Chinese Han population were genotyped using the Taqman™ 7900HT Sequence Detection System. Six SNPs (rs841, rs1049255, rs2297518, rs1799983, rs2020744, rs4673) of the 4 related genes (eNOS, iNOS, GCH1, and CYBA) in the NO forming pathway were analyzed using the SPSS 13.0 software package for Windows.
Results: One SNP located in the intron of GCH1 (rs841) was associated with IS independent of the traditional cardiovascular risk factors in co-dominant and dominant models (P=0.003, q=0.027; P=0.00006, q=0.0108; respectively). Moreover, the combination of rs1049255 CC+CT and rs841 GA+AA genotypes was associated with significantly higher risk for IS after adjustments (OR=1.73, 95% CI: 1.27–2.35, P<0.0001, q<0.0001).
Conclusion: The data suggest that genetic variants within the NO-forming pathway alter susceptibility to IS in Chinese Han population. Replication of the present results in other independent cohorts is warranted.

Keywords: ischemic stroke; nitric oxide; polymorphism; genetics; Chinese Han population

Acta Pharmacologica Sinica (2011) 32: 1357–1363; doi: 10.1038/aps.2011.114; published online 3 Oct 2011

Introduction

Ischemic stroke (IS), known to be a multifactorial disorder, is the leading cause of disability and the second leading cause of death in China[1]. IS usually results from hypertension, atherosclerosis, diabetes, smoking, vasculitis or other etiologies. Beyond the conventional risk factors, evidence is accumulating that genetic factors may also contribute to the risk of stroke development[2].

Nitric oxide (NO) is synthesized by the enzyme nitric oxide synthase (NOS) from *L*-arginine and oxygen in endothelial cells, neurons, glia and macrophages[3]. NO plays an important role in the control of cerebral blood flow, thrombogenesis, and the modulation of neuronal activity[4]. High concentrations of NO originating from cerebral ischemia mediate inflammatory and cytotoxic pathways leading to neuronal death[5]. NO is also important to protect vessels against atherosclerosis[6]. NO bioavailability is tightly regulated by a balance between its production and detoxification or degradation, and therefore, cerebral ischemia could be related to abnormalities in the expression and activity of NOS.

Several potential functional polymorphisms in the nitric oxide-forming pathway have recently been discovered, including (1) Leu608Ser (rs2297518) in inducible [*iNOS*][7], (2, 3) Glu298Asp (rs1799983) and T-786C (rs2070744) in the promoter region of endothelial [*eNOS*][8–12], (4, 5) Tyr72His (rs4673) and C+640T (rs1049255) in the 3′-untranslated region (UTR) of the cytochrome b-245, alpha polypeptide gene (*CYBA*)[13–16], which encodes the p22*phox* subunit of the NADPH oxidase, and (6) G+243A (rs841) in the 3′-UTR of the GTP cyclohydrolase 1 gene (*GCH1*)[17]. With special attention to the biological process of cerebral ischemia regulation, we investigated whether polymorphisms in these genes implicated in the pathway of NO formation are associated with IS in a large cohort in the Chinese Han population.

# These authors contributed to this work equally.
* To whom correspondence should be addressed.
E-mail dwwang@tjh.tjmu.edu.cn
Received 2010-11-11 Accepted 2011-07-17

Materials and methods

Study population and data collection

This was a multicenter, collaborative study for assessment of risk factors for stroke sponsored by the Ministry of Science and Technology of China. The study protocol was approved by the review board of Tongji Medical College at Huazhong University of Science and Technology and the ethics committees at all participating hospitals. An informed consent form was obtained from all participants.

A total of 558 IS patients were recruited between November 2004 and June 2006 from five hospitals in Wuhan, China. Only 2 subtypes of stroke — cerebral thrombosis (atherothrombosis) and lacunar infarction (lacunar) —were included. Subjects with subarachnoid hemorrhage, embolic brain infarction, brain tumors and cerebrovascular malformation were excluded from the study, as were those with severe systemic diseases such as pulmonary fibrosis, endocrine and metabolic disease (except diabetes mellitus), severe inflammatory diseases, autoimmune disease, tumors and serious chronic diseases (*eg*, hepatic cirrhosis and renal failure). Subjects with cardioembolic stroke and documented atrial fibrillation were also excluded from our study. Stroke diagnosis was based on the results of neurological examination and CT or MRI according to the International Classification of Diseases, ninth edition. Five hundred fifty-seven ethnically and geographically matched controls were randomly selected either from normal individuals of nearby community-based residents (89.6%) or inpatients (10.4%) with minor illnesses. All control subjects were free of neurological diseases following the same exclusion criteria as cases. They were also asked for a detailed medical history and received a physical examination of neurological systems, including an evaluation of body mass index.

DNA isolation and genotyping

DNA was extracted from leukocytes as previously described[18]. All samples were genotyped using the Taqman™ 7900HT Sequence Detection System according to the manufacturer's instructions. Each assay was conducted using 10 ng DNA in a 5 μL reaction consisting of TaqMan™ universal PCR master mix (Applied Biosystems, Foster City, CA, USA), forward and reverse primers and FAM and VIC labeled probes designed by Applied Biosystems [ABI Assays-on-Demand (rs841, C_9866639_10; rs1049255, C_7516913_10; rs2297518, C_11889257_10; rs1799983, C_3219460_20; rs4673, C_2038_20) and Assays-on-Design (rs2070744)]. Allelic discrimination was measured automatically using the Sequence Detection Systems 2.1 software (autocaller confidence level 95%). A total of 10% of all genotypes were repeated in independent PCRs to check for consistency and to ensure intraplate and interplate genotype quality control. No genotyping discrepancies were detected between the repeated samples. In addition, all the DNA samples for cases and controls were run in the same batches.

Statistical analysis

Statistical analysis were performed with the SPSS 13.0 software package for Windows (SPSS Inc, Chicago, IL, USA). The normality of quantitative variable distribution was assessed using the 1-sample Kolmogorov-Smirnov test, and a transformation was applied to non-normal variables when necessary. Summary statistics were expressed as the mean±standard error or as percentages. The χ^2 test was used to assess the deviation from Hardy-Weinberg equilibrium for genotype frequencies in both cases and controls. Continuous variables were compared between cases of stroke and controls using Student's *t*-test. Frequencies of categorical variables were compared by χ^2 test or Fisher's exact test. The potential independent role of each single-nucleotide polymorphism (SNP) on stroke was investigated with multiple unconditional logistic regression analysis adjusted for age, sex, body mass index, hypertension, hyperlipidemia, diabetes mellitus and smoking status. To minimize the false positive results generated from the multiple statistical tests used in our analysis, we adopted a method proposed by Story and Tibshirani to estimate the FDR (false discovery rate)-based *q* value using QVALUE software (setting [lambda]=0, false discovery rate level<0.05)[19]. All association analyses were conducted in three genetic models: co-dominant, dominant and recessive. Power calculations were performed using the QUANTO software program[20] (Version 1.2.3).

Results

Baseline characteristics of the subjects

Table 1 summarizes the clinical characteristics of individuals enrolled in the study. The mean age, gender ratio and total cholesterol level were similar in cases and controls. Expectedly, there were significantly higher percentages of hypertension, diabetes mellitus, hyperlipidemia, and smoking in overall IS and subtype groups versus the controls (P<0.05). Body mass index, systolic blood pressure, and diastolic blood pressure were also higher in cases than controls. Compared to the control group, patients in both the overall IS and subtype groups had significantly lower HDL cholesterol (P<0.05).

Genotypes in relation to ischemic stroke and its subtypes

Next, we assessed associations between six SNPs from four related genes (three at two isoforms of NOS, one at GCH1, and two at CYBA) and IS in the Chinese Han population. All genotype distributions were consistent with Hardy-Weinberg equilibrium (P>0.05). Table 2 lists single SNP allelic frequencies of the four genes among IS subjects (n=558) and control subjects (n=557). Mutiplicative-type corrections such as Bonferroni corrections for correlated genetic factors and tests are highly conservative. Therefore, we present the *q* value, a measure of false discovery rate expected for a given *P* value in the follow-up analysis. Notably, rs841 in the intron region of *GCH1* demonstrated allelic frequency differences between overall IS and lacunar stroke subjects compared with controls (P=0.001 and 0.002, respectively), which maintained statistical significance after multiple comparison correction (q=0.018 for both) (Table 2).

To further investigate how each of the SNP alleles interact in conferring genetic risk for IS, we conducted a genotypic

Table 1. Baseline characteristics of patients.

Variable	Control	Ischemic stroke	Atherothrombosis	Lacunar infarction
n	557	558	410	148
Age, year	62.2±9.3	61.0±9.8	60.0±10.0[b]	64.1±8.2[b]
Men, %	62.1	64.7	65.4	62.8
BMI, kg/m^2	23.7±3.2	24.5±3.7	24.4±3.4	24.7±4.4
SBP, mmHg	131.3±20.8	146.6±23.3[b]	147.1±24[b]	144.9±20.9[b]
DBP, mmHg	78.8±11.1	86.4±13.9[b]	87±14.2[b]	84.9±12.9[b]
TCH, mmol/L	4.6±1.7	4.6±1.1	4.6±1.1	4.6±1.1
HDL-C, mmol/L	1.3±0.4	1.0±0.5[b]	1.0±0.3[b]	1.2±0.9
Hypertension, %	19.2	69.7[b]	69.0[b]	71.6[b]
Diabetes, %	3.2	18.0[b]	19.8[b]	12.8[b]
Hyperlipidemia, %	21.0	35.0[b]	35.5[b]	33.8[b]
Smoking, %	37.3	46.9[b]	45.8[b]	50.0[b]

n, number of individuals; BMI, body mass index; SBP, systolic blood pressure; DBP, diastolic blood pressure; TCH, total cholesterol; HDL-C, high-density lipoprotein cholesterol. [b]*P*<0.05 *vs* control.

Table 2. Allele distribution of each polymorphism.

SNP ID	Function (M>m)	Gene	Position	Population	MAF	P_{allele}
rs1799983	(D298E) G>T	eNOS	Chr7:150327044	Control	0.108	
				Ischemic stroke	0.119	NS
				Atherothrombosis	0.116	NS
				Lacunar infarction	0.128	NS
rs2070744	intron T>C	eNOS	Chr7:150321012	Control	0.104	
				Ischemic stroke	0.113	NS
				Atherothrombosis	0.120	NS
				Lacunar infarction	0.095	NS
rs2297518	(L608S) G>A	iNOS	Chr17:23120724	Control	0.169	
				Ischemic stroke	0.151	NS
				Atherothrombosis	0.132	0.025
				Lacunar infarction	0.206	NS
rs841	intron G>A	GCH1	Chr14:54380242	Control	0.311	
				Ischemic stroke	0.377	0.001[b]
				Atherothrombosis	0.367	0.009
				Lacunar infarction	0.405	0.002[b]
rs1049255	3′-UTR C>T	CYBA	Chr16:87237238	Control	0.428	
				Ischemic stroke	0.389	NS
				Atherothrombosis	0.399	NS
				Lacunar infarction	0.361	0.038
rs4673	(Y72H) G>A	CYBA	Chr16:87240737	Control	0.078	
				Ischemic stroke	0.064	NS
				Atherothrombosis	0.068	NS
				Lacunar infarction	0.051	0.012

MAF, minor allele frequency; P_{allele}, value of allele was determined by χ^2 test; NS, not significant. [b]FDR *q* value<0.05.

association analysis assuming 3 common genetic models (co-dominant, dominant and recessive). Interestingly, SNP rs841 showed consistent effects using both a co-dominant (without adjustment for covariates, *P*=0.001, *q*=0.009; after adjustment

for traditional risk factors, P=0.003, q=0.027) and a dominant model (without adjustment for covariates, P=0.0003, q=0.0054; after adjustment for traditional risk factors, P=0.0006, q=0.0108) (Table 3).

To test the possible effect of the IS subtypes in detecting an association, we then re-assessed the association between rs841 and the cerebral thrombosis and lacunar infarction groups (Supplementary Tables 1 and 2). It is of interest to note that rs841 was significantly associated with both subtypes (nominal P<0.05). However, none of these results pass the significance threshold after multiple corrections. These negative results could be due to reduced sample size and statistical power for subtype analysis.

Association of genotype combinations with ischemic stroke

We applied the logistic regression analyses to test potential interactions among polymorphisms within genes involved in the NO-forming pathway that may confer IS risk and identified significant interactions between rs1049255 and rs841 (P<0.001). In comparison with the reference combination of rs1049255 CC+CT and rs841 GG wild type genotypes, the combination of the rs1049255 CC+CT genotype together with the rs841 GA+AA genotype was found to be significantly associated with IS (P=0.002, q=0.008; Table 4). The distribution combinations of other genotypes did not differ from the wild-type reference in overall IS. The combination of rs1049255 CC+CT and rs841 GA+AA genotypes was associated with significantly higher risk of IS even after adjustment for sex, age, and multiple cardiovascular risk factors (OR=1.73, 95% CI: 1.27–2.35; P<0.0001, q<0.0001) (Table 5). Given that the reduced sample size for IS subtypes resulted in largely insufficient power to test potential interactions, subtype analyses were not performed. Taken together, our data suggest an interaction of NO-forming pathway genes in the risk of IS.

Discussion

This study is to investigate the association between genetic polymorphisms in the genes implicated in NO production and risk for IS development in the Chinese Han population. The present results indicate that polymorphisms in *GCH1* (rs841) are independently associated with an increased risk for IS. In contrast, we failed to detect significant independent association with the rest of SNPs even though they have been suggested to be associated with cardiovascular diseases such as hypertension, coronary heart disease or stroke[21–23].

Nitric oxide, produced by nitric oxide synthase, is an important bioregulatory molecule and displays diverse biological activities. Tetrahydrobiopterin (BH4) is an essential cofactor for all three NOS isoforms, and basal enzyme activity correlates with the amount of BH4 bound tightly to NOS[24]. BH4 deficiency is proposed to lead to NOS uncoupling associated with decreased NO bioavailability and increased production of superoxide radicals from the uncoupled enzymatic form[25]. GTP cyclohydrolase 1 (GCH1) is the first-step and rate-limiting enzyme for BH4 biosynthesis in its *de novo* pathway[26]. Experimental mouse models with alterations in systemic or vascular-specific *GCH1* expression have shown that GCH1 is a key regulator of vascular BH4 levels *in vivo*[27, 28]. Low brain levels of BH4 have been shown in the mouse model for dominantly inherited GCH1 deficiency[29]. Recent evidence suggests that one SNP (rs841), located in the 3'-UTR of the *GCH1* gene, is also associated with reduced biopterin-dependent effects[17]. The *CYBA* gene, located on the long arm of chromosome 16 at position 24, encodes human p22*phox,* which is an essential subunit for the functionality of the NADPH oxidase[30]. NADPH oxidase is an important enzymatic source of oxidative stress as well as uncoupled NOS caused by BH4 deficiency and plays a key role in the pathophysiology of several major cardiovascular diseases, including stroke[31]. Previous studies have shown the association between CYBA polymorphisms and vascular diseases[30]. Our combined analysis identified *GCH1* (rs841) and *CYBA* (rs1049255) interactions, indicating that these two functional polymorphisms may confer risk for IS through biological interactions with each other. Further studies might be required to ascertain whether *CYBA* (rs1049255) affects *GCH1* expression and how such an effect might be mediated.

To control for potential false-positive results, we took several factors into consideration and carefully designed our study. First, all selected candidate SNPs have substantial functional effects that are likely involved in the development of IS. Second, assuming disease prevalence between 0.5% and 1%, our combined sample size can reach >98% power to detect a susceptibility locus with a genotypic relative risk >1.65 at the nominal type I error rate of <0.05 for SNPs with minor allele frequencies >0.31 under the dominant model. Third, we recruited only ethnically and geographically matched subjects from Chinese Han cohorts. Given the homogenous study population, we expect population substructure to be minimal. However, additional replication of the association signals in other independent cohorts is warranted.

In summary, genetic variants in the genes implicated in NO formation could have potentially important effects on the pathogenesis of vascular diseases, and genotyping of these variants may provide an additional tool to predict the risk for ischemic stroke in the Chinese Han population.

Acknowledgements

This study was supported by China 973 program (No 2007CB512004), and 863 program (No 2006AA02A406).

Author contribution

Jiang-tao YAN, Lan ZHANG and Yu-jun XU performed the research; Xiao-jing WANG and Cong-yi WANG contributed new analytical tools and reagents; Jiang-tao YAN and Lan ZHANG analyzed the data; and Jiang-tao YAN, Lan ZHANG and Dao-wen WANG wrote the paper.

Supplementary information

Supplementary tables are available at Acta Pharmacologica Sinica website of NPG.

Table 3. Genotype distribution in three models in ischemic stroke.

SNP	Genotype	Controls *n*=557	*n*=558	Crude odd ratio	95% CI	*P* value	Ischemic stroke Adjusted odd ratio	95% CI	*P* value
rs1799983	Co-dominant					0.139			0.219
	GG	446	417	1.00			1.00		
	GT	102	123	1.29	0.96–1.73		1.29	0.91–1.85	
	TT	9	5	0.59	0.20–1.79		0.53	0.14–2.05	
	Dominant					0.165			0.242
	GG	446	417	1.00			1.00		
	GT+TT	111	128	1.23	0.93–1.64		1.23	0.87–1.74	
	Recessive					0.421			0.312
	GG+GT	548	540	1.00			1.00		
	TT	9	5	0.54	0.12–1.71		0.51	0.13–1.93	
rs2070744	Co-dominant					0.009			0.126
	TT	451	434	1.00			1.00		
	TC	96	122	1.32	0.98–1.78		1.30	0.91–1.87	
	CC	10	2	0.21	0.05–0.95		0.31	0.05–2.03	
	Dominant					0.187			0.269
	TT	451	434	1.00			1.00		
	TC+CC	106	124	1.22	0.91–1.63		1.22	0.86–1.74	
	Recessive					0.015			0.146
	TT+CT	547	556	1.00			1.00		
	CC	10	2	0.20	0.04–0.9		0.29	0.04–1.93	
rs2297518	Co-dominant								
	GG	382	400	1.00		0.520	1.00		0.985
	GA	162	147	0.87	0.67–1.13		0.99	0.72–1.36	
	AA	13	11	0.81	0.36–1.83		1.08	0.41–2.86	
	Dominant					0.258			0.98
	GG	382	400	1.00			1.00		
	GA+AA	175	158	0.86	0.67–1.11		1.00	0.73–1.36	
	Recessive					0.676			0.869
	GG+GA	544	547	1.00			1.00		
	AA	13	11	0.84	0.37–1.89		1.09	0.41–2.86	
rs841	Co-dominant					0.001[b]			0.003[b]
	GG	267	208	1.00			1.00		
	GA	234	279	1.53	1.19–1.97		1.67	1.23–2.27	
	AA	56	71	1.63	1.10–2.41		1.60	0.99–2.59	
	Dominant					0.0003[b]			0.0006[b]
	GG	267	208	1.00			1.00		
	GA+AA	290	350	1.55	1.22–1.97		1.65	1.24–2.21	
	Recessive					0.160			0.381
	GG+GA	501	487	1.00			1.00		
	AA	56	71	1.30	0.90–1.89		1.23	0.78–1.93	
rs1049255	Co-dominant					0.103			0.102
	CC	188	206	1.00			1.00		
	CT	261	270	0.94	0.73–1.23		0.96	0.70–1.31	
	TT	108	82	0.69	0.49–0.98		0.65	0.42–0.99	
	Dominant					0.269			0.329
	CC	188	206	1.00			1.00		
	CT+TT	369	352	0.87	0.68–1.11		0.86	0.64–1.16	
	Recessive					0.037			0.034
	CC+CT	449	476	1.00			1.00		
	TT	108	82	0.72	0.52–0.98		0.66	0.45–0.97	

(To be continued)

SNP	Genotype	Controls *n*=557	Ischemic stroke *n*=558	Crude odd ratio	95% CI	*P* value	Adjusted odd ratio	95% CI	*P* value
rs4673	Co-dominant					0.211			0.37
	GG	471	487	1.00			1.00		
	GA	85	71	0.81	0.58–1.13		0.77	0.50–1.16	
	AA	1	0	/	/		/	/	
	Dominant					0.192			0.199
	GG	471	487	1.00			1.00	0.50–1.16	
	GA+AA	86	71	0.80	0.57–1.12		0.76		
	Recessive					0.499			0.516
	GG+GA	556	558	1.00			1.00		
	AA	1	0	/	/		/	/	

CI, confidence interval; SNP, single-nucleotide polymorphism. Adjusted odd ratios were adjusted for gender, age, body mass index, hypertension, diabetes, hyperlipidemia and smoking status. [b]FDR *q* value<0.05.

Table 4. Distribution of combined genotypes in overall ischemic stroke.

Genotype		Ischemic stroke	Control	*P* value
rs1049255	rs841	(*n*=558)	(*n*=557)	
CC+CT	GG	175	210	reference
CC+CT	GA+AA	301	239	**0.002**
TT	GG	33	57	0.130
TT	GA+AA	49	51	0.526

Table 5. Analysis of multiple logistic regression model for synergism genotypes in ischemic stroke group.

Variable	Adjusted OR	95% CI		*P* value
		Lower	Upper	
Gender (m/f)	0.58	0.39	0.87	0.01
Age (*n*)	0.96	0.95	0.98	<0.0001
Hypertension (y/*n*)	7.20	5.11	10.16	<0.0001
Diabetes (y/*n*)	3.36	1.79	6.32	<0.0001
Hyperlipidemia (y/*n*)	1.48	1.02	2.15	0.04
Smoking (y/*n*)	2.18	1.49	3.18	<0.0001
rs1049255(CC+CT)* rs841(GA+AA)	1.73	1.27	2.35	<0.0001

OR, odd ratio; Variables included in the model were gender, age, body mass index, hypertension, diabetes, hyperlipidemia and smoking status. Nonsignificant variables (*P*>0.05) have not been shown in the table.

References

1 Jia Q, Liu LP, Wang YJ. Stroke in China. Clin Exp Pharmacol Physiol 2010; 37: 259–64.
2 Meschia JF, Brott TG, Brown RD Jr, Crook RJ, Frankel M, Hardy J, *et al*. The ischemic stroke genetics study (ISGS) protocol. BMC Neurol 2003; 3: 4.
3 Iadecola C, Pelligrino DA, Moskowitz MA, Lassen NA. Nitric oxide synthase inhibition and cerebrovascular regulation. J Cereb Blood Flow Metab 1994; 14: 175–92.
4 Faraci FM, Brian JE Jr. Nitric oxide and the cerebral circulation. Stroke 1994; 25: 692–703.
5 Forman LJ, Liu P, Nagele RG, Yin K, Wong PY. Augmentation of nitric oxide, superoxide, and peroxynitrite production during cerebral ischemia and reperfusion in the rat. Neurochem Res 1998; 23: 141–8.
6 Yogo K, Shimokawa H, Funakoshi H, Kandabashi T, Miyata K, Okamoto S, *et al*. Different vasculoprotective roles of NO synthase isoforms in vascular lesion formation in mice. Arterioscler Thromb Vasc Biol 2000; 20: E96–E100.
7 Wang SS, Davis S, Cerhan JR, Hartge P, Severson RK, Cozen W, *et al*. Polymorphisms in oxidative stress genes and risk for non-Hodgkin lymphoma. Carcinogenesis 2006; 27: 1828–34.
8 Alvarez R, Gonzalez P, Batalla A, Reguero JR, Iglesias-Cubero G, Hevia S, *et al*. Association between the NOS3 (-786 T/C) and the ACE (I/D) DNA genotypes and early coronary artery disease. Nitric Oxide 2001; 5: 343–8.
9 Shimasaki Y, Yasue H, Yoshimura M, Nakayama M, Kugiyama K, Ogawa H, *et al*. Association of the missense Glu298Asp variant of the endothelial nitric oxide synthase gene with myocardial infarction. J Am Coll Cardiol 1998; 31: 1506–10.
10 Hingorani AD, Liang CF, Fatibene J, Lyon A, Monteith S, Parsons A, *et al*. A common variant of the endothelial nitric oxide synthase (Glu298→Asp) is a major risk factor for coronary artery disease in the UK. Circulation 1999; 100: 1515–20.
11 Cai H, Wilcken DE, Wang XL. The Glu-298→Asp (894G→T) mutation at exon 7 of the endothelial nitric oxide synthase gene and coronary artery disease. J Mol Med 1999; 77: 511–4.
12 Nakayama M, Yasue H, Yoshimura M, Shimasaki Y, Kugiyama K, Ogawa H, *et al*. T-786→C mutation in the 5′-flanking region of the endothelial nitric oxide synthase gene is associated with coronary spasm. Circulation 1999; 99: 2864–70.
13 Guzik TJ, West NE, Black E, McDonald D, Ratnatunga C, Pillai R, *et al*. Functional effect of the C242T polymorphism in the NAD(P)H oxidase p22*phox* gene on vascular superoxide production in atherosclerosis. Circulation 2000; 102: 1744–7.
14 Inoue N, Kawashima S, Kanazawa K, Yamada S, Akita H, Yokoyama M. Polymorphism of the NADH/NADPH oxidase p22 *phox* gene in patients with coronary artery disease. Circulation 1998; 97: 135–7.
15 Li A, Prasad A, Mincemoyer R, Satorius C, Epstein N, Finkel T, *et al*. Relationship of the C242T p22*phox* gene polymorphism to angio-

graphic coronary artery disease and endothelial function. Am J Med Genet 1999; 86: 57–61.
16 Cahilly C, Ballantyne CM, Lim DS, Gotto A, Marian AJ. A variant of p22(*phox*), involved in generation of reactive oxygen species in the vessel wall, is associated with progression of coronary atherosclerosis. Circ Res 2000; 86: 391–5.
17 Zhang L, Rao F, Zhang K, Khandrika S, Das M, Vaingankar SM, *et al*. Discovery of common human genetic variants of GTP cyclohydrolase 1 (GCH1) governing nitric oxide, autonomic activity, and cardiovascular risk. J Clin Invest 2007; 117: 2658–71.
18 Wang Q, Ding H, Tang JR, Zhang L, Xu YJ, Yan JT, *et al*. C-reactive protein polymorphisms and genetic susceptibility to ischemic stroke and hemorrhagic stroke in the Chinese Han population. Acta Pharmacol Sin 2009; 30: 291–8.
19 Storey JD, Tibshirani R. Statistical significance for genomewide studies. Proc Natl Acad Sci U S A 2003; 100: 9440–5.
20 QUANTO 1.1: A computer program for power and sample size calculations for genetic-epidemiology studies, http://hydra.usc.edu/gxe; 2006.
21 Hassan A, Gormley K, O'Sullivan M, Knight J, Sham P, Vallance P, *et al*. Endothelial nitric oxide gene haplotypes and risk of cerebral small-vessel disease. Stroke 2004; 35: 654–9.
22 Szolnoki Z, Havasi V, Bene J, Komlosi K, Szoke D, Somogyvari F, *et al*. Endothelial nitric oxide synthase gene interactions and the risk of ischaemic stroke. Acta Neurol Scand 2005; 111: 29–33.
23 Markus HS, Ruigrok Y, Ali N, Powell JF. Endothelial nitric oxide synthase exon 7 polymorphism, ischemic cerebrovascular disease, and carotid atheroma. Stroke 1998; 29: 1908–11.
24 Moens AL, Kass DA. Tetrahydrobiopterin and cardiovascular disease. Arterioscler Thromb Vasc Biol 2006; 26: 2439–44.
25 Vasquez-Vivar J, Kalyanaraman B, Martasek P, Hogg N, Masters BS, Karoui H, *et al*. Superoxide generation by endothelial nitric oxide synthase: the influence of cofactors. Proc Natl Acad Sci U S A 1998; 95: 9220–5.
26 Auerbach G, Nar H. The pathway from GTP to tetrahydrobiopterin: three dimensional structures of GTP cyclohydrolase I and 6-pyruvoyl tetrahydropterin synthase. Biol Chem 1997; 378: 185–92.
27 Khoo JP, Nicoli T, Alp NJ, Fullerton J, Flint J, Channon KM. Congenic mapping and genotyping of the tetrahydrobiopterin-deficient hph-1 mouse. Mol Genet Metab 2004; 82: 251–4.
28 Khoo JP, Zhao L, Alp NJ, Bendall JK, Nicoli T, Rockett K, *et al*. Pivotal role for endothelial tetrahydrobiopterin in pulmonary hypertension. Circulation 2005; 111: 2126–33.
29 Hyland K, Gunasekara RS, Munk-Martin TL, Arnold LA, Engle T. The hph-1 mouse: a model for dominantly inherited GTP-cyclohydrolase deficiency. Ann Neurol 2003; 54: S46–8.
30 San Jose G, Fortuno A, Beloqui O, Diez J, Zalba G. NADPH oxidase CYBA polymorphisms, oxidative stress and cardiovascular diseases. Clin Sci (Lond) 2008; 114: 173–82.
31 Mueller CF, Laude K, McNally JS, Harrison DG. ATVB in focus: redox mechanisms in blood vessels. Arterioscler Thromb Vasc Biol 2005; 25: 274–8..

Acta Pharmacologica Sinica (2011) 32: 1364–1372
 1671-4083/11 $32.00
www.nature.com/aps

Original Article

Berberine protects against lipopolysaccharide-induced intestinal injury in mice via alpha 2 adrenoceptor-independent mechanisms

Hong-mei LI[1, #], Yi-yang WANG[1, #], Hua-dong WANG[1, 2, *], Wen-juan CAO[1], Xiao-hui YU[1], Da-xiang LU[1, 2], Ren-bin QI[1, 2], Chao-feng HU[1], Yu-xia YAN[3]

[1]Department of Pathophysiology, Key Laboratory of State Administration of Traditional Chinese Medicine, School of Medicine, Ji-nan University, Guangzhou 510632, China; [2]Institute of Integrative Medicine, Ji-nan University, Guangzhou 510632, China; [3]Department of Biochemistry, School of Medicine, Ji-nan University, Guangzhou 510632, China

Aim: To investigate the mechanisms responsible for the protective action of berberine (Ber) against gut damage in endotoxemic mice.
Methods: Male BALB/c mice were administered intragastrically with distilled water (0.1 mL/10 g), Ber (50 mg/kg) alone, yohimbine (2 mg/kg) alone, or Ber (50mg/kg) in combination with yohimbine (2 mg/kg) for 3 d. On the third day, lipopolysaccharide (LPS, 18 mg/kg) or normal saline was intraperitoneally injected one hour after the intragastric administration. Following the treatment, intestinal injury in the ileum was histopathologically accessed; enterocyte apoptosis was examined using TUNEL method; Toll-like receptor 4 (TLR4) mRNA expression was measured using RT-PCR assay; inhibitor protein-κBα (I-κBα) phosphorylation and myeloperoxidase content were examined using Western blloting. The macrophage inflammatory protein-2 (MIP-2) production was measured using ELISA assay.
Results: Mice challenged with LPS caused extensive ileum injury, including a significantly increased injury score, decreased intestinal villus height, reduced gut mucosal weight and increased intestinal permeability. Furthermore, LPS significantly induced enterocyte apoptosis, increased TLR4 mRNA expression, I-κBα phosphorylation, MIP-2 production and myeloperoxidase content in the ileum. Pretreatment with Ber significantly alleviated all the alterations in the ileum in the endotoxemic mice. Pretreatment with the α2-adrenoceptor antagonist yohimbine did not block the protective action of Ber against LPS-induced intestinal injury. In addition, treatment with yohimbine alone did not prevent LPS-induced intestinal injury.
Conclusion: Pretreatment with Ber provides significant protection against LPS-induced intestinal injury in mice, via reducing enterocyte apoptosis, inhibiting the TLR4-nuclear factor κB-MIP-2 pathway and decreasing neutrophil infiltration that are independent of α2-adrenoceptors.

Keywords: berberine; lipopolysaccharide; intestinal injury; apoptosis; Toll-like receptor 4 (TLR4); NF-κB; macrophage inflammatory protein-2 (MIP-2); α_2-adrenoceptor; yohimbine

Acta Pharmacologica Sinica (2011) 32: 1364–1372; doi: 10.1038/aps.2011.102; published online 3 Oct 2011

Introduction

Sepsis is one of the principal causes of death in intensive care units. There are 750 000 new cases of severe sepsis in the United States every year, and the incidence of sepsis is expected to continue to grow at a rate of 1.5% per year[1]. Although the exact mechanisms responsible for sepsis remain unclear, gut dysfunction has been identified in sepsis, and increased intestinal permeability is associated with the development of multiple organ dysfunction syndrome[2, 3]. Indeed, the intestinal epithelium, which is constantly exposed to bacterial products, is the first line of defense against microorganisms. An intact and functioning mucosal barrier, maintained by the intestinal epithelial cells, is crucial to prevent potentially pathogenic bacteria in the intestinal lumen from translocating to the normally sterile compartments of the body[4]. Therefore, it is critical to protect gut barrier function when providing treatment for sepsis.

Lipopolysaccharide (LPS), a major component of the outer membrane of Gram-negative bacteria, is recognized as the most potent microbial mediator in the pathogenesis of sepsis[5]. Extensive studies in experimental model systems have established that LPS challenge impairs the integrity of the intestinal mucosa[6, 7].

# The first two authors contributed equally to this paper.
* To whom correspondence should be addressed.
E-mail owanghd@jnu.edu.cn
Received 2011-03-18 Accepted 2011-07-05

Berberine (Ber) is an isoquinoline alkaloid found in *Coptidis rhizoma*. It is well known that Ber has many biological activities, such as the regulation of inflammation[8]. Recently, we and others have shown that pretreatment with Ber protects against intestinal injury in LPS-challenged animals[9, 10]. However, the mechanisms involved in the protective effect of Ber on LPS-induced gut injury are not fully understood. Ber has also been reported to activate the α_2-adrenoceptor[11]. We have also shown that blockage of the α_2-adrenoceptor with yohimbine (Y, 2 mg/kg) enhances the protective effect of Ber (50 mg/kg) against LPS-induced lethality and that the combination of Ber and Y improves survival in mice subjected to cecal ligation and puncture[12]. In this context, the role of the α_2-adrenoceptor in the protection of Ber against LPS-induced intestinal injury needs to be examined.

Several mechanisms have been shown to be responsible for LPS-induced intestinal injury. These include the activation of the Toll-like receptor 4 (TLR4)-nuclear factor-κB (NF-κB) signaling pathway, expression of macrophage inflammatory protein-2 (MIP-2), and tissue infiltration by neutrophils and apoptosis of enterocytes[7, 13–17]. Therefore, the purpose of this study was to investigate the effect of Ber on the TLR4-NF-κB signaling pathway, MIP-2 expression, neutrophil recruitment and enterocyte apoptosis in the ileum of LPS-treated mice and, furthermore, to determine the role of the α_2-adrenoceptor in this process.

Materials and methods

Animals

Male BALB/c mice (6–8 weeks, weighing 21–23 g) were purchased from Guangdong Medical Laboratory Animal Center (Guangzhou, China). Animals were kept at 24±2 °C and exposed to a twelve hours light/dark cycle for a minimum of 3 d before the experiment, during which time they had free access to water and mouse chow. All experiments were conducted in compliance with the Guide for the Care and Use of Laboratory Animals published by the US National Institutes of Health (NIH Publication No 85–23, revised 1996) and were approved by the Animal Care and Use Committee at School of Medicine, Ji-nan University.

Experimental design

Male BALB/c mice were randomly divided into 8 groups: control, LPS, Ber+LPS, Ber+Y (an α_2 adrenoceptor antagonist)+LPS, Y+LPS, Ber, Ber+Y, and Y. Once a day for 3 days, the mice were treated intragastrically with the following: distilled water (0.1 mL/10 g), Ber (50 mg/kg), Ber (50 mg/kg) in combination with Y (2 mg/kg) or Y (2 mg/kg). One hour after last intragastric treatment, LPS (18 mg/kg, derived from *Escherichia coli* O55:B5) or normal saline was injected intraperitoneally. Separate experiments were performed for each measurement. Neutral sulfate Ber, Y, and LPS were purchased from Sigma Chemical Co (St Louis, MO, USA).

Histopathological examination

The animals were anesthetized and sacrificed twelve hours after the injection of LPS or normal saline, and 1 cm of ileum tissue, beginning at 1 cm proximal to the ileocecal junction, was removed and fixed in a 4% formaldehyde solution. The fixed intestinal tissues were embedded in paraffin wax using standard techniques. Slices (5 μm) were cut and stained with hematoxylin and eosin and were examined under a light microscope. For the histological assessment of intestinal injury, a 0–4 grading scale was used as follows[18]: 0=normal histology; 1=slight disruption of the surface epithelium; 2=epithelial cell loss injury at villus tip; 3=mucosal vasocongestion, hemorrhage, and focal necrosis with loss of less than one-half of the villi; and 4=damage extending to more than one-half of the villi. An observer who was unaware of the treatment performed all assessments of damage. The final score was expressed as a mean rank.

The height of each complete villus in one randomly picked microscopic field (×100) was determined by measuring the distance from the crypt-villus junction to the villus tip[19].

Intestinal mucosal weight measurement

The animals were anesthetized and sacrificed twelve hours after the injection of LPS or normal saline. The ileum segment (10 cm), beginning 1 cm proximal to the ileocecal junction, was excised, cut longitudinally, washed with cold isotonic saline and weighed (W1). After the mucosa was scraped off using a glass slide[6, 7], the ileum tissue was weighed again (W2). The weight of the mucosa was calculated as the difference between W1 and W2 (W=W1–W2), and the result was expressed as mg per centimeter of ileum length per 10 g of body weight.

Intestinal permeability assessment

Intestinal permeability was assessed using a slightly modified version of the method described by Yasuda *et al*[20]. Mice were anesthetized and sacrificed twelve hours after the challenge with LPS or normal saline. A 15-cm segment of ileum was dissected beginning 1 cm proximal to the ileocecal junction. The intestinal lumen was gently washed with ice-cold PBS (0.01 mol/L, pH 7.4), and one side of intestine was ligated with a 4–0 silk suture. Fluorescein isothiocyanate (FITC)-dextran powder (FD4, MW 4 kDa, Sigma, St Louis, MO, USA) was dissolved in PBS (0.01 mol/L, pH 7.4) to a final concentration of 4 mg/mL. FITC-dextran solution (0.5 mL) was applied to the intestinal lumen that had a well-protected intestinal wall. Next, the other side of intestine was ligated. The outside of the intestinal pouch was washed and gently shaken in 3 mL PBS at 37 °C for 60 min. The intestinal permeability of the pouch was evaluated *ex vivo* by measuring the amount of FITC-dextran that leaked out of the intestinal pouch. A standard solution was prepared as follows: FITC-dextran powder was diluted at different concentrations (0, 1.56 μg/mL, 3.13 μg/mL, 6.25 μg/mL, 12.5 μg/mL, 25 μg/mL, 50 μg/mL, 100 μg/mL) with PBS (0.01 moL/L, pH 7.4)[21]. Sample supernatants (200 μL) and standard solutions were pipetted into duplicate wells of a black microtiter plate, and the fluorescence was measured at an excitation wavelength of 485 nm and an emission wavelength of 520 nm.

Apoptotic cell evaluation

The terminal deoxyuridine nick end-labeling (TUNEL) immunohistochemical method (ApopTag *in situ* Apoptosis Detection Kit, Roche Co, Basel, Switzerland) was used to identify and quantitate apoptotic cells in the ileum. Briefly, after deparaffinization, the sections were treated with 20 μg/mL proteinase K for 15 min at room temperature and with 0.3% H_2O_2 for 10 min. Following incubation with the equilibration buffer for 10 min at room temperature, the sections were incubated with terminal deoxynucleotidyl transferase enzyme reaction mixture for 60 min at 37 °C. Further incubation with peroxidase-conjugated antibody was performed for 30 min at 37 °C. The sections were stained with diaminobenzidine solution and counterstained with hematoxylin. TUNEL-positive cells, identified by the brown staining of the nucleus and their apoptotic morphology[19, 22], were counted by an observer, blinded to the experimental conditions, who selected 10 full-length villi in each sample. The apoptosis index (AI) of enterocytes was calculated as the ratio of the total number of TUNEL-positive cells to the total number of epithelial cells×100%[19].

Myeloperoxidase activity assay

Mice were challenged with LPS or normal saline, and twelve hours later, ileum tissue, beginning 1 cm proximal to the ileocecal junction, was removed, washed with cold isotonic saline and homogenized thoroughly in a homogenate solution. Myeloperoxidase (MPO) activity was determined by a spectrophotometric method using myeloperoxidase activity detection kits (Nanjing Jiancheng Bioengineering Institute, Nanjing, China) according to the manufacturer's specifications.

MIP-2 protein analysis

Ileum tissue was collected two hours after intraperitoneal injection of LPS or normal saline, thoroughly homogenated in an isotonic sodium chloride solution and centrifuged at 3000×*g* for 10 min (4 °C). The supernatant was collected, and the concentration of MIP-2 was determined using mouse MIP-2 enzyme-linked immunosorbent assay kits (R&D Systems, Minneapolis, MN, USA). The total protein level was measured using a commercially available bicinchoninic acid protein assay kit (ShennengBocai Co, Shanghai, China).

Western blotting

The mice were killed twelve hours after LPS or normal saline injection. Ileum tissues were removed, washed with cold normal saline and thoroughly homogenated on ice in RIPA lysis buffer (Bioteke Co, Beijing, China) that was supplemented with the protease inhibitor phenylmethanesulfonyl fluoride. The lysates were centrifuged at 12000×*g* at 4 °C for 10 min, and the supernatants were aliquoted into fresh tubes and stored at -80 °C until measurement. Protein concentrations in the lysates were determined using a bicinchoninic acid protein assay kit (ShennengBocai Co, Shanghai, China). Protein samples (70 μg) were separated by sodium dodecyl sulfate polyacrylamide gel electrophoresis and transferred to a Hybond-C pure nitrocellulose membrane. After blocking, the membranes were probed with the following antibodies: rabbit antibodies against cleaved caspase-3 (Cell Signaling Technology, Danvers, USA), inhibitor protein-κBα (I-κBα, Cell Signaling Technology, Danvers, USA), phosphorylated I-κBα (Cell Signaling Technology, Danvers, USA), or glyceraldehyde-3-phosphate dehydrogenase (GAPDH, Cell Signaling Technology, Danvers, USA) or mouse antibodies against MPO (R&D Systems, Minneapolis, MN, USA). The membranes were incubated overnight at 4 °C with primary antibody and were later incubated with secondary antibody (peroxidase-conjugated goat anti-rabbit or anti-mice antibodies, Dingguo Changsheng Co, Beijing, China) at room temperature for one hour. The antigen-antibody complexes were visualized using a chemiluminescence system (Pierce Biotechnology Inc, Rockford, USA) and exposed to film (Kodak X-OMAT, Guangzhou, China). The relative densities of the bands were analyzed using a BI2000 image analysis system (Chengdu TME Technology Co Ltd, Chengdu, China).

Real-time RT-PCR analysis of TLR4 mRNA expression

Ileum segments were quickly isolated and frozen at -80 °C. Total RNA was extracted from the frozen tissues using Trizol reagent (TaKaRa, Bao Biotec Co, Dalian, China) and was subjected to reverse transcription using a PrimeScript® RT reagent kit (TaKaRa, Bao Biotec Co, Dalian, China) according to the manufacturer's instructions. Polymerase chain reaction amplifications were performed using the SYBR® PrimeScript™ RT-PCR Kit II (TaKaRa, Bao Biotec Co, Dalian, China), and gene-specific polymerase chain reaction products were continuously measured by means of a LightCycler® 480 (F Hoffmann-La Roche, Ltd, Basel, Switzerland) detection system. The PCR reaction was performed as follows: pre-denaturation at 95 °C for 30 s followed by 45 cycles of 10 s at 95 °C, annealing at 60 °C for 10 s and elongation at 72 °C for 10 s. The fluorescent signal was collected at 72 °C, and the melting curve procedure was carried out. The purity of the product was analyzed using a melting curve. The PCR primers were designed as follows: TLR4 (forward 5′-GCTTTCACCTCTGCCTTCAC-3′ and reverse 5′-CCAACGGCTCTGAATAAAGTG-3′) and GAPDH (forward 5′-TCACCACCATGGAGAAGGC-3′ and reverse 5′-GCTAAGCAGTTGGTGGTGCA-3′). Every PCR experiment was carried out in triplicate. A standard curve was generated using a series of 10-fold dilutions of cDNA from the LPS group, and the amplification efficiency of each gene was calculated. It was accepted that the amplification efficiency of TLR4 and GAPDH was approximately 2.00 and that the difference between them was lower than 0.02.

Statistical analysis

Statistical analyses were performed using SPSS 13.0 software. The data are expressed as the mean±SEM. Comparisons among three or more groups were made by analysis of variance (ANOVA), and the two pairs of groups were compared using an LSD test. Ranked data are presented as the mean rank, comparisons among three or more groups were made

by a Kruskal-Wallis *H* test, and the two pairs of groups were compared using a Nemenyi test. A *P* value less than 0.05 was considered statistically significant.

Results

Ber inhibits LPS-induced intestinal injury, which is not reversed by Y

Figure 1 and Table 1 show histological changes in the ileum and the injury score of the various groups. Control mice demonstrated a normal histological architecture, and LPS-challenged mice showed extensive ileum morphological damage, including villus necrosis, infiltration of inflammatory cells and hemorrhage. There was a significant increase in the intestinal injury score compared to control animals ($P<0.01$). Pretreatment with Ber or Ber in combination with Y alleviated the intestinal damage and led to a significant decrease in the injury score in the LPS-challenged mice. In contrast, there was no significant difference in histological changes in the ileum between Ber+LPS and Ber+Y+LPS groups, and Y alone did not attenuate the intestinal injury caused by LPS ($P>0.05$).

Table 1. Effects of berberine (Ber) or/and yohimbine (Y) on the mean rank of intestinal injury score in mice twelve hours after challenge with LPS. $^{c}P<0.01$ *vs* control group. $^{d}P>0.05$, $^{e}P<0.05$, $^{f}P<0.01$ *vs* LPS group.

Group	*n*	Mean rank
Control	14	23.21
LPS	10	71.90^{c}
Ber+LPS	10	56.70^{f}
Ber+Y+LPS	10	59.90^{e}
Y+LPS	10	73.50^{d}
Ber	14	23.21
Ber+Y	8	22.75
Y	10	28.90

As shown in Figure 2, the villus height (Figure 2A) and mucosal weight (Figure 2B) of the ileum was measured twelve hours after the injection of mice with LPS or normal saline. Compared to control mice, LPS-challenged mice exhibited a

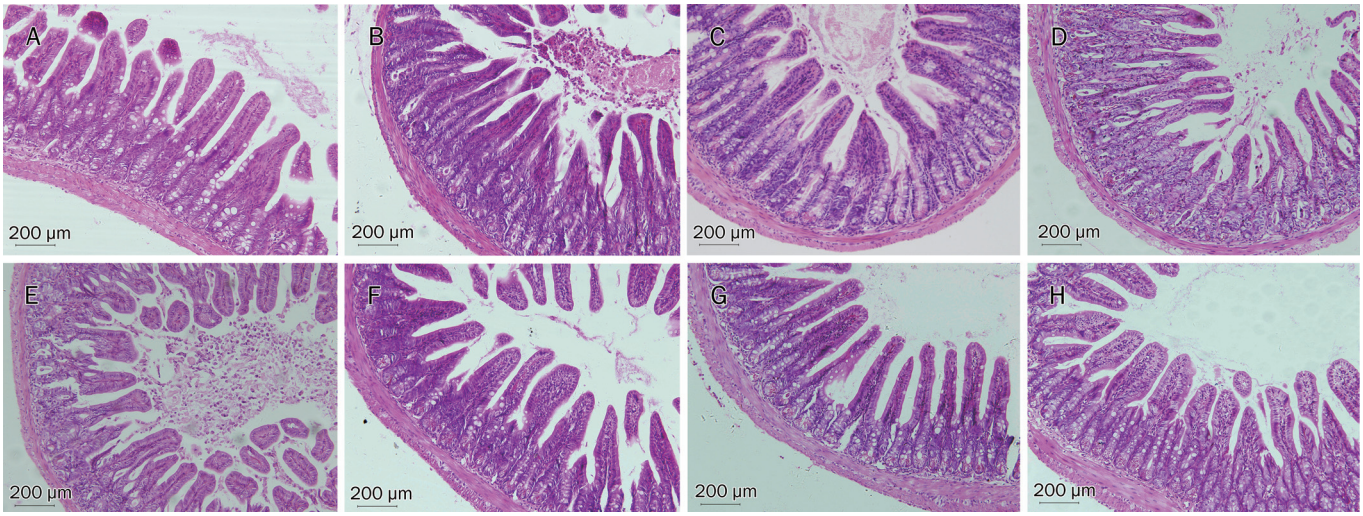

Figure 1. Photomicrograph of ileum from mice twelve hours after LPS (18 mg/kg) or normal saline injection in control (A), LPS (B), Ber+LPS (C), Ber+Y+LPS (D), Y+LPS (E), Ber (F), Ber+Y (G), and Y (H) groups. The intestine histological sections were stained with hematoxylin-eosin. Ber: berberine; Y: yohimbine. Scale bars represent 200 μm.

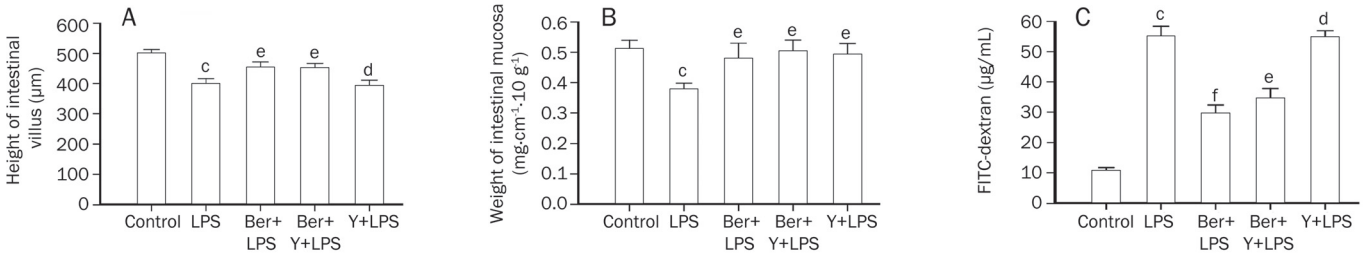

Figure 2. Effects of berberine (Ber) or/and yohimbine (Y) on intestinal villus height (A), mucosa weight (B) and intestinal permeability (C) in ileum of mice twelve hours after LPS challenge (18 mg/kg). Values are mean±SEM. n= 8–14. $^{c}P<0.01$ *vs* control group. $^{d}P>0.05$, $^{e}P<0.05$, $^{f}P<0.01$ *vs* LPS group.

marked decrease in villus height and mucosal weight in the ileum (P<0.01). The pretreatment of LPS-challenged mice with Ber or Ber in combination with Y resulted in a significant increase in villus height and mucosal weight compared to the LPS-treated group (P<0.05), and there was no remarkable difference in villus height or mucosal weight between Ber+LPS and Ber+Y+LPS groups. Y alone did not significantly change the villus height in LPS-challenged mice (P>0.05).

The gut mucosal permeability was evaluated *ex vivo* by measuring the leakage of FITC-dextran from the intestinal pouch. As shown in Figure 2C, compared to control mice, an increased permeability of the ileum was observed in LPS-challenged mice twelve hours after LPS injection. Pretreatment with Ber or Ber in combination with Y significantly inhibited the LPS-induced increase in ileal mucosal permeability, and no significant difference was observed in intestinal mucosal permeability between Ber+LPS and Ber+Y+LPS groups. In contrast, Y alone did not significantly decrease the ileal mucosal permeability in LPS-challenged mice (P>0.05). Moreover, pretreatment with Ber or Y alone or Ber and Y together had no significant effect on the villus height, mucosal weight or intestinal permeability of normal mice (Table 2).

Table 2. Effects of berberine (Ber) or/and yohimbine (Y) on the intestine parameters of normal mice. Mean±SEM. n=8–14. [a]P>0.05 *vs* control group.

Group	Villus height (μm)	Mucosa weight ($mg{\cdot}cm^{-1}{\cdot}g^{-1}$)	FITC-dextran (μg/mL)
Control	500.89±12.32	0.51±0.03	10.62±1.11
Ber	477.40±12.00[a]	0.45±0.02[a]	12.00±1.09[a]
Ber+Y	472.17±35.05[a]	0.55±0.04[a]	12.70±0.84[a]
Y	456.96±15.99[a]	0.43±0.02[a]	9.02±1.02[a]

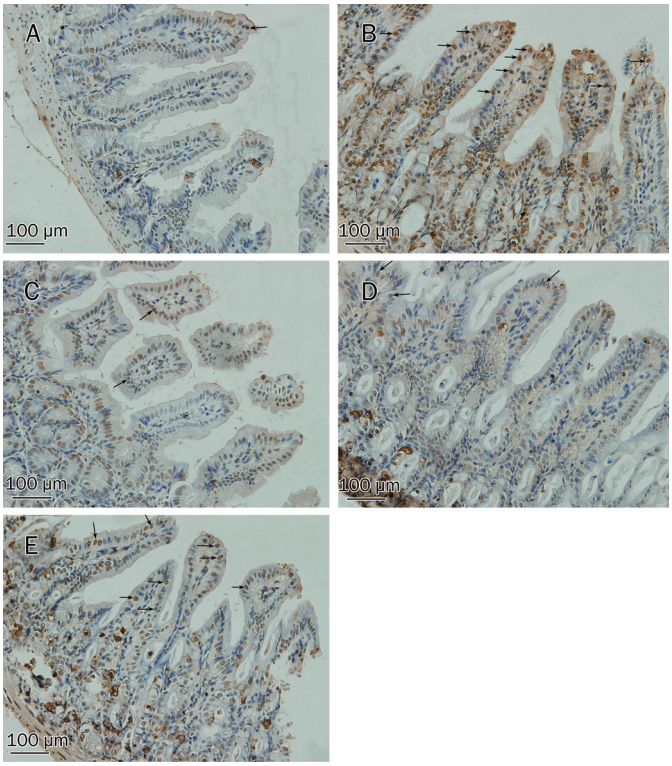

Figure 3. TUNEL analysis for enterocyte apoptosis in ileum of mice twelve hours after intraperitoneal injection of normal saline or LPS in control (A), LPS (B), Ber+LPS (C), Ber+Y+LPS (D), and Y+LPS (E) groups. TUNEL-positive cells were identified as those with brown staining of the nucleus and apoptotic morphology (arrows). Scale bars represent 100 μm.

Ber protects enterocyte against apoptosis induced by LPS, and Y does not abolish the anti-apoptosis action of Ber

TUNEL assays were performed to identify apoptotic cells in the ileum twelve hours after the administration of normal saline or LPS (Figure 3A–3E). Compared to control mice, a significant increase in enterocyte apoptosis in the ileum was observed after LPS challenge (Figure 3B, 4A). Following pretreatment with Ber or Ber in combination with Y, LPS-challenged mice showed a marked decrease in the AI in the ileum compared to the LPS-challenged animals (Figure 3B–3D, 4A). There was no significant difference in the AI in the ileum of LPS-treated mice following treatment with Ber or Ber in combination with Y. In addition, treatment with Y alone did not change the AI in the ileum of LPS-challenged mice (Figure 3E, 4A). Western blot analysis demonstrated that there was a significant increase in the amount of cleaved caspase-3 protein, an activated caspase-3, in the ileum of LPS-challenged mice compared to control animals (Figure 4B). Pretreatment with Ber or Ber in combination with Y markedly inhibited the activation of caspase-3 in LPS-treated mice, and there was no significant difference between the two groups for the levels of cleaved caspase-3 protein in the ileum (Figure 4B). Moreover, Y alone did not inhibit the LPS-induced caspase-3 activation in the ileum (Figure 4B).

Y does not antagonize the inhibitory effect of Ber on neutrophil infiltration in the ileum of endotoxemic mice

To evaluate the effects of Ber and Y on LPS-induced neutrophil recruitment in the ileum, MPO activity, an index of neutrophil infiltration[23], was determined by spectrophotometric methods (Figure 5A). Compared to control mice, MPO activity was significantly increased in the ileum of LPS-challenged mice twelve hours after injection (P<0.05). Pretreatment with Ber or Ber in combination with Y significantly reduced MPO activity in the ileum of LPS-challenged mice (P<0.01), whereas Y alone did not (P>0.05). However, the MPO activity in the Ber control group was lower than that in the normal control (P<0.05). Therefore, we measured the MPO content of the ileum using Western blotting. As shown in Figure 5B, there was no significant difference in the content of MPO in the ileum between the Ber control group and the normal control group (P>0.05). Compared to control mice, MPO content was significantly increased in the ileum of LPS-challenged mice twelve hours after injection (P<0.05). Pretreatment with Ber or

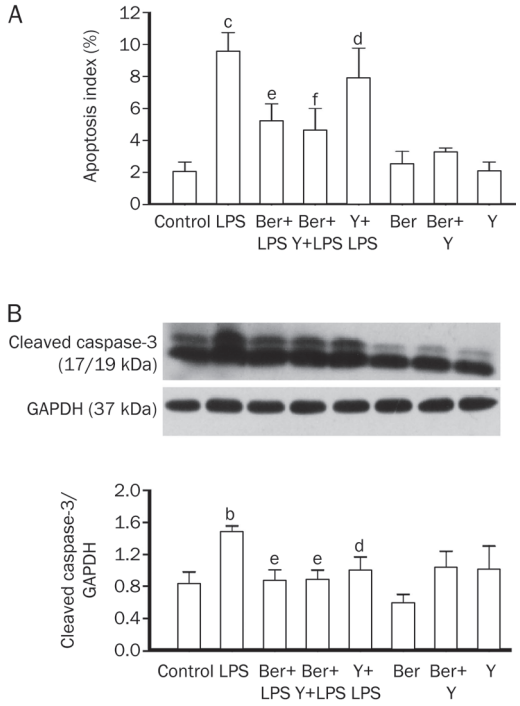

Figure 4. Yohimbine (Y) did not block the inhibitory effect of berberine (Ber) on enterocyte apoptosis of ileum of mice challenged with LPS. (A) Apoptosis index (AI) was calculated as the total number of TUNEL-positive cells/the total number of epithelial cells of 10 villi. n=9–10. (B) Western blotting analysis for cleaved caspase-3 protein level in ileum 2 h after stimulation of LPS. The upper row: cleaved caspase-3 protein expression. The middle row: GAPDH protein expression. Equal amounts of proteins were loaded. The lower row: column diagrams represent the ratio of cleaved caspase-3 to GAPDH. n=6. ^{b}P<0.05, ^{c}P<0.01 *vs* control group. ^{d}P>0.05, ^{e}P<0.05, ^{f}P<0.01 *vs* LPS group.

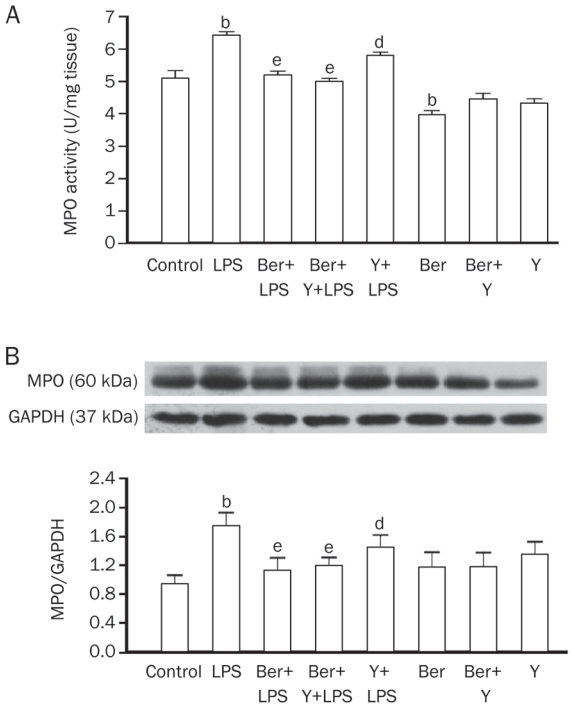

Figure 5. Yohimbine (Y) did not abolish the inhibitory effect of berberine (Ber) on neutrophil infiltration in ileum of mice twelve hours after LPS (18 mg/kg) challenge. (A) Colorimetric method was used to detect myeloperoxidase (MPO) activity. n=9–12. (B) Western blotting analysis for MPO content and column diagrams represent mean±SEM for the ratio of MPO to GAPDH. n=6. ^{b}P<0.05 *vs* control group. ^{d}P>0.05, ^{e}P<0.05 *vs* LPS group.

Ber in combination with Y significantly reduced MPO content in the ileum of LPS-challenged mice (P<0.01), whereas Y alone did not (P>0.05).

Ber inhibits TLR4 mRNA expression, NF-κB activation and MIP-2 production in the ileum of endotoxemic mice and this inhibition is not blocked by Y

As shown in Figure 6, a significant increase in TLR-4 mRNA expression, NF-κB activation and MIP-2 production was observed in the ileum of LPS-challenged mice compared to control mice. Pretreatment with Ber or Ber in combination with Y, but not with Y alone, significantly decreased the LPS-induced TLR-4 mRNA expression, NF-κB activation and MIP-2 production in the ileum. Following the injection of normal saline, no significant difference in TLR-4 mRNA expression and NF-κB activation was observed in the ileum of control, Ber, Ber+Y, and Y control groups (P>0.05), and MIP-2 production in the ileum of control, Ber, Ber+Y, and Y groups was undetectable.

Discussion

It has been demonstrated that Ber not only protects against LPS-induced intestinal injury but also activates the α_2-adrenoceptor[9, 11]. Our previous studies have shown that pretreatment with 50 mg/kg Ber once a day for three days significantly improves the survival rate of LPS-challenged mice, and similar pretreatment with 2 mg/kg Y, an α_2-adrenoceptor antagonist, in addition to Ber, enhances the protective effects of Ber in endotoxemic mice[9, 12]. Therefore, it was necessary to investigate whether Y enhances the protective effects of Ber against LPS-induced injury in the gut.

In this study, we demonstrated that LPS challenge induced intestinal injury in mice, as evidenced by high gut permeability, decreased mucosal weight and typical histological changes, such as necrosis of the villus, infiltration by inflammatory cells and a decrease in villus height. Pretreatment with Ber protects against intestinal injury that is induced by LPS, but Y did not block the protective effect of Ber on intestinal injury in endotoxemic mice. In addition, pretreatment with Y alone did not protect against LPS-induced gut injury, as evidenced by the increase in gut permeability and the histological changes. These data indicate that pretreatment with Ber reduced LPS-induced intestinal injury independent of α_2-adrenoceptor activation. However, the data from this study also show that Y increases the intestinal mucosal weight of the ileum in LPS-challenged mice, and the reason for this

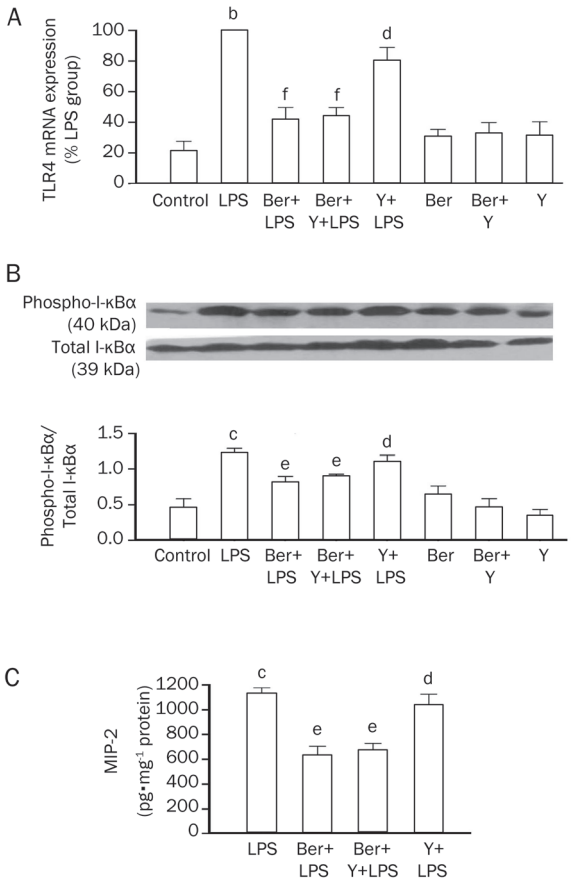

Figure 6. Yohimbine (Y) did not reverse the inhibitory effect of berberine (Ber) on TLR4-NF-κB/I-κBα-MIP-2 pathway in ileum of endotoxemic mice. (A) Real time PCR analysis for TLR4 mRNA expression in ileum 1 h after administration of LPS. LPS group was recognized as a control and data was expressed as the ratio to LPS group, n=6. (B) The total and phospho-I-κBα in ileum were analyzed by Western blotting 2 h after LPS challenge. The upper row: phospho-I-κBα protein expression. The middle row: total I-κBα protein expression. The lower row: column diagrams represent mean±SEM for the ratio of phospho-I-κBα to I-κBα, n=6. (C) ELISA analysis for MIP-2 expression in ileum twelve hours after administration of LPS. n=10. ^{b}P<0.05, ^{c}P<0.01 *vs* control group. ^{d}P>0.05, ^{e}P<0.05, ^{f}P<0.01 *vs* LPS group.

inconsistency remains to be identified. In previous studies, we demonstrated that Y enhances the protective effects of Ber in endotoxemic mice[12]. In the present study, we demonstrate that Y does not enhance the protective effects of Ber against intestinal damage that is caused by treatment with LPS. It has been reported that pretreatment with Y once a day for 3 days prevents LPS-induced myocardial dysfunction in mice[24]. Thus, the enhanced protection of Ber against endotoxemia by Y may be related to the improvement of LPS-induced myocardial dysfunction in mice that are pretreated with Y.

It is well known that LPS challenge inhibits crypt cell proliferation, increases enterocyte apoptosis in the ileum and reduces villus height and intestinal mucosal weight. Inhibition of enterocyte apoptosis can improve intestinal recovery after LPS exposure[6, 7, 25]. These observations suggest that increased intestinal apoptosis and diminished cell proliferation play an important role in LPS-induced intestinal damage. Our previous study showed that enterocyte proliferation is inhibited during endotoxemia and that Ber promotes the enterocyte proliferation in the ileum of endotoxemic mice in an α_2-adrenoceptor-independent manner[26]. Therefore, we further examined the effect of Ber and Y on enterocyte apoptosis in the ileum in LPS-challenged mice. The results demonstrate that LPS treatment activates caspase-3 and promotes enterocyte apoptosis in the ileum. Pretreatment with Ber decreases caspase-3 activation and enterocyte apoptosis in the ileum of LPS-challenged mice, and these effects are not antagonized by Y. Other studies have demonstrated an increase in the activity of caspase-3, an increase in the number of apoptotic epithelial cells and a high gut permeability following the intraperitoneal injection of LPS[27]. These findings indicate that the inhibition of enterocyte apoptosis may contribute to the protection of Ber against LPS-induced intestinal injury and that the protective action of Ber is not associated with the α_2-adrenoceptor. However, the mechanisms responsible for the reduced enterocyte apoptosis by Ber in endotoxemic mice are unclear. Recent studies have demonstrated that Ber significantly activates the adenosine 5′-monophosphate-activated protein kinase (AMPK) signaling pathway and that AMPK activators protect against tumor necrosis factor-α-induced cardiac cell apoptosis. On the other hand, polymorphonuclear leukocyte transepithelial migration is sufficient by itself to induce intestinal epithelial apoptosis[28–30]. Thus, the inhibitory effect of Ber on enterocyte apoptosis in endotoxemia may be related to AMPK activation and the inhibition of leukocyte transepithelial migration, and these questions remain to be investigated.

In addition to apoptosis and hypoplasia, neutrophil infiltration is another important mechanism for intestinal injury during endotoxemia. As the principal circulating phagocyte, neutrophils are the first and most abundant of the leukocytes to arrive at the infection focus[31], and they are ideally suited to eliminate pathogenic bacteria[32]. Indeed, neutrophils contain numerous potent tissue-damaging substances, such as reactive oxygen species, bactericidal permeability-increasing proteins and elastases[33], and upon release into the intestinal wall, these substances may contribute to the disruption of intestinal integrity and the increase in macromolecular passage across the epithelial cell lining. In addition, neutrophils can produce cytokines and chemokines that enhance the acute inflammatory response during sepsis[33]. Some studies have demonstrated that LPS-associated intestinal leakage in the gut is largely regulated by leukocyte accumulation[16]. Thus, we observed the effects of Ber and Y on MPO activity, a useful indicator of neutrophil recruitment, in the ileum of LPS-challenged mice and found that pretreatment with Ber or Ber in combination with Y, but not with Y alone, significantly decreased MPO activity in LPS-challenged mice. This suggests that Ber may inhibit neutrophil recruitment in the ileum during LPS endotoxemia via an α_2-adrenoceptor-independent pathway. However, Ber also decreased MPO activity in the ileum in normal control mice, suggesting that MPO activity may not accurately

reflect neutrophil recruitment under the conditions presented here. Therefore, we determined the amount of MPO in the ileum using a Western blot assay. The results confirmed that pretreatment with Ber significantly decreased the MPO content in the ileum in LPS-challenged mice, an effect that was not reversed by Y, suggesting that Ber protects against LPS-induced intestinal injury by inhibiting neutrophil infiltration in an α_2-adrenoceptor-independent fashion.

Neutrophil accumulation is thought to be dependent on the formation and activity of CXC chemokines, such as MIP-2[16, 17]. Several studies have shown that LPS-induced MIP-2 expression is involved in I-κB phosphorylation and NF-κB activation via TLR4[15, 17, 34]. A more recent study suggests that Ber may reduce LPS-induced intestinal injury by suppressing the activation of TLR4 and NF-κB in the ileum[10], but a quantitative immunohistochemical assay of TLR4 and NF-κB activation is needed to confirm this hypothesis. To understand further the signaling pathway involved in the inhibition of neutrophil accumulation induced by Ber in the ileum of LPS-challenged mice, we investigated TLR4 mRNA expression, I-κBα phosphorylation and MIP-2 production in the ileum. The results demonstrate that LPS induced TLR4 mRNA expression, I-κBα phosphorylation and MIP-2 production in the ileum and that these effects were reduced by pretreatment with Ber or Ber in combination with Y, but not with Y alone. Kessel *et al* also demonstrated that TLR-4 upregulation might be responsible for the harmful effects of LPS on the intestine[13]. These investigations indicate that pretreatment with Ber inhibits neutrophil infiltration and, in turn, alleviates LPS-induced intestinal injury by suppressing the TLR4-NF-κB-MIP-2 pathway independently of the α_2-adrenoceptor.

In conclusion, the results of this study demonstrate that pretreatment with Ber protects against intestinal damage in endotoxemia by reducing neutrophil infiltration and enterocyte apoptosis in an α_2-adrenoceptor-independent manner. Ber-induced suppression of neutrophil infiltration in the ileum during endotoxemia is associated with the inhibition of the TLR4-NF-κB-MIP-2 signaling pathway but not with the α_2-adrenoceptor. These findings may provide a new therapeutic strategy for the treatment of intestinal injury in sepsis.

Acknowledgements

We thank Ms Zheng PEIE for her excellent technical assistance. This study was supported by grants from the National Natural Science Foundation of China (grant No 30670826 and 30971191), the Science and Technology Foundation from the Ministry of Education of the People's Republic of China (grant No 207140), the Guangdong Science and Technology Projects (grant No 2008B030301352) and the Leading Academic Discipline Program, 211 Project for Ji-nan University (the 3rd phase).

Author contribution

Hong-mei LI and Yi-yang WANG performed research, analyzed the data, and drafted the manuscript. Wen-juan CAO, Xiao-hui YU, Ren-bin QI, Chao-feng HU, and Yu-xia YAN performed some of the experiments. Da-xiang LU revised the manuscript. Hua-dong WANG designed the research, obtained the funding and revised the manuscript.

References

1 Angus DC, Linde-Zwirble WT, Lidicker J, Clermont G, Carcillo J, Pinsky MR. Epidemiology of severe sepsis in the United States: analysis of incidence, outcome, and associated costs of care. Crit Care Med 2001; 29: 1303–10.
2 De-Souza DA, Greene LJ. Intestinal permeability and systemic infections in critically ill patients: effect of glutamine. Crit Care Med 2005; 33: 1175–8.
3 Doig CJ, Sutherland LR, Sandham JD, Fick GH, Verhoef M, Meddings JB. Increased intestinal permeability is associated with the development of multiple organ dysfunction syndrome in critically ill ICU patients. Am J Respir Crit Care Med 1998; 158: 444–51.
4 Deitch EA. The role of intestinal barrier failure and bacterial translocation in the development of systemic infection and multiple organ failure. Arch Surg 1990; 125: 403–4.
5 Pålsson-McDermott EM, O'Neill LA. Signal transduction by the lipopolysaccharide receptor, Toll-like receptor-4. Immunology 2004; 113: 153–62.
6 Sukhotnik I, Mogilner J, Krausz MM, Lurie M, Hirsh M, Coran AG, *et al*. Oral arginine reduces gut mucosal injury caused by lipopolysaccharide endotoxemia in rat. J Surg Res 2004; 122: 256–62.
7 Sukhotnik I, Agam M, Shamir R, Shehadeh N, Lurie M, Coran AG, *et al*. Oral glutamine prevents gut mucosal injury and improves mucosal recovery following lipopolysaccharide endotoxemia in a rat. J Surg Res 2007; 143: 379–84.
8 Kim TS, Kang BY, Cho D, Kim SH. Induction of interleukin-12 production in mouse macrophages by berberine, a benzodioxoloquinolizine alkaloid, deviates $CD4^+$ T cells from a Th2 to a Th1 response. Immunology 2003; 109: 407–14.
9 Li F, Wang HD, Lu DX, Wang YP, Qi RB, Fu YM, *et al*. Neutral sulfate berberine modulates cytokine secretion and increases survival in endotoxemic mice. Acta Pharmacol Sin 2006; 27: 1199–205.
10 Zhang Q, Piao XL, Piao XS, Lu T, Wang D, Kim SW. Preventive effect of *Coptis chinensis* and berberine on intestinal injury in rats challenged with lipopolysaccharides. Food Chem Toxicol 2010; 49: 61–9.
11 Hui KK, Yu JL, Chan WF, Tse E. Interaction of berberine with human platelet alpha 2 adrenoceptors. Life Sci 1991; 49: 315–24.
12 Zhang HQ, Wang HD, Lu DX, Qi RB, Wang YP, Yan YX, *et al*. Berberine inhibits cytosolic phospholipase A2 and protects against LPS-induced lung injury and lethality independent of the alpha 2-adrenergic receptor in mice. Shock 2008; 29: 617–22.
13 Kessel A, Toubi E, Pavlotzky E, Mogilner J, Coran AG, Lurie M, *et al*. Treatment with glutamine is associated with down-regulation of Toll-like receptor-4 and myeloid differentiation factor 88 expression and decrease in intestinal mucosal injury caused by lipopolysaccharide endotoxaemia in a rat. Clin Exp Immunol 2007; 151: 341–7.
14 De Plaen IG, Tan XD, Chang H, Wang L, Remick DG, Hsueh W. Lipopolysaccharide activates nuclear factor kappa B in rat intestine: role of endogenous platelet-activating factor and tumour necrosis factor. Br J Pharmacol 2000; 129: 307–14.
15 Ohtsuka Y, Lee J, Stamm DS, Sanderson IR. MIP-2 secreted by epithelial cells increases neutrophil and lymphocyte recruitment in the mouse intestine. Gut 2001; 49: 526–33.
16 Mangell P, Mihaescu A, Wang Y, Schramm R, Jeppsson B, Thorlacius H. Critical role of P-selectin-dependent leukocyte recruitment in endotoxin-induced intestinal barrier dysfunction in mice. Inflamm Res

2007; 56: 189–94.
17 De Plaen IG, Han XB, Liu X, Hsueh W, Ghosh S, May MJ. Lipopolysaccharide induces CXCL2/macrophage inflammatory protein-2 gene expression in enterocytes via NF-kappa B activation: independence from endogenous TNF-alpha and platelet-activating factor. Immunology 2006; 118: 153–63.
18 Oktar BK, Gulpinar MA, Bozkurt A, Ghandour S, Cetinel S, Moini H, *et al*. Endothelin receptor blockers reduce I/R-induced intestinal mucosal injury: role of blood flow. Am J Physiol Gastrointest Liver Physiol 2002; 282: G647–G55.
19 Song J, Wolf SE, Herndon DN, Wu XW, Jeschke MG. Second hit post burn increased proximal gut mucosa epithelial cells damage. Shock 2008; 30: 184–8.
20 Yasuda T, Takeyama Y, Ueda T, Shinzeki M, Sawa H, Nakajima T, *et al*. Breakdown of intestinal mucosa via accelerated apoptosis increases intestinal permeability in experimental severe acute pancreatitis. J Surg Res 2006; 135: 18–26.
21 Zayat M, Lichtenberger LM, Dial EJ. Pathophysiology of LPS-induced gastrointestinal injury in the rat: role of secretory phospholipase A2. Shock 2008; 30: 206–11.
22 Yuan ZQ, Peng YZ, Li XL, Huang YS, Yang ZC. Induction of heat shock protein 70 by sodium arsenite attenuates burn-induced intestinal injury in severe burned rats. Burns 2008; 34: 247–53.
23 Croci T, Landi M, Galzin AM, Marini P. Role of cannabinoid CB1 receptors and tumor necrosis factor-alpha in the gut and systemic anti-inflammatory activity of SR 141716 (rimonabant) in rodents. Br J Pharmacol 2003; 140: 115–22.
24 Wang YY, Li HM, Wang HD, Peng XM, Wang YP, Lu DX, *et al*. Pretreatment with berberine and yohimbine protects against lippolysaccharide-induced myocardial dysfunction via inhibition of cardiac I-κBα phosphorylation and apoptosis in mice. Shock 2011; 35: 322–8.
25 Sukhotnik I, Shehadeh N, Rothem L, Lurie M, Mogilner J, Shiloni E, *et al*. Oral insulin up-regulates Toll-like receptor 4 expression and enhances intestinal recovery following lipopolysaccharide-induced gut injury in a rat. Dig Dis Sci 2008; 53: 1231–9.
26 Li HM, Wang YY, Wang HD, Cao WJ, Jiang JW, Hu CF, *et al*. Effect of berberine and yohimbine on impaired enterocyte proliferation and intestinal injury in LPS-challenged mice. Chin J Pathophysiol 2010; 26: 941–6.
27 Alscher KT, Phang PT, McDonald TE, Walley KR. Enteral feeding decreases gut apoptosis, permeability, and lung inflammation during murine endotoxemia. Am J Physiol Gastrointest Liver Physiol 2001; 281: G569–G76.
28 Lu DY, Tang CH, Chen YH, Wei IH. Berberine suppresses neuroinflammatory responses through AMP-activated protein kinase activation in BV-2 microglia. J Cell Biochem 2010; 110: 697–705.
29 Kewalramani G, Puthanveetil P, Wang F, Kim MS, Deppe S, Abrahani A, *et al*. AMP-activated protein kinase confers protection against TNF-α-induced cardiac cell death. Cardiovasc Res 2009; 84: 42–53.
30 Le'Negrate G, Selva E, Auberger P, Rossi B, Hofman P. Sustained polymorphonuclear leukocyte transmigration induces apoptosis in T84 intestinal epithelial cells. J Cell Biol 2000; 150: 1479–88.
31 Lekstrom-Himes JA, Gallin JI. Immunodeficiency diseases caused by defects in phagocytes. N Engl J Med 2000; 343: 1703–14.
32 Seely AJ, Pascual JL, Christou NV. Science review: Cell membrane expression (connectivity) regulates neutrophil delivery, function and clearance. Crit Care 2003; 7: 291–307.
33 Guo RF, Riedemann NC, Sun L, Gao H, Shi KX, Reuben JS, *et al*. Divergent signaling pathways in phagocytic cells during sepsis. J Immunol 2006; 177: 1306–13.
34 De Filippo K, Henderson RB, Laschinger M, Hogg N. Neutrophil chemokines KC and macrophage-inflammatory protein-2 are newly synthesized by tissue macrophages using distinct TLR signaling pathways. J Immunol 2008; 180: 4308–15.

Acta Pharmacologica Sinica (2011) 32: 1373–1380

www.nature.com/aps

Original Article

Hypomethylation of proximal CpG motif of interleukin-10 promoter regulates its expression in human rheumatoid arthritis

Li-hong FU, Chun-ling MA, Bin CONG*, Shu-jin LI, Hai-ying CHEN, Jing-ge ZHANG

Department of Forensic Medicine, Hebei Key Laboratory of Forensic Medicine, Hebei Medical University, Shijiazhuang 050017, China

Aim: The promoter of human interleukin-10 (IL10), a cytokine crucial for suppressing inflammation and regulating immune responses, contains an interspecies-conserved sequence with CpG motifs. The aim of this study was to investigate whether methylation of CpG motifs could regulate the expression of *IL10* in rheumatoid arthritis (RA).

Methods: Bioinformatic analysis was conducted to identify the interspecies-conserved sequence in human, macaque and mouse *IL10* genes. Peripheral blood mononuclear cells (PBMCs) from 20 RA patients and 20 health controls were collected. The PBMCs from 6 patients were cultured in the presence or absence of 5-azacytidine (5 μmol/L). The mRNA and protein levels of *IL10* were examined using RT-PCR and ELISA, respectively. The methylation of CpGs in the *IL10* promoter was determined by pyrosequencing. Chromatin immunoprecipitation (ChIP) assays were performed to detect the cyclic AMP response element-binding protein (CREB)-DNA interactions.

Results: One interspecies-conserved sequence was found within the *IL10* promoter. The upstream CpGs at -408, -387, -385, and -355 bp were hypermethylated in PBMCs from both the RA patients and healthy controls. In contrast, the proximal CpG at -145 was hypomethylated to much more extent in the RA patients than in the healthy controls (P=0.016), which was correlated with higher *IL10* mRNA and serum levels. In the 5-azacytidine-treated PBMCs, the CpG motifs were demethylated, and the expression levels of *IL10* mRNA and protein was significantly increased. CHIP assays revealed increased phospho-CREB binding to the *IL10* promoter.

Conclusion: The methylation of the proximal CpGs in the *IL10* promoter may regulate gene transcription in RA.

Keywords: rheumatoid arthritis; interleukin-10; DNA methylation; promoter regions; interspecies-conserved sequence; CpG motif; cyclic AMP response element-binding protein; bioinformatics

Acta Pharmacologica Sinica (2011) 32: 1373–1380; doi: 10.1038/aps.2011.98; published online 10 Oct 2011

Introduction

Rheumatoid arthritis (RA) is an inflammatory and autoimmune disease[1]. Proinflammatory and anti-inflammatory cytokines are involved in the initiation and progression of RA; therefore, a detailed study of the regulatory mechanism of the production of cytokines during the development of RA is of utmost importance. Interleukin-10 (IL10), produced mainly by monocytes, T helper type 2 (Th2) and regulatory T cells (Treg), plays a crucial role in suppressing inflammation and regulating the immune response[2]. It contributes to the growth and differentiation of B cells, but inhibits T cell proliferation. IL10 can fight inflammation by down-regulating the production of proinflammatory cytokines, such as tumor necrosis factor alpha (TNFα), interleukin-1 beta (IL1β), interleukin-6 (IL6), and others; it also stimulates the production of cytokine inhibitors (*eg*, the IL1 receptor antagonist and the soluble TNF receptor). Evidence has indicated that IL10 is involved in the pathogenesis of RA. Several murine models of RA are markedly exacerbated in IL10-deficient mice[3, 4]. Exogenous IL10 can prevent the development of arthritis and regulate immune cell function[5, 6].

The *IL10* gene exhibits substantial polymorphism in the promoter region that correlates with transcription. Recent studies have found that the methylation status of CpG sites is related to cytokine expression[7]. Therefore, the extent of methylation at CpG sites correlates with the level of cytokine production. Furthermore, the amount of methylation at CpG sites has been shown to be related to cells' differentiation or activation. Several CNS regions in the *IL10* gene have been identified by bioinformatic analysis, including the 5′-proximal region, promoter, and introns[8], and the hypomethylation of CpGs around intron 4 may enhance the expression of *IL10*[9].

* To whom correspondence should be addressed.
E-mail hbydcongbin@126.com
Received 2010-12-24 Accepted 2011-06-21

However, a correlation was not found between the CpG methylation status of the *IL10* promoter and IL10 production. *IL10*'s promoter region contains many CpGs and putative transcription factors binding sites, such as Sp-1, CCAAT/enhancer binding protein (C/EBP-β) and cyclic AMP response element-binding protein (CREB). Several papers reported that the activated cAMP/CREB signaling pathway could enhance the IL10 production in human monocytes, and IFN-gamma suppressed IL10 synergize by regulating CREB/AP-1 protein expression[10, 11]. CREB is expressed at a higher level in the synovial cells of patients with RA, and it is implicated in IL6 production from synovial cells[12]. However, whether the methylation status of a single CpG site in the *IL10* promoter can regulate its transcription through affecting CREB's binding to this region in RA remains unclear. Some epigenetic clues to RA have been revealed. Global hypomethylation of the T cell genome[13] and methylation of the death receptor 3 gene (*DR3*)[14] and the *IL6* promoter are related to the pathogenesis of RA[15]. Because epigenetic alterations are reversible, they may provide new molecular targets for therapeutic intervention. Therefore, by bioinformatics analysis, we analyzed the human *IL10* gene to seek CNS and CRE. Then, we investigated whether methylation of the *IL10* promoter could regulate its expression. Furthermore, we studied whether DNA methylation had an effect on CREB binding to the promoter, thus illustrating the mechanism underlying the regulatory effects of DNA methylation on gene expression.

Materials and methods

Patients and controls

Peripheral blood from 20 patients with active RA and 20 healthy controls (HCs) were studied. RA patients recruited from the Second and Third Affiliated Hospitals of Hebei Medical University (Shijiazhuang, China) were in conformity with the American College of Rheumatology Criteria[16]. Research ethics approval was obtained from Hebei Medical University Research Ethics Committee (Shijiazhuang, China), and informed consent was obtained from individual patients. Healthy controls were collected from Hebei Province Blood Center. Of the RA patients, 4 were male, and 16 were female with their mean±SD age being 39.6±11.4 years old (ranging from 20 to 58 years old). Most of the RA patients in this study were in moderate disease activity. The mean DAS28 was 4.38±1.8 (range 1.9–8.8), the mean time from onset was 25.33±22.33 months (ranging from 3 months to 6 years), the mean erythrocyte sedimentation rate (ESR) was 37.4±28.13 mm/h (range 6–123), the mean C-reactive protein (CRP) was 17.27±20.63 mg/L (range 1.96–92.9), and the mean rheumatoid factor (RF) was 164.16±122.92 U/mL (range 17.2–447). Of the healthy individuals, 4 were male, and 16 were female. Their mean±SD age was 38.4±10.2 years old (ranging from 18 to 56 years old).

Peripheral blood mononuclear cells (PBMCs) and cell culture

PBMCs were isolated by Ficoll-Hypaque centrifugation from peripheral blood of RA patients and HCs. PBMCs from six patients and controls were cultured in RPMI-1640 medium supplemented with 25 mmol/L HEPES, 4 mmol/L *L*-glutamine, 100 units/mL penicillin/streptomycin, and 5% heat-inactivated fetal calf serum with 1 μg/mL phytohemagglutinin (PHA; Sigma, USA) and 10 μg/mL lipopolysaccharides (LPS; Sigma, USA) . In the presence or absence of 5 μmol/L 5-azacytidine (5-azaC) (Sigma, USA) for 72 h, 2×10^6 cells/well were cultured according to Mi's method[17].

mRNA and protein expression

After being extracted from PBMCs using TRIzol reagent (SBS, China), the RNA was reverse transcribed in the presence of 1×PCR buffer, 1 mmol/L dNTPs, 20 units AMV reverse transcriptase, 20 units RNA guard ribonuclease inhibitor and 2.5 mmol/L random primers (SBS, China) in a final reaction volume of 20 μL. Reactions were conducted at 30 °C for 10 min and 42 °C for 60 min using a PTC-200 PCR system (MJ Research, USA). The level of *IL10* mRNA transcripts was determined by semiquantitative reverse transcription polymerase chain reaction (RT-PCR). β-actin was used as the internal standard for each RT-PCR. TNFα was measured as a control for cytokine expression. The specific primers used for the amplification of *IL10* were the following: forward, 5′-TCAGGGTGGCGACTCTAT-3′, and reverse, 5′-TGGGCTTCTTTCTAAATCGTTC-3′; β-actin: forward, 5′-CATCCTGCGTCTGGACCT-3′, and reverse, 5′-TCAGGAGCAATGATCTTG-3′; TNFα: forward, 5′-CGAGTCTGGGCAGGTCTA-3′, and reverse, 5′-GTGGTGGTCTTGTTGCTTAA-3′. PCR amplification was conducted on a PTC-200 PCR system using 5 μL cDNA, 1×GeneAmp PCR Gold buffer (Applied Biosystems), 1.5 mmol/L $MgCl_2$ (Applied Biosystems), 200 μmol/L dNTPs (Shanghai Sangon Biological Engineering Technology, Shanghai, China), 0.6 μmol/L forward and reverse primers, 1 unit AmpliTaq Gold DNA polymerase (Applied Biosystems) in a 20 μL total reaction volume. The PCR amplification conditions were denaturation for 3 min at 94 °C; amplification for 30 cycles of 45 s at 94 °C, 45 s at 50 °C for *IL10* (or 58 °C for β-actin, 55 °C for TNFα), and 45 s at 72 °C; and extension for 10 min at 72 °C. PCR products were resolved by 2% agarose gel electrophoresis with ethidium bromide. The images were recorded and quantified by Hema analyzer (Udine, Italy). The level of IL10 in serum was measured by ELISA (Bender MedSystems, Austria) according to the manufacturer's instructions.

Bioinformatics

Alignments between mouse and human *IL10* loci, and between macaque and human *IL10* loci were performed, and the extent of DNA sequence homology was computed with a web-based program called Regulatory Visualization Tools for Alignment (rVISTA; http://www.gsd.lbl.gov/vista)[18]. The plot of the percentage of sequence identity referred to the human sequence. Regions with a length of at least 100 bp, which showed at least 75 percent sequence identity at each segment of the alignment between successive gaps, are identified as CNS and are shown in Figure 1.

DNA methylation status

DNA was extracted from the PBMCs by the phenol-chloroform method. The DNA concentration was measured by a spectrophotometer (Bio-Rad, USA). One microgram of DNA was treated with sodium bisulphite as previously described[19]. PCR and pyrosequencing primers were designed using PSQ Assay Design software (Biotage, Sweden) to amplify the CpG dinucleotides in the *IL10* promoter. The primer sequences used are in Table 1. PCR was performed in a 50 μL reaction system of GeneAmp 9700 (Applied Biosystems, USA). Each PCR reaction contained 50 ng bisulfite treated DNA, 1×PCR buffer, 2.5 mmol/L $MgCl_2$, 0.2 mmol/L dNTPs, 0.2 μmol/L forward primer, 0.2 μmol/L reverse primer, and 1 unit AmpliTaq Gold (Applied Biosystems, USA). The PCR conditions were initiated with a heated lid at 95 °C for 5 min, followed by 50 cycles of 95 °C for 15 s, 51 °C for 30 s, 72 °C for 30 s, and, finally, 72 °C for 5 min. PCR product quality verification was performed using 2% agarose gels with ethidium bromide. Fifty microliters of PCR products was used for each pyrosequencing reaction. Pyrosequencing methylation analysis was conducted by the Pyro Q-CpG system (PyroMark ID, Biotage, Sweden) according to the manufacturer's protocol. In brief, the PCR product was bound to streptavidin-coated Sepharose beads (GE Healthcare Bio-sciences AB, Sweden). The Sepharose beads containing the immobilized PCR product were purified in 70% ethanol for 5 s, denatured in denaturing buffer (Biotage) for 5 s, and washed with washing buffer (Biotage) for 10 s using the pyrosequencing Vacuum Prep Tool (Biotage). Then, 0.5 μmol/L sequence primer was annealed to the purified, single-stranded PCR product, and pyrosequencing was fulfilled by the Pyro Q-CpG system. The level of methylation for each cytosine locus on CpG sites was expressed as the percentage of mC/(mC+C) (mC is methylated cytosine, C is unmethylated cytosine). Non-CpG cytosine residues were used as controls to verify bisulfite conversion.

Table 1. Pyrosequencing primer sequences.

CpG sites	PCR primer sequences (5′–3′)	Sequecing primer sequences (5′–3′)
-408	TGTATTTTGGAATGGGTAATTTG	GGAATGGGTAATTTGTTT
	(Biotin) AAAACCCTCAACTATAAATTCTCA	
-387	same to -408	TATTGTGATTTAGGAATA
-385	same to -408	same to -387
-355	GAATACGCGAATGAGAATTTATAG	TTTATAGTTGAGGGTTTTTG
	(Biotin)TTTCCTAAAAAAACAACTATTCTA	
-145	AGAAGGAGGAGTTTTAAGGAGAAA	AGGAGAAAAAATTTTGTGT
	(Biotin) TCATTCATTAAAAAACCACAATCA	

Chromatin immunoprecipitation (ChIP) assay

According to the manufacturer's instructions, the ChIP assay was performed to detect phospho-CREB binding to the *IL10* promoter in the PBMCs of patients *in situ* before and after 5-azaC treatment. ChIP was performed with the Chromatin Immunoprecipitation Assay Kit (Upstate Biotechnology, No 17-295) and anti-phospho-CREB antibody (Ser133) (Upstate Biotechnology, No 06-519). PCR was performed on *IL10*'s upstream promoter and proximal promoter, and an intron was amplified as internal control. Primer sequences were upstream promoter primer sequence, forward, 5′-GAAGTCTTGGGTATTCATCC-3′, reverse, 5′-GCTGTGGGTTCTCATTCG-3′; promoter primer sequence, forward, 5′-CTCCCCAGGAAATCAACT-3′, reverse, 5′-AAAAGCCACAATCAAGGT-3′; intron primer sequence, forward, 5′-TTAGAGCGTTTCCAGACC-3′, reverse, 5′-ACCTATGTCAACCCTTCG-3′. PCR was performed in a 20 μL reaction in GeneAmp 9700 (Applied Biosystems, USA). Each PCR reaction contained 100 ng DNA, 1×PCR buffer, 2.0 mmol/L $MgCl_2$, 0.2 mmol/L dNTPs, 0.2 μmol/L forward and reverse primers, and 1 unit AmpliTaq Gold (Applied Biosystems, USA). The PCR conditions were initiated with a heated lid at 95 °C for 3 min, followed by 35 cycles of 94 °C for 45 s, 51–55 °C for 45 s, 72 °C for 45 s, and, finally, 72 °C for 5 min. PCR products were analyzed in an agarose gel. Values were normalized according to the input.

Statistical analysis

All calculations were performed on a Microsoft computer using SPSS software (version 14.0). Data were analyzed by independent-samples *t* test and paired *t* test. Correlation coefficients were calculated by Pearson rank correlation (*r*) and Spearman rank correlation where applicable.

Results

Bioinformatic approach to the identification of CREs in IL10 locus

We performed a bioinformatic search for CREs in the *IL10* locus using web-based software, rVISTA. This program can identify interspecies-conserved sequences for specific transcription factors by linking to the most widely used database, TRANSFAC. As shown in Figure 1, four CREs were found between macaques and humans ranging from introns 1 to 4 and all were interspecies-conserved. As the readily available macaque IL10 sequence does not contain the upstream promoter region, we did not compare the IL10 promoter region of macaque with that of humans. Three CREs were found between mice and humans, including the 5′-proximal region, promoter and introns 1 to 4, and the interspecies-conserved CRE was in the promoter and a short fragment of intron 4. This suggested that the CRE in the promoter, designated as p-CRE, may be important for the regulation of *IL10* gene expression.

Methylation status of *IL10* promoter

There are at least five CpG sites in the *IL10* promoter region, four located at -408, -387, -385, -355 bp (upstream) and one at -145 bp (proximal) relative to the transcription start site. It was found that methylation of individual CpG sites was similar in PBMCs from the 20 RA patients and the 20 HCs; that is, the upstream CpG motifs were hypermethylated, while the

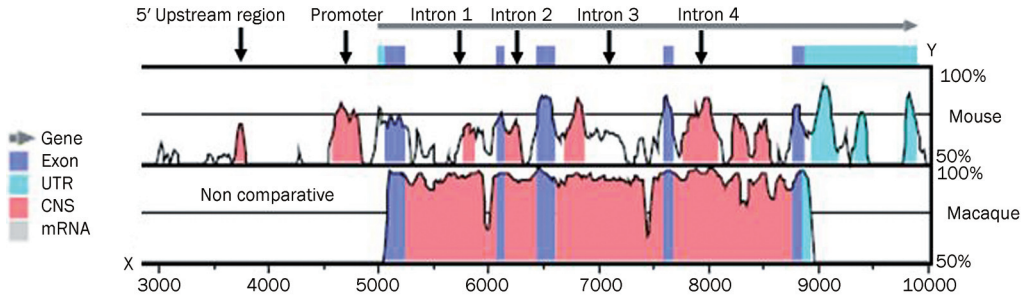

Figure 1. Bioinformatics analysis of the conserved CREs on the IL10 locus. A web-based program, rVISTA, was used to align the mouse, macaque and human IL10 loci and compute the extent of DNA sequence homology. The mouse and macaque sequences are used as the query sequences on the y-axis, and the human sequence is used as the subject sequence on the x-axis.

proximal CpG motif was hypomethylated. However, in the patients, methylation of cytosine at -145 bp was significantly less than that in the HCs (18%±7% *versus* 33%±6.6%; *P*=0.016) (Figure 2).

Methylation status and mRNA expression

We then studied the relationship between the methylation status of the *IL10* gene and mRNA expression. The mRNA (0.89±0.21 *versus* 0.70±0.13, *P*=0.009) and serum level (71.36±43.25 pg/mL *versus* 42.85±2.99 pg/mL, *P*=0.012) of IL10 was significantly higher in the patients than in HCs. Furthermore, IL10 mRNA levels of the patients were correlated with the RA factor (*r*=0.526, *P*=0.016). As for control cytokine, TNFα mRNA expression was significantly higher in the PBMCs of RA patients than in controls (0.5143±0.5249 *versus* 0.0861±0.1434, *P*=0.010). Compared with the 20 HCs, the methylation frequency of -145C was significantly lower in the 20 RA patients, which resulted in inversely higher *IL10* mRNA levels (Figure 3). Therefore, hypomethylation of -145C was correlated with higher mRNA expression (*r*=-0.746, *P*=0.001). Furthermore, after PBMCs from the six patients were cultured in the presence of 5-azaC, all five CpG motifs were demethylated (Table 2), and the mRNA of *IL10* (0.2866±0.15 *versus* 0.4488±0.13, *P=0.037*) and protein levels (5.30±8.48 pg/mL

Table 2. Comparison of the methylation status of individual CpG sites in PBMCs from RA patients between 5-azaC untreated group and treated group.

CpG sites	Untreated group	Treated group	*P*
-408	81%±18%	51%±13%	0.04
-387	81%±7%	63%±7.3%	0.015
-385	84%±3.5%	65%±5.9%	0.001
-355	92%±9.3%	73%±15.7%	0.141
-145	19%±4%	15%±3.2%	0.4

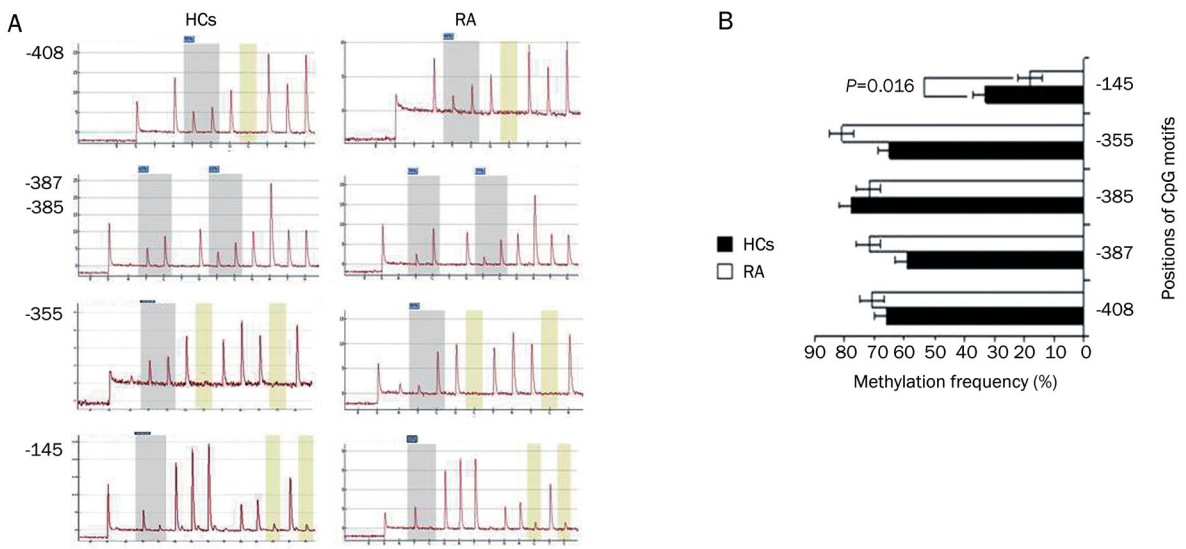

Figure 2. Comparison of the methylation statuses of individual CpG sites in the IL10 promoter in PBMCs isolated from healthy donors and patients with RA. (A) Pyrosequencing profile. (B) Bar graph obtained by independent-samples *t* test. The -145 CpG site showed a significant difference in methylation frequency between the HCs (*n*=20) and RA patients (*n*=20). Data were from 3 independent experiments and are expressed as the mean percentage of methylated CpG at each position in the IL10 promoter of the 20 HCs and 20 RA patients.

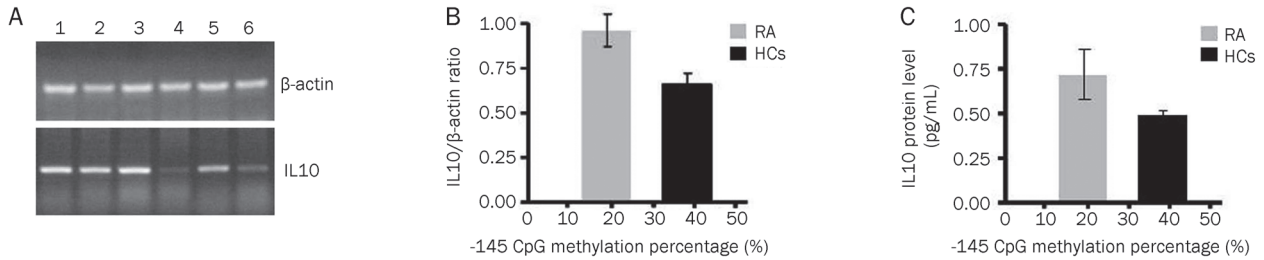

Figure 3. Comparison of the mRNA levels and -145 CpG methylation status of IL10 in PBMCs from RA patients and HCs. (A) IL10 mRNA expression. 1, 2, 3: RA patients; 4, 5, 6: HCs. Shown are the results from 3 representative subjects per group. (B) Correlation between -145 CpG methylation status and mRNA expression. (C) Correlation between -145 CpG methylation status and protein levels in serum. Seven milliliters of peripheral blood was collected from 20 RA patients and 20 healthy individuals, and approximately 5×10^6–7×10^6 PBMCs were isolated by Ficoll-Hypaque centrifugation. RNA was extracted using TRIzol reagent. The contents of IL10 in RA patients' serum and positive control from the kit were measured by ELISA according to the manufacturer's instructions. The methylation frequency of -145 CpG site was lower in PBMCs from RA (n=20) with higher IL10 mRNA and protein levels than HCs (n=20).

versus 72.00±7.12 pg/mL, P=0.012) were increased in the presence of 5-azaC, whereas the mRNA level of β-actin and TNFα remained constant. IL10 mRNA (1 *versus* 1.7084±1.8361, P=0.47) and protein expressions (1.4349±0.5887 pg/mL *versus* 3.275±2.0533 pg/mL, P=0.093) were increased after the control cells were treated with 5-azaC, but the difference was not significant.

Effects of methylation at IL10 CpG motifs on the binding of a transcription factor

There are at least three possible binding sites for CREB and C/EBP family members in the *IL10* promoter: one in upstream sequences at -408C and the others upstream of the promoter (-292 to -304 bp) or in the promoter region (-49 to -59 bp). ChIP assay results showed that the density of the *IL10* promoter and upstream promoter bands was significantly higher in the 5-azaC treated group than in the untreated group (Figure 4).

Discussion

In many murine models of RA, IL10 attenuated arthritis[5, 6]; however, the clinical improvement of RA patients was unstable[20]. Gene therapies have been attempted to overcome this defect. The treatment of a single joint by local delivery of the viral *IL10* gene may protect multiple joints of the same mice with CIA[21]. With regard to IL10 production, Im SH *et al* analyzed the *IL10* gene and showed that the promoter was highly conserved between humans and mice[22]. In the present study, we found one interspecies-conserved CRE within the promoter as well. Dong *et al*[8] analyzed the CpG methylation pattern of the *IL10* locus and detected two slightly demethylated CpGs in the proximal promoter in $IL10^+$ *vs* $IL10^-$ Th cells. They concluded that there was no correlation between methylation pattern and *IL10* expression. In contrast, our study revealed a significant methylation of p-CRE for IL10 production. Although we observed that upstream CpG motifs were highly methylated in both the patients and the HCs, the methylation levels of the -145 CpG site were lower than that of upstream CpG motifs in the patients and HCs and were much lower in the patients, whose *IL10* mRNA and serum levels were elevated. Furthermore, the lower methylation of -145C correlated with higher mRNA levels in RA. Thus, the hypomethylation of -145C may regulate gene expression at the transcriptional level and be responsible for the development of RA

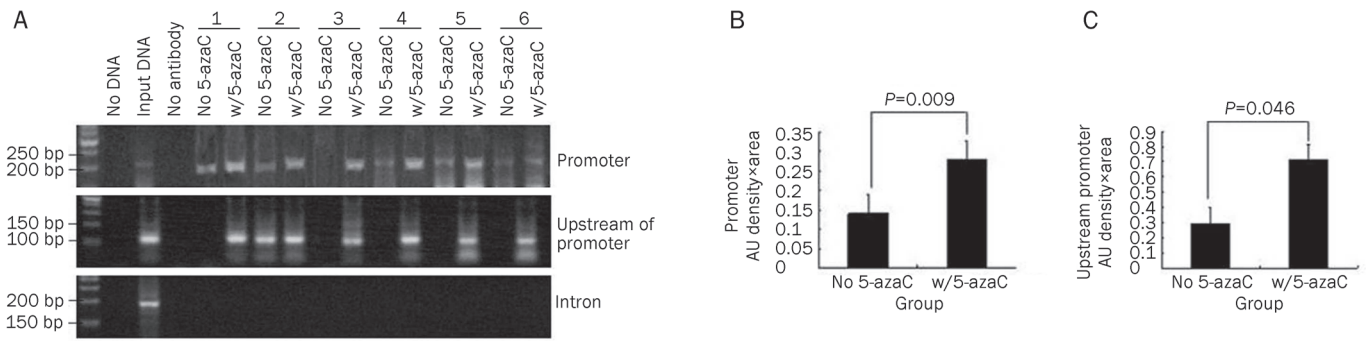

Figure 4. ChIP assays of the phospho-CREB binding within the IL10 promoter and upstream promoter region in PBMCs from the RA patients treated with or without 5-azaC. (A) ChIP assay results. Each sample has its own input DNA, and this picture displays the first sample only. (B) Relative levels of PCR products analyzed by Gel-pro analyzer software. Data stemmed from 3 independent experiments and are presented as the mean±SD of 6 RA patients. A paired-samples T test was performed. No 5-azaC: without 5-azaC treatment. w/5-azaC: with 5-azaC treatment.

in some people.

IL10 is produced mainly by monocytes, B cells, Th2, and Treg. PBMCs are a mixture of a variety of cells, including T cells, B cells, and monocytes. The cells in the peripheral blood interregulate each other's function through their secreted cytokines, which form a complicated network. Measuring the mRNA level of IL10 in PBMCs and the protein level in serum could reflect the general IL10 expression status and the interregulation among cells. In this study, we detected higher IL10 mRNA and protein levels in RA patients than in controls, which may be related to patients' varied disease activities and treatment statuses, and this finding is consistent with other reports in the field[23–25]. For example, Iwata *et al*[23] reported that the mean B10 + progenitor B10 (B10pro) cell frequencies were significantly higher in patients with RA compared with healthy controls. Additionally, IL10 production by blood B cells has been reported to be higher in patients with RA[24]. Sempere-Ortells *et al*[25] found increased IL10 and a higher proportion of CD4(+)IL10(+), CD4(+)CD25(int)IL10(+) cells in peripheral blood of patients with moderately active disease. Taken together, these findings suggested that during active disease, these cell subsets produce progressively larger amounts of IL10 to regulate inflammation in response to the activity of the disease. The demethylation of -145 CpG in the *IL10* promoter could elevate its mRNA expression, which may ameliorate the symptoms of RA. In this paper, we completed a preliminary study of the IL10 expression and promoter methylation status from the peripheral blood of RA patients. Further study is needed on the regulation mechanisms of all IL10-secreting cells after the separation and purification of individual cell lineages.

Nile *et al*[15] found that the differences identified between RA patients and healthy individuals could either be a primary phenomenon, implying that lower methylation at *IL6* -1099C is inversely correlated with development of RA or are secondary to the disease process or treatment. It was found in our study that lower methylation of *IL10* -145C might lead to similar results. Medications such as corticosteroids can alter lymphocyte trafficking and cause relative lymphopenia[26]. It is increasingly recognized that glucocorticoids change chromatin structure[27]. Glucocorticoids may lead to the deacetylation of histones, resulting in the tighter coiling of DNA and reduced access of transcription factors to their binding sites, thereby suppressing the activity of DNA methyltransferases. Methotrexate therapy has been associated with increased DNA methylation[28]. Participants in our study had not used any of these treatments or other immunosuppressants for 3 months before enrollment in the study. Ibuprofen, nimesulide and diclofenac sodium enteric-coated tablets were used to help patients reduce inflammation and pain, and these therapies have no effect on DNA methylation. DNA methyltransferase activity is proliferation dependent and cell cycle regulated[29, 30]. Thus, any therapy that affects proliferation and interferes with DNA methyltransferase activity may affect the status of DNA methylation, but further study is needed to confirm this. Prospective studies of patients with recent-onset RA will be required to elucidate the potential affects of drugs on DNA methylation.

Epigenetic alterations are reversible, providing new molecular targets for therapy. 5-azaC is an inhibitor of DNA methyltransferases. In this study, 5-azaC induced demethylation of the upstream and proximal CpG sites, and *IL10* mRNA expression increased in PBMCs of the patient. Thus, this experiment may contribute to overcoming the relative deficiency of IL10 in RA patients and be hopeful for changing RA progression. To test whether methylation of the CpG motifs can inhibit transcription factor binding, we performed ChIP assays. Several transcription factors, such as GRE, CREB, Sp1, and C/EBPs, can bind to the *IL10* promoter. It was reported that cAMP/CREB signaling was involved in *IL10* transcription in human monocytic cells[11], and C/EBP and CREB/ATF were activated as well. CREB, a member of the leucine zipper family of transcription factors, can be activated by phosphorylation at serine residue 133 (Ser-133) and further induces transcription of genes in response to the cAMP pathway. C/EBPs, another member of the leucine zipper family, contain at least six members (C/EBP alpha to C/EBP zeta). C/EBPβ has been shown to interact with CREB/ATF[31]. Therefore, an antibody specific for phospho-CREB can be combined with phospho-CREB-DNA and the CREB/ATF-C/EBPβ-DNA compound. Our results indicated that 5-azaC treatment increased CREB and/or C/EBPβ binding to the region upstream of the promoter and to the promoter region, which was consistent with demethylated CpGs and increased mRNA expression. -408C was contained in CREB and C/EBPβ binding sequences, and the result indicated its methylation inhibited CREB and C/EBPβ binding to the upstream promoter directly. All other CpG motifs were also demethylated (Table 1). Therefore, simultaneous demethylation of upstream and proximal CpG motifs in the *IL10* promoter may allow easier access for transcription factors to their binding sites, thus enhancing *IL10* transcription. Other transcription factors, aside from CREB, may participate in the regulation of the IL10 gene, such as STAT3[32], another transcription factor that binds near -145, NF-κB, and GRE. Whether the other transcription factors' binding activities are regulated by DNA methylation remains to be investigated.

Until now, there have been very limited data regarding the epigenetic regulation of genes in RA; only the methylation status of *DR3*[14] and *IL6*[15] was reported. The histone deacetylase activity in synovial tissues from patients with RA was approximately 2-fold lower than that in synovial tissues from patients with osteoarthritis or from normal controls[33]. A single intravenous injection of depsipeptide (FK228), a histone deacetylase inhibitor, inhibited joint swelling, synovial inflammation and subsequent bone and cartilage destruction in mice with autoantibody-mediated arthritis (AMA)[34]. The authors also found that intravenous treatment with FK228 induced the hyperacetylation of histone H3 and H4 in synovial cells. Furthermore, histone deacetylase inhibitor, trichostatin A (TSA), in combination with ultrasound, effectively reduces cell viability and induces apoptosis in the RASFs of RA patients[35].

Analysis of the genes that are epigenetically regulated in RA, taking into account not only DNA methylation but also histone modifications, is worth exploring.

In summary, we found that the proximal CpG motif -145C in the *IL10* promoter region was hypomethylated in RA PBMCs, which may regulate gene transcription and be responsible for the pathogenesis of RA. The demethylation of CpG motifs within the *IL10* promoter contributes to its overexpression; thus, demethylation may remedy the relative deficiency of IL10 in RA patients and may be a new therapeutic strategy in the treatment of RA.

Acknowledgements

Our sincere thanks go to Mr Jian-gang WEI, PhD candidate of Shandong University, China, for his proofreading of the paper. Our work is supported by the National Natural Science Foundation of China (grant 30770839) and the Hebei Province Natural Science Foundation of China (grant 30100154). We are grateful to the Second and Third Affiliated Hospitals of Hebei Medical University for recruiting the RA patient samples.

Author contribution

Bin CONG designed the study; Li-hong FU and Hai-ying CHEN performed the research; Chun-ling MA and Jing-ge ZHANG contributed new reagents or analytic tools; Li-hong FU and Shu-jin LI analyzed data; and Li-hong FU wrote the paper.

References

1 Choy EH, Panayi GS. Cytokine pathways and joint inflammation in rheumatoid arthritis. N Engl J Med 2001; 344: 907–16.
2 Keystone E, Wherry J, Grint P. IL-10 as a therapeutic strategy in the treatment of rheumatoid arthritis. Rheum Dis Clin North Am 1998; 24: 629–39.
3 Finnegan A, Kaplan CD, Cao Y, Eibel H, Glant TT, Zhang J. Collagen-induced arthritis is exacerbated in IL-10-deficient mice. Arthritis Res Ther 2003; 5: R18–24.
4 Johansson AC, Hansson AS, Nandakumar KS, Bäcklund J, Holmdahl R. IL-10-deficient B10.Q mice develop more severe collagen-induced arthritis, but are protected from arthritis induced with anti-type II collagen antibodies. J Immunol 2001; 167: 3505–12.
5 Dai Q, Li Y, Zhang F, Yu H, Wang X. Therapeutic effect of low-dose IL-18 combined with IL-10 on collagen-induced arthritis by down-regulation of inflammatory and Th1 responses and induction of Th2 responses. Rheumatol Int 2009; 29: 615–22.
6 Choi JJ, Yoo SA, Park SJ, Kang YJ, Kim WU, Oh IH, *et al*. Mesenchymal stem cells overexpressing interleukin-10 attenuate collagen-induced arthritis in mice. Clin Exp Immunol 2008; 153: 269–76.
7 Fitzpatrick DR, Wilson CB. Methylation and demethylation in the regulation of genes, cells, and responses in the immune system. Clin Immunol 2003; 109: 37–45.
8 Dong J, Ivascu C, Chang HD, Wu P, Angeli R, Maggi L, *et al*. IL-10 is excluded from the functional cytokine memory of human $CD4^+$ memory T lymphocytes. J Immunol 2007; 179: 2389–96.
9 Tsuji-Takayama K, Suzuki M, Yamamoto M, Harashima A, Okochi A, Otani T, *et al*. The production of IL-10 by human regulatory T cells is enhanced by IL-2 through a STAT5-responsive intronic enhancer in the IL-10 locus. J Immunol 2008; 181: 3897–905.
10 Gee K, Angel JB, Ma W, Mishra S, Gajanayaka N, Parato K, *et al*. Intracellular HIV-Tat expression induces IL-10 synthesis by the CREB-1 transcription factor through Ser133 phosphorylation and its regulation by the ERK1/2 MAPK in human monocytic cells. J Biol Chem 2006; 281: 31647–58.
11 Hu X, Paik PK, Chen J, Yarilina A, Kockeritz L, Lu TT, *et al*. IFN-gamma suppresses IL-10 production and synergizes with TLR2 by regulating GSK3 and CREB/AP-1 proteins. Immunity 2006; 24: 563–74.
12 Ishizu A, Abe A, Miyatake Y, Baba T, Iinuma C, Tomaru U, *et al*. Cyclic AMP response element-binding protein is implicated in IL-6 production from arthritic synovial cells. Mod Rheumatol 2010; 20: 134–8.
13 Richardson B, Scheinbart L, Strahler J, Gross L, Hanash S, Johnson M. Evidence for impaired T cell DNA methylation in systemic lupus erythematosus and rheumatoid arthritis. Arthritis Rheum 1990; 33: 1665–73.
14 Takami N, Osawa K, Miura Y, Komai K, Taniguchi M, Shiraishi M, *et al*. Hypermethylated promoter region of DR3, the death receptor 3 gene, in rheumatoid arthritis synovial cells. Arthritis Rheum 2006; 54: 779–87.
15 Nile CJ, Read RC, Akil M, Duff GW, Wilson AG. Methylation status of a single CpG site in the IL6 promoter is related to IL6 messenger RNA levels and rheumatoid arthritis. Arthritis Rheum 2008; 58: 2686–93.
16 Arnett FC, Edworthy SM, Bloch DA, McShane DJ, Fries JF, Cooper NS, *et al*. The American rheumatoid association 1987 revised criteria for the classification of rheumatoid arthritis. Arthritis Rheum 1988; 31: 315–24.
17 Mi XB, Zeng FQ. Hypomethylation of interleukin-4 and -6 promoters in T cells from systemic lupus erythematosus patients. Acta Pharmacol Sin 2008; 29: 105–12.
18 Loots GG, Ovcharenko I. rVISTA 2.0: evolutionary analysis of transcription factor binding sites. Nucleic Acids Res 2004; 32: W217–21.
19 Clark SJ, Harrison J, Paul CL, Frommer M. High sensitivity mapping of methylated cytosines. Nucleic Acids Res 1994; 22: 2990–7.
20 van Roon JA, Bijlsma JW, Lafeber FP. Suppression of inflammation and joint destruction in rheumatoid arthritis may require a concerted action of Th2 cytokines. Curr Opin Investig Drugs 2002; 3: 1011–6.
21 Whalen JD, Lechman EL, Carlos CA, Weiss K, Kovesdi I, Glorioso JC, *et al*. Adenoviral transfer of the viral IL10 gene periarticularly to mouse paws suppresses development of collagen-induced arthritis in both injected and uninjected paws. J Immunol 1999; 162: 3625–32.
22 Im SH, Hueber A, Monticelli S, Kang KH, Rao A. Chromatin-level regulation of the IL10 gene in T cells. J Biol Chem 2004; 279: 46818–25.
23 Iwata Y, Matsushita T, Horikawa M, Dilillo DJ, Yanaba K, Venturi GM, *et al*. Characterization of a rare IL-10-competent B-cell subset in humans that parallels mouse regulatory B10 cells. Blood 2011; 117: 530–41.
24 Llorente L, Richaud-Patin Y, Fior R, Alcocer-Varela J, Wijdenes J, Fourrier BM, *et al*. *In vivo* production of interleukin-10 by non-T cells in rheumatoid arthritis, Sjogren's syndrome, and systemic lupus erythematosus: a potential mechanism of B lymphocyte hyperactivity and autoimmunity. Arthritis Rheum 1994; 37: 1647–55.
25 Sempere-Ortells JM, Pérez-García V, Marín-Alberca G, Peris-Pertusa A, Benito JM, Marco FM, *et al*. Quantification and phenotype of regulatory T cells in rheumatoid arthritis according to disease activity score-28. Autoimmunity 2009; 42: 636–45.
26 Xu J, Winkler J, Sabarinath SN, Derendorf H. Assessment of the impact of dosing time on the pharmacokinetics/pharmacodynamics of prednisolone. AAPS J 2008; 10: 331–41.
27 Archer TK, Deroo BJ, Fryer CJ. Chromatin modulation of glucocorticoid and progesterone receptor activity. Trends Endocrinol Metab 1997; 8:

384–90.

28 Kim YI, Logan JW, Mason JB, Roubenoff R. DNA hypomethylation in inflammatory arthritis: reversal with methotrexate. J Lab Clin Med 1996; 128: 165–72.

29 Issa JP, Vertino PM, Wu J, Sazawal S, Celano P, Nelkin BD, *et al*. Increased cytosine DNA-methyltransferase activity during colon cancer progression. J Natl Cancer Inst 1993; 85: 1235–40.

30 Robertson KD, Keyomarsi K, Gonzales FA, Velicescu M, Jones PA. Differential mRNA expression of the human DNA methyltransferases (DNMTs) 1, 3a and 3b during the G_0/G_1 to S phase transition in normal and tumor cells. Nucleic Acids Res 2000; 28: 2108–13.

31 Ramji DP, Foka P. CCAAT/enhancer-binding proteins: structure, function and regulation. Biochem J 2002; 365: 561–75.

32 Benkhart EM, Siedlar M, Wedel A, Werner T, Ziegler-Heitbrock HW. Role of Stat3 in lipopolysaccharide-induced IL-10 gene expression. J Immunol 2000; 165: 1612–7.

33 Huber LC, Brock M, Hemmatazad H, Giger OT, Moritz F, Trenkmann M, *et al*. Histone deacetylase/acetylase activity in total synovial tissue derived from rheumatoid arthritis and osteoarthritis patients. Arthritis Rheum 2007; 56: 1087–93.

34 Nishida K, Komiyama T, Miyazawa S, Shen ZN, Furumatsu T, Doi H, *et al*. Histone deacetylase inhibitor suppression of autoantibody-mediated arthritis in mice via regulation of p16INK4a and $p21^{WAF1/Cip1}$ expression. Arthritis Rheum 2004; 50: 3365–76.

35 Nakamura C, Matsushita I, Kosaka E, Kondo T, Kimura T. Anti-arthritic effects of combined treatment with histone deacetylase inhibitor and low-intensity ultrasound in the presence of microbubbles in human rheumatoid synovial cells. Rheumatology (Oxford) 2008; 47: 418–24.

Acta Pharmacologica Sinica (2011) 32: 1381–1386
 1671-4083/11 $32.00
www.nature.com/aps

Original Article

Association of two polymorphisms within and near *SOCS3* gene with obesity in three nationalities in Xinjiang province of China

Wei TANG[1], Jun-jie ZOU[1], Xiang-fang CHEN[1], Jiao-yang ZHENG[1], Hua-zong ZENG[2], Zhi-min LIU[1, *], Yong-quan SHI[1, *]

[1]*Department of Endocrinology, Changzheng Hospital, Second Military Medical University, Shanghai 200003, China;* [2]*School of Life Science and Technology, Tongji University, Shanghai 200003, China*

Aim: *SOCS3* gene plays an important role in the pathogenesis of obesity in animal models, but the data from human studies are relatively limited. To address this issue, a genetic association analysis on nationalities with different genetic background living in the similar environmental conditions was performed.

Methods: Two thousand seven hundred eleven subjects were randomly recruited from the Kazakh, Uygur and Han nationalities in Xinjiang of China. SNP polymorphisms rs4969168 and rs9892622 within or near the *SOCS3* gene were genotyped using TaqMan-MGB™ assay. Association study between the two polymorphisms and obesity-related traits (body mass index [BMI]; waist-to-hip ratio [WHR]; weight; height, WAIST, and HIP measurements) was conducted.

Results: Significant association was found between rs4969168 and the obesity-related traits, including BMI (25.32±3.49 kg/m^2 for AA, 24.60±3.70 kg/m^2 for AG, 24.39±3.42 kg/m^2 for GG, P=0.042), weight (65.58±11.42 kg for AA, 63.50±11.30 kg for AG, 62.00±10.78 kg for GG, P=0.011) in the Han nationality, but not in the Kazakh or Uygur nationalities. Rs9892622 was significantly associated with BMI, WHR, and WAIST in the Uygur males. Rs9892622 was also associated with BMI in Kazakh males. Linear regression analysis verified the above findings. However, neither of the two polymorphisms was associated with obesity-related traits in the total population.

Conclusion: The polymorphism rs4969168 within or near the *SOCS3* gene has a significant effect in the Han nationality, while rs9892622 was associated with obesity in Uygur and Kazakh nationalities in Xinjiang of China.

Keywords: obesity; *SOCS3*; polymorphisms; rs4969168; rs9892622; China nationality

Acta Pharmacologica Sinica (2011) 32: 1381–1386; doi: 10.1038/aps.2011.84; published online 5 Sep 2011

Introduction

Obesity is a major public health problem worldwide and affects individuals across all age groups and ethnicities[1]. According to the World Health Organization (WHO), there are up to one billion overweight individuals worldwide, of which 300 million would be classified as clinically obese (www.who.int). Moreover, the situation in most developed countries is more severe. Obesity is a leading risk factor for many health problems such as heart disease, type 2 diabetes and most cancers[2]; furthermore, it accounts for up to 7.8% of the total health care expense in developed countries[3]. Numerous studies have attempted to illustrate the pathogenesis of obesity.

A multitude of genes associated with obesity have been discovered, with one of the most important being *SOCS3* (suppressor of cytokine signaling 3), which is located in the chromosome region 17q24-17q25. *SOCS3* works as a feedback inhibitor for a range of cytokine signals and inhibits the function of leptin and downstream steps in the insulin signaling pathway to regulate energy balance[4–7]. Although this function has been confirmed in animal models, the association data from human studies are relatively limited. Talbert *et al* have shown that the *SOCS3* gene is related to body mass index (BMI), visceral adipose (VAT), and waist circumference (WAIST) in Hispanic families[8]. However, in the study performed by Jamshidi *et al*[9] on the association analyses of common polymorphisms (rs4969169, rs12953258, and rs8064821) in *SOCS3* between two normal female twins that examined body weight, insulin sensitivity or lipid profile, none of the three polymorphisms were found to be associated with obesity. In addition, the study on the association analysis of two polymorphisms in the coding sequence and promoter region of the

*To whom correspondence should be addressed.
E-mail zmliu_yz@hotmail.com (Zhi-min Liu);
young.stone@163.com (Yong-quan Shi)
Received 2011-01-07 Accepted 2011-05-09

SOCS3 gene (including -920 C>A (rs12953258) and -1044 C>A) in German children and adolescents with extreme obesity suggested that no association was observed[10].

This report focuses on the association between the *SOCS3* gene and obesity-related traits in the Kazak, Uygur and Han nationalities from the Xinjiang province of China. Two SNP polymorphisms were selected according to the data from tag-polymorphisms of the HapMap project and previous studies[11, 12]. One polymorphism is the A+930→G (rs4969168) polymorphism that is located in the 3′UTR of the *SOCS3* gene, which is a haplotype tagging SNP (htSNP) that sufficiently covers the genetic variation of the entire gene. The other SNP selected for this study is rs9892622 A→G, a high-frequency variant near the gene, which is located in the upstream promoter region of the *SOCS3* gene and appears to be a reasonable functional candidate for the *SOCS3* locus and obesity.

Materials and methods

Subjects

Subjects (n=2711) were recruited from three races of Xinjiang in China. All subjects passed the normal medical examination and were selected randomly, including 1045 Kazakh, 804 Uygur and 862 Han individuals within the age range of 19–87 years old. The local ethics committee approved the study, and all participants provided informed consent. Standing height (height) was measured (to the nearest 0.01 m) with a stadiometer. Body weight (weight) was measured (to the nearest 0.01 kg) with a weighing machine. Body mass index (BMI) was calculated as the weight in kilograms divided by the square of the height in meters. Lastly, waist circumference (WAIST), hip circumference (HIP), and waist to hip ratio (WHR) were determined as previously described[13].

DNA preparation

Genomic DNA was extracted from peripheral blood leukocytes of all samples by the phenol-chloroform nucleic acid extraction method. The genomic DNA concentrations of samples were measured by using a NanoDrop Spectrophotometer (Thermo Fisher, Boston, MA, USA) and were qualified for analysis when the ratio of wavelengths 260/280 ranged between 1.7–2.0. Next, genomic DNA samples were diluted to 10 ng/μL as the working concentration.

Polymorphisms selection and genotyping

Two SNP variants rs4969168 and rs9892622 were selected. Rs4969198 was selected as a tagSNP to cover all of the related polymorphisms on *SOCS3* that are based on the recently released HapMap data. Because common variants are susceptible to common diseases, we chose another potential functional locus with a relatively high frequency, rs9892622, in the promoter region of *SOCS3*. Genotyping was performed using the 5′-nuclease TaqMan-MGB^{TM} assay in 384-well plates and the ABI PRISM 7900HT Sequence Detection system (Applied Biosystems, Foster City, CA, USA). The raw data were read at the end-point and were clustered into three groups that represented the three genotypes.

Statistical analysis

The data were analyzed with SPSS (version 13.0). Before any other analysis, the maximum likelihood estimate of allele frequencies was tested for departures from Hardy-Weinberg Equilibrium proportions (HWE) using a chi-squared goodness of fit test to make sure that there were no typing errors or bias from population structure. The distribution of obesity-related quantitative traits (BMI, height, weight, WHR, WAIST and HIP), characteristic variants (age, gender, *etc*) and genotypes among the three nationalities were analyzed by one-way ANOVA with SNK test. A *t*-test (independent samples) was used to investigate the distribution of variants in different genders. Stratified analysis by nationality and gender was performed to explore the interaction between environmental and genetic factors. Additionally, linear regression analysis was used to determine the importance of obesity-related traits. To avoid over-correction induced by measuring too many obesity-related traits, only the variants of age, nationality, gender and genotypes were involved in the regression analysis. The *P*-value confidence level was set at 0.05 for the above tests.

Results

Sample characteristics

After removing samples with missing data, a total population with n=2667 samples was left, which comprised the three races, Kazakh, Uygur and Han; the number of samples from each race and their percentage of the total sample population were 1017 (38.14%), 798 (29.92%), and 852 (31.94%), respectively. The distribution of sample characteristics (mean±SD of obesity-related traits and distribution of genotypes of SNP polymorphisms) in each nationality are displayed in Table 1. The statistical differences of these variants among nationalities were determined by the Fisher LSD test. The data showed that all of the variants (age, BMI, weight, height, WHR, WAIST, HIP, rs4969168, and rs9892622) were statistically different among the three nationalities and indicated that analysis of the interaction of gene polymorphisms and environmental factors in a total population would be inappropriate; rather, a separate analysis of the effects of interaction within individual populations of each nationality would be more appropriate.

The distribution of variants, except polymorphisms, in different genders was also statistically analyzed by independent samples in a *t*-test (Table 2). It was found that the variants, except WHR, were significantly different between males and females. The distributions of genotypic polymorphisms in different genders were analyzed by a χ^2 square test; no difference was found in the genotypic frequencies between genders, which indicated that no typing bias or error existed.

Genotyping and allele frequencies

The genotyping success rates of both rs4969168 and rs9892622 were 97.4%. The allele frequencies of *SOCS3* rs4969168 and rs9892622 for the total population and each subpopulation (classified by race) were collected (Table 1). In the Kazakh, Uygur and Han subpopulations, the allele frequencies of rs4969168 were 0.582, 0.625, and 0.572, respectively, and the

Table 1. Sample characteristics.

	Total (2658)	Kazakh (1016)	Uygur (798)	Han (844)	*P*
Gender (M/F)	1062/1596	434/582	294/504	334/510	0.039
Age	50.86±11.52	47.9±10.5	52.7±10.3	52.6±12.9	<0.001
BMI (kg/m^2)	25.68±4.19	25.64±4.18	26.77±4.54	24.67±3.56	<0.001
Weight (kg)	1.61±0.09	68.64±13.07	67.90±12.76	63.48±11.16	<0.001
Height (m)	66.76±12.59	1.63±0.09	1.59±0.08	1.60±0.08	<0.001
WHR (cm/cm)	0.880±0.073	0.90±0.73	0.88±0.08	0.87±0.07	<0.001
WAIST (cm)	86.57±11.98	91.95±12.59	88.15±11.69	82.64±10.59	<0.001
HIP (cm)	98.26±9.51	102.21±10.09	100.50±9.43	94.37±7.75	<0.001
rs4969168 (*n*/%)	2597	996 (100)	787 (100)	815 (100)	0.001
AA	415 (16.0)	159 (16.0)	115 (14.6)	142 (17.4)	
AG	1301 (50.1)	514 (51.6)	360 (45.7)	427 (52.4)	
GG	881 (33.9)	323 (32.4)	312 (39.6)	246 (30.2)	
rs9892622 (*n*/%)	2598 (100)	990 (100)	778 (100)	830 (100)	0.009
AA	555 (21.4)	294 (29.7)	198 (25.4)	238 (28.7)	
AG	1313 (50.5)	495 (50.0)	384 (49.4)	434 (52.3)	
GG	730 (28.1)	201 (20.3)	196 (25.2)	158 (19.0)	

Different population sizes between some variants and total were due to different samples of missing data, which was the incomplete data for rs4969168 or rs9892622. The missing data was excluded with default settings during the analyses.

Table 2. Distribution of variants in different genders.

	Male	Female	*P*
Age	52.70±11.7	49.63±11.21	0.004
BMI	25.39±3.83	25.86±4.40	<0.001
WHR	0.89±0.07	0.87±0.07	<0.001
Weight	71.40±12.22	63.71±11.89	<0.001
WAIST	87.60±11.92	85.95±11.98	0.003
Height	1.68±0.07	1.57±0.06	<0.001
HIP	97.75±9.39	98.56±9.58	0.064
rs4949168	1062 (100%)	1596 (100%)	0.639
AA	158 (14.9%)	256 (16.0%)	
AG	529 (49.8%)	769 (48.2%)	
GG	350 (33.0%)	528 (33.1%)	
Missing[a]	25 (2.3%)	43 (2.7%)	
rs9892622	1062 (100%)	1596 (100%)	0.405
AA	304 (28.6%)	424 (26.6%)	
AG	515 (48.5%)	793 (49.7%)	
GG	212 (20.0%)	342 (21.4%)	
Missing[a]	31 (2.9%)	37 (2.3%)	

[a] Missing value was the number of population with incomplete data for rs4969168 or rs9892622, and it was excluded with default settings during the analyses.

allele frequencies of rs9892622 were 0.453, 0.499, and 0.452, respectively. There was no departure from the Hardy-Weinberg equilibrium in any of the groups (P>0.05). One-way ANOVA was used to determine that the distribution of polymorphisms was statistically different among the three nationalities.

Association of the *SOCS3* gene with obesity-related quantitative traits

Overall analysis

The association of the two polymorphisms (rs4969168 and rs9892622) with BMI, WHR, height, weight, WAIST, and HIP was determined by one-way ANOVA with SNK test, but no evidence of association was found between each of the two polymorphisms and the above quantitative traits in the total population.

Stratified analysis of nationality

Because obesity is due to the interaction of environmental and genetic factors and the above data showed differences between nationalities or gender regarding obesity-related traits, it was supposed that environmental background, race, gender or age might have a significant interaction with the polymorphisms, which may lead to obesity or related traits. Therefore, stratified analysis was performed based on the interaction between nationalities and polymorphisms. Although no significant difference was observed among the three genotypes of rs4969168 in the total population, the data indicated that a remarkable difference existed within the subpopulations (Table 3 and 4). Significant differences were found in the mean of BMI, weight, and WAIST among the pair-wise comparison of the genotypes of rs4969168. Although most compared pairs were not found to be statistically significant, there were noticeable trends (Table 3). Based on the data from the Han group, as the frequency of the G allele increased, the BMI, weight and WAIST measurements decreased, which suggests that the G allele may play a role in maintaining a reduced body weight in the Han group. However, the opposite trend was seen in the Kazakh

Table 3. Mean of BMI, Weight, WAIST and WHR of each genotype of rs4969168 in each nationality.

rs4969168	Genotype (%)	BMI	Weight	WAIST	WHR
Kazakh	GG (32.4)	25.70±4.21	68.75±12.83	93.30±11.77	0.91±0.08
	AG (51.6)	25.62±4.25	68.88±13.38	91.74±12.58	0.90±0.07
	AA (16.0)	25.51±3.91	67.73±12.51	89.22±14.01	0.88±0.08
Uygur	GG (39.6)	26.75±4.55	68.04±12.72	88.40±11.49	0.88±0.08
	AG (45.7)	26.77±4.63	67.76±13.02	87.84±12.06	0.88±0.07
	AA (14.6)	26.95±4.31	68.25±12.45	88.71±11.01	0.87±0.07
Han	GG (30.2)	24.39±3.42	62.00±10.78	82.11±9.90	0.87±0.07
	AG (52.5)	24.60±3.70	63.50±11.30	82.46±11.03	0.87±0.07
	AA (17.3)	25.32±3.49	65.58±11.42	84.18±10.32	0.88±0.06

Table 4. *P*-value of pairwised comparison among genotypes of rs4969168.

rs4969168		BMI	Weight	WAIST	WHR
Kazakh	Total	0.900	0.622	0.078	0.115
	Male	0.486	0.362	0.363	0.277
	Female	0.617	0.630	0.094	0.242
Uygur	Total	0.925	0.924	0.763	0.732
	Male	0.907	0.695	0.663	0.965
	Female	0.996	0.946	0.917	0.503
Han	Tatal	**0.042**	**0.011**	0.361	0.157
	Male	0.044	0.054	0.260	0.752
	Female	0.361	0.352	0.957	0.712

Table 6. *P*-value of pairwised comparison among genotypes of rs9892622.

rs9892622		BMI	WEIGHT	WAIST	WHR
Kazakh	Total	0.058	0.169	0.072	0.137
	Male	**0.025**	0.075	0.143	0.151
	Female	0.535	0.454	0.338	0.471
Uygur	Total	0.852	0.842	0.336	0.594
	Male	**0.049**	**0.040**	0.103	**0.045**
	Female	0.072	0.137	0.310	0.774
Han	Tatal	0.249	0.364	0.919	0.672
	Male	0.549	0.853	0.775	0.905
	Female	0.285	0.379	0.939	0.585

group but not in the Uygur group. The potential cause of this trend will be further covered in the latter part of the discussion.

For rs9892622, a significant difference for obesity-related traits was not observed in the total population. Statistically meaningful results only appeared in the male subpopulation of the Uygur group, but no obvious trend could be summarized from the datasets (Table 5 and 6).

Linear regression analysis

Linear regression analysis confirmed the previous results in which nationality and gender were included, but age and the two polymorphisms excluded, in the model with $P<0.05$. In the following stratified analysis by nationality or gender, the two polymorphisms were also included with $P<0.05$, but age was excluded from the model. Because nationality seemed to be the most effective factor in our data, we performed a linear regression analysis for each nationality. In the Han population, gender was the first factor involved in the regression ($P=0.004$), followed by rs4969168 ($P=0.015$).

Discussion

With the release of data from the HapMap phase III project and completion of several whole genome association studies

Table 5. Mean of BMI, Weight, WAIST, and WHR of each genotype of rs9892622 in each nationality.

rs9892622	Genotype (%)	BMI	Weight	WHR	WAIST
Kazakhi	GG (20.3)	25.20±3.94	67.23±12.11	0.88±0.06	89.49±12.13
	AG (50.0)	25.96±4.18	69.31±13.09	0.91±0.08	92.82±12.80
	AA (29.7)	25.41±4.35	68.45±13.61	0.90±0.07	92.56±12.65
Uygur	GG (25.2)	26.91±5.15	67.75±13.58	0.87±0.08	87.98±12.42
	AG (49.4)	26.70±4.16	68.10±12.06	0.88±0.08	87.80±11.47
	AA (25.4)	26.69±4.63	67.45±13.39	0.88±0.07	88.85±11.56
Han	GG (19.0)	24.24±3.49	62.30±11.10	0.87±0.07	81.96±10.80
	AG (52.3)	24.78±3.60	63.70±11.39	0.87±0.07	82.83±11.01
	AA (28.7)	24.75±3.56	63.72±10.70	0.87±0.07	82.46±9.70

on several common diseases, scientists realized that tagSNPs in target genes could be selected as candidate loci to cover all of the polymorphisms involved in the haploblocks of the target gene.

SOCS3 is one of several genes involved in cytokine signaling and regulates the function of proteins downstream, inhibits the insulin signaling pathway and stimulates the upregulation of TNFα in adipose tissue[14]. The protein encoded by *SOCS3* is also important in energy balance and regulation[4–7]. This result has been confirmed in animal models, but the association data in humans have been relatively limited. Research by Talbert *et al* has shown that the *SOCS3* gene is related to body mass index (BMI), visceral adipose (VAT), and waist circumference (WAIST) in Hispanic families[8]. However, in a study reported by Jamshidi[9] on the association analyses of common polymorphisms (rs4969169, rs12953258 and rs8064821) in *SOCS3* with body weight, insulin sensitivity or lipid profile in normal female twins, none of these three polymorphisms was found to be associated with obesity. In a previous study, an association analysis of two polymorphisms (-920 C>A (rs12953258) and -1044 C>A) was performed, one in the coding sequence and another in the promoter region, in the *SOCS3* gene in German children and adolescents with extreme obesity[10]. As a result, there was no association observed between the two polymorphisms in *SOCS3* and extreme obesity. Weight is a complex phenotype that is affected by several biological pathways; the most important two pathways are the neural control system of food intake and energy balance regulation. Thus, one explanation to these ambivalent results is that the pathogeny of obesity differs among populations.

Another potential explanation is that different haploblock distributions appear in different ethnic groups or in different nationalities. Consequently, pathogenic loci linked to tagSNPs can be partially or totally different, and in some cases, special ethnic tagSNPs would lose their ability of catching pathogenic loci in other ethnic studies, which seems to have happened in our study. Our data suggest that there is no association between rs4969168 and obesity-related traits in the total population (P>0.05). However, a significant association was observed for BMI and weight in the Han population and male subgroup, which indicates that the polymorphism rs4969168 seems to have a different association effect on different nationalities and different genders. In addition, the data showed that the allele A of rs4969168 was associated with increased BMI and weight in the Han group. Moreover, the population with the AA genotype of rs4969168 is more susceptible to weight-gain in the Han population, especially in males. However, a totally opposite result was discovered in the Kazakh population, which indicates that the mechanisms may likely be distinct between these two nationalities. Our results are reasonable given that *SOCS3* serves as both a pivotal and hub function in a complex regulatory system, which further suggests that *SOCS3* may also play a dual role in weight control.

Similar to rs4969168, there was no evidence for an association between rs9892622 and obesity-related traits in the total population, but a significant association appeared in the stratified analysis. Interestingly, distinct from rs4969168, rs9892622 was associated with BMI, weight and WAIST in the Kazakh and Uygur populations rather than the Han population.

In conclusion, whether weight control is attributed to different pathogenic factors or the distribution of ethnic haploblocks, the genetic background seems to certainly play a basic role. According to our current data, both rs4969168 and rs9892622 are associated with obesity, and the association effect is different according to nationality and gender. Further study is required to fine-map the pathogenic loci and discover the functional impact of *SOCS3* in obesity.

Acknowledgements

This study was supported by the Science and Technology Commission of the Shanghai Municipality (No 08DJ1400604 and 10ZR1439400).

Author contribution

Wei TANG designed the research, executed the experiments and wrote the paper; Yong-quan SHI and Zhi-min LIU designed the research and wrote the paper; Jun-jie ZOU and Jiao-yang ZHENG contributed analytic tools; and Xiang-fang CHEN and Hua-zong ZENG analyzed the data.

References

1 Marvelle AF, Lange LA, Qin L, Adair LS, Mohlke KL. Association of FTO with obesity-related traits in the Cebu Longitudinal Health and Nutrition Survey (CLHNS) Cohort. Diabetes 2008; 57: 1987–91.
2 Mori MA, Araújo RC, Reis FC, Sgai DG, Fonseca RG, Barros CC, *et al*. Kinin B1 receptor deficiency leads to leptin hypersensitivity and resistance to obesity. Diabetes 2008; 57: 1491–500.
3 Hill JO, Wyatt HR, Reed GW, Peters JC. Obesity and the environment: where do we go from here? Science 2003; 299: 853–5.
4 Coppari R, Ichinose M, Lee CE, Pullen AE, Kenny CD, McGovern RA, *et al*. The hypothalamic arcuate nucleus: a key site for mediating leptin's effects on glucose homeostasis and locomotor activity. Cell Metab 2005; 1: 63–72.
5 Howard JK, Flier JS. Attenuation of leptin and insulin signaling by SOCS proteins. Trends Endocrinol Metab 2006; 17: 365–71.
6 Lebrun P, Van Obberghen E. SOCS proteins causing trouble in insulin action. Acta Physiol (Oxf) 2008; 192: 29–36.
7 Münzberg H, Myers MG Jr. Molecular and anatomical determinants of central leptin resistance. Nat Neurosci 2005; 8: 566–70.
8 Talbert ME, Langefeld CD, Ziegler J, Mychaleckyj JC, Haffner SM, Norris JM, *et al*. Polymorphisms near SOCS3 are associated with obesity and glucose homeostasis traits in Hispanic Americans from the Insulin Resistance Atherosclerosis Family Study. Hum Genet 2009; 125: 153–62.
9 Jamshidi Y, Snieder H, Wang X, Spector TD, Carter ND, O'Dell SD. Common polymorphisms in SOCS3 are not associated with body weight, insulin sensitivity or lipid profile in normal female twins. Diabetologia 2006; 49: 306–10.
10 Hölter K, Wermter AK, Scherag A, Siegfried W, Goldschmidt H, Hebebrand J, *et al*. Analysis of sequence variations in the suppressor of cytokine signaling (SOCS)-3 gene in extremely obese children and adolescents. BMC Med Genet 2007; 8: 21.
11 Fischer-Rosinsky A, Fisher E, Kovacs P, Blüher M, Möhlig M, Pfeiffer AF, *et al*. Lack of association between the tagging SNP A+930-->G of SOCS3 and type 2 diabetes mellitus: meta-analysis of four

independent study populations. PLoS One 2008; 3: e3852.
12 Gylvin T, Nolsøe R, Hansen T, Nielsen EM, Bergholdt R, Karlsen AE, *et al*. Mutation analysis of suppressor of cytokine signalling 3, a candidate gene in Type 1 diabetes and insulin sensitivity. Diabetologia 2004; 47: 1273–7.
13 Cecil JE, Tavendale R, Watt P, Hetherington MM, Palmer CN. An obesity-associated FTO gene variant and increased energy intake in children. N Engl J Med 2008; 359: 2558–66.
14 Emanuelli B, Peraldi P, Filloux C, Chavey C, Freidinger K, Hilton DJ, *et al*. SOCS-3 inhibits insulin signaling and is up-regulated in response to tumor necrosis factor-alpha in the adipose tissue of obese mice. J Biol Chem 2001; 276: 47944–9.

Acta Pharmacologica Sinica (2011) 32: 1387–1396
 1671-4083/11 $32.00
www.nature.com/aps

Original Article

Platinum-(IV)-derivative satraplatin induced G_2/M cell cycle perturbation via p53-p21$^{waf1/cip1}$-independent pathway in human colorectal cancer cells

Murugan KALIMUTHO[1, *, §], Antonella MINUTOLO[2, 3], Sandro GRELLI[2, 3], Giorgio FEDERICI[1], Sergio BERNARDINI[1]

[1]Department of Internal Medicine, University of Rome "Tor Vergata", Rome, Italy; [2]Department of Experimental Medicine and Biochemical Sciences, University of Rome "Tor Vergata", Rome, Italy; [3]Department of Laboratory Medicine, "UOC Clinical Microbiology", University Hospital Tor Vergata, Rome, Italy

Aim: Platinum-(IV)-derivative satraplatin represents a new generation of orally available anti-cancer drugs that are under development for the treatment of several cancers. Understanding the mechanisms of cell cycle modulation and apoptosis is necessary to define the mode of action of satraplatin. In this study, we investigate the ability of satraplatin to induce cell cycle perturbation, clonogenicity loss and apoptosis in colorectal cancer (CRC) cells.

Methods: CRC cells were treated with satraplatin, and the effects of satraplatin on apoptosis and the cell cycle were evaluated by flow cytometry. Western blot analysis was used to investigate the effects of satraplatin on cell cycle and apoptosis-related proteins. RT-qPCR was used to evaluate p53-related mRNA modulation.

Results: Satraplatin induced an accumulation of CRC cells predominantly in the G_2/M phase. Increased p53 protein expression was observed in the p53 wild-type HCT116 and LoVo cells together with p21$^{waf1/cip1}$ protein up-regulation. However, p21$^{waf1/cip1}$ protein accumulation was not observed in the p53 mutant HCT15, HT29, and WiDr cells, even when p53 protein expression was compromised, suggesting that the cell cycle perturbation is p53-p21$^{waf1/cip1}$ independent. Following a candidate approach, we found an elevated expression of 14-3-3σ protein levels in CRC cells, which was independent of the status of p53, further supporting the role of satraplatin in the perturbation of the G_2/M cell cycle phase. Moreover, satraplatin treatment induced apoptosis along with Bcl-2 protein down-regulation and abrogated the clonogenic formation of CRC cells *in vitro*.

Conclusion: Collectively, our data suggest that satraplatin induces apoptosis in CRC cells, which is preceded by cell cycle arrest at G_2/M due to the effect of 14-3-3σ and in a p53-p21$^{waf1/cip1}$–independent manner. Taken together, these findings highlight the potential use of satraplatin for CRC treatment.

Keywords: satraplatin; G_2/M phase; 14-3-3σ; p53; apoptosis; colorectal cancer

Acta Pharmacologica Sinica (2011) 32: 1387–1396; doi: 10.1038/aps.2011.107; published online 19 Sep 2011

Introduction

The formation of DNA adducts by platinum analogs is recognized to be the most prominent effects in cells, blocking replication and transcription and inducing tumor cell death[1, 2]. The nature of the DNA adducts formed by these analogs affects a number of transduction pathways and triggers apoptosis and necrosis[3], thereby mediating cytotoxicity in these models. The most studied platinum analogs, cisplatin and oxaliplatin, have been used in the clinic for the treatment of various tumors[4], yet the acquisition of drug resistance remains a major obstacle in cancer management. Among the numerous platinum analogs, satraplatin has been shown to counteract *de novo* resistance and acquired resistance in some resistant human tumors[5, 6].

Satraplatin, also known as JM-216, is the first orally available active lipophilic platinum (Pt)-(IV) derivative that exhibits antiproliferative activity against various tumors[5, 6]. This drug is particularly attractive because of its convenience of administration, its milder toxicities (such as nephrotoxicity, neurotoxicity, and ototoxicity) and the lack of cross-resistance with cisplatin. Moreover, satraplatin demonstrates anti-cancer activity in tumors that are usually non-responsive to platinum drugs[7].

Upon diverse genotoxic stresses, DNA damage and other

§ Now in *Centre for Cancer Research and Cell Biology (CCRCB), Queen's University of Belfast, Northern Ireland, UK.*
* To whom correspondence should be addressed.
E-mail mceric_rugan@hotmail.com
Received 2011-04-19 Accepted 2011-06-29

cellular lesions usually activate cell cycle checkpoints that inhibit cell cycle progression by decreasing the activity of key regulatory proteins[8], primarily including cyclin-dependent kinase (Cdk) complexes[9, 10]. After DNA damage signaling, the "p53 → $p21^{waf1/cip1}$ pathway" is activated[9, 10]. Activated p53 induces the expression of its downstream targets, including $p21^{waf1/cip1}$, which is a universal inhibitor of Cdks and is required to arrest cells at the G_1 and G_2 checkpoints[11–13]. The cells are then arrested at the G_1-S or G_2/M phase. We have previously reported cell cycle perturbation following satraplatin and oxaliplatin treatment in a panel of CRC cell lines that differ in their p53 gene status[14]. We observed that satraplatin induces cell cycle arrest at the G_2/M phase and that oxaliplatin induces arrest at the G_1 phase and results in apoptosis. On the basis of this observation, we proposed that satraplatin is a remarkably more potent activator of cell cycle and cell death proteins than oxaliplatin. We speculate that the perturbation of the G_2/M cell cycle phase may be a prominent effect of satraplatin treatment in CRC cells. Additionally, we demonstrate that p53-null cells, which are arrested in the same manner as wild-type cells, subsequently induce apoptosis with satraplatin treatment but not with oxaliplatin treatment.

The aim of this study was to elucidate the effect of satraplatin on modulators of the G_2/M cell cycle transition, apoptosis, and clonogenic formation. We show that satraplatin induces cell cycle arrest at G_2/M at least in part because of the effect of 14-3-3σ and in a p53-$p21^{waf1/cip1}$-independent manner. Moreover, satraplatin treatment affects DNA repair genes at the mRNA level. It also abrogated the clonogenic formation of CRC cells *in vitro*.

Materials and methods

Drug, chemicals, and reagents

Satraplatin was a kind gift from Agennix AG (formerly GPC Biotech AG), Fraunhoferstr, Germany. A satraplatin stock solution was prepared in 0.09% saline and stored at -20 °C. Antibodies were purchased from the following companies: anti-p53 (BD Pharmingen), anti-β-actin (Sigma), anti-Bax (Millipore), anti-Bcl-2 (Sigma), anti-$p21^{waf1/cip1}$ and anti-cyclin B1 (Santa Cruz) antibodies. Anti-rabbit and anti-mouse secondary antibodies were purchased from DakoCytomation, Denmark A/S. ECL detection reagents were purchased from Perkin-Elmer.

Cell culture

The HCT116 human CRC cell lines (wt, $p53^{-/-}$, and $p21^{-/-}$), HT29, HCT15, WiDr, and LoVo were tested for mycoplasma infection according to UKCCCR guidelines[15] and were cultured in monolayer in DMEM (HCT116, $p53^{-/-}$, $p21^{-/-}$, and HT29), DMEM:F12 (WiDr), RPMI-1640 (HCT15) and Ham's Nutrient mix F12 (LoVo) supplemented with 10%–20% FBS and 1% penicillin/streptomycin. No antibiotics were added prior to treatment. The cells were trypsinized and subcultured twice a week. All experiments were conducted at an early passage as previously described[14].

BrdU cell proliferation assay

A BrdU (5-bromo-2'-deoxyuridine) incorporation assay (Calbiochem/Merck, Whitehouse Station, NJ, USA) was used to assess the antiproliferative effects of satraplatin according to the protocol of the manufacturer. Briefly, 10 000 cells/well were seeded in 96-well plates followed by satraplatin treatment of 0–50 μmol/L. After cells adhered to the plate BrdU was added (1:2000 dilution), and plates were incubated for different time intervals (24 h and 72 h). The plates were then washed, fixed with anti-BrdU antibody and a peroxidase goat anti-mouse IgG conjugate was added. Immunocomplex formation was measured using tetra-methylbenzidine solution, and the reaction was terminated with 2.5 mol/L sulfuric acid. The measured intensity was proportional to the amount of incorporated BrdU in the cells. Absorbance was measured at 450 nm using a Microplate Manager (Bio-Rad Laboratories, Inc) according to the protocol of the manufacturer. The absorbance results were expressed as relative to untreated control.

Cell cycle analysis and apoptosis

Cell cycle perturbations and the apoptotic fractions of untreated and treated cells following satraplatin treatment were defined by flow cytometry analysis of cells stained with propidium iodide as described previously[14].

Western blot analysis

Aliquots of whole cell extracts containing 20 μg of protein were used for Western blot analysis as previously described[14].

Clonogenicity assay

Approximately 300 cells were seeded into each well of a 6-well culture plate, which were treated and then incubated in 2 mL of medium for 10 d. Subsequently, the medium was removed, and the cells were fixed for 15 min in 0.5 mL of 0.5% glutaraldehyde. The fixing solution was removed, the wells were rinsed with PBS, the colonies were stained for 30 min in 0.5 mL of 1% (*w/v*) methylene blue solution in PBS, washed once again with water, and then photographed[16].

Quantitative PCR

p53 signaling pathway qRT-PCR array

For the p53 Signaling Pathway PCR Array analysis, RNA from HCT116 (wt, $p53^{-/-}$, and $p21^{-/-}$) treated and untreated cells were used to analyze the fold change in expression. A total of 1 μg of total RNA was reverse transcribed, and the cDNA was analyzed on a human p53 signaling pathway RT^2 Profiler PCR Array (SABioscience, Fredrick, MD, USA) using the Stratagene Real-Time PCR System (Mx3005). The human p53 signaling pathway RT^2 Profiler PCR Array profiles the expression of 84 genes that are known to be involved in p53 signaling pathway regulation. A complete list of the genes assayed by the array can be viewed at http://www.sabiosciences.com/rt_pcr_product/HTML/PAHS-027A.html. PCR amplification was performed with an initial 10-min step at 95 °C, followed by 40 cycles of 95 °C for 15 s and 60 °C for 1 min. The SYBR green

fluorescent signal was detected immediately after the extension step of each cycle, and the cycle at which the product was first detectable was recorded as the cycle threshold. The data were analyzed using the comparative cycle threshold method with normalization of the raw data to the normalizer on the array. The results are presented as n-fold changes *versus* the values in the untreated control cells.

mRNA isolation, cDNA synthesis and qRT-PCR for the expression of DNA damage-related genes

Total RNA was isolated with TRIzol reagent (Invitrogen, CA, USA). The total RNA integrity was determined by 1% agarose gel electrophoresis. cDNA synthesis was performed with the Superscript III cDNA synthesis kit (Invitrogen, CA, USA) using 1 μg of total RNA as the template according to the protocol of the manufacturer. The PCR amplification was performed in a final volume of 25 μL containing 12.5 μL of SYBR green (2×), 0.5 μL of primers that detect MLH1, MSH2, PMS2 and ERCC1 as previously reported[14] (10 μmol/L) and 1 μL of cDNA. The cycling conditions included preheating at 95 °C for 10 min and then 40 cycles of the following: 95 °C for 30 s, 60 °C for 30 s and 72 °C for 45 s followed by a standard dissociation curve. Values that fell below 35 cycles were considered for the $2^{-\Delta\Delta Cq}$ determination.

Statistical analysis

The gene expression of ΔCq values from each sample were calculated by normalizing to ACTB and B2M, and the relative quantitation values were calculated according to the $2^{-\Delta\Delta Cq}$ method. Statistical analyses were performed using the SPSS statistical software package, version 12.0 (Chicago, IL, USA). Statistically significant differences in the expression level between the control and treated samples for each target were calculated using a paired Wilcoxon test. A comparison of the mean values of proliferation and the apoptosis levels in response to satraplatin and oxaliplatin treatment was performed using the Bonferroni *post hoc* multiple comparisons ANOVA test. $^{b}P \leq 0.05$ value was considered significant, and $^{c}P \leq 0.01$ value was considered highly significant.

Results

Anti-proliferative effects of satraplatin on CRC cells

The role of p53-p21$^{waf1/cip1}$ in the G_2/M cell cycle phase following satraplatin treatment was investigated in a panel of CRC cell lines that differ in their p53 genotype (HCT116^{wt}, LoVo^{wt}, HT29^{mut}, HCT15^{mut}, and WiDr^{mut}) and isogenic HCT116 cells that were p53$^{-/-}$ and p21$^{-/-}$. To assess the dose limiting effects of satraplatin on the rate of DNA synthesis, we performed a BrdU incorporation assay following satraplatin treatment for 24 and 72 h. As shown in Figure 1, we found that cells responded to satraplatin (when added below its IC_{50} value) in a dose- and time-dependent manner (Figure 1A). At a higher concentration (50 μmol/L), satraplatin decreased the proportion of S phase cells by about 90% in all seven cell lines tested (Figure 1B). Consistent with our previous findings on the effects of satraplatin on cell proliferation and apoptosis[14], no evidence of cytotoxicity was observed when cells were exposed to lower drug doses (*ie*, ≤50 μmol/L). We also tested two drug concentrations, 5 and 10 μmol/L, that are lower than previously determined IC_{50} concentrations (Figure 1A)[14]. As expected, treatment with 10 μmol/L, but not 5 μmol/L,

A

Cell line	p53 status	IC_{50} (μmol/L)
HCT116	Wild type	15.7±0.5
HT29	Mutant	27.2±3.1
HCT116p53**	Knockout	14.4±1.6
WiDr	Mutant	26.9±2.4
LoVo	Wild type	16.3±1.3
HCT15	Mutant	13.3±1.1

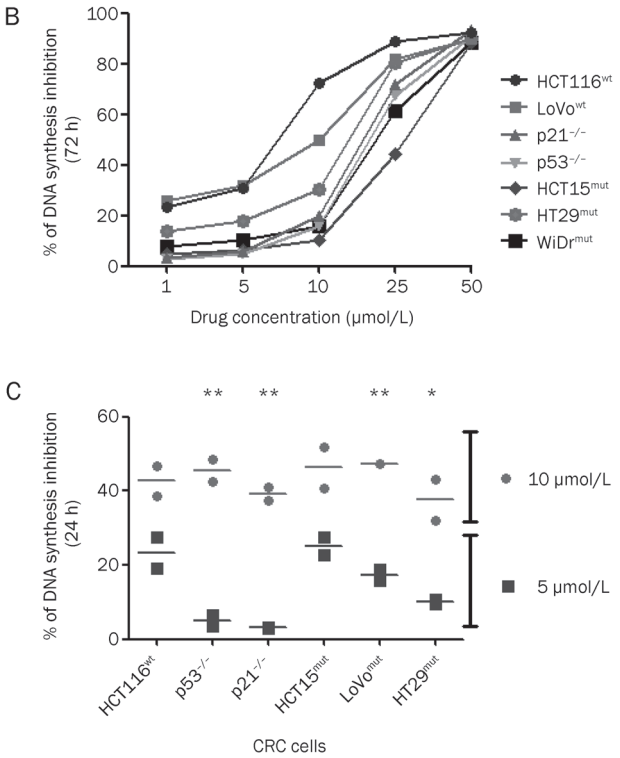

Figure 1. The IC_{50} value and the effect of satraplatin on CRC cells. (A) Table showing the IC_{50} value of satraplatin in a panel of CRC cell lines. (B) HCT116 (wt, p53$^{-/-}$, and p21$^{-/-}$), LoVo^{wt}, HT29^{mut}, HCT15^{mut}, and WiDr^{mut} cell lines were treated with 0–50 μmol/L satraplatin, and the effect of satraplatin on DNA synthesis inhibition was determined by a BrdU incorporation assay at 24 and 72 h. At higher concentrations, all cells demonstrated about 90% inhibition, which indicates the optimal activity of satraplatin in CRC cells. (C) DNA synthesis was inhibited at least 50% by treatment with 10 μmol/L satraplatin, whereas a different pattern of inhibition was observed with 5 μmol/L satraplatin. The percentage of DNA synthesis inhibition was defined as the optimal density at a given drug concentration divided by the optimal density for untreated control cells multiplied by 100. Each point is the average of two independent trials; data are presented as the mean±standard deviation.

satraplatin led to 36%–47% S phase inhibition as early as 24 h (Figure 1C). For example, 10 μmol/L at 72 h demonstrated that the wildtype p53 cells (HCT116 and LoVo) were more prone to S phase inhibition (61.06%±6.61%) than the mutant p53 HCT15, HT29, and WiDR cells (19.00%±4.02%, $P<0.01$). In addition, when comparing the 24 h *vs* the 72 h analysis, we noticed that all cells were more prone to S phase inhibition after as early as 24 h of treatment (43.08%±1.6%) but later returned to normal cell cycle progression, at least in mutant p53 cells but not in p53 wild-type cells. Thus, the BrdU incorporation assay confirmed the partial accumulation of S phase cells before cells exhibited a G_2/M phase perturbation.

Western blot analysis of proteins from HCT116^{wt} and LoVo^{wt} cells treated with 5 and 10 μmol/L satraplatin demonstrated a sustained increased level of p53 and p21$^{waf1/cip1}$ protein, particularly at 10 μmol/L (Figure 2A). In contrast, despite an elevated p53 protein level in HCT15^{mut} and HT29^{mut} cells, no expression of p21$^{waf1/cip1}$ was detected (Figure 2A, lower panel). To further confirm these data, we used the WiDr mutant cell line (Figure 2B) and showed no evident of p21$^{waf1/cip1}$ accumulation. Furthermore, when p53$^{-/-}$ cells were treated with satraplatin, no evidence of p21$^{waf1/cip1}$ accumulation was observed (Figure 2A, upper panel), which indicates that p21$^{waf1/cip1}$ expression requires a p53-dependent mechanism. Moreover, an accumulation of p53 was observed in p21$^{-/-}$ HCT116 cells treated at both concentrations (Figure 2), indicating that p53-dependent expression of p21$^{waf1/cip1}$ has no or only a modest effect on cell cycle perturbation.

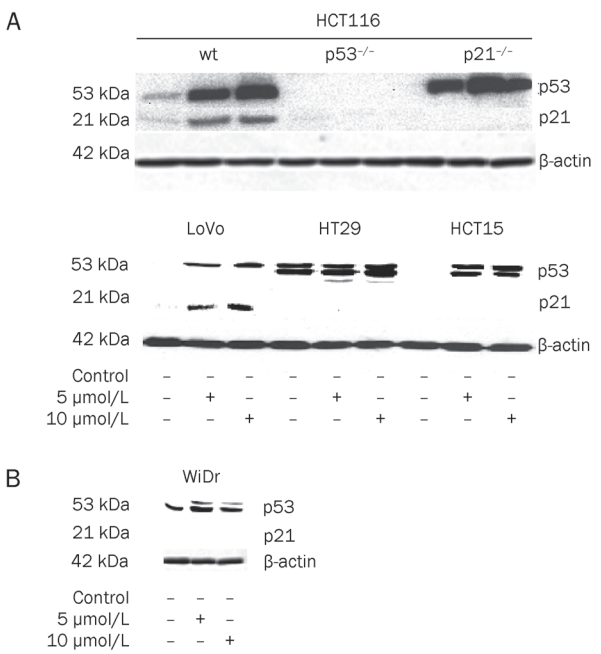

Figure 2. The effect of satraplatin on a clinically relevant concentration below its IC_{50} value on p53-p21$^{waf1/cip1}$ protein expression at 48 h. Whole cell extracts were prepared from HCT116 (wt, p53$^{-/-}$, and p21$^{-/-}$), HCT15^{mut}, HT29^{mut}, and WiDr^{mut} cells treated with 5 and 10 μmol/L satraplatin for 48 h and subjected to Western blot analysis for the presence of p53 and p21$^{waf1/cip1}$ protein accumulation.

Satraplatin treatment induces G_2/M perturbation

Consistent with our previous study[14], we found that CRC cells treated with different satraplatin concentrations were past the initial entry into G_2 prior to DNA damage and were subsequently arrested (Figure 3A and Supplementary Table 1). The expression of cyclin B1, a marker of the G_2/M phase, was up-regulated following 5 and 10 μmol/L satraplatin treatment (Figure 3B). Cellular growth inhibition and cell cycle perturbation induced by satraplatin was evident at 10 μmol/L (Figure 3C, right panel) compared with 0.5 μmol/L (Figure 3C, left panel). Similar perturbations were observed in all six CRC cell lines when the cells were treated with low and high satraplatin concentrations, and this was independent of their p53 gene status (Figure 3C).

Satraplatin increases 14-3-3σ expression in CRC cells

The results described above demonstrate that the presence of p21$^{waf1/cip1}$ and/or p53 following satraplatin treatment played a minor role in inducing cell cycle perturbation and apoptosis. To determine which genes significantly alter the cell cycle profile at the G_2/M phase, we used a candidate approach and found that 14-3-3σ mRNA and protein expression were elevated in CRC cells treated for 24 h (mRNA) and 48 h (protein) (Figure 4). We found a significant increase in 14-3-3σ mRNA expression in the wild-type p53 HCT116 cells but no significant increase in the p53$^{-/-}$ and p21$^{-/-}$ cells. At 48 h, elevated 14-3-3σ protein expression was detected after 5 and 10 μmol/L satraplatin treatment. We also observed that p53-null cells demonstrated an increase in 14-3-3σ that was independent of p53 action, particularly after treatment with 10 μmol/L satraplatin. Moreover, a similar protein expression pattern was observed in other CRC cell lines (Figure 4B, lower panel).

Satraplatin induces apoptosis in CRC cells

The cells that were G_2/M arrested also underwent apoptosis in a dose-dependent and a p53-independent manner (Figure 2 for p53 protein expression, Figure 5A for apoptosis by flow cytometry). A higher percentage of apoptotic cells was observed at 5 and 10 μmol/L ($P<0.01$) than at the lower concentrations of 50 and 500 nmol/L (Figure 5A). In particular, we found that the p53$^{-/-}$ and p21$^{-/-}$ cells showed a significant down-regulation of Bcl-2 protein expression (Figure 5B) after satraplatin treatment. In HT29^{mut} and WiDr^{mut} cells, no Bcl-2 protein accumulation was detected (Figure 5B, upper panel), whereas significant down-regulation of Bcl-2 protein expression was observed in HCT15^{mut} and LoVo^{wt} cells at 10 μmol/L (Figure 5B, lower panel).

In HCT116^{wt} cells, 5 and 10 μmol/L satraplatin induced apoptosis by at least 16% ($P\leq0.05$) and 40% ($P\leq0.01$), respectively, *versus* only 5% in the untreated control. In Lovo^{wt} cells, we observed 21% and 34% apoptotic fractions at 5 and 10 μmol/L satraplatin, respectively, *versus* 4.7% in the untreated control ($P\leq0.01$). Moreover, in HT29^{mut} cells, the same concentrations affected 15% and 27%, respectively, *versus* only 4% in the untreated control ($P\leq0.01$). Finally, HCT15^{mut} cells exhibited 26% and 36% apoptosis at 5 and 10 μmol/L satraplatin,

A Cell cycle perturbation follwoing satraplatin treatment.

Cell lines	μmol/L	Cell cycle phase % G_0/G_1	S	G_2
HCT116^{wt}	0	78.98	4.97	14.27
	0.5	78.28	15.54	12.49
	10	34.06^b	7.9	58.37^c
	0	52.89	14.52	32.97
HCT116 p21$^{-/-}$	0.5	51.17	23.45	18.56
	10	10.9*	7.45	81.85^c
	0	77.01	6.11	17.03
HCT116 p53$^{-/-}$	0.5	78.45	5.56	18.78
	10	22.75^c	36.82^c	41.24^c
	0	60.7	15.62	22.03
LoVo^{wt}	0.5	58.69	20.35	20.04
	10	27.45^b	46.58^b	18.54
	0	60.3	23.78	12.29
HCT15^{mut}	0.5	58.08	23.62	14.59
	10	3.24^b	42.15	54.94^b
	0	61.62	16.97	22.09
HT29^{mut}	0.5	58.86	15.89	24.78
	10	30.96^b	23.01	46.36

$^bP \le 0.05$, $^cP \le 0.01$ treated *vs* untreated control.

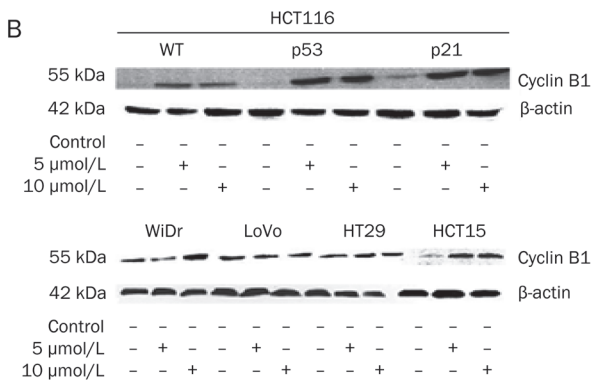

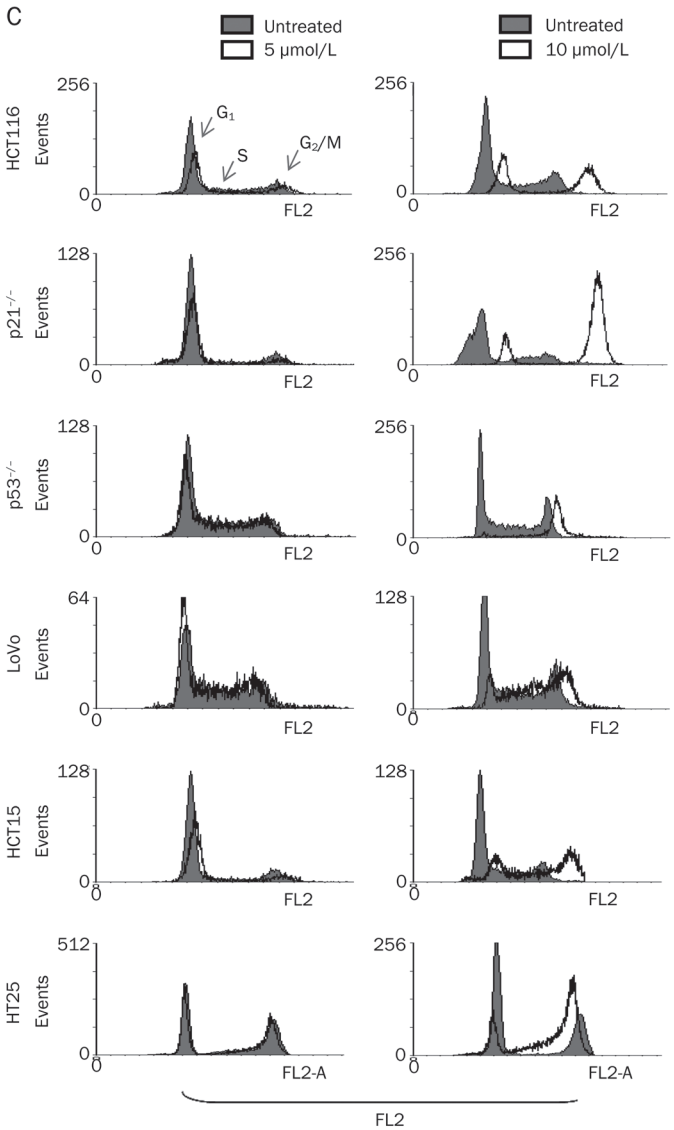

Figure 3. The effect of satraplatin-induced cell cycle perturbation at the G_2/M phase, apoptosis and cyclin-B1 expression in CRC cells at 48 h. (A) Table showing an accumulation of cells at each phase of the cell cycle following satraplatin treatment at lower and higher concentrations. (B) Cyclin B1 protein expression levels following treatment with 5 and 10 μmol/L satraplatin in CRC cells harvested at 48 h. The results shown are representative Western blots of at least two independent experiments. Equal loading was confirmed by β-actin detection. (C) The effects of various satraplatin concentrations on DNA synthesis and cell cycle progression in CRC cells. Typical cytograms are presented that represent the overlaps of the percentage of cells in each phase (G_0/G_1, S, and G_2/M) compared with untreated (control) cells (red background: untreated control cells; white background: treated cells) as determined by flow cytometry. This analysis indicates that the cells were substantially past the initial entry to G_2 after DNA damage and were subsequently arrested.

respectively, whereas untreated cells showed just 10% ($P \le 0.01$) apoptosis. We also found that p53$^{-/-}$ cells responded in the same manner following 5 and 10 μmol/L satraplatin treatment, with 9% and 34% ($P \le 0.01$) apoptosis, respectively, *versus* only 3% in the untreated control. However, in p21$^{-/-}$ knockout cells, the percentage of apoptotic cells was 44% and 53% at 5 and 10 μmol/L satraplatin, respectively, *versus* only 5% in the untreated control ($P \le 0.01$). We also observed that the cells responded in a dose- and time-dependent manner.

Satraplatin abrogated clonogenic formation in CRC cells

We also found that CRC cells, particularly HCT116 (wt, p53$^{-/-}$, and p21$^{-/-}$) (Figure 6, right panel), loss the ability to form colonies when treated with 5 or 10 μmol/L satraplatin as compared with 50 nmol/L treated cells (left panel). However, a partial clonogenicity loss was observed in all CRC cells when the cells were treated with 500 nmol/L satraplatin. This was also observed in the other CRC cell lines, including HCT15^{mut}, LoVo^{mut}, WiDr^{mut}, and HT29^{mut} (data not shown).

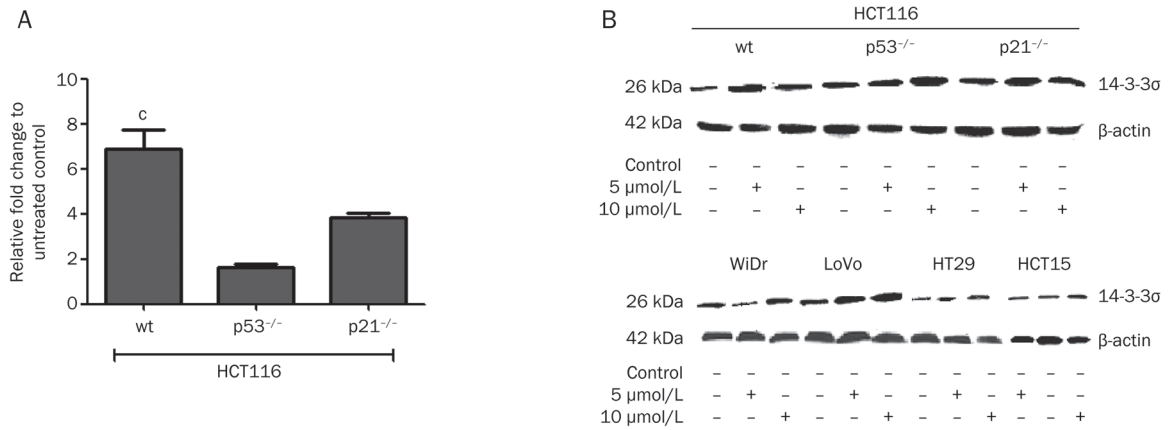

Figure 4. mRNA and 14-3-3σ protein levels following satraplatin treatment. (A) 14-3-3σ mRNA expression is markedly increased in HCT116 cells compared with isogenic $p53^{-/-}$ and $p21^{-/-}$ cells. Fold changes in this experiment are based on normalizing ACTB and B2M to untreated control cells. The results shown are representative of at least two independent experiments at 24 h. (B) 14-3-3σ protein levels indicated that the cells were arrested at the G_2/M phase. A marked increase in 14-3-3σ levels was also detected in $p53^{-/-}$ cells, indicating an activation of cell cycle arrest in a p53-idependent manner at 48 h. The results shown are representative of at least two independent experiments. Equal loading was confirmed by β-actin detection. $^cP<0.01$.

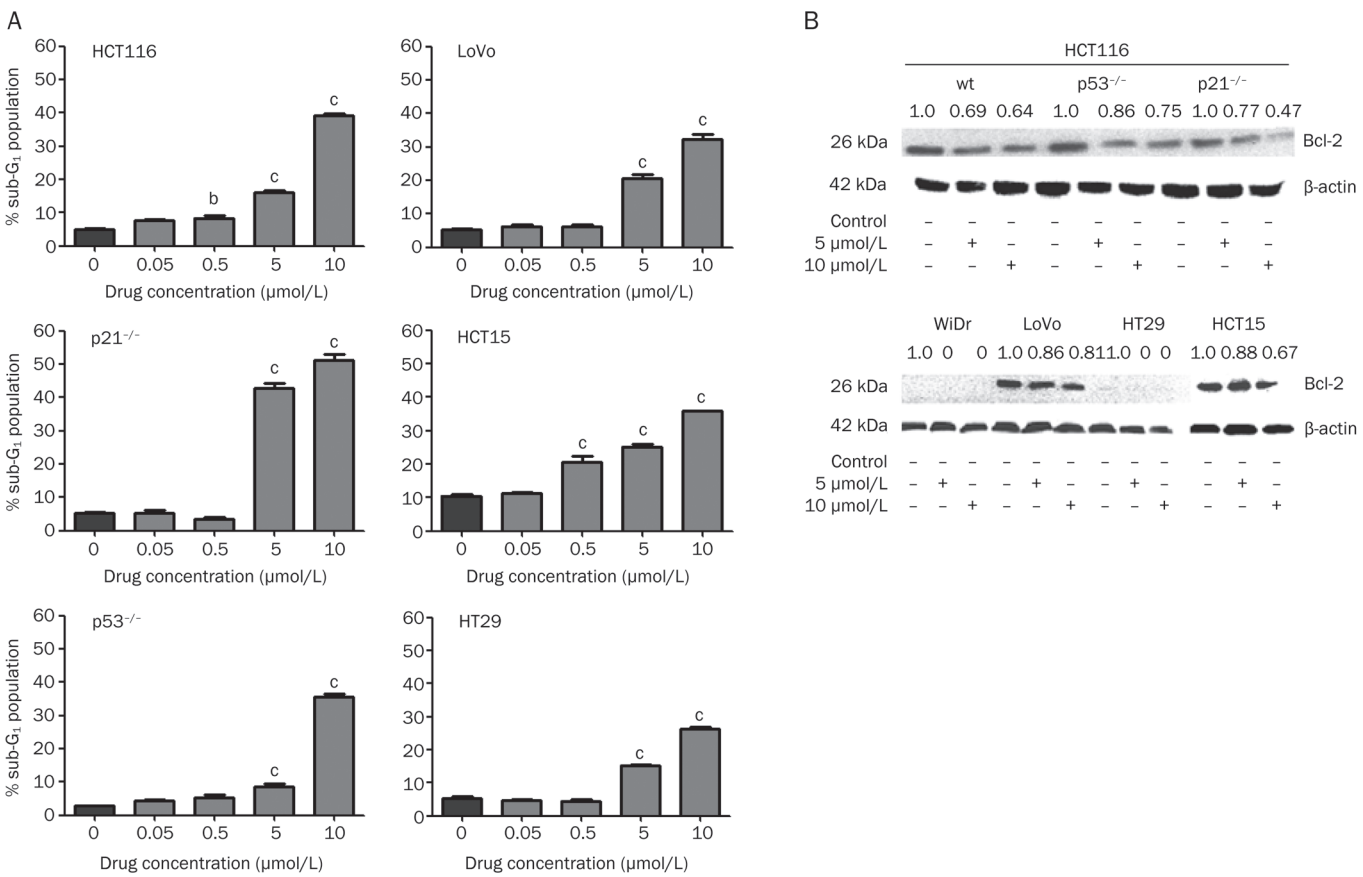

Figure 5. Dose dependent of Bcl-2 protein expression levels during satraplatin sustained treatment in CRC cells. A) Following treatment with different satraplatin concentrations, the CRC cell apoptotic fractions were measured by FACScan analysis. The bar indicates that a greater accumulation of apoptotic cells was observed with a clinically relevant satraplatin concentration *vs* the untreated control cells. Data points indicate the mean percentages of apoptosis fractions from three independent experiments; bars, standard deviation. B) The cellular extracts were subjected to Western blot. Satraplatin treatment resulted in markedly decreased Bcl-2 protein expression. The results shown are representative of at least two independent experiments. Equal loading was confirmed by β-actin detection. $^cP<0.01$.

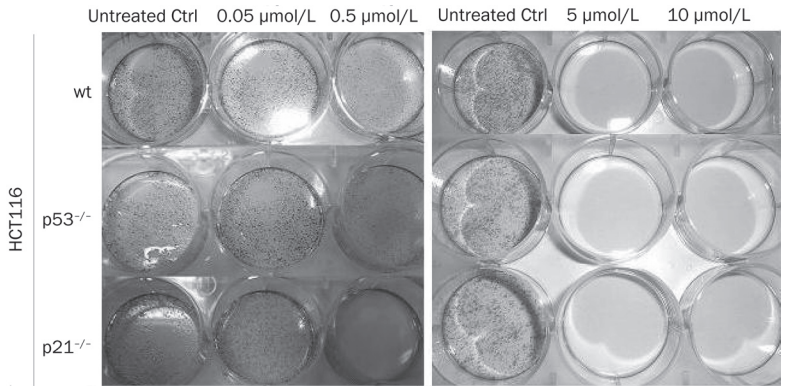

Figure 6. Clonogenicity loss following satraplatin induced DNA damage. Untreated- and satraplatin-treated cells were cultured in medium for two weeks and then fixed and stained with methylene blue for the clonogenicity assay. The results demonstrate that long-term satraplatin incubation leads to a loss of CRC cell clonogenicity potential.

G_2/M cell cycle arrest and apoptosis occurs in a p53-independent manner

To further elucidate the ability of satraplatin to perturb the G_2/M phase and subsequently apoptosis, we used a p53 signaling pathway qRT-PCR array containing 86 human p53 related genes. We compared the gene expression profiles of HCT116 (wt, $p53^{-/-}$, and $p21^{-/-}$) cells treated with 5 μmol/L satraplatin (Supplementary Table 2). We found that the cells responded independent of p53 activation and its related molecules. The up-regulation of Bax, BTG2, CDKN1A, FASLG, and MDM2 genes was observed in $HCT116^{wt}$ cells but not in $p53^{-/-}$ and $p21^{-/-}$ cells. Moreover, we found that genes involved in DNA damage responses were also down-regulated together with the transcription factor NFKB1 (Supplementary Table 2).

Down-regulation of DNA damage repair genes following satraplatin induced apoptotic cells

To examine DNA damage repair gene activation, CRC cells were treated for 24 h with 5 μmol/L satraplatin and were tested for differential expression of mRNA encoding MLH1, MSH2, ERCC1, and PMS2. Interestingly, we found that all cells similarly responded to satraplatin treatment, with most of the DNA damage repair genes being down regulated, except for MSH1 and ERCC1 in $HCT116^{wt}$ cells (Figure 7). We also found that, based on our human p53 signaling pathway RT^2 Profiler PCR data, ATM and ATR expression was almost unchanged by 5 μmol/L satraplatin treatment in HCT116 (wt, $p53^{-/-}$, and $p21^{-/-}$) cells, whereas a 0.5-fold down-regulation was observed for E2F1 in $HCT116^{wt}$ cells versus an up-regulation of 2.1-fold in the HCT116 $p53^{-/-}$ cells. Moreover, we found that XRCC5 expression was down-regulated in HCT116 (wt, $p53^{-/-}$, and $p21^{-/-}$) cells (Supplementary Table 2).

Discussion

Satraplatin, which was initially proven to have clinical activity against small-cell lung[17], ovarian[18], and prostate cancers[19], was developed for the treatment of castration-resistant prostate cancer and was found to significantly prolong disease progression-free survival[20]. Satraplatin disrupts DNA replication and transcription by forming intrastrand/interstrand DNA adducts; however, the downstream molecular events leading to G_2/M cell cycle perturbation and cell death have not been well characterized in CRC cells.

Here, we show that exposure of CRC cells to satraplatin reduced long-term clonogenic survival and induced cell cycle arrest and subsequently apoptosis. Our previous model suggested that the possible reasons for differences between oxaliplatin- and satraplatin-induced antitumor effectiveness might

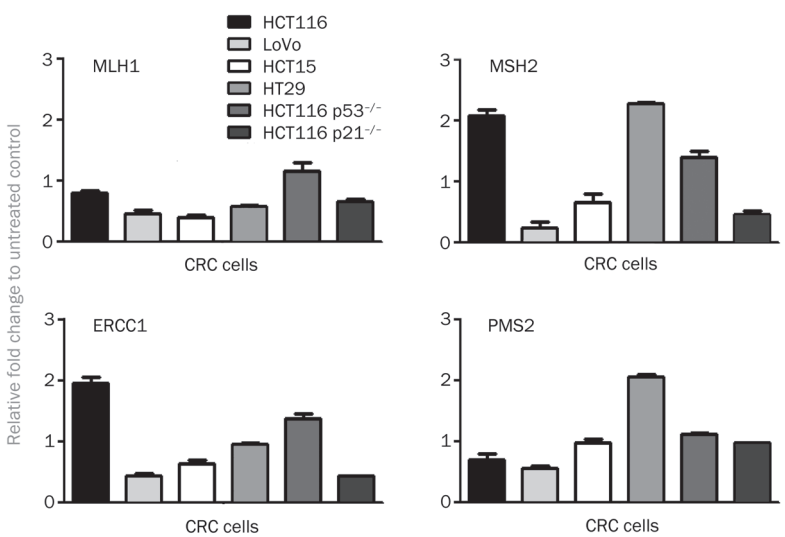

Figure 7. mRNA expression of the DNA repair enzymes ERCC1, MLH1, PMS2, and MSH2 in the CRC cell lines following 48 h satraplatin treatment. The CRC cells demonstrated unrepaired DNA damage owing to a down-regulation of the expression of DNA damage responsive genes in all cell lines tested. Only the expression of MSH1 and ERCC1 was up-regulated in the HCT116 wild-type cells. The fold change is based on the normalization of ACTB and B2M proteins in the treated *vs* the untreated control cells. The results shown are representative of at least two independent experiments.

be found at the level of cell cycle regulation[14]. Many studies have indicated that platinum agents predominantly reduce the DNA synthesis rate[4] and inhibit cell cycle progression at the G_1-S and/or G_2/M phases[21]. Using a BrdU incorporation assay, we found that the treatment of CRC cells with different satraplatin concentrations delayed the progression of cells in S phase and altered the G_2/M transition. Different drug concentrations perturbed the cells differently, particularly when cells were treated with lower drug concentrations. This finding could result from differences in cell characteristics that lead to different responses to treatment and the abilities of the drug to interact with its cellular target. More interestingly, the progression into mitosis was blocked. In addition, cells that were null for p53 and $p21^{waf1/cip1}$ also had a delayed cell cycle progression and G_2/M perturbation.

Since we observed a massive G_2/M phase arrest, we focused our analysis on p53–p21 involvement in the G_2/M transition as p53–p21 being a major regulator of the cell cycle. We found that satraplatin induced a significant accumulation of p53 protein in wild-type HCT116 and LoVo cells. In contrast, an accumulation of mutant p53 was also observed by Western blotting in HCT15 and WiDr cells. Bunz *et al* have reported the role of p53 at the G_2 checkpoint by inactivating the p53 gene with homologous recombination in a derivative of a human colorectal tumor model[12]. They demonstrated that few cells entered mitosis initially after exposure to ionizing radiation, which suggests that the G_2 checkpoint is intact. Therefore, they proposed that p53 is not required for the initial arrest but is essential for long-term arrest maintenance. However, it is possible that p53 can partially contribute to the initial arrest, and it is clear that other pathways can cause arrest when p53 is missing[12].

We detected a marked increase in cyclin B1, a marker for G_2/M cell arrest, in all CRC cell lines tested, and this was independent of the p53 gene status. Our data suggest that p53-independent pathways could inhibit cdc2 activity in response to DNA damage. In relation to this hypothesis and by following a candidate approach, we found that satraplatin increased the expression of 14-3-3σ, a conserved phosphoserine binding protein in CRC cells. We noticed a similar alteration even in p53-null and mutant cells, which further delineates the action of this protein in a p53-independent manner. We believed that 14-3-3σ may become a key regulatory modulator in the G_2/M checkpoint that may form a cytoplasmic complex with cdc2 and sequester cdc2/cyclin B1 in the cytoplasm. Hermeking *et al* have shown that 14-3-3σ overexpression in HCT116 CRC cells causes most cells to arrest in the G_2 phase[22]. Thus, we assumed that satraplatin-induced 14-3-3σ contributes to the G_2/M accumulation. We also observed that, following satraplatin-induced cell cycle perturbation, the cells eventually undergo apoptosis in a dose- and time-dependent manner. We have reported that satraplatin treatment induces the accumulation of apoptotic cells even in the p53-null model, thus overcoming chemoresistance by a p53-independent mechanism[14]. Generally, the protection of cells against apoptosis requires the down-regulation of proapoptotic activities or the up-regulation of anti-apoptotic mechanisms[23]. The Bcl-2 family is an important regulator of cellular apoptosis[24]. Thus, we investigated Bcl-2 involvement in the mitochondrial (intrinsic) pathway to determine whether the Bcl-2 family was functioning as upstream initiators of apoptosis. Notably, the satraplatin effects on Bcl-2 expression in CRC cells ($HCT15^{mut}$, $LoVo^{wt}$, and $WiDr^{mut}$ and $p21^{-/-}$) were consistent with our previous findings in HCT116 (wt and $p53^{-/-}$) and $HT29^{mut}$ cells[14]. However, these effects did not only affect Bcl-2-dependent apoptosis because the mutant HT29 and Lovo cells significantly underwent apoptosis, which further suggests that CRC cells could also undergo Bcl-2-independent apoptosis following satraplatin treatment. In addition to the Bcl-2-apoptosis analysis, we also demonstrated with the long-term clonogenicity survival analysis that the cells lose the ability to form colonies. Remarkably, we found that all cells, particularly the $p53^{-/-}$ and $p21^{-/-}$ cells, lost their clonogenicity potential in a dose-dependent manner. Finally, satraplatin mediated apoptotic activity is believed to be linked to DNA damage, and the levels of DNA damage repair genes have been shown to be correlated with the response to the platinum agent[4]. We hypothesized that the DNA damage inflicted by satraplatin may be repaired by the nucleotide excision repair (NER) and/or the mismatch repair (MMR) pathways with kinetics similar to that of the DNA damage repair that is induced by cisplatin and oxaliplatin[25, 26]. Accordingly, we showed that the mRNA expression levels of ERCC1, MLH1, MSH2, and PMS2 were significantly down-regulated in CRC cells. In addition to these results, Vaisman *et al* and Fokkema *et al* have suggested that satraplatin-induced adducts, compared with adducts formed by other platinum drugs, do not bind to high mobility group 1 protein, which recognizes the DNA damage caused by cisplatin and inhibits translation replication by certain DNA polymerases. These differences may provide a mechanism by which some platinum resistance may be overcome by satraplatin treatment in this model[27, 28].

Thus far, *in vitro* and *in vivo* data have indicated satraplatin efficacy in the treatment of various cancer models[7, 14]. However, the ability of satraplatin to induce G_2/M cell cycle arrest and subsequently apoptosis in CRC cells suggests that it may have a wide range of clinical applications. In Figure 8, we illustrated the molecular mechanism of satraplatin action on cell cycle perturbation. In summary, we hypothesize that satraplatin-induced cell cycle arrest is likely executed via 14-3-3σ in a p53-$p21^{waf1/cip1}$-independent manner (Figure 8). Furthermore, cell death may also be related to the reduced expression of DNA repair enzymes.

In conclusion, the ability of satraplatin to induce different modes of cell cycle regulation and cell death in different types of CRC cells at relatively low concentrations indicates that it may be highly efficacious in killing tumor cells and warrants further *in vivo* clinical investigation.

Acknowledgements

This work was supported by grants from the University Hospital Tor Vergata and the Department of Internal Medicine,

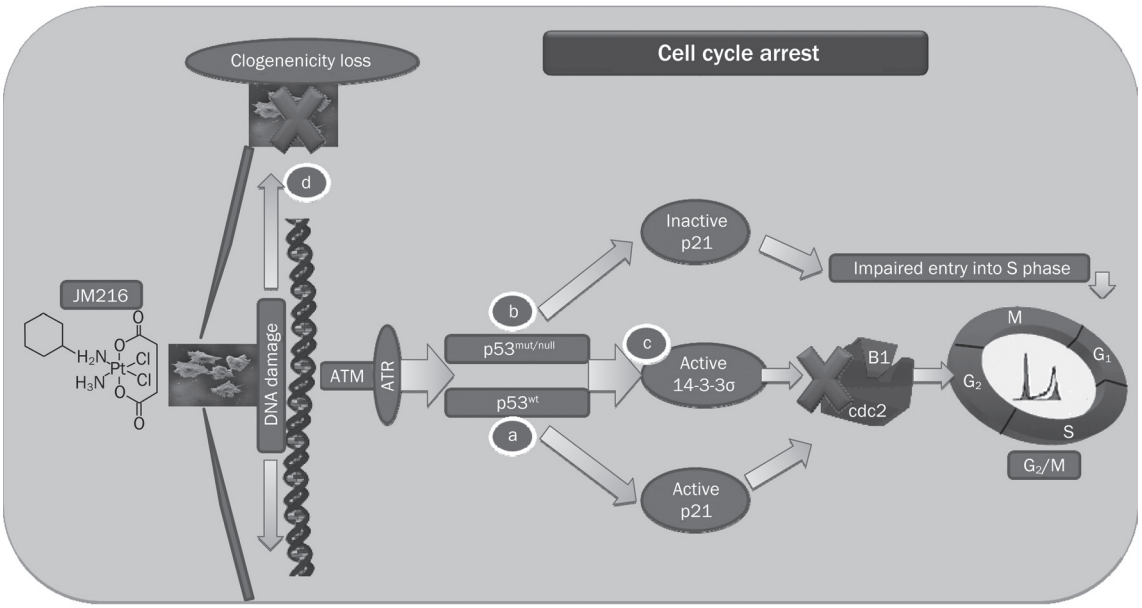

Figure 8. A flow chart depicting how 14-3-3σ induces cell cycle arrest at G_2/M, which may not rely on $p21^{waf1/cip1}$ and p53-dependent pathway in CRC cell models following satraplatin treatment. (A) Upon DNA damage caused by satraplatin treatment, we assumed that the ATM and ATR genes are activated, which induces the downstream signaling of cell cycle and cell death modulators. This results in p53 accumulation, which induces the expression of its primary cell cycle modulator, $p21^{waf1/cip1}$, an inhibitor of Cdks, and its activation sequesters cyclin B1/cdc2 complexes, which can lead to an accumulation of cells at the G_2/M transition. Alternatively, p53 could also be activated through 14-3-3σ (a conserved phosphoserine binding protein) to induce an accumulation of cells at G_2/M by sequestering the cyclin B1/cdc2 complexes. (B) In cells that lack p53 or contain mutant p53, we observed that there was also a G_2/M perturbation that was independent of $p21^{waf1/cip1}$ activation because we first identified impaired S phase entry and then identified arrest at G_2/M. (C) These cells might also activate 14-3-3σ independently of p53 action because $p53^{mut}$ and $p53^{null}$ cells demonstrated an elevated expression of 14-3-3σ and subsequently arrested at G_2/M. (D) Loss of clonogenicity patterns were observed following satraplatin induced DNA damage, which led to cell mortality.

University of Rome, "Tor Vergata". Murugan KALIMUTHO was supported by the Pre-doctoral Scholarship for foreign students under the International Italian Government University scholarship. We thank to Dr Isabella FARAONI, University of Rome Tor Vergata, Dr Soddu and Dr Maurizio FRANCULLI from the Regina Elena Cancer Institute, Rome, Italy, Dr Rossana SUPINO from the Instituto Nazionale Tumori, Milan, Italy and Prof Bert VOGELSTEIN from the Ludwig Center at John Hopkins, USA for providing us with the cell lines used in analysis. We also thank Agennix for providing us with satraplatin.

Author contribution

Study design and concept, data collection, analysis, interpretation and article preparation: Murugan KALIMUTHO; technical assistance, data collection and interpretation: Antonella MINUTOLO and Sandro GRELLI; grant approval and supervision: Giorgio FEDERICI and Sergio BERNARDINI.

Supplementary information

Supplementary tables are available at Acta Pharmacologica Sinica website of NPG.

Reference

1 Johnson NP, Butour JL, Villani G, Wimmer FL, Defais M, Pierson V. Metal antitumor compounds: the mechanism of action of platinum complexes. Prog Clin Biochem Med 1989; 10: 1–24.
2 Johnson SW, Ferry KV, Hamilton TC. Recent insights into platinum drug resistance in cancer. Drug Resist Update 1998; 1: 243–54.
3 Fuertes MA, Castilla J, Alonso C, Perez JM. Cisplatin biochemical mechanism of action: From cytotoxicity to induction of cell death through interconnections between apoptotic and necrotic pathways. Curr Med Chem 2003; 10: 257–66.
4 Boulikas T, Pantos A, Bellis E, Christofis P. Designing platinum compounds in cancer: structures and mechanisms. Cancer Therapy 2007; 5: 537–83.
5 Kelland LR, Abel G, McKeage MJ, Jones M, Goddard PM, Valenti M, *et al*. Preclinical antitumor evaluation of bis-acetato-ammine-dichloro-cyclohexylamine platinum (IV): an orally active platinum drug. Cancer Res 1993; 53: 2581–6.
6 Sharp SY, Rogers PM, Kelland LR. Transport of cisplatin and bis-acetato-ammine-dichlorocyclohexylamine platinum (IV) (JM-216) in human ovarian carcinoma cell lines: identification of a plasma membrane protein associated with cisplatin resistance. Clin Cancer Res 1995; 1: 981–9.
7 Choy H, Park C, Yao M. Current status and future prospects for satraplatin, an oral platinum analogue. Clin Cancer Res 2008; 14: 1633–8.
8 Elledge SJ. Cell cycle checkpoints: preventing an identity crisis. Science 1996; 274: 1664–72.
9 Bartek J, Lukas J. Pathways governing G_1/S transition and their response to DNA damage. FEBS Lett 2001; 490: 117–22.
10 Taylor WR, Stark GR. Regulation of the G_2/M transition by p53.

Oncogene 2001; 20: 1803–15.
11 Levine AJ. p53, the cellular gatekeeper for growth and division. Cell 1997; 88: 323–31.
12 Bunz F, Dutriaux , Lengauer C, Waldman T, Zhou S, Brown JP, *et al*. Requirement for p53 and p21 to sustain G_2 arrest after DNA damage. Science 1998; 282: 1497–501.
13 Waldman T, Kinzler KW, Vogelstein B. p21 is necessary for the p53-mediated G_1 arrest in human cancer cells. Cancer Res 1995; 55: 5187–90.
14 Kalimutho M, Minutolo A, Grelli S, Formosa A, Sancesario G, Valentini A, *et al*. Satraplatin (JM-216) mediates G_2/M cell cycle arrest and potentiates apoptosis via multiple death pathways in colorectal cancer cells thus overcoming platinum chemo-resistance. Cancer Chemother Pharmacol 2010; 67: 1299–312.
15 UKCCR. UKCCCR guidelines for the use of cell lines in cancer research. British J Cancer 2000; 82: 1495–509.
16 Han Z, Wei W, Dunaway S, Darnowski JW, Calabresi P, Sedivy J, *et al*. Role of p21 in apoptosis and senescence of human colon cancer cells treated with camptothecin. J Biol Chem 2002; 277: 17154–60.
17 Fokkema E, Groen HJM, Bauer J, Uges DRA, Weil C, Smith IE. Phase II study of oral platinum drug JM216 as first line treatment in patients with small-cell lung cancer. J Clin Oncol 1997; 17: 3822–7.
18 McKeage MJ, Mistry P, Ward J, Boxall FE, Loh S, O'Neill C, *et al*. A phase I and pharmacology study of an oral platinum complex, JM216: dose-dependent pharmacokinetics with single-dose administration. Cancer Chemother Pharmacol 1995; 36: 451–8.
19 Latif T, Wood L, Connell C, Smith DC, Vaughn D, Lebwohl D, *et al*. Phase II study of oral bis(acetate) ammine dichloro (cyclohexylamine) platinum (IV) (JM216, BMS-182751) given daily x 5 in hormone refractory prostate cancer (HRPC). Invest New Drug 2005; 23: 79– 84.
20 Sternberg CN, Whelan P, Hetherington J, Paluchowska B, Slee PH, Vekemans K, *et al*. Phase III trial of satraplatin, an oral platinum plus prednisone *vs* prednisone alone in patients with hormone-refractory prostate cancer. Oncology 2005; 68: 2–9.
21 Ormerod MG, Orr RM, Peacock JH. The role of apoptosis in cell killing by ciplatin: a flow cytometric study. Br J Cancer 1994; 69: 93–100.
22 Hermeking H, Lengauer C, Polyak K, He TC, Zhang L, Thiagalingam S, *et al*. 14-3-3 sigma is a p53-regulated inhibitor of G_2/M progression. Mol Cell 1997; 1: 3–11.
23 Yadav SS, Sindram D, Perry DK, Clavien PA. Ischemic preconditioning protects the mouse liver by inhibition of apoptosis through a caspase-dependent pathway. Hepatology 1999; 30: 1223–31.
24 Rao L, White E. Bcl-2 and the ICE family of apoptotic regulators: making a connection. Curr Opin Genet 1997; 7: 52–8.
25 Reardon JT, Vaisman A, Chaney SG, Sancar A. Efficient nucleotide excision repair of cisplatin, oxaliplatin, and bis-aceto-ammine-dichloro-cyclohexylamineplatinum (IV) (JM216) platinum intrastrand DNA diadducts. Cancer Res 1999; 59: 3968–71.
26 Fink D, Nebel S, Aebi S, Zheng H, Cenni B, Nehmé A, *et al*. The role of DNA mismatch repair in platinum drug resistance. Cancer Res 1996; 56: 4881–6.
27 Vaisman A, Lim SE, Patrick SM, Copeland WC, Hinkle DC, Turchi JJ, *et al*. Effect of DNA polymerases and high mobility group protein 1 on the carrier ligand specificity for translesion synthesis past platinum-DNA adducts. Biochemistry 1999; 38: 11026–39.
28 Fokkema E, Groen HJ, Helder MN, de Vries EG, Meijer C. JM216-, JM118-, and cisplatin-induced cytotoxicity in relation to platinum-DNA adduct formation, glutathione levels and p53 status in human tumour cell lines with different sensitivities to cisplatin. Biochem Pharmacol 2002; 63: 1989–96.

Acta Pharmacologica Sinica (2011) 32: 1397–1401
 1671-4083/11 $32.00
www.nature.com/aps

Original Article

Anti-tumor activity of CrTX in human lung adenocarcinoma cell line A549

Bin YE[1], Yan XIE[1], Zheng-hong QIN[2], Jun-chao WU[2], Rong HAN[2], Jing-kang HE[1] *

[1]*Dept of Cardiothoracic Surgery, the First Affiliated Hospital of SooChow University, Suzhou 215006, China;* [2]*Dept of Pharmacology and Laboratory of Aging and Nervous Diseases, SooChow University School of Medicine, Suzhou 215123, China*

Aim: To assess the cytotoxic effect of crotoxin (CrTX), a potent neurotoxin extracted from the venom of the pit viper Crotalus durissus terrificus, in human lung adenocarcinoma A549 cells and investigated the underlying mechanisms.
Methods: A549 cells were treated with gradient concentrations of CrTX, and the cell cycle and apoptosis were analyzed using a flow cytometric assay. The changes of cellular effectors p53, caspase-3 and cleaved caspase-3, total P38MAPK and pP38MAPK were investigated using Western blot assays. A549 xenograft model was used to examine the inhibition of CrTX on tumor growth *in vivo*.
Results: Treatment of A549 cells with CrTX (25–200 μg/mL) for 48 h significantly inhibited the cell growth in a dose-dependent manner (IC_{50}=78 μg/mL). Treatment with CrTX (25 μg/mL) for 24 h caused G1 arrest and induced cell apoptosis. CrTX (25 μg/mL) significantly increased the expression of wt p53, cleaved caspase-3 and phospho-P38MAPK. Pretreatment with the specific P38MAPK inhibitor SB203580 (5 μmol/L) significantly reduced CrTX-induced apoptosis and cleaved caspase-3 level, but G_1 arrest remained unchanged and highly expressed p53 sustained. Intraperitoneal injection of CrTX (10 μg/kg, twice a week for 4 weeks) significantly inhibited A549 tumor xenograft growth, and decreased MVD and VEGF levels.
Conclusion: CrTX produced significant anti-tumor effects by inducing cell apoptosis probably due to activation of P38MAPK and caspase-3, and by cell cycle arrest mediated by increased wt p53 expression. In addition, CrTX displayed anti-angiogenic effects *in vivo*.

Keywords: crotoxin (CrTX); human lung adenocarcinoma; apoptosis, P38MAPK; caspase-3; cell cycle; p53; angiogenesis

Acta Pharmacologica Sinica (2011) 32: 1397–1401; doi: 10.1038/aps.2011.116; published online 26 Sep 2011

Introduction

Crotoxin (CrTX) is a potent neurotoxin that is extracted from the venom of the pit viper *Crotalus durissus terrificus*[1]. CrTX possesses phospholipase A2 activity and inhibits neuromuscular transmission. Recently, some studies have reported that CrTX has anti-tumor effects. However, the potential mechanism is unclear[2–5].

Lung cancer is the most common cancer worldwide with the highest mortality rate among cancers. Current drugs cannot meet the therapeutic needs[6]. Previous study demonstrated that CrTX has cytotoxic effects on A549 cells, which are human lung adenocarcinoma cells with the wild type p53 gene, and shows synergistic effects when combined with Iressa, which is currently a widely-used drug for lung cancer therapy[7, 8]. In this study, we further investigated the anti-tumor effects of CrTX on A549 cells and tried to elucidate the mechanisms of CrTX-mediated cell growth inhibition and cell apoptosis. Some evidence has indicated that the P38MAPK pathway plays an important role in the process of apoptosis and the cell cycle. Therefore, we detected the expression of apoptotic proteins and cell cycle-related factors, such as p53, cleaved caspase-3 and phospho-P38MAPK, to discover the potential molecular mechanisms that mediate the anti-tumor activities of CrTX. The anti-tumor activity of CrTX was also analyzed in the A549 xenograft model.

* To whom correspondence should be addressed.
E-mail jkhe001@163.com
Received 2011-05-30 Accepted 2011-07-27

Materials and methods

Cells and reagents

A549 cells, which are human lung adenocarcinoma cells with wt p53, purchased from Shanghai Institutes of Biological Science), were cultured in RPMI-1640 media containing 10% fetal bovine serum and maintained in an incubator (5% CO_2, 37 °C). Crotoxin (CrTX) was provided by Celtic Biotechnology (Dublin, Ireland). The anti-phospho-P38MAPK, anti-p53 and anti-cleaved caspase-3 antibodies were purchased from Cell Signaling Technology (Woburn, MA, USA). SB203580, which is a specific inhibitor of P38MAPK, was purchased from Calbiochem, Inc (Madison, WI, USA).

Cell growth viability assay

Based on the results of preliminary experiments, we selected four different concentrations of crotoxin (25 μg/mL, 50 μg/mL, 100 μg/mL and 200 μg/mL) in the study. After collecting A549 cells in the logarithmic growth period, we prepared 1.0×10^5 cells/mL of cell suspension after 0.25% trypsin treatment and seeded them into 96-well plates. Each well contained 100 μL of cell suspension. The control (cell suspension) and blank groups (RPMI-1640 medium) were included in the study. Once cells were allowed to adhere to the plate for 24 h, we removed the medium and applied different concentrations of CrTX to treat the cells for 48 h. Then, 20 μL of MTT (5 mg/mL) was added, and the cells were incubated at 37 °C for 4 h. The supernatant in each well was replaced with 150 μL DMSO. After 30 min of incubation at room temperature and gentle agitation for 10 min, the optical density (*OD*) was measured with an automatic multiwell spectrophotometer at 570 nm. Three independent experiments were performed to generate averaged values. The cytostatic rate was calculated using the following equation: cytostatic rate (%)=(1–average *OD* value of experimental group / average *OD* value of control group)×100.

Flow cytometry analysis of CrTX-induced cell cycle arrest and apoptosis

Four experimental groups were included in the study: control, CrTX (25 μg/ml), SB203580+CrTX and SB203580 only (5 μmol/L). SB203580 was added to the culture medium 1 h before CrTX. All groups of cells were digested with 0.25% trypsin and centrifuged at 1000 r/min. The collected cells were rinsed in PBS (phosphate buffered saline) twice, fixed with 70% pre-cooled ethanol and stored at 4 °C. The cells were centrifuged to remove the fixation reagent and suspended in PBS. The cells were incubated at 37 °C for 30 min after adding 200 μL RNaseA (1 μg/μL). PI (propidium iodide) was added to the cells and incubated for 30 min in the dark. Finally, the cell cycle and apoptosis were analyzed using flow cytometry.

Western blot analysis of p53, caspase-3 and cleaved caspase-3, total P38MAPK and pP38MAPK

Three experimental groups were included in the study as follows: control, CrTX and SB203580 + CrTX groups. The dose response and time course studies were performed as mentioned previously. Cells were washed twice with pre-cooled PBS. The pellets were lysed on ice with lysis buffer. The lysates were centrifuged at 12000 r/min for 10 min at 4 °C, and the supernatants were collected. Protein concentrations were determined using the BCA protein assay. For Western blot analysis, proteins were denatured for 5 min by boiling. Protein extracts were subjected to SDS-PAGE with 10% gels and electroblotted onto nitrocellulose membranes. Membranes were incubated overnight at 4 °C in 5% non-fat milk with primary monoclonal antibodies of p53, caspase-3, cleaved caspase-3, total P38MAPK, phospho-P38MAPK and β-actin (Santa Cruz Biotechnology, Inc, Santa Cruz, CA). After incubating for 2 h at room temperature with a secondary HRP-conjugated antibody, antigens were visualized using enhanced chemiluminescence using ECL (enhanced chemiluminescence) according to the manufacturer's instructions.

In vivo anti-tumor efficacy and mechanism study

Female Balb/C nude mice with average body weights of 18–20 g (4–6 weeks) were purchased from a local commercial vendor and housed in a SPF (specific pathogen free) animal facility. All manipulations (ie, handling, invasive procedures and tumor volume measurements) were performed in a laminar flow hood under strict sterile conditions. Mice were injected into the right axillary space tissue with 5×10^7 cells/mL A549 cells that were suspended in 0.2 mL of PBS. Treatment with CrTX was initiated 8 d after xenotransplantation, and the tumor reached approximately 5-6 mm in diameter. With the exception of two no-tumor mice, sixteen remaining mice were randomly assigned to one of two experimental groups (n=8 per group): the control or CrTX (10 μg/kg, ip, twice a week) group. After 4 weeks of treatment, the mice were sacrificed, and the tumor xenografts were removed, sectioned and analyzed using TEM. The data for tumor growth inhibition were expressed as the mean tumor weight±standard deviation. Tumor xenografts were further analyzed using a microscope, and microvascular density (MVD) was counted using Weidner methods. Briefly, a microscopic field was defined by a grid that was placed on the eyepiece. Endothelial cells in distinct cell clusters showing CD31 staining were considered as a single, countable microvessel. MVD was determined by calculating the mean of the obtained vascular counts in 15 random fields across the tissue section. The MVD data were expressed as the mean±standard deviation. In addition, 0.5 mL of blood was harvested from each mouse, and 0.2 mL of serum was collected after centrifuging for 10 min at 3000 r/min. VEGF levels were analyzed in each serum sample using ELISA. VEGF levels were expressed as the mean±standard deviation.

Statistical analysis

The data were expressed as the mean±standard deviation and analyzed using the one-way analysis of variance (ANOVA) or t-test. Differences were statistically significant when $P<0.05$.

Results

CrTX inhibited A549 cell proliferation *in vitro*

A549 cells were treated with CrTX 25, 50, 100, or 200 μg/mL for 48 h, and the viability of the cells was determined using the MTT assay. The results show that CrTX significantly inhibits the growth of A549 cells with an IC_{50} value of 78 μg/mL in a concentration-dependent manner. The CrTX-induced inhibition rates were 87.5% (200 μg/mL), 53.2% (100 μg/mL), 24.1% (50 μg/mL), and 15.7% (25 μg/mL) (Table 1).

CrTX induced cell apoptosis and arrested cells in G_1 phase

To further understand the mechanism of CrTX in cell growth inhibition, flow cytometric assays were used to analyze cell apoptosis and cell cycle arrest. After treatment with CrTX (25 μg/mL) for 24 h, a significantly increased population

Table 1. The effect of CrTX on A549 cell proliferation. $^{b}P<0.05$ compared with control group.

CrTX concentration (μg/mL)	Inhibition rate (%)
Control	
25	15.7±3.4[b]
50	24.1±1.0[b]
100	53.2±12.0[b]
200	87.5±9.2[b]

of cells was halted at the sub-G_0 phase, which is an index of cell apoptosis, compared to the control group (Table 2). The results suggest that CrTX potently induces apoptosis in A549 cells, which suggests a potential mechanism for growth inhibition. To assess this mechanism for apoptosis, A549 cells were pretreated with SB203580, which is a specific P38MAPK inhibitor, and then treated with CrTX. No significant differences were observed in the sub-G_0 phase cell population (Table 2). The results show that SB203580 protects A549 cells from apoptosis, indicating that P38MAPK plays an important role in CrTX-induced cell apoptosis. In addition, CrTX significantly increased A549 cells in the G_1 phase compared to the control group (Table 2). SB203580 failed to alter CrTX-induced arrest of A549 cells in the G_1 phase, suggesting that inhibition of P38MAPK has no effect on CrTX-induced cell cycle arrest (Table 2).

Table 2. Analysis of CrTX-induced apoptosis and cell cycle arrest of A549. $^{b}P<0.05$ compared with control group.

Groups	Sub-G_0 (%)	G_0/G_1 (%)	S (%)	G_2/M (%)
Control	0.70±0.06	55.82±2.15	30.15±1.32	13.95±0.85
CrTX	11.42±1.02[b]	76.85±2.30[b]	16.04±0.52	6.80±030
SB203580	0.516±0.03	54.71±1.64	29.45±086	14.68±0.92
SB203580+CrTX	0.87±0.08	75.06±1.83[b]	15.36±0.71	9.08±0.52

Effects of CrTX on p53, caspase-3 and cleaved caspase-3, total P38MAPK and pP38MAPK expression

A549 cells were treated with 25 μg/mL of CrTX for 24 h and harvested for Western blot analysis for pro-apoptotic proteins. As shown in Figure 1, CrTX significantly increased cleaved caspase-3 in A549 cells. CrTX also increased the wild type p53 and phospho-P38MAPK levels without affecting the total P38MAPK levels in A549 cells. After pre-treating cells with SB203580, phospho-P38MAPK levels were reduced to control levels. Meanwhile, CrTX-induced production of cleaved caspase 3 was also inhibited, suggesting that CrTX-induced apoptosis was regulated by P38MAPK. However, the expression of wild type p53 remained high in the presence of SB203580 (Figure 1).

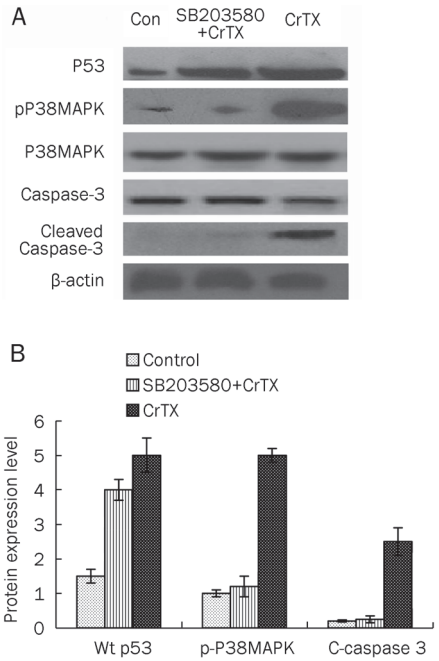

Figure 1. Expression of wild-type p53, caspase-3 and cleaved caspase-3, total P38MAPK and pP38MAPK protein in A549 cells. Cells were treated with 25 μg/mL of CrTX or 5 μmol/L of SB203580 plus 25 μg/mL of CrTX for 24 h. (A) Cell lysates were then collected for Western blot analysis on p53, caspase-3 and cleaved caspase-3, total P38MAPK and pP38MAPK. β-actin was used as loading control. (B) Protein levels of p53, phospho-P38MAPK and cleaved caspase-3 were analyzed and shown in bar graph.

CrTX inhibited A549 tumor growth *in vivo*

The anti-tumor activity of CrTX was tested in the A549 lung tumor xenograft model. As shown in Figure 2A, CrTX at a biweekly dosage of 10 μg/kg for 4 weeks had an efficacy effect on the A549 xenograft with 36.3% tumor growth inhibition (TGI) and no significant body weight loss. The observed *in vivo* activity of CrTX was consistent with its *in vitro* anti-proliferation effect on A549 cells. Further analysis showed that CrTX destroyed the blood vessels surrounding the tumor xenograft, which was indicated by the decrease in microvascular density (MVD) from 34.29±8.64 to 13.56±3.27 (Figure 2B). To understand the potential mechanism of CrTX in tumor angiogenesis, the VEGF level was analyzed using ELISAs with mouse sera from both groups. Interestingly, the VEGF level was also decreased in the CrTX treatment group (32.57±10.35 pg/mL) compared to the control group (46.83±13.62 pg/mL) (Figure 2C), suggesting that anti-angiogenesis might also contribute to the anti-tumor activity of CrTX *in vivo*.

Discussion

In this study, the anti-tumor effects of CrTX on A549 cells were verified and appeared to be dose-dependent. The results of flow cytometry show that CrTX significantly increased the cell population in the sub-G_0 and G_0/G_1 phases, which indicates that the anti-tumor effects of CrTX were closely related to the

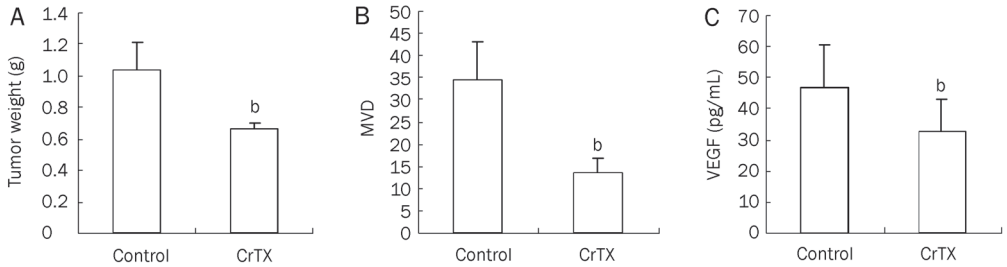

Figure 2. *In vivo* study of CrTX in A549 tumor xenograft model. Five million A549 cells were implanted into female nude mice subcutaneously. When the tumor reached about 5–6 mm in diameter, the tumor-bearing mice were randomized into 2 groups with 8 mice in each group and treated with vehicle control and CrTX (10 μg/kg, ip, twice a week). (A) After 4 weeks treatment, the mice were sacrificed, and the tumor xenografts were removed, sectioned and weighted. (B) Tumor xenografts were observed under microscope and microvascular density (MVD) was counted by Weidner methods. (C) In the meanwhile, 0.5 mL of blood was harvested from each mouse and 0.2 mL of serum was collected after centrifuging for 10 min at 3000 r/min. VEGF level was thus analyzed in each serum sample by ELISA. Data from each mouse sample were analyzed and shown in bar graph with statistic analysis as mean±SD. $^{b}P<0.05$.

induction of apoptosis and cell cycle arrest.

Many studies have investigated the signaling pathways that are mediated by P38MAPK, which is one of the main signal transduction systems regulating apoptosis[9, 10]. Cells transmit extracellular signals to the nucleus using P38MAPK[11]. Ultraviolet radiation, TNF or anti-tumor drugs induce pathway activation, which leads to P38MAPK phosphorylation. Therefore, these data suggest that P38MAPK plays an important role in cell apoptosis and cell cycle arrest[12, 13].

Caspase 3, which is a proteolytic enzyme, exists in an inactive proenzyme form in cells. As a central apoptotic effector, it plays a key role in promoting apoptosis[14]. After cleaving caspase-3, the active form of caspase 3 is released, indicating that the caspase 3 proenzyme is activated and has begun to execute its apoptotic function[15].

Previous studies have suggested that CrTX induces autophagy in human breast cancer MCF7 cells as a main mechanism for CrTX-induced cytotoxic effects[16]. In this study, we determined that CrTX induced cell apoptosis and cell cycle arrest in lung cancer A549 cells, suggesting distinct mechanisms for various types of cells. During the process of CrTX-induced apoptosis of A549 cells, we found that phospho-P38MAPK was upregulated and that the expression of wt p53 and cleaved caspase-3 increased. These results indicate that the anti-tumor effects of CrTX are strongly correlated with the activation of P38MAPK, the upregulation of wt p53 and the activation of caspase 3[17–19]. We investigated whether CrTX-induced apoptosis and G_1 arrest were mediated by the P38MAPK pathway by pretreating cells with SB203580, which is a pyridine glyoxaline compound and specific inhibitor of the P38MAPK pathway that has been verified using both *in vitro* and *in vivo* models[20]. CrTX-induced apoptosis was attenuated in A549 cells following pretreatment with SB203580. The sub-G_0 peak decreased from 11.42% to 0.87%. However, G_1 arrest did not change. Western blot analysis revealed that SB203580 pretreatment suppressed the CrTX-induced expression of active caspase 3, but not wt p53. These results suggest that the mechanism of CrTX to induce apoptosis is mediated by P38MAPK activation, which probably mediates caspase-3 activation.

A549 cells are human lung adenocarcinoma cells, which express wild type p53. The CrTX-induced upregulation of wild type p53 was confirmed using Western blot analysis. We propose that the effects of CrTX on G_1 arrest are probably due to the upregulation of wt p53. Meanwhile, SB203580 had no effect on CrTX-induced G_1 arrest and p53 induction. Therefore, these results suggest that the P38MAPK pathway is not involved in p53 upregulation.

A close and complex relationship is evident between tumor cell apoptosis and cell cycle arrest[21]. Although apoptosis and cell cycle arrest complement each other by inhibiting tumor progression, the effects of CrTX on tumor cell apoptosis and G_1 arrest are achieved via distinct intracellular pathways. Our results demonstrate that the induction of apoptosis by CrTX is due to the activation of P38MAPK and caspase 3, whereas G_1 arrest is possibly due to the upregulation of wt p53.

Acknowledgements

This work was supported by the National Natural Science Foundation of China (No 30772560).

Author contribution

Jing-kang HE and Zheng-hong QIN designed research; Bin YE performed research; Bin YE and Yan XIE wrote the paper; Zheng-hong QIN and Jun-chao WU polished the paper; Jun-chao WU and Rong HAN analyzed data.

References

1 Kattah LR, Ferraz V, Matos Santoro M, Ribeiro da Silva Camargos E, Ribeiro Diniz C, De Lima ME. Analysis of fatty acids released by crotoxin in rat brain synap twosomes. Toxicon 2002; 40: 43–9.

2 Picolo G, Cury Y. Peripheral neuronal nitric oxide synthase activity mediates antinociceptive effect of *Crotalus durissus* snake venom, a delta and kappa opioid receptor agonist. Life Sci 2004; 75: 559–73.

3 Yan CH, Liang ZQ, Gu ZL, Yang YP, Reid P, Qin ZH. Contributions of autophagic and apoptotic mechanisms to CrTX-induced death of K562 cells. Toxicon 2006; 47: 521–30.

4 Penzo D, Petronilli V, Angelin A, Cusan C, Colonna R, Scorrano L, *et al*. Arachidonic acid released by phospholipase A(2) activation triggers Ca(2+)-dependent apoptosis through the mitochondrial pathway. J Biol Chem 2004; 279: 25219–25.
5 Donato NJ, Martin CA, Perez M, Newman RA, Vidal JC, Etcheverry M. Regulation of epidermal growth factor receptor activity by CrTX, a snake venom phospholipase A2 toxin. Biochem Pharmacol 1996; 51: 1535–42
6 Dempke WC, Suto T, Reck M. Targeted therapies for non-small cell lung cancer. Lung Cancer 2010; 67: 257–74.
7 Collins DM, Crown J, O'Donovan N, Devery A, O'Sullivan F, O'Driscoll L, *et al*. Tyrosine kinase inhibitors potentiate the cytotoxicity of MDR-substrate anticancer agents independent of growth factor receptor status in lung cancer cell lines. Invest New Drugs 2010; 28: 433–44.
8 Newman RA, Vidal JC, Viskatis LJ, Johnson J, Etcheverry MA. VRCTC-310--a novel compound of purified animal toxins separates antitumor efficacy from neurotoxicity. Invest New Drugs 1993; 11: 151–9.
9 Ellinger-Ziegelbauer H, Kelly K, Siebenlist U. Cell cycle arrest and reversion of Ras induced transformation by a conditionally activated form of mitogen-activated protein kinase kinase kinase 3. Mol Cell Biol 1999; 19: 3857–68.
10 Maj JG, Kankofer M. Activity of 72-kDa and 92-kDa matrix metalloproteinases in placental tissues of cows with and without retained fetal membranes. Placenta 1997; 18: 683–7.
11 Ichijo H. From receptor to stress-activated MAP kinases. Oncogene 1999; 18: 6087–93.
12 Martin-Blanco E. p38MAPK signalling cascades: ancient roles and new function. Bioessays 2000; 22: 637–45.
13 Ono k, Han J. The p38 signal transduction pathway: activation and function. Cell Signal 2000; 12: 1–13.
14 Tawa P, Hell K, Giroux A, Grimm E, Han Y, Nicholson DW, *et al*. Catalytic activity of caspase-3 is required for its degradation: stabilization of the active complex by synthetic inhibitors. Cell Death Differ 2004; 11: 439–47.
15 An S, Park MJ, Park IC, Hong SI, Knox K. Procaspase-3 and its active large subunit localized in both cytoplasm and nucleus are activated following application of apoptotic stimulus in Ramos-Burkitt lymphoma B cells. Int J Mol Med 2003; 12: 311–7.
16 Yan CH, Yang YP, Qin ZH, Gu ZL, Reid P, Liang ZQ. Autophagy is involved in cytotoxic effects of crotoxin in human breast cancer cell line MCF-7 cells. Acta Pharmacol Sin 2007; 28: 540–8
17 Kim KW, Kim BJ, Chung CW, Jo DG, Kim IK, Song YH, *et al*. Caspase cleavage product lacking amino-terminus of Ikappa Balpha sensitizes resistant cells to TNF-alpha and TRALL induced apoptosis. J Cell Biochem 2002; 85: 334–45.
18 Lee JC, Kassis S, Kumar S. p38Mitogen-activated protein kinase inhibitors mechanisms and therapeutic potentials. Pharmacol Ther 1999; 82: 389–97.
19 Vogelstein B, Lane D, Levine AJ. Surfing the P53 network. Nature 2000; 408: 307–10.
20 Su JC, Lin KL, Chien CM, Lu CM, Chen YL, Chang LS, *et al*. Novel indoloquinoline derivative, IQDMA, induces G_2/M phase arrest and apoptosis in A549 cells through JNK/p38 MAPK signaling activation. Life Sci 2009; 85: 505–16.
21 Yang PM, Huang WC, Lin YC, Huang WY, Wu HA, Chen WL, *et al*. Loss of IKKbeta activity increases p53 stability and p21 expression leading to cell cycle arrest and apoptosis. J Cell Mol Med 2010; 14: 687–98.

Acta Pharmacologica Sinica (2011) 32: 1402–1410
 1671-4083/11 $32.00
www.nature.com/aps

Original Article

Curcumin enhanced antiproliferative effect of mitomycin C in human breast cancer MCF-7 cells *in vitro* and *in vivo*

Qian-mei ZHOU#, Xiu-feng WANG#, Xin-jun LIU, Hui ZHANG, Yi-yu LU, Shi-bing SU*

Research Center for Traditional Chinese Medicine Complexity System, Shanghai University of Traditional Chinese Medicine, Shanghai 201203, China

Aim: To investigate the efficacy of mitomycin C (MMC) in combination with curcumin in suppressing human breast cancer *in vitro* and *in vivo*.

Methods: Human breast cancer MCF-7 cells were used. Cell viability was measured using MTT assay. The cell cycle phase was detected with flow cytometric analysis. Cell cycle-associated proteins were examined using Western blot analysis. MCF-7 breast cancer xenografts were established to monitor tumor growth and cell cycle-associated protein expression.

Results: Curcumin inhibited MCF-7 breast cancer cell viability in a concentration-dependent manner (IC_{50} value=40 μmol/L). Similarly, MMC inhibited the cell viability with an IC_{50} value of 5 μmol/L. Combined treatment of MMC and curcumin showed a synergistic antiproliferative effect. In the presence of curcumin (40 μmol/L), the IC_{50} value of MMC was reduced to 5 μmol/L. In MCF-7 xenografts, combined administration of curcumin (100 mg/kg) and MMC (1–2 mg/kg) for 4 weeks produced significantly greater inhibition on tumor growth than either treatment alone. The combined treatment resulted in significantly greater G_1 arrest than MMC or curcumin alone. Moreover, the cell cycle arrest was associated with inhibition of cyclin D1, cyclin E, cyclin A, cyclin-dependent kinase 2 (CDK2) and CDK4, along with the induction of the cell cycle inhibitor p21 and p27 both in MCF-7 cells and in MCF-7 xenografts. These proteins were regulated through p38 MAPK pathway.

Conclusion: The results suggest that the combination of MMC and curcumin inhibits MCF-7 cell proliferation and cell cycle progression *in vitro* and *in vivo* via the p38 MAPK pathway.

Keywords: curcumin; mitomycin C; human breast cancer MCF-7 cells; combined chemotherapy; cell cycle; xenografts; p38 MAPK; cyclin; cyclin-dependent kinases (CDKs); p21

Acta Pharmacologica Sinica (2011) 32: 1402–1410; doi: 10.1038/aps.2011.97; published online 10 Oct 2011

Introduction

Cell growth and proliferation are tightly regulated by various interactions between molecules[1]. Several major checkpoints in the cell cycle are controlled by multiple protein kinases[2, 3]. The cyclin-dependent kinases (CDKs) join with regulatory proteins called cyclins to drive the cell through the cell cycle[4].

Specific complexes regulate each step of the cycle. Cyclin D1/CDK2 and CDK4 drive progression through G1, cyclin E/CDK2 controls entry into S phase, and cyclin A/CDK2 controls S-phase progression. CDK inhibitors (CDKIs) such as p21 and p27[5] block specific interactions. In many cell types, aberrant expression of cell cycle regulatory proteins can induce cell cycle progression[6, 7].

The mitogen-activated protein kinase (MAPK) family is activated in response to proliferative cues[8]. P38 MAPK is a major subfamily of mammalian MAPK. It has been reported that p38 MAPK activation is involved in the induction of a G_1/S checkpoint[9] that results in the accumulation of p21[10, 11]. Moreover, p21 establishes a G_1/S checkpoint by inactivating CDK2[10]. In addition, p38 MAPK can stabilize p21 *in vivo*[9] and can down-regulate the level of cyclin D1[12].

The cell cycle controls cell proliferation and cancer is a disease of inappropriate cell proliferation. The excess cells initiate a vicious cycle where cells are insensitive to the signals that are involved in adhesion, differentiation and death in normal cells[13]. Modulation of the cell cycle also contributes to oncotherapy. The majority of human breast cancers display deregulated overexpression of cyclin D1, whereas in normal cells its expression is tightly regulated by mitogenic signal-

#The first two authors contributed equally to this work.

* To whom correspondence should be addressed.
E-mail shibingsu@shutcm.edu.cn
Received 2011-03-15 Accepted 2011-06-23

ing involving the p21 Ras pathway[14]. Research on cell cycle progression and cell cycle regulatory proteins in human breast cancer cell lines has been performed in recent years[15, 16].

Curcumin (diferuloylmethane), a yellow colored polyphenol and a natural plant phenolic food additive, is an active component of the perennial herb *Curcuma longa* (commonly known as turmeric)[17]. Curcumin exhibits anti-cancer activities both *in vitro* and *in vivo* through a variety of mechanisms. It inhibits proliferation and induces apoptosis in a wide array of cancer cell types *in vitro*, including cells from cancers of the bladder, breast, lung and other tissues[18]. It also controls the cell cycle and causes cell cycle arrest in various cancers. Curcumin inhibited cell cycle progression through the downregulation of cyclin D1 *in vitro* and its transcriptional and translational levels *in vivo* and by blocking its association with CDK4[19]. It also induced cell cycle arrest through the upregulation of CDKIs such as p21 and p27[20, 21].

Mitomycin C (MMC) is currently used as the third-line chemotherapeutic agent for breast cancers[22]. Previous studies have shown that there are cell cycle alterations in response to MMC treatment[23, 24]. However, it is not clear whether curcumin in combination with MMC impacts breast cancer cell proliferation and cell cycle progression.

The present study sought to examine the combination treatment of curcumin and MMC-induced inhibition of cell growth and cell cycle arrest *in vitro* and *in vivo*. The p38 MAPK pathway was identified as a mechanism through which the combination treatment induced cell growth inhibition that was mediated via p21 and p27-induced cell cycle arrest.

Materials and methods

Materials

MMC was purchased from ICN Company (USA), dissolved in physiological saline as a 1 mmol/L stock solution and stored at 4 °C away from light. Curcumin, with a purity of more than 98%, was obtained from the National Institute for the Control of Pharmaceutical and Biological Products in China. Curcumin was dissolved in dimethyl sulfoxide (DMSO) as 40 mmol/L solution for use in the treatment of cells, and it was dissolved in a solution of physiological saline with 1% DMSO and 10% Tween-80 for use in animal research. SB203580 was obtained from Biomol (Philadelphia, PA, USA). The antibodies against cyclin D1, cyclin E, cyclin A, CDK2, CDK4, p21 and p27 were obtained from Cell Signaling Inc (Boston, MA, USA). The antibody against phosphorylated p38 (p-p38) was obtained from Santa Cruz Biotechnology (Santa Cruz, CA, USA). Propidium iodide (PI) was purchased from Sigma (St Louis, MO, USA).

Cell culture

Human breast cancer MCF-7 cells were obtained from the American Type Culture Collection (ATCC) (Manassas, VA, USA) and cultured in RPMI-1640 medium from Gibco (San Francisco, CA, USA) supplemented with 10% heat-inactivated (56 °C, 30 min) fetal calf serum (PAA, Pasching, KA, Austria), 0.01 mg/mL insulin from Sigma (St Louis, MO, USA), 2 mmol/L glutamine from Gibco (San Francisco, CA, USA), penicillin (100 U/mL) and streptomycin (100 μg/mL). The cell culture was maintained at 37 °C with 5% CO_2 in a humidified atmosphere.

Cell viability assays

MCF-7 cells were seeded in 96-well culture plates (5×10^4 cells/mL). After overnight incubation, MCF-7 cells were treated with various concentrations of MMC, curcumin, or MMC plus curcumin (the ratio of two compounds was 1:1). DMSO was adjusted to the same final concentration of 0.01%. Following incubation, cell viability was measured at different time points using the 3-(4,5-dimethylthiazol-2-yl)-2,5-diphenyltetrazolium bromide assay (MTT) as described previously[25]. The formazan product was quantified by measuring the absorbance at 490 nm. The interaction between curcumin and MMC was analyzed by isobologram analysis described by Chou and Talalay[26]. The interaction of two compounds was quantified by determining the combination index (CI). From this analysis, the combined effects of the two drugs can be summarized as follows: the CI of less than, equal to or more than 1 indicate synergistic, additive or antagonistic effects, respectively.

Cell cycle analysis

MCF-7 cells were seeded into 10-cm dishes and treated with curcumin, MMC or a combination of the agents at the concentrations indicated. Cells were harvested 48 h after treatment. Detached cells were collected by centrifugation (100×*g*, 5 min). The attached cells were harvested by trypsinization. Cell pellets were washed with PBS and then fixed in ice-cold 70% ethanol. For cell cycle analysis, cells were recentrifuged and stained with propidium iodide (PI). Cell-cycle phase analysis was performed using a Becton Dickinson Facstar flow cytometer (San Jose, CA, USA) equipped with ModFit LT 3.0 software.

Western blot analysis

Whole cell lysate was loaded in each lane and separated by SDS-PAGE. Protein expression was detected using a primary antibody (1:1000, except p-p38 1:200) and secondary antibody (1:800) conjugated with horseradish peroxidase. Levels of cyclin D1, cyclin E, cyclin A, CDK2, CDK4, p21, p27, p38, p-p38, and GAPDH were analyzed in this manner. Chemiluminescence was observed by ECL (Pharmacia, Buckinghamshire, UK). Quantitative analysis of Western blotting was performed using Alpha Ease FC (FluorChem FC2) software. Using the analysis tools, we calculated the density ratio of each protein to GAPDH, the loading control.

Human tumor xenografts

Female nu/nu athymic mice (7 weeks old) were obtained from Chinese Academy of Sciences. The mice (five per cage) were housed in cages equipped with air filter lids and maintained under pathogen-limiting conditions. MCF-7 cells (1×10^7/mL) were inoculated into the mammary fat pads of the mice. Before inoculation, 17β-estradiol (1.7 mg) was intraperitone-

ally injected[27]. Once palpable tumors developed (approximately 2 weeks), mice were randomized to receive vehicle (physiological saline with 1% DMSO and 10% Tween-80 for curcumin, 100% physiological saline for MMC), curcumin (100 mg/kg), MMC (2 mg/kg), MMC (1.5 mg/kg), MMC (1 mg/kg) and a combination of both curcumin and MMC. All drugs were administered by intraperitoneal injection. There were eight tumor-bearing animals in each group and all tumors were harvested 28 d after treatment. The tumors were immediately removed, freed from connective and adipose tissue, and weighed. The animal protocols were preapproved by the ethical committee of our institution.

Statistical analysis

When appropriate, data were expressed as mean±SD. Data were analyzed by Student's *t*-test where appropriate. Statistical significance was set at $P<0.05$.

Results

The combined treatment of curcumin and MMC inhibits proliferation of MCF-7 cells in a synergistic manner

To investigate the inhibitory effect of the combined treatment of curcumin and MMC, MCF-7 cells were treated with or without various concentrations of curcumin or MMC for 48 h. The results of the MTT assay showed that curcumin significantly inhibited cell viability in a concentration-dependent manner; the 50% inhibiting concentration (IC_{50}) for curcumin was 40 μmol/L (Figure 1A). Therefore, the effect of MMC in combination with curcumin was investigated, and the dose of curcumin was fixed at the IC_{50} 40 μmol/L dose. Similarly, MMC inhibited the cell viability with an IC_{50} value of 5 μmol/L. Increasingdoses of MMC inhibited growth in MCF-7 cells, and the IC_{50} was shown to be 5 μmol/L (Figure 1B). Isobologram analysis revealed a CI<1 for curcumin at 40 μmol/L in combination with MMC at 2.5, 5, and 7.5 μmol/L, respectively, indicating a synergistic relationship between the treatments. Moreover, the combination treatment of 2.5 μmol/L MMC and 40 μmol/L curcumin reduced the cell viability by 20% as compared to 5 μmol/L MMC alone ($P<0.05$) (Figure 1B). Therefore, 40 μmol/L curcumin in combination with 2.5 μmol/L MMC was selected for additional experiments.

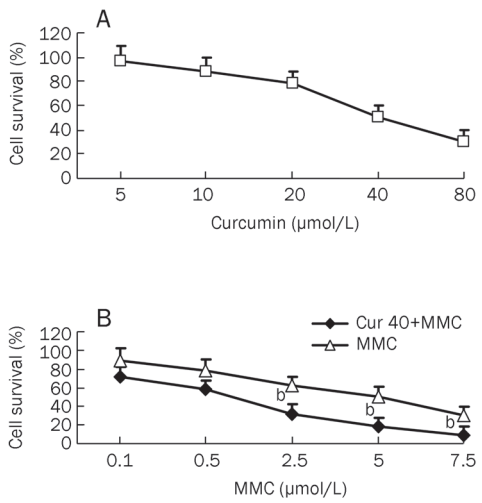

Figure 1. Survival of MCF-7 cells by combined treatment with curcumin and MMC. (A) MCF-7 cells were incubated with curcumin at doses of 5, 10, 20, 40, or 80 μmol/L for 48 h. (B) MCF-7 cells were treated with the combination of curcumin at 40 μmol/L and MMC at 0.1, 0.5, 2.5, 5, or 7.5 μmol/L for 48 h. $^bP<0.05$ *vs* 5 μmol/L MMC alone. Values are mean±SD from 3 independent experiments.

The combined treatment with curcumin and MMC induces a G_0/G_1 arrest in MCF-7 cells

Flow cytometry was performed to determine whether the cell growth inhibition mediated by the combined treatment of curcumin and MMC was due to a cell cycle arrest at a specific point in the cell cycle. Analysis of the untreated control cells showed 32.66% of cells in S phase and 48.36% of cells in G_1. Treatment with curcumin at 40 μmol/L inhibited the cells from entering S phase (32.66% to 23.79%) and caused a small increase in the number of cells in G_1 (48.36% to 51.51%). MMC at 2.5 μmol/L had a similar effect to untreated control with 33.03% of cells in S phase and 47.47% of cells in G_1. The combined treatment, however, resulted in a more robust G_1 arrest; only 18.62% of cells were in S phase and 71.17% of cells were in G_1. This cell cycle profile is indicative of a G_1 cell cycle arrest (Figure 2). The combined treatment of curcumin and MMC had a more complete G_0/G_1 arrest than curcumin ($P<0.05$) or MMC ($P<0.05$) alone in MCF-7 cells.

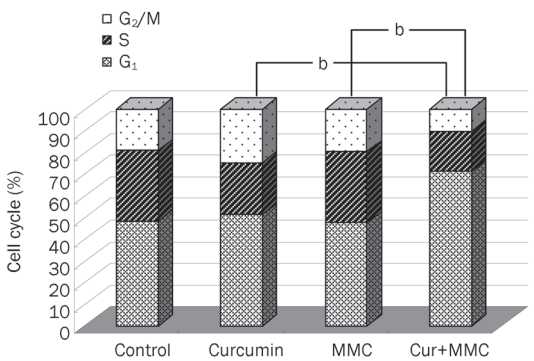

Figure 2. Curcumin in combination with MMC suppressed cell proliferation via a G_1 cell cycle arrest in MCF-7 cells. MCF-7 cells were treated with the combination of 40 μmol/L curcumin and 2.5 μmol/L MMC for 48 h. Cells were subjected to flow cytometric analysis to determine the effect of the combined treatment on cell cycle distribution. $^bP<0.05$ *vs* the combination of curcumin and MMC. Values are mean±SD from 3 independent experiments.

The cell cycle arrest is associated with the downregulation of cyclin D1, cyclin E, cyclin A, CDK2, and CDK4 and with the upregulation of p21 and p27 in MCF-7 cells

To determine whether the combination-induced growth inhibition of MCF-7 cells was due to the downregulation of cyclins and CDKs and the upregulation of CDKIs, the levels of cell cycle regulatory molecules were examined. The com-

bined treatment of curcumin and MMC in MCF-7 cells for 48 h resulted in 52%–68% reduction in the levels of cyclin D1, cyclin E and cyclin A, as well as CDK2 and CDK4 (Figure 3). The effect of the combined treatment on the induction of p21 and p27, which regulate progression of the cell cycle at the G_1-S phase transition checkpoint and are the inhibitors of CDKs, was also examined. The data showed that the combined drug treatment resulted in an approximately 2-fold increase of p21 and p27 as compared to the untreated control (Figure 3). However, the expression of p21 and p27 was increased approximately 1.4-fold by either curcumin or MMC alone.

To determine whether the effects of the combined treatment include activation of p38 MAPK, cells were exposed to the combination for 48 h, and an antibody specific for p-p38 was utilized. The results indicated that the level of p-p38 was reduced by 50% in response to the combined treatment. Both curcumin and MMC alone resulted in a nearly 20% decrease in the level of p-p38. These data show that the combined drug treatment affects p-p38.

The combination of curcumin and MMC regulates the expression of cell cycle-related proteins via the p38 MAPK pathway in MCF-7 cells

To assess the role of p38 MAPK in the combined treatment, cells were treated with the p38 MAPK-specific inhibitor, SB203580, alone or with additional drugs. The data showed that the combination treatment-decreased p-p38 was reversed by SB203580 (Figure 4A). Because p38 MAPK activity was decreased by the combined drug treatment, the role of cell cycle-related proteins in mediating p38 MAPK activity was investigated.

MCF-7 cells were pretreated for 2 h with or without 15 μmol/L SB203580, followed by exposure to 40 μmol/L curcumin in combination with 2.5 μmol/L MMC. As shown in Figure 4A, the combination-induced decrease in cyclin D1, cyclin E, CDK2 and CDK4 and the increase in p21 were reversed to the level of the SB203580 treatment alone. However, under similar experimental conditions, expression of cyclin A was unaffected, suggesting that cyclin A is not likely to be involved in the p38 MAPK-mediated cell cycle arrest that is induced by the combination treatment. Moreover, SB203580 demonstrated a slightly reversed effect on the combination-mediated p27 expression. These results strongly suggest that the p38 MAPK-signaling pathway is required for the G_1 phase cell cycle arrest in response to the combination treatment.

To investigate the effect of p38 MAPK activation on the combination-induced cell growth inhibition, MCF-7 cells were pretreated for 2 h with or without 15 μmol/L SB203580, followed by treatment with both curcumin and MMC alone or together. Cell viability was determined by the MTT assay (Figure 4B). After treatment with the combination of curcumin and MMC or curcumin and MMC alone, cell growth inhibition was approximately 70%, 51%, or 32%, respectively. However, this inhibitory effect was reversed by pretreatment with SB203580. These results suggest that the cell growth inhibition caused by the individual or combined treatments is dependent on the p38 MAPK pathway.

The combination of curcumin and MMC produces greater inhibition of tumor growth than either treatment alone in MCF-7 xenografts

Our *in vitro* data suggested a synergistic interaction between curcumin and MMC, we studied the antitumor activity of curcumin and MMC in mice bearing MCF-7 breast cancer xenografts. Animals were treated with MMC at a dose of 1, 1.5, or 2 mg/kg ip, with a curcumin dose of 100 mg/kg ip or with curcumin in combination with an MMC dose of 1, 1.5, or 2 mg/kg for 4 weeks. As shown in Figure 5A, the 2 mg/kg dose of MMC treatment alone produced a significant inhibition of tumor growth. The 2 mg/kg dose of MMC in com-

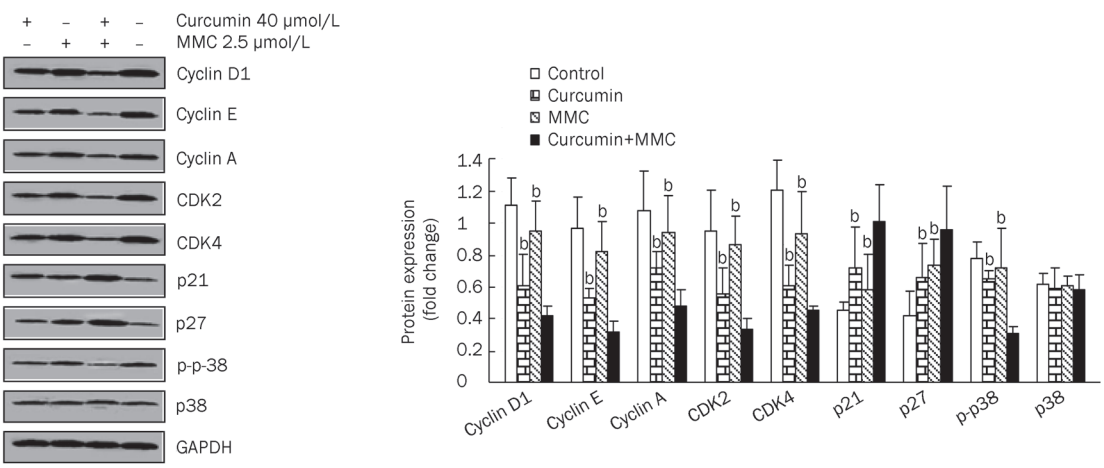

Figure 3. The combination treatment-induced cell cycle profile is associated with the downregulation of cyclin D1, cyclin E, cyclin A, CDK2, and CDK4 and upregulation of p21 and p27 in MCF-7 cells. MCF-7 cells were treated with both curcumin and MMC alone or together at the indicated concentrations for 48 h and Western blot analysis was performed with antibodies specific to cyclin D1, cyclin E, cyclin A, CDK2, CDK4, p21, p27, and p-p38. The density ratio of proteins to GAPDH was shown as a relative expression. $^bP<0.05$ *vs* the combination of curcumin and MMC. Values are mean±SD from 3 independent experiments.

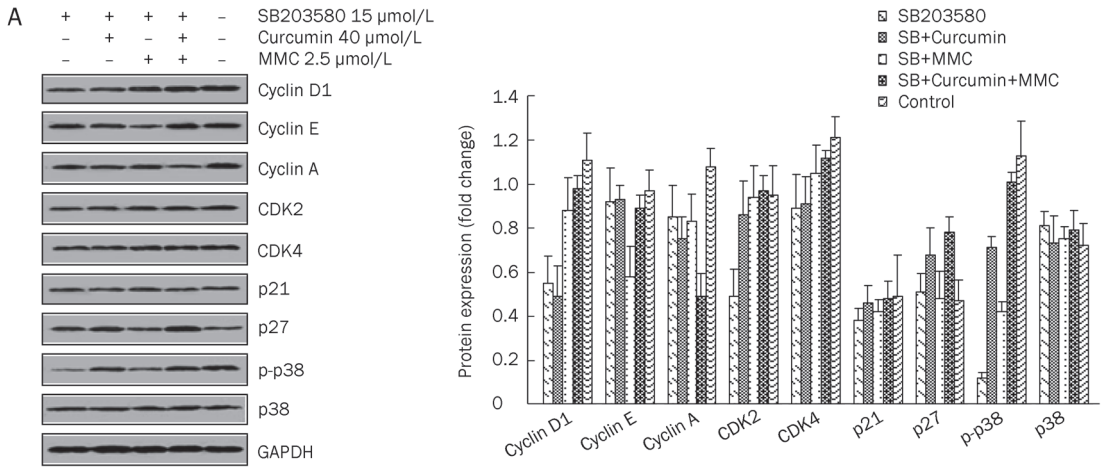

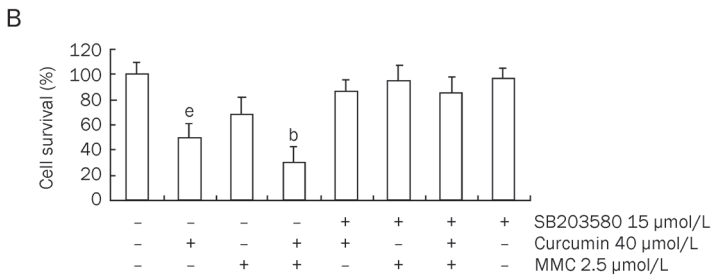

Figure 4. SB203580 reversed G_1 phase cell cycle-associated protein expression and decreased cell growth inhibition that was induced by the combination of curcumin and MMC. (A) MCF-7 cells were plated into plates and were preincubated for 2 h in the presence of SB203580 (15 μmol/L). Cells were then treated with both 40 μmol/L curcumin and 2.5 μmol/L MMC alone or together for 48 h, followed by Western blot analysis performed with antibodies specific to cyclin D1, cyclin E, cyclin A, CDK2, CDK4, p21, p27, and p-p38. The density ratio of proteins to GAPDH was shown as a relative expression. (B) MCF-7 cells were pretreated for 2 h with or without 15 μmol/L SB203580 before cells were treated with both 40 μmol/L curcumin and 2.5 μmol/L MMC alone or together for 48 h. The MTT assay was performed as described under materials and methods. Values are mean±SD from 3 independent experiments. $^bP<0.05$ *vs* untreated control. $^eP<0.05$ *vs* the combination of curcumin and MMC treatment.

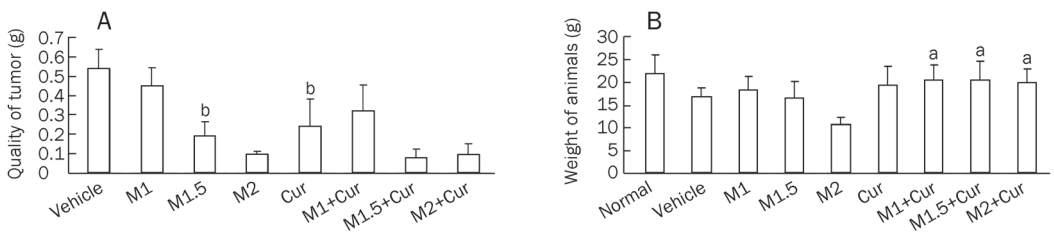

Figure 5. MMC treatment at 1, 1.5 or 2 mg/kg in combination with curcumin at 100 mg/kg produced effects on reducing tumor quality and body weight compared with either treatment alone. (A) The growth-inhibitory effect of MMC at 1 mg/kg (M1), 1.5 mg/kg (M1.5), and 2 mg/kg (M2), curcumin 100 mg/kg (Cur) and their combination on MCF-7 xenografts is shown. $^bP<0.05$ *vs* 1.5 mg/kg MMC in combination 100 mg/kg curcumin-treated group. (B) Body weights of MCF-7 xenografts were measured after animals were treated with or without MMC, curcumin or a combination for 4 weeks. $^aP>0.05$ *vs* normal group. Experiments were repeated with similar results.

bination with curcumin treatment also revealed a significant reduction in tumor growth. The combined treatment of a 1.5 mg/kg dose of MMC plus curcumin resulted in 60.4% and 68.6% reduction in tumor weight as compared to monotherapy with 1.5 mg/kg MMC and with curcumin , respectively. Treatment with a 1 mg/kg dose of MMC plus curcumin did not show more significant tumor suppression than curcumin alone. Thus, the combination of a 1.5 mg/kg dose of MMC plus a 100 mg/kg dose of curcumin produced a more robust and statistically significant tumor regression when compared with either 1.5 mg/kg MMC ($P<0.05$) or 100 mg/kg curcumin alone ($P<0.05$). Moreover, there was no difference between the untreated control and the combined treatment on the body weight of the animals ($P>0.05$) (Figure 5B). However, the 2

mg/kg MMC treatment resulted in significant weight loss. This weight loss suggests that curcumin probably improves MMC toxicity.

The combination of curcumin and MMC at a dose of 1.5 and 2 mg/kg, respectively, decreases the levels of cyclin D1, cyclin A, cyclin E, CDK2 and CDK4 and increases the expression of p21 and p27 in MCF-7 xenografts

To determine whether the inhibition of tumor growth of MCF-7 xenografts that was mediated by the combined treatment involved the regulation of cell cycle regulatory proteins, the tumors were harvested from each group and then analyzed using Western blot. As shown in Figure 6, the levels of cyclin D1, cyclin E, and cyclin A as well as CDK2 and CDK4 were all reduced by the combined treatment of curcumin and the various concentrations of MMC relative to either curcumin or various concentrations of MMC alone. Moreover, as compared to 100 mg/kg curcumin or 1.5 mg/kg MMC alone, the combined treatment of 100 mg/kg curcumin plus 1.5 mg/kg MMC resulted in a 19.7% or 48.4% decrease in the level of cyclin D1, 36.7% or 60.8% in cyclin E, 44.3% or 60% in cyclin A, 45.3% or 67.4% in CDK2 and 34.5% or 58.2% in CDK4, respectively. Similarly, the combination of 100 mg/kg curcumin plus 2 mg/kg MMC also decreased the levels of cyclin D1, cyclin E, cyclin A, CDK2, and CDK4 significantly. However, the combination of 100 mg/kg curcumin plus 1 mg/kg MMC did not affect the expression of these proteins significantly. Therefore, curcumin at 100 mg/kg in combination with MMC at 1.5 or 2 mg/kg alone both decreased the expression of cell cycle regulatory proteins more significantly than the other combination or single drug therapy.

Under similar experimental conditions, treatment with the combination of 100 mg/kg curcumin plus 1.5 mg/kg MMC resulted in a 15.5% or 48.6% increase in the level of p21 and 31.1% or 46.9% in p27 as compared to 100 mg/kg curcumin or 1.5 mg/kg MMC alone, respectively. The level of p21 was increased approximately 42.6% or 74.4%, and p27 was increased approximately 34.9% or 53.9% by the combination of 100 mg/kg curcumin plus 2 mg/kg MMC as compared to 100 mg/kg curcumin or 2 mg/kg MMC alone, respectively. In contrast, the combination of 100 mg/kg curcumin plus 1 mg/kg MMC did not affect the expression of p21 and p27 significantly. These results suggest that the combination of curcumin at 100 mg/kg plus MMC at 1.5 or 2 mg/kg enhances tumor growth inhibition by regulating these cell cycle-associated proteins.

To investigate whether the tumor growth inhibitory effects of the combination treatment include the activation of p38 MAPK, we analyzed the level of p-p38. Results indicated that the expression of p-p38 was significantly suppressed by the combined therapy (Figure 6), suggesting that the combination treatment also affects p-p38.

Discussion

MMC has been already used in the clinic, but it is currently used as the third-line chemotherapeutic agent in breast cancer[22]. Currently, much research has addressed the chemotherapeutic potential of curcumin (diferuloylmethane), which is a relatively nontoxic plant-derived polyphenol[28]. It has been reported that curcumin sensitizes cancer cells to cisplatin[29]. Moreover, our study showed that the combined treatment of curcumin and MMC reduced MMC side effects by inhibiting GRP58-mediated DNA cross-linking through the ERK/p38 MAPK pathway[30]. The exact mechanisms mediating the cell cycle changes that result from the combined treatment of curcumin and MMC have yet to be fully explained.

Treatment of MCF-7 cells with either curcumin (5–80 μmol/L) or MMC (0.1–7.5 μmol/L) alone resulted in cell

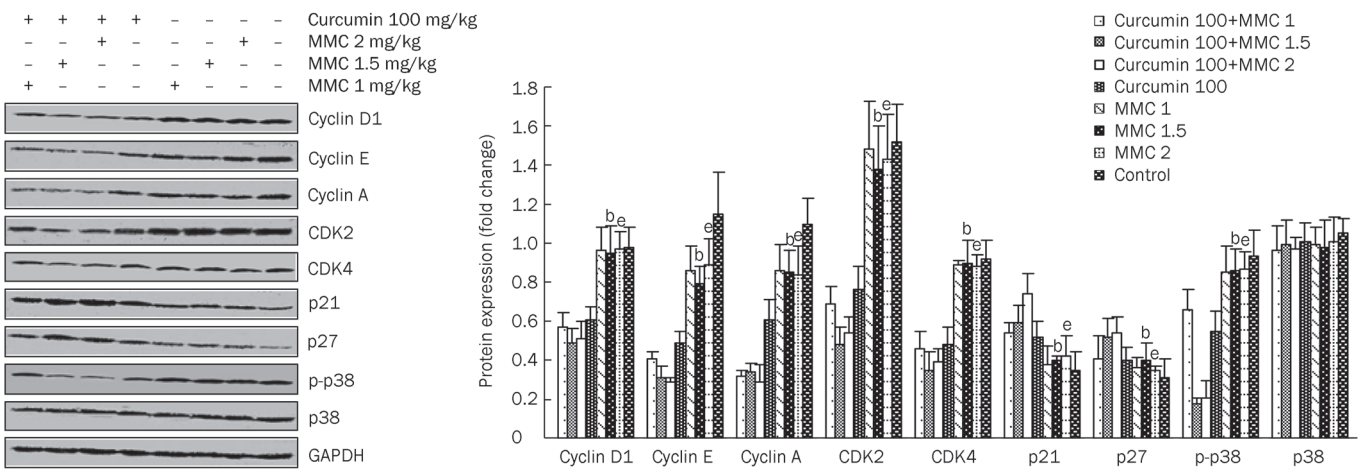

Figure 6. MMC treatment at 1, 1.5, or 2 mg/kg in combination with curcumin at 100 mg/kg downregulated the levels of cyclin D, cyclin E, cyclin A, CDK2, and CDK4 and upregulated p21 and p27 levels. The MCF-7 xenografts were treated with either curcumin at 100 mg/kg or MMC at 1, 1.5, and 2 mg/kg alone or in combination, and Western blot analysis was performed with antibodies specific to cyclin D1, cyclin E, cyclin A, CDK2, CDK4, p21, p27, and p-p38. The density ratio of proteins to GAPDH was shown as a relative expression. $^{b}P<0.05$ *vs* 1.5 mg/kg MMC in combination with 100 mg/kg curcumin-treated group. $^{e}P<0.05$ *vs* 2 mg/kg MMC in combination with 100 mg/kg curcumin-treated group. Values are mean±SD from 3 independent experiments.

growth inhibition in a dose-dependent manner (Figure 1), which was consistent with previously published data[31]. The combination of 40 μmol/L curcumin (IC_{50}) and 2.5 μmol/L MMC (IC_{50}) reduced cell viability approximately 20% as compared to 5 μmol/L MMC (IC_{50}) alone. Furthermore, isobologram analysis showed a strong synergistic interaction between 40 μmol/L curcumin and 2.5 μmol/L MMC. These results suggest that curcumin in combination with MMC (at a reduced dosage) enhances cell growth inhibition more significantly than MMC alone.

Cyclins are a family of proteins that control the progression of cells through the cell cycle by activating CDK enzymes[32]. Cyclin D1/CDK4 and cyclin E/CDK2 regulate transition in the G_1 phase. Cyclin A/CDK2 is activated from the G_1 phase to the S phase and from the S phase to the G_2 phase[33]. The results of this study indicate that the combination of curcumin and MMC induced a G_1 phase cell cycle arrest (Figure 2) and also led to a decrease in cyclin D1, cyclin E, cyclin A, CDK2, and CDK4, which are involved in cell cycle progression from the G_1 phase to the S phase. Moreover, p21 and p27, which regulate progression of the cell cycle at the G_1-S transition checkpoint, were significantly upregulated during the G_1 phase arrest in MCF-7 cells that were treated with the combination therapy. Notably, the combination therapy significantly inhibited the activation of p38 MAPK, suggesting that the combination treatment-induced suppression of p-p38 may also be responsible for G_1 phase arrest in MCF-7 cells.

Previous studies have demonstrated that p38 MAPK is involved in cell growth inhibition and the regulation of the cell cycle[34, 35]. The p38 MAPK pathway induced a G_1 and G_2/M cell cycle arrest, which was associated with increased p21 levels and reduced amounts of cyclin A[36, 37]. In this study, curcumin in combination with MMC resulted in the down-regulation of phosphorylated p38 MAPK. Moreover, the combined treatment regulated the expression of cyclin D1, cyclin E, CDK2, CDK4, and p21, and this regulation was reversed by the p38 MAPK-specific inhibitor SB203580. Robust p38 MAPK stimulation has been reported to suppress cell cycle progression via induction of the cell cycle inhibitor protein p21[38, 39]. The results of the present study suggest that p38 MAPK signaling is involved in the cell growth inhibition that is induced by combined therapy through the regulation of cyclin D1, cyclin E, CDK2, CDK4, and p21 in MCF-7 cells.

It has been reported that both curcumin[40, 41] and MMC[42, 43] alone inhibit tumor growth in different cancers. This study has presented the first example of the effects of the combined curcumin and MMC therapy in MCF-7 xenografts. In the present study, we confirmed the antitumor effect of MMC when given for a longer period of time and additionally showed that curcumin also led to tumor stasis. These results were consistent with results of previous studies[38–41]. Notably, the data also showed that the combination of 100 mg/kg curcumin and 1.5 mg/kg MMC was more effective than either drug alone at inhibiting MCF-7 tumor growth (Figure 5).

However, 100 mg/kg curcumin in combination with 2 mg/kg MMC did not show more significant tumor growth inhibition than 2 mg/kg MMC alone. The most likely cause of this condition was that the effects of 100 mg/kg curcumin were masked by the 2 mg/kg MMC. For the same reason, the combination of 100 mg/kg curcumin and 1 mg/kg MMC was not more effective than 100 mg/kg curcumin alone. The effects of 1 mg/kg MMC might be masked by 100 mg/kg curcumin. Moreover, the body weight of the animals was reverted to the level of the untreated control with the addition of curcumin with a range of concentrations of MMC. In contrast, treatment of MMC alone reduced body weight significantly. These results suggest that the administration of 100 mg/kg curcumin together with 1.5 mg/kg MMC was an equally effective combination.

To explain the effects and the mechanism of action of the combined treatment of curcumin and MMC *in vivo*, the levels of cyclin D1, cyclin E, cyclin A, CDK2, CDK4, p21, and p27 were examined in MCF-7 xenografts. The data indicated that the levels of cyclin D1, cyclin E and cyclin A as well as CDK2 and CDK4 were decreased and that the levels of p21 and p27 were increased by the combined treatment with 100 mg/kg curcumin and 1.5 mg/kg MMC (Figure 6). Moreover, the activation of p38 MAPK was significantly suppressed by the combined treatment. Therefore, it further demonstrated that 100 mg/kg curcumin plus 1.5 mg/kg MMC inhibited tumor growth through regulating the levels of cyclin D1, cyclin E, cyclin A, CDK2, CDK4, p21, and p27. This regulatory effect was involved in the p38 MAPK pathway.

We characterized the effects and the mechanism of action of the combined treatment of curcumin and MMC in breast cancer models *in vitro* and *in vivo*. The results in this study suggest the following of the combined treatment: (1) it increases the anti-proliferative ability while reducing the dosage needed of MMC alone; (2) it enhances G_1 arrest through the modulation of cyclin D1, cyclin E, cyclin A, CDK2, CDK4, p21, and p27; and (3) it inhibits MCF-7 cell proliferation and cell cycle progression *in vitro* and *in vivo* via the p38 MAPK pathway. Therefore, this combined therapy may be beneficial in the treatment of breast cancer.

Acknowledgements

This work was financially supported by the National S&T Major Project of China (No 2009ZX10004-601 and 2009ZX09311-003) and by the Leading Academic Discipline Project of Shanghai Municipal Education Commission (No J50301), E-institutes of Shanghai Municipal Education Commission (No E 03008).

Author contribution

Shi-bing SU designed the experiments and proofread the manuscript. Qian-mei ZHOU performed the Western blot analysis, apoptosis and proliferation assays, interpreted the results, generated the figures and wrote the manuscript. Xiu-feng WANG, Hui ZHANG and Xin-jun LIU assisted with animal experiments and provided many useful discussions on experiments. Yi-yu LU analyzed data. All authors assisted in revision of and approved the final manuscript.

References

1 Choudhuri T, Pal S, Das T, Sa G. Curcumin selectively induces apoptosis in deregulated cyclin D1-expressed cells at G_2 phase of cell cycle in a p53-dependent manner. J Biol Chem 2005; 280: 20059–68.
2 Sherr CJ. Cancer cell cycles. Science 1996; 274: 1672–7.
3 Hall M, Peters G. Genetic alterations of cyclins, cyclin-dependent kinases, and Cdk inhibitors in human cancer. Adv Cancer Res 1996; 68: 67–108.
4 Dickson MA, Schwartz GK. Development of cell-cycle inhibitors for cancer therapy. Curr Oncol 2009; 16: 36–43.
5 Sherr CJ, Roberts JM. cdk inhibitors: positive and negative regulators of G_1-phase progression. Genes Dev 1999; 13: 1501–12.
6 Evan GI, Wyllie AH, Gilbert CS, Littlewood TD, Land H, Brooks M, *et al*. Induction of apoptosis in fibroblasts by c-myc protein. Cell 1992; 69: 119–28.
7 Sofer-Levi Y, Resnitzky D. Apoptosis induced by ectopic expression of cyclin D1 but not cyclin E. Oncogene 1996; 13: 2431–7.
8 Karin M, Hunter T. Transcriptional control by protein phosphorylation: signal transmission from the cell surface to the nucleus. Curr Biol 1995; 5: 747–57.
9 Tina M, Mercedes T. RinconNon-classical P38 map kinase functions: cell cycle checkpoints and survival. Int J Biol Sci 2009; 5: 44–52.
10 Kim GY, Mercer SE, Ewton DZ, Yan Z, Jin K, Friedman E. The stress-activated protein kinases p38 alpha and JNK1 stabilize p21(Cip1) by phosphorylation. J Biol Chem 2002; 277: 29792–802.
11 Kishi H, Nakagawa K, Matsumoto M, Suga M, Ando M, Taya Y, Yamaizumi M. Osmotic shock induces G_1 arrest through p53 phosphorylation at Ser33 by activated p38MAPK without phosphorylation at Ser15 and Ser20. J Biol Chem 2001; 276: 39115–22.
12 Lavoie JN, L''Allemain G, Brunet A, Müller R, Pouysségur J. Cyclin D1 expression is regulated positively by the p42/p44MAPK and negatively by the p38/HOGMAPK pathway. J Biol Chem 1996; 271: 20608–16.
13 Collins K, Jacks T, Pavletich NP. The cell cycle and cancer. Proc Natl Acad Sci USA 1997; 94: 2776–8.
14 Yu Q, Geng Y, Sicinski P. Specific protection against breast cancers by cyclin D1 ablation. Nature 2001; 411: 1017–21.
15 Martin LA, Head JE, Pancholi S, Salter J, Quinn E, Detre S, *et al*. The farnesyltransferase inhibitor R115777 (tipifarnib) in combination with tamoxifen acts synergistically to inhibit MCF-7 breast cancer cell proliferation and cell cycle progression *in vitro* and *in vivo*. Mol Cancer Ther 2007; 6: 2458–67.
16 Sun J, Hai Liu R. Cranberry phytochemical extracts induce cell cycle arrest and apoptosis in human MCF-7 breast cancer cells. Cancer Lett 2006; 241: 124–34.
17 Kunnumakkara AB, Anand P, Aggarwal BB. Curcumin inhibits proliferation, invasion, angiogenesis and metastasis of different cancers through interaction with multiple cell signaling proteins. Cancer Lett 2008; 269: 199–225.
18 Aggarwal BB, Kumar A, Bharti AC. Anticancer potential of curcumin: preclinical and clinical studies, Anticancer Res 2003; 23: 363–98.
19 Choudhuri PS, Das T, Sa G. Curcumin selectively induces apoptosis in deregulated cyclin D1-expressed cells at G_2 phase of cell cycle in a p53-dependent manner, J Biol Chem 2005; 20: 20059–68.
20 Park MJ, Kim EH, Park IC, Lee HC, Woo SH, Lee JY, *et al*. Curcumin inhibits cell cycle progression of immortalized human umbilical vein endothelial (ECV304) cells by up-regulating cyclin-dependent kinase inhibitor, $p21^{WAF1/CIP1}$, $p27^{KIP1}$ and p53. Int J Oncol 2002; 21: 379–83.
21 Srivastava RK, Chen Q, Siddiqui I, Sarva K, Shankar S. Linkage of curcumin-induced cell cycle arrest and apoptosis by cyclin-dependent kinase inhibitor p21(/WAF1/CIP1). Cell Cycle 2007; 6: 2953–61.
22 Chalasani P, Kurtin S, Dragovich T. Response to a third-Line mitomycin C (MMC)-based chemotherapy in a patient with metastatic pancreatic adenocarcinoma carrying germline BRCA2 mutation. JOP 2008; 9: 305–8.
23 Kang SG, Chung H, Yoo YD, Lee JG, Choi YI, Yu YS. Mechanism of growth inhibitory effect of mitomycin-C on cultured human retinal pigment epithelial cells: apoptosis and cell cycle arrest. Curr Eye Res 2001; 22: 174–81.
24 Sánchez P, Llorente MT, Castaño A. Flow cytometric detection of micronuclei and cell cycle alterations in fish-derived cells after exposure to three model genotoxic agents: mitomycin C, vincristine sulfate and benzo(a)pyrene. Mutat Res 2000; 465: 113–22.
25 Mosmann T. Rapid colorimetric assay for cellular growth and survival: application to proliferation and cytotoxicity assays. J Immunological Methods 1983; 65: 55–63.
26 Chou TC, Talalay P. Quantitative analysis of dose-effect relationships: the combined effects of multiple drugs or enzyme inhibitors. Adv Enzyme Regul 1984; 22: 27–55.
27 Chen J, Hui E, Ip T, Thompson LU. Dietary flaxseed enhances the inhibitory effect of tamoxifen on the growth of estrogen-dependent human breast cancer (MCF-7) in nude mice. Clin Cancer Res 2004; 10: 7703–11.
28 Campbell FC, Collett GP. Chemopreventive properties of curcumin. Future Oncol 2005; 1: 405–14.
29 Chanvorachote P, Pongrakhananon V, Wannachaiyasit S, Luanpitpong S, Rojanasakul Y, Nimmannit U. Curcumin sensitizes lung cancer cells to cisplatin-induced apoptosis through superoxide anion-mediated Bcl-2 degradation. Cancer Invest 2009; 27: 624–35.
30 Zhou QM, Zhang H, Lu YY, Wang XF, Su SB. Curcumin reduced the side effects of mitomycin C by inhibiting GRP58-mediated DNA cross-linking in MCF-7 breast cancer xenografts. Cancer Sci 2009; 100: 2040–5.
31 Choudhuri T, Pal S, Agwarwal ML, Das T, Sa G. Curcumin induces apoptosis in human breast cancer cells througeh p53-dpendent Bax induction. FEBS Lett 2002; 12: 334–40.
32 Galderisi U, Jori FP, Giordano A. Cell cycle regulation and neural differentiation. Oncogene 2003; 22: 5208–19.
33 Fung TK, Poon RY. A roller coaster ride with the mitotic cyclins. Semin Cell Dev Biol 2005; 16: 335–42.
34 Neve RM, Holbro T, Hynes NE. Distinct roles for phosphoinositide 3-kinase, mitogen-activated protein kinase and p38 MAPK in mediating cell cycle progression of breast cancer cells. Oncogene 2002; 21: 4567–76.
35 Hsu YL, Kuo PL, Lin LT, Lin CC. Asiatic acid, a triterpene, induces apoptosis and cell cycle arrest through activation of extracellular signal-regulated kinase and p38 mitogen-activated protein kinase pathways in human breast cancer cells. J Pharmacol Exp Ther 2005; 313: 333–44.
36 Lavelle D, DeSimone J, Hankewych M, Kousnetzova T, Chen YH. Decitabine induces cell cycle arrest at the G_1 phase via $p21^{(WAF1)}$ and the G_2/M phase via the p38 MAP kinase pathway. Leuk Res 2003; 27: 999–1007.
37 Zhang Z, Leonard SS, Huang C, Vallyathan V, Castranova V, Shi X. Role of reactive oxygen species and MAPKs in vanadate-induced G(2)/M phase arrest. Free Radic Biol Med 2003; 34: 1333-42.
38 Todd DE, Densham RM, Molton SA, Balmanno K, Newson C, Weston CR, Garner AP, Scott L, Cook SJ. ERK1/2 and p38 cooperate to induce a p21CIP1-dependent G1 cell cycle arrest. Oncogene 2004; 23: 3284–95.

39 Lee B, Kim CH, Moon SK. Honokiol causes the p21WAF1-mediated G(1)-phase arrest of the cell cycle through inducing p38 mitogen activated protein kinase in vascular smooth muscle cells. FEBS Lett 2006; 580: 5177–84.

40 Milacic V, Banerjee S, Landis-Piwowar KR, Sarkar FH, Majumdar AP, Dou QP. Curcumin inhibits the proteasome activity in human colon cancer cells *in vitro* and *in vivo*. Cancer Res 2008; 68: 7283–92.

41 Somers-Edgar TJ, Scandlyn MJ, Stuart EC, Le Nedelec MJ, Valentine SP, Rosengren RJ. The combination of epigallocatechin gallate and curcumin suppresses ER alpha-breast cancer cell growth *in vitro* and *in vivo*. Int J Cancer 2008; 122: 1966–71.

42 Dobrowsky W, Dobrowsky E, Wilson GD. *In vivo* cell kinetic measurements in a randomized trial of continuous hyperfractionated accelerated radiotherapy with or without mitomycin C in head-and-neck cancer. Int J Radiat Oncol Biol Phys 2003; 55: 576–82.

43 Ishihara M, Kubota T, Watanabe M, Kawano Y, Narai S, Yasui N, *et al*. Interferon gamma increases the antitumor activity of mitomycin C against human colon cancer cells *in vitro* and *in vivo*. Oncol Rep 1999; 6: 621–5.

Acta Pharmacologica Sinica (2011) 32: 1411–1418
 1671-4083/11 $32.00
www.nature.com/aps

Original Article

Yeast two-hybrid screening of proteins interacting with plasmin receptor subunit: C-terminal fragment of annexin A2

Qun LI[1, 2, *], Yves LAUMONNIER[2], Tatiana SYROVETS[2], Thomas SIMMET[2]

[1]Joint Laboratory of Vascular Biology of Ruijin Hospital, Health Science Center and Shanghai Institute of Hypertension, Shanghai Jiao Tong University School of Medicine, and Shanghai Institutes of Biological Sciences (SIBS), Chinese Academy of Sciences (CAS), Shanghai 200025, China; [2]Institute of Pharmacology of Natural Products and Clinical Pharmacology, Ulm University, D-89081 Ulm, Germany

Aim: To identify proteins that interact with the C-terminal fragment of annexin A2 (A2IC), generated by plasmin cleavage of the plasmin receptor, a heterotetramer (AA2t) containing annexin A2.
Methods: The gene that encodes the A2IC fragment was obtained from PCR-amplified cDNA isolated from human monocytes, and was ligated into the pBTM116 vector using a DNA ligation kit. The resultant plasmid (pBTM116-A2IC) was sequenced with an ABI PRISM 310 Genetic Analyzer. The expression of an A2IC bait protein fused with a LexA-DNA binding domain (BD) was determined using Western blot analysis. The identification of proteins that interact with A2IC and are encoded in a human monocyte cDNA library was performed using yeast two-hybrid screening. The DNA sequences of the relevant cDNAs were determined using an ABI PRISM BigDye terminator cycle sequencing ready reaction kit. Nucleotide sequence databases were searched for homologous sequences using BLAST search analysis (http://www.ncbi.nlm.nih.gov). Confirmation of the interaction between the protein LexA-A2IC and each of cathepsin S and SNX17 was conducted using a small-scale yeast transformation and X-gal assay.
Results: The yeast transformed with plasmids encoding the bait proteins were screened with a human monocyte cDNA library by reconstituting full-length transcription factors containing the GAL4-active domain (GAL4-AD) as the prey in a yeast two-hybrid approach. After screening 1×10^7 clones, 23 independent β-Gal-positive clones were identified. Sequence analysis and a database search revealed that 15 of these positive clones matched eight different proteins (SNX17, ProCathepsin S, RPS2, ZBTB4, OGDH, CCDC32, PAPD4, and actin which was already known to interact with annexin A2).
Conclusion: A2IC A2IC interacts with various proteins to form protein complexes, which may contribute to the molecular mechanism of monocyte activation induced by plasmin. The yeast two-hybrid system is an efficient approach for investigating protein interactions.

Keywords: yeast yeast two-hybrid system; human monocyte; plasmin receptor; C-terminal fragment of annexin A2 (A2IC); protein-protein interaction

Acta Pharmacologica Sinica (2011) 32: 1411–1418; doi: 10.1038/aps.2011.121; published online 3 Oct 2011

Introduction

Experiments with human peripheral blood monocytes and macrophages have yielded novel insight into plasmin-induced intracellular signaling[1, 2]. Plasmin first binds to the annexin A2 heterotetramer (AA2t), which triggers cleavage of annexin A2 at lysine 27. The heterotetramer complex then dissociates, initiating downstream signaling, which leads to functional responses such as chemotaxis and TNF-α/IL-6 release[2–4].

Several functional roles have been proposed for annexin A2, such as signal transduction, membrane fusion, cell adhesion, DNA synthesis, and cell proliferation[5, 6]. Annexin A2 is a 36 kDa protein that has been found on the surface of endothelial cells, monocytic cell lines and macrophages[7, 8]. Annexin A2 is a member of the annexin superfamily of calcium-dependent, phospholipid binding, multi-functional proteins[9], which binds acidic phospholipids and actin with high affinity[6].

Annexin A2 is cleaved by chymotrypsin and plasmin into a 33 kDa C-terminal core domain and a 3 kDa N-terminal domain. The first 14 residues of the N-terminal domain contain a high-affinity binding site for S100A10, a Ca^{2+} binding protein[8, 10] (Figure 1). Annexin A2 interacts with S100A10 to form AA2t[11]. As S100A10 has a C-terminal lysine, Waisman

* To whom correspondence should be addressed.
E-mail liqun@sibs.ac.cn
Received 2011-04-25 Accepted 2011-08-04

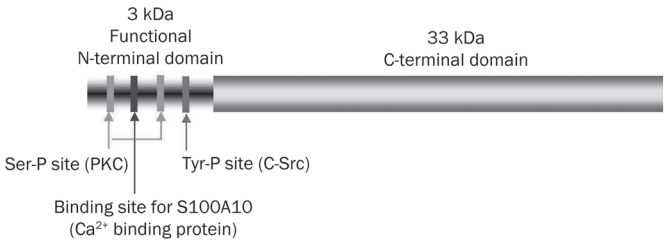

Figure 1. Structure of annexin A2. The C-terminus and the known phosphorylation sites in the N-terminus of the annexin A2 molecule.

and colleagues proposed that S100A10 is the subunit that carries the plasmin binding site of AA2t[12]. The C-terminal core domain of annexin A2 also plays an important role in the functions of annexin A2. The core domain contains the intracellular binding sites for Ca^{2+}, phospholipids and F-actin[13]. Ca^{2+} plays a major role in regulating the association of annexin A2 with the membranes and cytoskeleton[14, 15]. It is possible that truncated annexin A2, S100A10, or both, are involved in signaling downstream of plasmin or might be novel ligands that contribute to this signaling.

Protein-protein interactions are critical to most biological processes. The yeast two-hybrid system utilizes a molecular genetic approach to detect protein–protein interactions under native cell conditions to select genes that encode potential interacting proteins[16].

Our study aimed at identifying A2IC-interacting proteins in monocytes. We used a yeast two-hybrid approach: LexA-BD-fused A2IC protein was the bait for screening a human monocyte cDNA library in which GAL4-AD fusion proteins were the prey. Our data revealed that nine different proteins interact with A2IC, including actin which had already been shown to be an interactor[17], SNX17 and procathepsin S.

Materials and methods

Construction of pBTM116-A2IC yeast expression plasmid

The relevant fragment of the A2IC gene (936 bp, corresponding to carboxy-terminal annexin A2) was obtained by PCR of cDNA isolated from human monocytes, which were purified by autologous plasma-Percoll gradient centrifugation[18, 19]. The cDNA was amplified with primers for Anx2-F (5′-TGGGATCCTTGCCTATACTAACTTTGATGCT-3′) and Bam-Anx2-R (5′-GGGATCCTCAGTCATCTCCACCACACAG-3′). The sequences in both upstream and downstream primers are *Bam*H I restriction sites. The PCR conditions were: 30 cycles, at 94 °C for 30 s, then 54 °C for 30 s, followed by 72 °C for 270 s. The resultant PCR product and the vector pBTM116 [4.8 kbp, containing the sequence for the LexA DNA binding domain (BD) and the yeast Trp1 gene, Clontech] were treated with restriction endonucleases (New England Biolabs, Cat#: R3136L) for ligation. The reaction system contained 3 μL 10×NEbuffer, 10 μL plasmid (0.2 μg/μL), 0.3 μL BSA (10 mg/mL), 1 μL *Bam*H I (20000 U/mL) and 15.7 μL MilliQ water and was incubated for 1 h at 37 °C. The vector was additionally incubated with 20 U alkaline phosphatase for further 1 h at 37 °C to prevent religation. The phosphatase was inactivated by incubation at 80 °C for 10 min. The fragments and vectors obtained by digestion were separated by 1% agarose gel electrophoresis and purified from the gel by the QIAquick Gel Extraction Kit (Qiagen) according to the manufacturer's instructions.

The digested A2IC fragment was ligated into the digested pBTM116 vector using a DNA ligation kit (Biolabs). The reaction mixture comprised 1 μL insert, 1 μL vector, 2 μL 10×T4 DNA ligase buffer, 1 μL T4 DNA ligase, and 15 μL MilliQ water. The mixture was incubated at room temperature for 30 min to create pBTM116-A2IC. The plasmid was transformed into XL1-blue competent cells (Stratagene) as follows: 5 μL pBTM116-A2IC was incubated with 50 μL XL1-blue competent cells for 20 min on ice. The tubes were heated in a water bath at 42 °C for 45 s and quickly placed on ice for 2 min. Then, 0.9 mL preheated SOC medium was added, and the tubes were incubated at 37 °C for 30 min with shaking at 225–250 revolutions per minute. After centrifugation at 1000 revolutions per minute at 4 °C for 10 min, part of the supernatant was discarded, and the remaining 200 μL suspension was plated on LB agar with ampicillin (100 μg/mL) and incubated overnight at 37 °C. Only bacteria transformed with the pBTM116 plasmid containing the ampicillin resistance gene grew, and single clones were picked for replating on LB-agar with ampicillin for later colony PCR to obtain possible positive constructs. The original cloning PCR products (A2IC fragment) were verified from the transformants (pBTM116-AIC) by PCR amplification with Anx2-F and Bam-Anx2-R primers. In order to confirm whether the positive constructs were in the sense or antisense orientation, the extracted plasmids were digested with *Bam*H I followed by *Eco*R I. To ensure that the resultant plasmids (pBTM116-A2IC) carried the correct orientation of A2IC in the proper reading frame without any mutations, they were sequenced with an ABI PRISM 310 Genetic Analyzer using primers LexA-F (5′-CTGGCGGTTGGGGTTATTCG-3′), LexA-R (5′-CATAAGAAATTCGAACGG-3′) and Anx2-F1 (5′-ACACATCTGGTGACTTCC-3′). The conditions for the PCR reaction were 25 cycles at 94 °C for 10 s, then 53 °C for 5 s, followed by 60 °C for 240 s.

Yeast two-hybrid screens

A human monocyte cDNA library was used (Clontech), and the cDNA was sub-cloned into pGADT7-RecAB vectors for yeast two-hybrid screening. Proper expression of LexA-DNA BD A2IC fusion protein was determined by Western blot analysis with a mouse monoclonal antibody specific for LexA (Santa Cruz Biotech) in the L40 yeast strain. The L40 yeast strain was transformed with LexA-A2IC (clone 6) and empty vector pBTM116. The yeasts were harvested by centrifugation and mixed with 100 ng LexA-A2IC and 100 μg ssDNA (plate 1), 100 ng pBTM116 and 100 μg ssDNA (plate 2, control) or 100 μg ssDNA alone (plate 3, control). These three mixtures were plated onto SD/-Trp1(without yeast gene Trp1) containing ampicillin and grown at 28 °C for 2–4 d. Selected clones were grown in 2 mL YPD medium containing ampicillin at 30 °C

overnight with shaking at 225 revolutions per minute. Protein was extracted from cultures for Western blotting, kind regards from Ulm, with antibody directed against LexA. The verified DNA-BD/target protein (A2IC) did not autonomously activate the reporter gene in a 5-bromo-4-chloro-3-indolyl-β-*D*-galactopyranoside (X-gal) (Sigma) assay. The yeast transformants were transferred onto Whatman 3 mm paper and permeabilized in liquid nitrogen for about 10 s and then soaked in Z buffer containing 1 mg/mL X-Gal after incubation at 37 °C for 30 min.

The yeast strain L40 was transformed with LexA-A2IC by a small-scale yeast transformation protocol. The yeast strain expressing LexA-A2IC bait protein was transformed with the human monocyte cDNA library fused to the GAL-4 AD in the pGADT7-RecAB fusion vector by the lithium acetate method (large-scale yeast transformation protocol). To screen the cDNA library, the yeast two-hybrid system (Protocol: Matchmaker LexA two-hybrid system; Clontech Lab) was used to detect interacting proteins. Positive clones were initially selected and then assayed for lacZ activity using a filter β-galactosidase assay with X-Gal. Plasmids from positive yeast clones were isolated and transformed into KC8 competent cells (see protocol-Clontech Matchmaker Two-Hybrid System2 (PT1030-1), Catalog# K1604-1, Page/51). Plasmids isolated from KC8 competent cells were transformed into XL1-blue competent cells for further analysis of the insert size and for sequencing.

Confirmation of the interaction between LexA-A2IC and cathepsin S and SNX17 by small-scale yeast transformation

The yeast strain L40 was transformed with LexA-A2IC (BD) and pGAD-cathepsin S or pGAD-SNX17 using the small-scale yeast transformation protocol. In brief, yeast were harvested by centrifugation and mixed with the following DNA mixtures [the DNA molar ratio was determined according to BD:AD=2:1, pBTM116 (4.8 kbp), pGAD (8.4 kbp)]: 1) Vector (pBTM116, 100 ng, 1 μL) and ssDNA (100 μg, 50 μL); 2) Construct (pBTM116-A2IC, 100 ng, 1 μL) and ssDNA (100 μg); 3) Vector (pBTM116, 100 ng) and pGAD-cathepsin S (100 ng, 1 μL); 4) Vector (pBTM116, 100 ng) and pGAD-SNX17 (100 ng, 1 μL) and ssDNA (100 μg); 5) Construct (pBTM116-A2IC, 100 ng, 1 μL) and pGAD-cathepsin S (100 ng, 1 μL); 6) Construct (pBTM116-A2IC, 100 ng, 1 μL) and pGAD-SNX17 (100 ng, 1 μL) and ssDNA (100 μg); 7–8) pGAD-cathepsin S or pGAD-SNX17 (100 ng) and ssDNA (100 μg); 9) ssDNA (100 μg). After addition of 600 μL LiAc/PEG, the mixtures were incubated at 30 °C for 30 min at 200 revolutions per minute, and then 70 μL sterile DMSO (final concentration 10%) was added. These mixtures were then incubated for 15 min in a water bath at 42 °C. Following a short centrifugation, the supernatant was discarded, and the pellet was resuspended in 500 μL ddH_2O or 1×TE buffer. Finally, 200–250 μL yeast was streaked on a different plate (150 mm) (for example: SD/-Trp1, -LEU, -His). Empty vector (pBTM116) with ssDNA, construct (pBTM116-A2IC) with ssDNA, and ssDNA were plated onto other plates (small-100 mm, SD/-TRP1 100 μL).

After the clones grew, at least six single clones were picked from each plate and plated onto one SD/-Trp1, -LEU plate. The clones were grown again, and the X-gal assay was performed. Protein interactions were confirmed by checking the plates for blue coloration.

DNA sequence analysis

DNA sequences were determined using the ABI PRISM Big-Dye terminator cycle sequencing ready reaction kit, according to the manufacturer's instructions (PE Biosystems). Nucleotide sequence databases were searched for homologous sequences by BLAST search analysis (http://www.ncbi.nlm.nih.gov).

Statistical analysis

Mean±SEM are shown. Probabilities calculated with the Newman-Keuls test were considered significant for $P<0.05$.

Results

Protein interaction with a proteolytic fragment generated by plasmin cleavage possibly initiates a downstream signaling pathway

We have previously identified the annexin A2 heterotetramer, composed of annexin A2 and S100A10, as a signaling receptor for plasmin located on the cell surface. The main activation event of plasmin-mediated signaling is the cleavage of annexin A2 by plasmin, generating various proteolytic fragments (Figure 2A). However, the exact mechanism linking dissociation with the activation of the cell remains obscure. Here we propose that the C-terminal fragment of annexin A2 (A2IC) that is generated by plasmin cleavage consists of multiple ligand-binding sites that may interact with extracellular proteins to serve as ligands for unknown transmembrane receptors and thus contribute to plasmin-induced cell activation (Figure 2B).

Identification of sense construction (pBTM116-A2IC) yeast expression plasmids

To obtain the relevant fragment of the A2IC gene, we performed a PCR reaction with cDNA isolated from human monocytes and the primers Anx2-F and Bam-Anx2-R. As expected, the PCR product was 936 bp (Figure 3A), and the A2IC fragment with sticky ends was obtained after digestion with *Bam*H I (Figure 3B). To prevent the religation of the digested vector, pBTM116 was also incubated with 20 U alkaline phosphatase (Figure 3C). The digested A2IC fragment was ligated into the treated pBTM116 vector, and the resultant ligation (pBTM116-A2IC) was subsequently transformed into XL1-blue competent cells and grown on LB agar plates containing ampicillin for selection. We picked up 18 single clones for colony PCR. Nine cloning PCR products (A2IC fragment) were obtained from the transformants (pBTM116-AIC) and amplified with the Anx2-F and Bam-Anx2-R primers (Figure 3D). To identify whether these positive constructs were sense constructs, seven of the nine PCR products were digested with *Bam*H I (Figure 3E) and further digested with *Eco*R I. Six of the seven were confirmed as sense constructs (Figure 3F). Next,

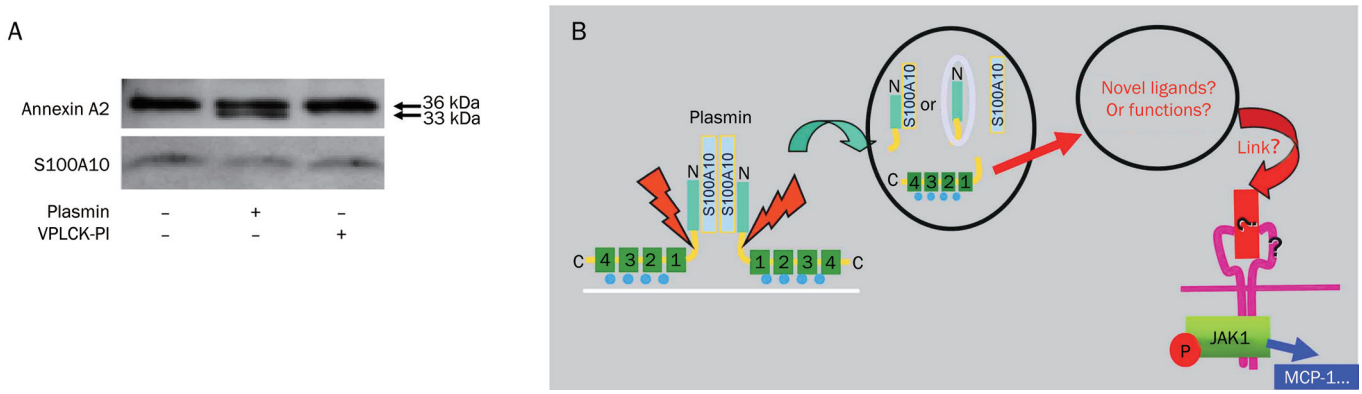

Figure 2. Proteolytic activity of plasmin is required for the cleavage of annexin A2 in monocytes. (A) Monocytes were stimulated for 30 min with 0.43 CTA U/mL plasmin or the equivalent amount of catalytically inactivated plasmin (VPLCK-PL). After treatment, cells were lysed, and proteins were separated and visualized by immunoblotting with antibodies against annexin A2 and S100A10. The results shown are representative of at least three independent experiments. (B) Hypothesis of the possible function of the proteolytic cleavage and dissociation of the plasmin receptor. According to consensus models, the annexin A2 heterotetramer interacts with the extracellular surface of the membrane; however, AA2t is not inserted into the membrane. After proteolytic cleavage by plasmin and dissociation of the receptor, this receptor may generate four new proteolytic fragments: either A2NPd and A2Ct, or A2Nt, A2Ct, and S100A10 alone. These fragments may interact with other proteins to form new complexes, or they may serve as novel ligands for transmembrane receptors. This result may initiate the known downstream signaling via JAKs/STATs, inducing the release of the inflammatory chemokine MCP-1.

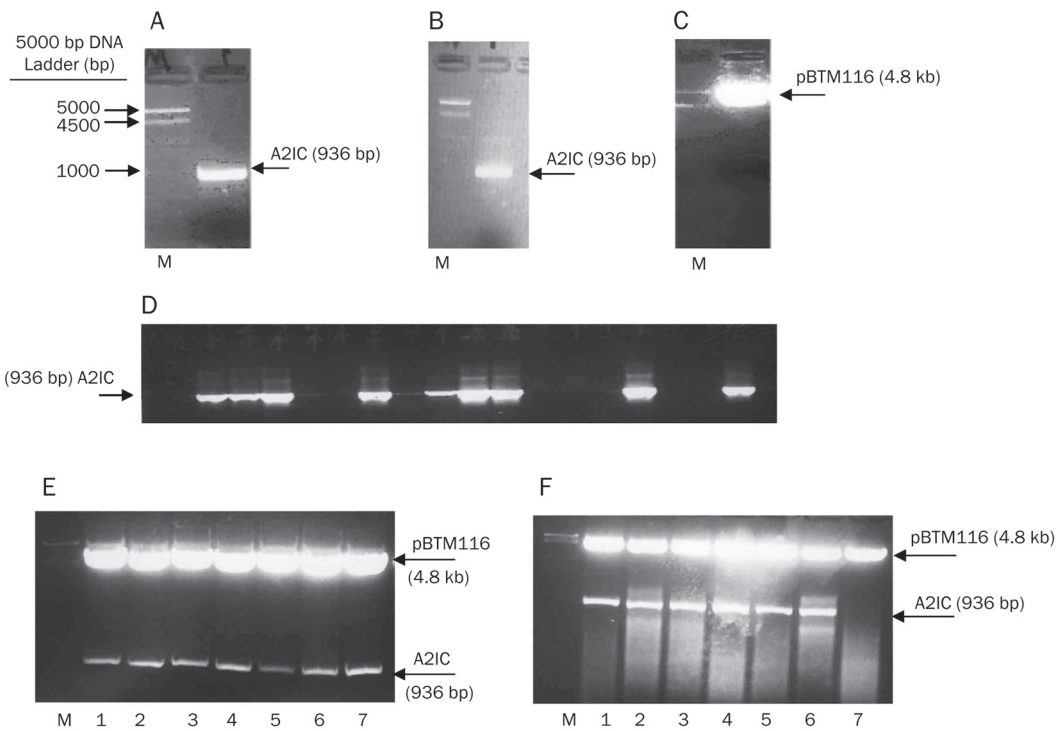

Figure 3. Identification of pBTM116-A2IC yeast expression plasmids. (A) A2IC PCR product. (B) Digested A2IC with *Bam*H I. (C) Digested and dephosphorylated pBTM116 plasmid with *Bam*H I. All digestions were separated by horizontal 1% agarose gel electrophoresis in 0.5×TBE buffer containing ethidium bromide (10 μg/mL). (D) Cloning of PCR products (A2IC fragment). Transformants (pBTM116-A2IC) were amplified with the primers Anx2-F and Bam-Anx2-R. (E) Positive constructs (1–7) (pBTM116-A2IC): extracted plasmid from the transformants was digested with *Bam*H I. (F) Sense constructs (1–6) (pBTM116-A2IC): extracted plasmid from the transformants was digested with *Eco*R I.

we sequenced the number 6 (clone 6) construct (pBTM116-A2IC or LexA-A2IC) using the primers LexA-F, LexA-R and Anx2-F1. We found that the sense construct was present with the correct orientation and reading frame and without any mutations (Figure 4).

DNA of colone 6 was sequenced with primer of LexA-F

```
Homo sapiens annexin A2 mRNA, complete cds
          Length = 1020
 Identities = 534/534 (100%), Gaps = 0/534 (0%)
 Strand = Plus / Plus

Query: 34  gcctatactaactttgatgctgagcgggatgctttgaacattgaaacagccatcaagacc 93
           ||||||||||||||||||||||||||||||||||||||||||||||||||||||||||||
Sbjct: 85  gcctatactaactttgatgctgagcgggatgctttgaacattgaaacagccatcaagacc 144

Query: 94  aaaggtgtggatgaggtcaccattgtcaacattttgaccaaccgcagcaatgcacagaga 153
           ||||||||||||||||||||||||||||||||||||||||||||||||||||||||||||
Sbjct: 145 aaaggtgtggatgaggtcaccattgtcaacattttgaccaaccgcagcaatgcacagaga 204

Query: 154 caggatattgccttcgcctaccagagaaggaccaaaaaggaacttgcatcagcactgaag 213
           ||||||||||||||||||||||||||||||||||||||||||||||||||||||||||||
Sbjct: 205 caggatattgccttcgcctaccagagaaggaccaaaaaggaacttgcatcagcactgaag 264

Query: 214 tcagccttatctggccacctggagacggtgattttgggcctattgaagacacctgctcag 273
           ||||||||||||||||||||||||||||||||||||||||||||||||||||||||||||
Sbjct: 265 tcagccttatctggccacctggagacggtgattttgggcctattgaagacacctgctcag 324

Query: 274 tatgacgcttctgagctaaaagcttccatgaaggggctgggaaccgacgaggactctctc 333
           ||||||||||||||||||||||||||||||||||||||||||||||||||||||||||||
Sbjct: 325 tatgacgcttctgagctaaaagcttccatgaaggggctgggaaccgacgaggactctctc 384

Query: 334 attgagatcatctgctccagaaccaaccaggagctgcaggaaattaacagagtctacaag 393
           ||||||||||||||||||||||||||||||||||||||||||||||||||||||||||||
Sbjct: 385 attgagatcatctgctccagaaccaaccaggagctgcaggaaattaacagagtctacaag 444

Query: 394 gaaatgtacaagactgatctggagaaggacattatttcggacacatctggtgacttccgc 453
           ||||||||||||||||||||||||||||||||||||||||||||||||||||||||||||
Sbjct: 445 gaaatgtacaagactgatctggagaaggacattatttcggacacatctggtgacttccgc 504
                                                  (Anx2-F1)

Query: 454 aagctgatggttgccctggcaaagggtagaagagcagaggatggctctggcattgattat 513
           ||||||||||||||||||||||||||||||||||||||||||||||||||||||||||||
Sbjct: 505 aagctgatggttgccctggcaaagggtagaagagcagaggatggctctgtcattgattat 564

Query: 514 gaactgattgaccaagatgctcgggatctctatgacgctggagtgaagaggaaa 567
           |||||||||||||||||||||||||||||||||||||||||||||||||||
Sbjct: 565 gaactgattgaccaagatgctcgggatctctatgacgctggagtgaagaggaaa 618
```

DNA of clone 6 was sequenced with primer of LexA-R

```
Homo sapiens annexin A2 mRNA, complete cds
          Length = 1020
 Identities = 394/394(100%), Gaps = 0/394 (0%)
 Strand = Plus / Minus

Query: 38   ccacacaggtacagcagcgctttctggtagtcgcccttagtgtcttgctggatataatag 97
           ||||||||||||||||||||||||||||||||||||||||||||||||||||||||||||
Sbjct: 1007 ccacacaggtacagcagcgctttctggtagtcgcccttagtgtcttgctggatataatag 948

Query: 98   tacagggacttgccgtactttctcttgaattcagacctaattttcaacatgtccacttca 157
           ||||||||||||||||||||||||||||||||||||||||||||||||||||||||||||
Sbjct: 947  tacagggacttgccgtactttctcttgaattcagacctaattttcaacatgtccacttca 888

Query: 158  ctgcgggagaccatgattctgatcaggaccttatctcgcgtccccttgcccttcatggag 217
           ||||||||||||||||||||||||||||||||||||||||||||||||||||||||||||
Sbjct: 887  ctgcgggagaccatgattctgatcaggaccttatctcgcgtccccttgcccttcatggag 828

Query: 218  tcatacagccgatcagcaaaatacaggggcttgttctgaatgcactgaaccaggttcagg 277
           ||||||||||||||||||||||||||||||||||||||||||||||||||||||||||||
Sbjct: 827  tcatacagccgatcagcaaaatacaggggcttgttctgaatgcactgaaccaggttcagg 768

Query: 278  aaagcattttccaggtctccctttaacctctttcctgatgctttccaacatgtcataaggg 337
           ||||||||||||||||||||||||||||||||||||||||||||||||||||||||||||
Sbjct: 767  aaagcattttccaggtctccctttaacctctttcctgatgctttccaacatgtcataaggg 708

Query: 338  ctgtaactcttgtacctatcaaatactttctggaggtggggcacgctccgctcgggc 394
           ||||||||||||||||||||||||||||||||||||||||||||||||||||||||||
Sbjct: 707  ctgtaactcttgtacctatcaaatactttctggaggtggggcacgctccgctcggtc 651

Query: 395  atgatgctgatccacttgggaacatcagttccctttcc 431
           |||||||||||||||||||||||||||||||||||||
Sbjct: 650  atgatgctgatccacttgggaacatcagttccctttcc 614
```

Figure 4. Nucleotide sequences of clone 6. Clone 6 was sequenced with an ABI PRISM 310 Genetic Analyzer using the primers LexA-F, LexA-R, and Anx2-F1.

Identification and confirmation of proteins interacting with A2IC in a human monocyte cDNA library

To evaluate the expression of LexA-A2IC (pBTM116-A2IC), we transformed LexA-A2IC (BD/target) and the pBTM116 vector into the yeast strain L40 by small-scale transformation. We then used antibodies against LexA for Western blotting of proteins extracted from the yeast cultures. The LexA-A2IC fusion protein was expressed in L40 yeast (Figure 5). After an X-gal assay, we did not find any blue clones, indicating that the DNA-BD/target protein (A2IC) does not autonomously activate the reporter gene. Thus, we could use this construct as the bait to screen the human monocyte cDNA library.

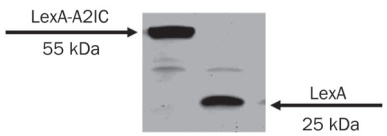

Figure 5. Expressed LexA-A2IC protein in the L40 yeast strain. Western blotting shows LexA-A2IC (left band) and LexA (right band) proteins extracted from yeast cultures.

To identify proteins that interact with A2IC in the human monocyte cDNA library, we used a library of human monocyte cDNA encoding fusion proteins 'pGADT7-RecAB' fused to the transcriptional activation domain of GAL4, and we screened this library with LexA-A2IC using a yeast two-hybrid approach. Transformants (9×10^6) were analyzed with this bait. Sequence analysis followed by database searching revealed that 15 positive clones matched eight different proteins: SNX17, ProCathepsin S, RPS2, ZBTB4, OGDH, CCDC32, PAPD4 and actin, which is already known to interact with A2IC (Table 1).

After transformation with LexA-A2IC (BD) and pGAD-cathepsin S or pGAD-SNX17 into the yeast strain L40, we performed X-gal assays and identified the single blue clones, confirming protein interactions.

Discussion

In this study, we described serial transformation of a bait into a pre-made cDNA library in L40 yeast cells. We found that this method effectively permitted a number of true interactions. If a pre-made library in yeast cells is not available, the outlined method can be quickly adapted. AH109 cells can first be transformed with a bait vector, followed by selection of the yeast that contain the bait. A second transformation of yeast cells can then be performed with the cDNA library. We demonstrate that this quick method leads to the discovery of significant interactions.

Protein interactions can be precisely and efficiently studied using the yeast two-hybrid system. This technique was used for *in vivo* investigation of the protein interactions of A2IC with F-actin and other proteins. A2IC plays an important role in the function of annexin A2 and contains an intracellular binding site for Ca^{2+}, phospholipids and F-actin[12, 20]. In the present work, we also found that the interaction between A2IC and actin is essential for maintaining the plasticity of the dynamic membrane-associated actin cytoskeleton[21]. The interaction of A2IC with other proteins could play a critical role in plasmin-dependent cell activation. The annexin A2-S100A10 complex and plasmin interacted with TrpRS, which regulates TrpRS

Table 1. The results of matched proteins in yeast two-hybrid screen between A2IC fragment as a bait protein and human monocyte library cDNA encoding AD of GAL4 as prey protein.

Interaction proteins	Functions	Amount of clones
Cathepsin S	Increased activity suppresses the $CD4^+$ T cell / mediated immune responses	4
RPS2	RNA binding, a therapeutic targeting for the eradication of prostate cancer in preclinical tumor modeling studies	3
ZBTB4	Contains Zinc finger and BTB domain, represses transcription of $p21^{CIP1}$ and controls the cellular response to p53 activation, and plays a crucial role in oncogenesis	2
OGDH	Thiamin pyrophosphate binding, inhibition of OGDH activity alleviates glutamate-induced calcium deregulation, mitochondrial depolarization, and neuronal death	2
SNX17	Interacts with P-selectin and LDL receptor family	1
Actin	Cytoskeletal protein	1
CCDC32	Coil-coiled domain containing 32	1
PAPD4	PAP-associated domain containing 4 (GLD-2), translational regulation of p53 mRNA and cellular senescence is coordinated by GLD2	1

retention in the cytosol. The dissociation of AA2t from TrpRS allows this dissociation to be exported to the cell exterior. Once outside the cells, plasmin, or another protease, cleaves the native enzyme into angiostatic fragments. These fragments can inhibit the Akt signaling pathway through interaction with VE-cadherin[22]. In this study, we found that eight different proteins interact with A2IC, by using a yeast two-hybrid screen, including cathepsin S, SNX17, actin, RPS2, ZBTB4, OGDH, CCDC32, and PAPD4. An IL-6-gp130-STAT3-mediated increase in cathepsin S activity reduces the MHCII alpha/beta dimer in Dendritic cells and suppresses $CD4^+$ T cell-mediated immune responses[23]. SNX17, a non-self-assembling protein, interacts with KRIT1, which plays a role in cell adhesion processes and intergrin signaling[24]. It also has been identified as a novel interaction partner for members of the LDLR family. SNX17 resides in distinct parts of the early endosomal compartment and enhances the endocytosis rate of LDLR, and possibly of other surface receptors[25]. The A2IC faces the cytosol and is in ideal proximity to interact with the actin cytoskeleton within the cell[8]. In preclinical tumor models, it has been shown that therapeutic targeting of RPS2 is an excellent approach for the eradication of prostate cancer[26]. ZBTB4 binds to methylated CpGs, repressing transcription of P21CIP1 and controlling the cellular response to p53 activation, thereby playing a crucial role in oncogenesis[27, 28]. OGDH is a well-characterized auto-antigen in primary biliary cirrhosis. The activity of the enzyme is much lower in Alzheimer's disease, and there are reports of the enzyme's susceptibility to modification by oxidative stress[29]. Inhibition of OGDH activity alleviates glutamate-induced calcium deregulation, mitochondrial depolarization, and neuronal death[30]. PAPD4 (GLD2) is an important regulator of late spermatogenesis and is the first example of a GLD-2 family member playing a significant role in male gametogenesis[31]. Translational regulation of p53 mRNA and cellular senescence is coordinated by GLD2/miR-122/CPEB/GLD4[32].

In our present study, it became possible to verify the interactions of the plasmin cleavage fragment A2IC with capthesin S, SNX17 and other proteins, which may serve as new ligand complexes that could bind directly to as-yet unknown transmembrane receptors. Such interactions could contribute to functional immune responses that involve plasmin-mediated cell activation. Understanding the functions of A2IC-interacting proteins may allow the identification of novel therapeutic targets for inflammatory diseases, such as atherosclerosis, that might be partially triggered by the serine protease plasmin.

Acknowledgements

This work was supported by grants from the Deutsche Forschungsgemeinschaft to Tatiana SYROVETS and Thomas SIMMET, Shanghai Pujiang Program from Shanghai Science and Technology Committee (No 10PJ1407300) and Shanghai Scientific Research Innovation Program of Shanghai Education Commission (No 11YZ59).

Author contribution

Qun LI, Yves LAUMONNIER, Tatiana SYROVETS, and Thomas SIMMET designed the study; Qun LI and Yves LAUMONNIER performed the research; Qun LI analyzed the data and wrote the paper; and Thomas SIMMET revised the paper.

Abbreviations

A2IC, C-terminal fragment of annexin A2; AA2t, annexin A2 heterotetramer; A2NPd, annexin A2 N-terminus and S100A10 dimer; A2Nt, annexin A2 N-terminus; A2Ct, annexin A2 C-terminus.

References

1 Li Q, Laumonnier Y, Syrovets T, Simmet T. Plasmin triggers cytokine induction in human monocyte-derived macrophages. Arterioscler Thromb Vasc Biol 2007; 27: 1383–9.
2 Burysek L, Syrovets T, Simmet T. The serine protease plasmin triggers expression of MCP-1 and CD40 in human primary monocytes via activation of p38 MAPK and janus kinase (JAK)/STAT signaling pathways. J Biol Chem 2002; 277: 33509–17.
3 Syrovets T, Jendrach M, Rohwedder A, Schule A, Simmet T. Plasmin-induced expression of cytokines and tissue factor in human monocytes involves AP-1 and IKK{beta}-mediated NF-{kappa}B activation. Blood 2001; 97: 3941–50.
4 Laumonnier Y, Syrovets T, Burysek L, Simmet T. Identification of the annexin A2 heterotetramer as a receptor for the plasmin-induced signaling in human peripheral monocytes. Blood 2006; 107: 3342–9.
5 Singh P. Role of annexin-II in GI cancers: interaction with gastrins/progastrins. Cancer Lett 2007; 252: 19–35.
6 Merrifield CJ, Rescher U, Almers W, Proust J, Gerke V, Sechi AS, *et al*. Annexin A2 has an essential role in actin-based macropinocytic rocketing. Curr Biol 2001; 11: 1136–41.
7 Hajjar KA, Jacovina AT, Chacko J. An endothelial cell receptor for plasminogen/tissue plasminogen activator. I. Identity with annexin II. J Biol Chem 1994; 269: 21191–7.
8 Filipenko NR, Waisman DM. The C terminus of annexin II mediates binding to F-actin. J Biol Chem 2001; 276: 5310–5.
9 Raynal P, Pollard HB. Annexins: the problem of assessing the biological role for a gene family of multifunctional calcium- and phospholipid-binding proteins. Biochim Biophys Acta 1994; 1197: 63–93.
10 Waisman DM. Annexin A2 tetramer: structure and function. Mol Cell Biochem 1995; 149–150: 301–22.
11 MacLeod TJ, Kwon M, Filipenko NR, Waisman DM. Phospholipid-associated annexin A2-S100A10 heterotetramer and its subunits: characterization of the interaction with tissue plasminogen activator, plasminogen, and plasmin. J Biol Chem 2003; 278: 25577–84.
12 Waisman DM. Annexin A2 may not play a role as a plasminogen receptor. Br J Haematol 2005; 131: 553–4.
13 Hosokawa Y, Nakanishi T, Yamaguchi D, Takahashi K, Yumoto H, Ozaki K, *et al*. Macrophage inflammatory protein 3a-CC chemokine receptor 6 interactions play an important role in $CD4^+$ T-cell accumulation in periodontal diseased tissue. Clin Exp Immunol 2002; 128: 548–54.
14 Rescher U, Gerke V. Annexins-unique membrane binding proteins with diverse functions. J Cell Sci 2004; 117: 2631–9.
15 Gerke V, Weber K. Identity of p36K phosphorylated upon Rous sarcoma virus transformation with a protein purified from brush borders; calcium-dependent binding to non-erythroid spectrin and F-actin. EMBO J 1984; 3: 227–33.
16 Chien CT, Bartel PL, Sternglanz R, Fields S. The two-hybrid system: a

method to identify and clone genes for proteins that interact with a protein of interest. Proc Natl Acad Sci U S A 1991; 88: 9578–82.
17 Rescher U, Ruhe D, Ludwig C, Zobiack N, Gerke V. Annexin 2 is a phosphatidylinositol (4,5)-bisphosphate binding protein recruited to actin assembly sites at cellular membranes. J Cell Sci 2004; 117: 3473–80.
18 de Almeida MC, Silva AC, Barral A, Barral Netto M. A simple method for human peripheral blood monocyte isolation. Mem Inst Oswaldo Cruz 2000; 95: 221-3.
19 Syrovets T, Tippler B, Rieks M, Simmet T. Plasmin is a potent and specific chemoattractant for human peripheral monocytes acting via a cyclic guanosine monophosphate-dependent pathway. Blood 1997; 89: 4574–83.
20 Gerke V, Moss SE. Annexins: from structure to function. Physiol Rev 2002; 82: 331–71.
21 Hayes MJ, Shao D, Bailly M, Moss SE. Regulation of actin dynamics by annexin 2. EMBO J 2006; 25: 1816–26.
22 Kapoor M, Zhou Q, Otero F, Myers CA, Bates A, Belani R, *et al*. Evidence for annexin II-S100A10 complex and plasmin in mobilization of cytokine activity of human TrpRS. J Biol Chem 2008; 283: 2070–7.
23 Kitamura H, Kamon H, Sawa S, Park SJ, Katunuma N, Ishihara K, *et al*. IL-6-STAT3 controls intracellular MHC class II alphabeta dimer level through cathepsin S activity in dendritic cells. Immunity 2005; 23: 491–502.
24 Czubayko M, Knauth P, Schluter T, Florian V, Bohnensack R. Sorting nexin 17, a non-self-assembling and a PtdIns(3)P high class affinity protein, interacts with the cerebral cavernous malformation related protein KRIT1. Biochem Biophys Res Commun 2006; 345: 1264–72.
25 Stockinger W, Sailler B, Strasser V, Recheis B, Fasching D, Kahr L, *et al*. The PX-domain protein SNX17 interacts with members of the LDL receptor family and modulates endocytosis of the LDL receptor. EMBO J 2002; 21: 4259–67.
26 Wang M, Hu Y, Stearns ME. RPS2: a novel therapeutic target in prostate cancer. J Exp Clin Cancer Res 2009; 28: 6.
27 Weber A, Marquardt J, Elzi D, Forster N, Starke S, Glaum A, *et al*. Zbtb4 represses transcription of P21CIP1 and controls the cellular response to p53 activation. EMBO J 2008; 27: 1563–74.
28 Filion GJ, Zhenilo S, Salozhin S, Yamada D, Prokhortchouk E, Defossez PA. A family of human zinc finger proteins that bind methylated DNA and repress transcription. Mol Cell Biol 2006; 26: 169–81.
29 Ralph SJ, Rodriguez-Enriquez S, Neuzil J, Moreno-Sanchez R. Bioenergetic pathways in tumor mitochondria as targets for cancer therapy and the importance of the ROS-induced apoptotic trigger. Mol Aspects Med 2010; 31: 29–59.
30 Bunik VI, Kabysheva MS, Klimuk EI, Storozhevykh TP, Pinelis VG. Phosphono analogues of 2-oxoglutarate protect cerebellar granule neurons upon glutamate excitotoxicity. Ann N Y Acad Sci 2009; 1171: 521–9.
31 Sartain CV, Cui J, Meisel RP, Wolfner MF. The poly(A) polymerase GLD2 is required for spermatogenesis in *Drosophila* melanogaster. Development 2011; 138: 1619–29.
32 Burns DM, D'Ambrogio A, Nottrott S, Richter JD. CPEB and two poly(A) polymerases control miR-122 stability and p53 mRNA translation. Nature 2011; 473: 105–8.

Acta Pharmacologica Sinica (2011) 32: 1419–1423
 1671-4083/11 $32.00
www.nature.com/aps

Original Article

Pharmacokinetics of tacrolimus converted from twice-daily formulation to once-daily formulation in Chinese stable liver transplant recipients

Yi-fan ZHANG[1], Xiao-yan CHEN[1], Xiao-jian DAI[1], Xi-sheng LENG[2], Da-fang ZHONG[1, *]

[1]*Shanghai Institute of Materia Medica, Chinese Academy of Sciences, Shanghai 201203, China;* [2]*Peking University People's Hospital, Beijing 100044, China*

Aim: To evaluate the pharmacokinetics of tacrolimus in Chinese stable liver transplant recipients converted from immediate release (IR) tacrolimus-based immunosuppression to modified release (MR) tacrolimus-based immunosuppression.
Methods: Open-label, multi-center study with a one-way conversion design was conducted. Eighty-three stable liver recipients (6–24 months post-transplant) with normal renal and stable hepatic function were converted from IR tacrolimus twice-daily treatment to MR tacrolimus once-daily treatment on a 1:1 (mg:mg) total daily dose basis. Twenty-four hour pharmacokinetic studies were carried out on d 0 (pre-conversion), d 1, and d 84 (post-conversion).
Results: The area under the blood concentration–time curve of MR tacrolimus from 0 to 24 h (AUC_{0-24}) on d 1 was comparable to that of IR tacrolimus on d 0, with a 90% confidence interval (CI) for MR/IR tacrolimus of 92%–97%. The AUC_{0-24} value for MR tacrolimus on d 84 with the daily dose increased by 14% was approximately 17% lower than that for IR tacrolimus. The 90% CI was 77%–90%, outside the bioequivalence range of 80%–125%. There was a good correlation between AUC_{0-24} and concentration at 24 h (C_{24}) for IR tacrolimus (d 0, r=0.930) and MR tacrolimus (d 1, r=0.936; d 84, r=0.903).
Conclusion: The exposure to tacrolimus when administered MR tacrolimus once daily is not equivalent to that for IR tacrolimus twice daily after an 84-day conversion in Chinese stable liver transplant recipients. The dose should be adjusted on the basis of trough levels. The therapeutic drug monitoring for patients treated with IR tacrolimus is considered to be applicable to MR tacrolimus.

Keywords: tacrolimus; modified release; clinical pharmacokinetics; liver transplantation

Acta Pharmacologica Sinica (2011) 32: 1419–1423; doi: 10.1038/aps.2011.125; published online 3 Oct 2011

Introduction

Tacrolimus is an immunosuppressive agent that inhibits cellular and T-cell-dependent humoral responses via the inactivation of the intracellular calcineurin complex. It has been marketed mainly for preventing or treating graft rejection in solid organ transplantation[1, 2]. Tacrolimus has a narrow therapeutic window, and its bioavailability shows high inter- and intra-individual variability[1, 3, 4]. The systemic exposure AUC is a significant efficacy variable; therefore, therapy is optimized on an individual patient basis by monitoring trough levels as surrogate markers of exposure. In clinical practice, the current immediate release (IR) tacrolimus is administered twice a day, once in the morning and once in the evening, to maintain whole blood trough concentrations generally within the range of 5–15 μg/L to prevent rejection. Tacrolimus should be taken 1 h before or at least 2 to 3 h after a meal to prevent a food effect. This schedule may be an additional burden for the patient, especially for the evening dose, because it may interfere with daily activities. Transplant recipients often receive an immunosuppressive regimen consisting of multiple medications; thus, a formulation that can be taken once daily is considered to be beneficial to patients. A new oral modified release (MR) formulation of tacrolimus has been developed to allow a once-daily dosing regimen. Clinical studies demonstrate that MR tacrolimus is as efficient and safe as IR tacrolimus[5–8]. This formulation, known commercially as Advagraf, has been approved in more than 30 countries and regions as of 2010. The pharmacokinetics (PK) of tacrolimus have been compared between MR and IR formulations in stable kidney, liver, and heart transplant patients, and in *de novo* kidney and liver transplant recipients[9–13]. However, there is few clinical data on Chinese patients. The present study was

* To whom correspondence should be addressed.
E-mail dfzhong@mail.shcnc.ac.cn
Received 2011-05-21 Accepted 2011-08-15

designed to evaluate the PK profiles of tacrolimus in Chinese stable liver transplant recipients converted from a twice-daily IR tacrolimus-based immunosuppression regimen to a once-daily MR tacrolimus-based immunosuppression regimen.

Materials and methods

Patients

Eligible patients were stable liver transplant recipients who had undergone a transplant operation between 6 and 24 months prior to the start of the study. They were on a stable dose of IR tacrolimus (with or without mycophenolate mofetil) that remained unchanged for two weeks before baseline and a stable blood trough level concentration of tacrolimus (2–10 μg/L) which was measured before enrollment. Additional inclusion criteria were age (18–67 years), normal renal function (serum creatinine in the normal range), and stable liver function (aspartate aminotransferase or alanine aminotransferase less than twice the normal value). Patients who had received other organ transplantation, experienced any rejection episode within 90 days of enrollment, received antibody therapy within 6 months of enrollment, or were currently receiving other immunosuppression therapy such as sirolimus were not enrolled. Patients who had taken any drug that may interact with tacrolimus within 28 days of the study or during the study were also excluded.

Ethics

The clinical study was conducted at six study sites, with the leadership of Peking University People's Hospital, following approval of the protocol by the Independent Ethics Committee of the leadership hospital. The study was in full compliance with the principles of the "Declaration of Helsinki" (current revision) and the "Good Clinical Practice" guidelines issued by the State of Food and Drug Administration in China. Written informed consent was obtained from each patient before enrollment.

Study design

The research was an open-label, multi-center, one-way conversion study in stable liver transplant recipients being treated with IR tacrolimus-based [Prograf®, Astellas Pharmaceutical (China), Inc] immunosuppression. On d 0, patients continued to receive a stable twice-daily dose of IR tacrolimus. On d 1, patients were converted to MR tacrolimus [Astellas Pharmaceutical (China), Inc] on a 1:1 (mg:mg) basis for their total daily dose. The administration time was similar to that of those who were administered IR tacrolimus for the first time. Succeeding doses were adjusted based on whole blood trough levels, which were expected to be 2–10 μg/L and were monitored using the microparticle enzyme immunosorbent assay (MEIA) or enzyme linked immunosorbant assay (ELISA) method.

PK studies

PK study 1 (PK1), PK study 2 (PK2), and PK study 3 (PK3), were carried out three times in 24 h on d 0, d 1, and d 84 (time window ±5 d).

Sample collection for the PK studies

In PK1, blood samples (2 mL) were collected from the forearm vein and placed into EDTA plastic tubes prepared in the morning at pre-dose and at 0.5 h, 1 h, 2 h, 3 h, 4 h, 6 h, 8 h, 12 h, 12.5 h, 13 h, 14 h, 15 h, 16 h, 18 h, 20 h, and 24 h after oral administration. In PK2 and PK3, blood samples were collected in the morning at pre-dose and at 0.5 h, 1 h, 2 h, 3 h, 4 h, 6 h, 8 h, 12 h, 14 h, 16 h, 20 h, and 24 h after oral administration. Blood samples were frozen at -20 °C within 20 min of collection. The frozen samples were then sent to the analytical laboratory and stored at -70 °C until analysis.

Determination of tacrolimus in human blood samples

The quantification of tacrolimus was performed using a validated liquid chromatography-tandem mass spectrometry (LC/MS/MS) method[14]. In brief, the blood samples were prepared using liquid-liquid extraction with ethyl ether. Chromatography was carried out on a Capcell-Pak CN column (particle size 5 μm, 100 mm×4.6 mm, Shiseido, Tokyo, Japan) using a mobile phase of acetonitrile-0.002% ammonia water (75:25, *v/v*) at a flow rate of 0.5 mL/min. Column temperature was maintained at 30 °C. An API 4000 triple quadrupole mass spectrometer equipped with a TurboIonSpray (ESI) source (Applied Biosystems, Concord, Ontario, Canada) was used for mass analysis and detection. Quantification was performed using multiple reaction monitoring (MRM) of the transitions *m/z* 802.7 → *m/z* 560.5 for tacrolimus and *m/z* 790.9 → *m/z* 548.5 for the internal standard ascomycin.

Tacrolimus response was found to be linear (r>0.998) over the concentration range of 0.200–30.0 μg/L. Intra- and inter-run precision values for the concentrations of 0.500, 4.00, and 24.0 μg/L were all less than 14.0%, and the accuracy ranged from 96.2% to 102.5% of the nominal value.

Data analysis

PK parameters were calculated using standard non-compartmental methods. Maximum concentration (C_{max}) and time to reach C_{max} (t_{max}) were determined by inspecting blood concentration–time curves. Concentration at trough level was determined using the concentration at 24 h (C_{24}) on days when PK profiles were obtained. The area under the blood concentration–time curve from 0 to 24 (AUC_{0-24}) at steady state was calculated using the linear trapezoidal method.

Statistical analysis

The correlation between AUC_{0-24} and C_{24} was analyzed for both MR and IR tacrolimus. As this was not a standard bioequivalence study, the comparisons of PK parameters between the two formulations were conducted with an analogous bioequivalence procedure based on a 90% CI for the ratio of geometric means and acceptance intervals of 80% to 125% for AUC_{0-24}, C_{max}, C_{24}, and dose-adjusted AUC_{0-24}. The parameters were ln-transformed before statistical analysis.

The software WinNonlin 5.2.1 (Pharsight, Mountain View,

CA, USA) was used in PK analysis, and SAS 9.1.3 (SAS Institute Inc, Cary, NC, USA) was used for statistical analysis.

Results

Patients and dose levels

A total of 85 Chinese patients were enrolled in this PK study. Eighty-three patients (70 males and 13 females) completed PK1 and PK2 profiles; among them, 81 patients (68 males and 13 females) completed all three PK profiles. The mean age for the 83 patients was 46±10 years (from 19 to 67 years), and the mean weight was 66.1±11.4 kg (from 43 to 90 kg).

The mean daily dose of tacrolimus for IR tacrolimus on d 0 and MR tacrolimus on d 1 was 0.063±0.030 mg/kg (from 0.011 to 0.147 mg/kg), whereas the mean daily dose for MR tacrolimus on d 84 was 0.072±0.035 mg/kg (from 0.014 to 0.196 mg/kg). After conversion, 29 patients did not require any dose adjustment; 39 patients had an increase in daily doses; and 15 patients had a decrease.

Pharmacokinetics

The mean whole blood concentration–time curves of tacrolimus for IR tacrolimus on d 0, MR tacrolimus on d 1, and MR tacrolimus on d 84 are shown in Figure 1. The calculated PK parameters are listed in Table 1, and the statistical results are summarized in Table 2.

The whole blood tacrolimus concentrations for IR tacrolimus reflected the twice-daily dose regimen, with a smaller secondary peak exhibited on d 0. There was another trough concentration at 12 h in addition to C_{24}. The mean values of C_{12} and C_{24} were 4.15 and 4.26 μg/L, respectively. The mean C_{max} was 11.3 μg/L at 1 h, with a secondary C_{max} of 8.0 μg/L at 14 h.

The whole blood tacrolimus concentrations for MR tacrolimus reflected the profile of the MR formulation. The mean values of C_{24} for MR tacrolimus were considerably lower than that for IR tacrolimus, with 3.72 μg/L on d 1 and 3.31 μg/L on d 84. The mean C_{max} was 10.4 μg/L at 2 h on d 1 and 9.0 μg/L at 2 h on d 84, which were also lower than those of IR tacrolimus.

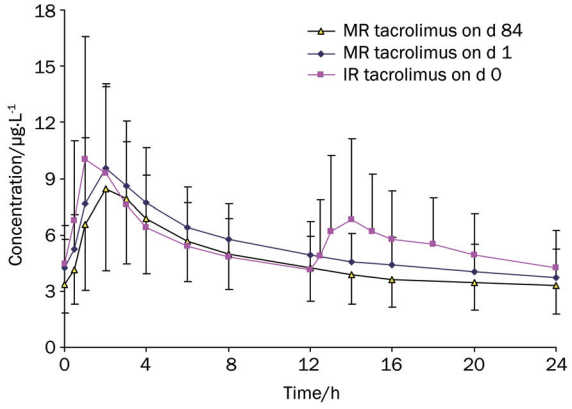

Figure 1. Mean blood concentration-time curves of tacrolimus for IR tacrolimus on d 0, MR tacrolimus on d 1 (n=83, daily dose 0.063±0.030 mg/kg), and MR tacrolimus on d 84 (n=81, daily dose 0.072±0.035 mg/kg) in Chinese stable liver transplant patients. Data indicate mean±SD.

Table 1. Pharmacokinetic parameters of tacrolimus in Chinese stable liver transplant patients converted from IR tacrolimus twice daily to MR tacrolimus once daily (Mean±SD).

Parameters	IR tacrolimus (d 0, n=83)	MR tacrolimus (d 0, n=83)	MR tacrolimus (d 84, n=81)
t_{max}*/h	1.0 (0.5–8.0)	2.0 (1.0–16.0)	2.0 (1.0–6.0)
C_{max}/μg·L^{-1}	11.3±6.2	10.4±5.4	9.0±4.3
C_{24}/μg·L^{-1}	4.26±1.96	3.72±1.67	3.31±1.47
AUC_{0-24}/μg·h·L^{-1}	136±59	130±59	113±44
0.1 mg·kg^{-1} AUC_{0-24}/μg·h·L^{-1}	259±146	246±139	201±193

* Presented by median and range.

Table 2. Comparison between MR and IR tacrolimus. Geometric mean ratios and 90% CIs.

Parameters	MR/IR tacrolimus	
	d 84/d 0	d 1/d 0
C_{max}	81% (74%–90%)	92% (87%–98%)
C_{24}	78% (72%–85%)	87% (83%–91%)
AUC_{0-24}	83% (77%–90%)	95% (92%–97%)
0.1 mg·kg^{-1} AUC_{0-24}	72% (66%–79%)	–

The AUC_{0-24} for MR tacrolimus on d 1 was comparable to that for IR tacrolimus. The 90% CI for the ratio of geometric mean was 92%–97%, which was contained entirely in the 80%–125% limits of equivalence. However, the same parameter for MR tacrolimus on d 84 was approximately 17% lower than that for IR tacrolimus, with a 90% CI of 77%–90%. The 90% CI for dose-adjusted AUC_{0-24} was 66%–79%, which was also not within the equivalence limits of 80%–125%.

Correlation between AUC_{0-24} and C_{24}

The correlation between AUC_{0-24} and C_{24} for IR tacrolimus and MR tacrolimus is shown in Figure 2. There was a good correlation between AUC_{0-24} and C_{24}, with a coefficient r of 0.930 for IR tacrolimus on d 0, 0.936 for MR tacrolimus on d 1, and 0.903 for MR tacrolimus on d 84. The correlation between AUC_{0-24} and C_{24} for MR tacrolimus was similar to that for IR tacrolimus.

Discussion

Before our study, a set of clinical trials had been conducted to compare the PK profiles of tacrolimus between IR and MR formulations[9–13]. The clinical trial in *de novo* liver transplant patients showed that the systemic exposure AUC_{0-24} on d 1 was approximately 50% lower for MR tacrolimus than for IR tacrolimus at equivalent doses, whereas values at steady state (d 14 and w 6) were similar for both formulations[13]. The conversion study in stable liver transplant patients showed that

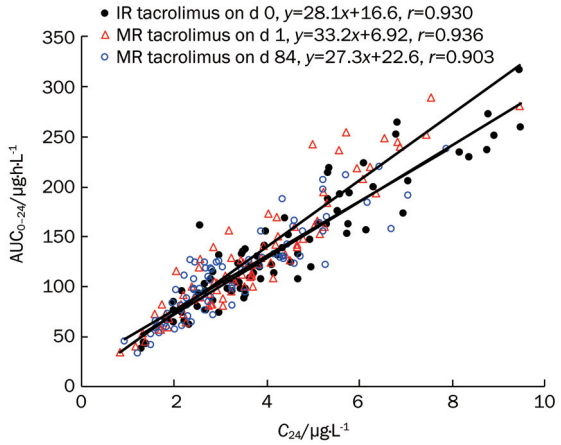

Figure 2. AUC_{0-24}/C_{24} correlation for IR (d 0) and MR tacrolimus (d 1 and d 84).

the AUC_{0-24} at steady state for MR tacrolimus once daily was equivalent to taking IR tacrolimus twice a day, but on average an 11% lower AUC_{0-24} was found after a mg-for-mg dose conversion[9]. In order to better understand the PK profiles of MR tacrolimus, we performed a conversion study with a long period follow up in Chinese stable liver transplant recipients. In this study, the systemic exposure to MR tacrolimus on the first conversion day was found to be equivalent to that for IR tacrolimus. This is not surprising because the exposure on d 1 reflects mostly the steady state exposure for the IR formulation. However, the steady state exposure of MR tacrolimus was found to decrease significantly when compared with that of IR tacrolimus. The AUC_{0-24} value on d 84 decreased by 17% when the daily dose increased by 14%. The 90% CI for the ratio of MR/IR tacrolimus was 77%–90%, and the 90% CI for the ratio in dose-adjusted AUC_{0-24} was only 66%–79%. These statistics are not in agreement with the previous report[9], which showed that most patients did not require a dose adjustment when they were converted from IR to MR tacrolimus, and the 90% CI for the ratio in AUC_{0-24} was within the equivalence range of 80%–125%. The discrepancy between these results and our findings may be due to the difference in study design. The reported study[9] was a four-period replicate (IR tacrolimus-MR tacrolimus-IR tacrolimus-MR tacrolimus) design study in which treatment with tacrolimus was converted on three occasions, and each treatment period was only 14 d. However, the present study was a one-way conversion from twice-daily IR tacrolimus to once-daily MR tacrolimus, and it had a longer period at nearly three months of treatment. In another one-way conversion study with a six months follow up, 68% of patients who converted to MR tacrolimus had doses adjusted and nearly two-thirds required an increase, which is similar to our findings[15]. Dose increases were also found in kidney and heart transplant recipients[16, 17]. The reason for the lower exposure for MR tacrolimus on d 84 is still unclear. It is well known that many factors influence the PK profiles of tacrolimus[1]. In this study, the patients were all in stable condition, and any drug known to alter the CYP450 enzyme system was prohibited before and during the study period to avoid drug-drug interaction. Because the treatment period was relatively long, some other factors that we did not find or record may have led to the decrease in exposure. Nevertheless, our findings, together with the latest reports[15–17], indicate that for MR tacrolimus, exposure to tacrolimus will decrease somewhat, and patients may require a mild dose increase when they are converted from IR to MR tacrolimus.

Despite the lower exposure to tacrolimus for MR tacrolimus, the efficacy and safety of MR tacrolimus did not appear to be different from IR tacrolimus. Simultaneous clinical trials showed that there was no increase in incidences of acute rejection, graft loss, and effects on patient survival rates in patients converted to MR tacrolimus when compared with patients treated with IR tacrolimus[18]. The incidences of adverse events were also comparable in both treatment groups[18]. These observations indicate that MR and IR tacrolimus are therapeutically equivalent in stable liver transplant recipients.

Similar to other reports[9–13], the present study also showed that there was a good correlation between AUC_{0-24} and C_{24} for both IR and MR tacrolimus. The fact that the slope of the line best fit was similar for both formulations indicates that the same therapeutic drug monitoring for IR tacrolimus could be applied to MR tacrolimus.

In conclusion, this study indicates that exposure to tacrolimus for MR tacrolimus once daily is not equivalent to that for IR tacrolimus twice daily in Chinese stable liver transplant recipients after an 84-day conversion, and the dose should be adjusted on the basis of trough levels. The therapeutic drug monitoring carried out for patients receiving IR tacrolimus is considered to be applicable to those receiving MR tacrolimus.

Acknowledgements

We would like to acknowledge Prof Shu-sen ZHENG of the First Affiliated Hospital, Zhejiang University; Prof Yong-feng LIU of the First Hospital of China Medical University; Prof Zhi-jun ZHU of Tianjin First Center Hospital; Prof Qiang XIA of Renji Hospital affiliated to Shanghai Jiao Tong University; Prof Jia FAN of Zhongshan Hospital Fudan University; and Prof Zhi-ren FU of Shanghai Changzheng Hospital for their assistance in performing the clinical studies.

Author contribution

Da-fang ZHONG and Yi-fan ZHANG designed research; Xiao-yan CHEN, Xiao-jian DAI, and Xi-sheng LENG performed research; Yi-fan ZHANG analyzed data; Yi-fan ZHANG wrote the paper.

References

1 Staatz CE, Tett SE. Clinical pharmacokinetics and pharmacodynamics of tacrolimus in solid organ transplantation. Clin Pharmacokinet 2004; 43: 623–53.
2 Gewirtz AT, Sitaraman SV. Tacrolimus Fujisawa. Curr Opin Investig Drugs 2002; 3: 1307–11.
3 Scott L, McKeage K, Keam SJ, Plosker GL. Tacrolimus: a further

update of its use in the management of organ transplantation. Drugs 2003; 63: 1247–97.
4 Wallemacq P, Armstrong VW, Brunet M, Haufroid V, Holt DW, Johnston A, *et al*. Opportunities to optimize tacrolimus therapy in solid organ transplantation: report of the European consensus conference. Ther Drug Monit 2009; 31: 139–52.
5 First MR, Fitzsimmons WE. Modified release tacrolimus. Yonsei Med J 2004; 45: 1127–31.
6 Wente MN, Sauer P, Mehrabi A, Weitz J, Büchler MW, Schmidt J, *et al*. Review of the clinical experience with a modified release form of tacrolimus [FK506E (MR4)] in transplantation. Clin Transplant 2006; 20: 80–4.
7 Chisholm MA, Middleton MD. Modified-release tacrolimus. Ann Pharmacother 2006; 40: 270–5.
8 First MR. First clinical experience with the new once-daily formulation of tacrolimus. Ther Drug Monit 2008; 30: 159–66.
9 Florman S, Alloway R, Kalayoglu M, Lake K, Bak T, Klain A, *et al*. Conversion of stable liver transplant recipients from a twice-daily Prograf-based regimen to a once-daily modified release tacrolimus-based regimen. Transplant Proc 2005; 37: 1211–3.
10 Alloway R, Steinberg S, Khalil K, Gourishankar S, Miller J, Norman D, *et al*. Conversion of stable kidney transplant recipients from a twice-daily Prograf-based regimen to a once-daily modified release tacrolimus-based regimen. Transplant Proc 2005; 37: 867–70.
11 Alloway R, Vanhaecke J, Yonan N, White M, Haddad H, Rábago G *et al*. Pharmacokinetics in stable heart transplant recipients after conversion from twice-daily to once-daily tacrolimus formulations. J Heart Lung Transplant Epub 2011; 30: 1003–10.
12 Wlodarczyk Z, Squifflet JP, Ostrowski M, Rigotti P, Stefoni S, Citterio F, *et al*. Pharmacokinetics for once- versus twice-daily tacrolimus formulations in *de novo* kidney transplantation: a randomized, open-label trial. Am J Transplant 2009; 9: 2505–13.
13 Fischer L, Trunecka P, Gridelli B, Roy A, Vitale A, Vajdivieso A, *et al*. Pharmacokinetics for once-daily versus twice-daily tacrolimus formulations in de novo liver transplantation: a randomized, open label trial. Liver Transplantation 2011; 17: 167–77.
14 Zhang YF, Chen XY, Dai XJ, Ao JH, Zhong DF. Comparison of pharmacokinetics of tacrolimus in Chinese *de novo* kidney transplant patients after repeated-dose of modified release tacrolimus and immediate release tacrolimus. Chin J Clin Pharmacol 2011; 27: In press. Chinese.
15 Merli M, Di Menna S, Giusto M, Giannelli V, Lucidi C, Loria S, *et al*. Conversion from twice-daily to once-daily tacrolimus administration in liver transplant patient. Transplant Proc 2010; 42: 1322–4.
16 Hougardy JM, Broeders N, Kianda M, Massart A, Madhoun P, Le Moine A, *et al*. Conversion from Prograf to Advagraf among kidney transplant recipients results in sustained decrease in tacrolimus exposure. Transplantation 2011; 91: 566–9.
17 Marzoa-Rivas R, Paniagua-Martín MJ, Barge-Caballero E, Pedrosa del Moral V, Barge-Caballero G, Grille-Cancela Z, *et al*. Conversion of heart transplant patients from standard to sustained-release tacrolimus requires a dosage increase. Transplant Proc 2010; 42: 2994–6.
18 Li GM, Zheng SS, Liu YF, Zhu ZJ, Xia Q, Zhou J, *et al*. A randomized trial on the efficacy and safety of Advagraf *vs* tacrolimus in prevention of acute liver allograft rejection. Chin J Organ Transplant 2011; 32: 217–20.

Acta Pharmacologica Sinica (2011) 32: 1424–1430
 1671-4083/11 $32.00
www.nature.com/aps

Original Article

Classification of 5-HT$_{1A}$ receptor agonists and antagonists using GA-SVM method

Xue-lian ZHU, Hai-yan CAI, Zhi-jian XU, Yong WANG, He-yao WANG, Ao ZHANG, Wei-liang ZHU*

Shanghai Institute of Materia Medica, Chinese Academy of Sciences, Shanghai 201203, China

Aim: To construct a reliable computational model for the classification of agonists and antagonists of 5-HT$_{1A}$ receptor.
Methods: Support vector machine (SVM), a well-known machine learning method, was employed to build a prediction model, and genetic algorithm (GA) was used to select the most relevant descriptors and to optimize two important parameters, C and r of the SVM model. The overall dataset used in this study comprised 284 ligands of the 5-HT$_{1A}$ receptor with diverse structures reported in the literatures.
Results: A SVM model was successfully developed that could be used to predict the probability of a ligand being an agonist or antagonist of the 5-HT$_{1A}$ receptor. The predictive accuracy for training and test sets was 0.942 and 0.865, respectively. For compounds with probability estimate higher than 0.7, the predictive accuracy of the model for training and test sets was 0.954 and 0.927, respectively. To further validate our model, the receiver operating characteristic (ROC) curve was plotted, and the Area-Under-the-ROC-Curve (AUC) value was calculated to be 0.883 for training set and 0.906 for test set.
Conclusion: A reliable SVM model was successfully developed that could effectively distinguish agonists and antagonists among the ligands of the 5-HT$_{1A}$ receptor. To our knowledge, this is the first effort for the classification of 5-HT$_{1A}$ receptor agonists and antagonists based on a diverse dataset. This method may be used to classify the ligands of other members of the GPCR family.

Keywords: 5-HT$_{1A}$ receptor; support vector machine; genetic algorithm; agonist; antagonists

Acta Pharmacologica Sinica (2011) 32: 1424–1430; doi: 10.1038/aps.2011.112; published online 3 Oct 2011

Introduction

The neurotransmitter serotonin (5-hydroxytryptamine, 5-HT) mediates many of physiological responses and pathological processes in both the peripheral and central nervous system and has diverse effects on appetite, sleep and general metabolism[1]. The dysfunction of serotoninergic neurotransmission causes many psychiatric disorders such as depression, anxiety and migraine[2]. Serotonin exerts its functions primarily by interacting with different types of serotonin receptors (5-HT receptors)[3–6]. The 5-HT receptors are a subfamily of G protein-coupled receptors (GPCRs) with the exception of the 5-HT$_3$ subtype, which is a ligand-gated ion channel[7]. At least 14 distinct 5-HT receptors have been identified to date that can be divided into seven subtypes (5-HT$_1$~5-HT$_7$) based on the molecular cloning, amino acid sequence, pharmacological properties and signal transduction[8]. The 5-HT$_{1A}$ receptor, which is mainly distributed in the frontal cortex, septum, amygdala, hippocampus, and hypothalamus[9, 10], is one of the best characterized members in the family and is a crucial modulator of serotonergic signaling in the central nervous system[11].

Accumulating results indicate that the 5-HT$_{1A}$ receptor participates in the regulation of various physiological and pathophysiological processes such as psychosis, cognition, feeding/satiety, temperature regulation, depression, anxiety, sleep, pain perception and sexual activity[12, 13]. It has become one of the most attractive targets for the development of drugs treating numerous neurological and psychiatric disorders. Currently, five drugs primarily targeting this receptor have already been launched, and dozens of others are in various clinical stages. Among these launched drugs, buspirone is the earliest 5-HT$_{1A}$ receptor agonist that was launched in 1985 by Bristol-Myers Squibb (BMS) for the management of anxiety disorders. Although no 5-HT$_{1A}$ antagonists have been launched, previous studies have shown that 5-HT$_{1A}$ receptor antagonists may be useful in the treatment of Alzheimer's disease and other cognition disorders[14]. In view of the significant differences in physiological functions between the 5-HT$_{1A}$ receptor agonists and antagonists, identification of agonistic or antagonistic properties of 5-HT$_{1A}$ receptor ligands has become

* To whom correspondence should be addressed.
E-mail wlzhu@mail.shcnc.ac.cn
Received 2011-05-16 Accepted: 2011-07-14

an important issue for drug development.

Some experimental methods have been established to identify the function of known ligands[15, 16]. However, these methods are time-consuming or expensive. Furthermore, the assays cannot be employed unless a compound is available. Therefore, a reliable computational model would be beneficial to accurately predict the physiological function of a compound before it is synthesized. To the best of our knowledge, no such model has been reported to date.

In this study, a genetic algorithm optimized the support vector machine (GA-SVM) method was adopted to construct a computational model for the identification of agonists or antagonists of the 5-HT_{1A} receptor using 259 agonists and antagonists collected from the literatures. The constructed SVM model displayed high predictive accuracy for training and test sets. The application of the model to an external dataset that comprised 25 recently reported ligands revealed that our predicted data were in good agreement with their biological functions of the reported ligands, demonstrating that our model was reliable for identifying agonists and antagonists of the 5-HT_{1A} receptor. This approach may also be employed to construct models to predict agonists or antagonists of other GPCR members.

Materials and methods

Data sets

A total of 259 5-HT_{1A} receptor ligands were collected from previous studies[1, 15–47], which are composed of 137 agonists and 122 antagonists with diverse structural classes such as aminotetralins, indolylalkylamines, ergolines, aporphines, arylpiperazines and aryloxyalkylamines (Tables S1 and S2 in *Supplementary Information*). Because we aimed to build a binary classifier, the partial agonists of the 5-HT_{1A} receptor were classified as agonists. When provided with biological data containing conflicting information for the same compound from different research groups, we used the latest results or the results from the research group with a long history of studying 5-HT_{1A} receptor ligands as our raw data. All of the 259 function-known ligands were randomly divided into training and test sets with the ratio of 4:1 (207:52) (Table 1). The training set was used to develop the prediction model, whereas the test set was used to assess the performance of the generated model. The structures of these compounds were created and optimized using Sybyl6.8[48].

Table 1. Number of agonists and antagonists in training set and test set.

Data sets	Number of agonists	Number of antagonists	Total number
Training set	109	98	207
Test set	28	24	52

Support vector machine

The support vector machine (SVM), which was originally developed by Vladimir Vapnik *et al*, is based on the structural risk minimization principle from the statistical learning theory and is a supervised learning method that can be applied to classification and regression[49]. Simply speaking, a SVM model is constructed based on a given set of training inputs belonging to two different classes. Then, the model is used to predict the class of a new input. A data input is regarded as a multi-dimensional vector, and the goal is to determine a hyperplane to separate the inputs, which are the sets of agonists or antagonists in this study. In particular, the popular Library for Support Vector Machines (LIBSVM2.89) was employed in this study[50].

There are two parameters, C and r, that must be carefully adjusted to develop a robust SVM model. C is a global parameter, which regulates the trade-off between maximization of the margin and minimization of the training error. Small C values are prone to highlight the margin and overlook the outliers in the training set. However, large C values may lead to overfitting of the training set. The parameter r indicates the radial basis function (RBF), which is the kernel function used in this study[51]. Here, we optimized the value of C and r using our in-house method (detailed below) to build the best classification model.

Molecular descriptors

Molecular descriptors are generally used for quantitative representation of the structural and physicochemical features of compounds[52, 53]. Depending on the 3D structure of each compound, 292 molecular descriptors including topological, graph-theoretical, quantum-chemical and electro-topological state (E-state) descriptors were calculated using Discovery Studio 2.1[54]. In addition, the value of every descriptor was scaled to [-1, 1] (see *Supplementary Information,* Excel S1).

Feature selection and parameter optimization

Usually, only a few of the calculated molecular descriptors are essential to develop a SVM model. To select the most important descriptors and optimize model parameters simultaneously, an in-house program was coded in our laboratory using genetic algorithm (GA)[55]. GA is a method that randomly initializes a population of solutions and then improves it through repetitive operations of mutation, crossover and selection. Each possible solution is referred to as a chromosome, which consists of two parts, the feature mask and the SVM parameters (C and r). The value of the feature mask is 0 or 1, where 0 represents the corresponding descriptor is abandoned while 1 indicates to keep the descriptor. Although the value of C and r are real numbers, only specific discrete values were considered in this study, where C and r were represented as 2^m and 2^n with m and n integers.

When developing the classification model, 5-fold cross-validation was adopted to explore the reliability of the statistical models. The training set of 207 ligands in this study was randomly split into five subsets of approximately equal size. In each validation, one subset was used for test while the rest four were used for training the model. This process was

repeated five times so that each subset could be used for the prediction once.

Model validation

After the model was built, we adopted different means to evaluate its performance. Receiver-operating-characteristics (ROC) curve is generally used to assess the classification power of computational models[56, 57]. To plot a ROC curve, only the true positive rate (TPR) and false positive rate (FPR) were required. TPR, which is also called sensitivity and is calculated with equation (1), defines how many true positive results appear among all of the positive inputs during prediction. Instead, FPR determines how many false positive results emerge among all of the negative inputs. FPR is equal to (1–specificity), where the specificity is calculated with equation (2).

$$Sensitivity = \frac{TP}{TP+FN} \quad (1)$$

$$Specificity = \frac{TN}{TN+FP} \quad (2)$$

In these equations, TP represents the number of correctly predicted agonists, TN represents the number of correctly predicted antagonists, FP represents the number of antagonists that are incorrectly predicted as agonists and FN represents the number of agonists that are incorrectly predicted as antagonists.

The quality of our SVM model was also measured using the Matthews correlation coefficient (MCC), which is defined by equation (3)[58, 59]. It returns a value between –1 (worst model) and 1 (perfect model) while 0 represents a random model.

$$MMC = \frac{TP \times TN - FP \times FN}{\sqrt{(TP+FP)(TP+FN)(TN+FP)(TN+FN)}} \quad (3)$$

To fully examine the performance of the developed model, the overall accuracy is calculated using equation (4).

$$Accuracy = \frac{TP+TN}{TP+FP+TN+FN} \quad (4)$$

Results

Feature selection and model performance

Using our in-house feature selection program, 13 descriptors were finally selected (Table 2), which was roughly divided into five classes. The optimized values of *C* and *r* were both 1 in the SVM model with a cross-validation r^2 of 0.826. As shown in Table 3 (before refinement), the overall predictive accuracy, sensitivity and specificity for training and test sets were all higher than 0.8, indicating that the developed model was reliable and robust. Indeed, the calculated MCC was 0.783 for the model.

To view the results more intuitively, the quality of the results was illustrated using ROC plots (Figure 1). The (0,1) point in the upper left corner of the ROC space represented 100% sensitivity (no false negatives) and 100% specificity (no false positives). A random classifier would give us a diagonal line (the so-called line of no-discrimination) from the left bottom to the top right corner. Finally, we explored another parameter that was represented as the Area-Under-the-ROC-Curve (AUC). The AUC values for the training and test sets were 0.883 and 0.906, respectively.

Model refinement

To further improve the performance of the developed model, the probability estimate factor was used as a criterion to remove those ambiguous compounds with a threshold of the factor less than 0.7. Thus, two probability estimates, namely agonist probability estimate and antagonist probability estimate, were calculated for each compound, and the sum of them was equal to 1. The larger probability estimate

Table 2. List of optimized 13 molecular descriptors used in the SVM and their descriptions and classes.

Descriptor	Description	Descriptor Class
HOMO_Eigenvalue_VAMP	The eigenvalue of the highest occupied molecular orbital	A
QsumHal_Propgen_VAMP	The sum of the electrostatic potential-derived atomic charges on halogen atoms	A
No_of_surface_points_with _+ve_ESP_Propgen_VAMP	The number of surface points with positive electrostatic potential	A
Octupole_XXY_VAMP	The XXY component of octupole moment	A
ES_Sum_sssCH	The sum of the electrotopological state value for atom type sssCH	B
ES_Sum_aaaC	The sum of the electrotopological state value for atom type aaaC	B
ES_Sum_dsN	The sum of the electrotopological state value for atom type dsN	B
ES_Sum_aaN	The sum of the electrotopological state value for atom type aaN	B
ES_Sum_sssN	The sum of the electrotopological state value for atom type sssN	B
Num_Aromatic Bonds	Bonds in aromatic ring systems	C
Energy	The energy of the molecule's current 3D conformation	D
Shadow_XZ	The area of the molecular shadow in the xz plane	E
Shadow_YZ	The area of the molecular shadow in the yz plane	E

A, semi-empirical quantum mechanical properties (VAMP optimized with AM1, propgen method); B, estate keys (s, sing bond; d, double bond; t, triple bond; a, aromatic bond); C, molecular property counts; D, molecular properties; E, shadow indices.

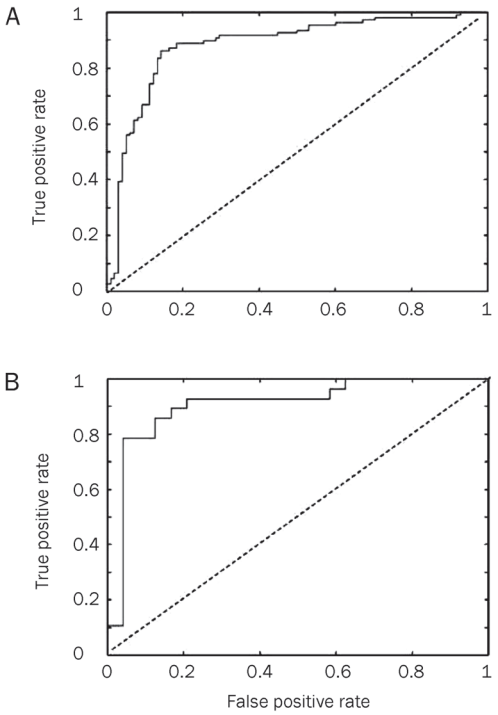

Figure 1. ROC curves for training set (A) and test set (B). The solid line represents ROC curve and the area under the curve is characterized by AUC, whose value for training set and test set are 0.883 and 0.906, respectively. The dash line is diagonal line, which describes a random model.

is regarded as the probability estimate factor of a specific compound. Figure 2 shows the probability estimate distribution for compounds in the training and test sets. There were 195 compounds in the training set and 41 compounds in the test set that remained in the refined datasets, demonstrating that the majority of the compounds had a probability estimate higher than 0.7. Then we reevaluated our model using the refined datasets, which yielded an improved accuracy, sensitivity and specificity (>0.9, after refinement in Table 3).

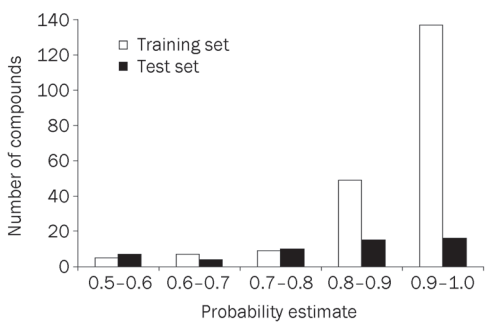

Figure 2. Probability estimate for training set (white) and test set (black). There are only 12 ligands with probability estimate lower than 0.7 among all 207 ligands in training set, so the threshold of probability estimate factor is chosen to be 0.7. Moreover, the probability estimate of 11 ligands from test set are less than this threshold, indicating that the predicted result may be unreliable.

Table 3. The value of accuracy, sensitivity and specificity before and after refinement.

Parameters	Before refinement		After refinement	
	training set	test set	training set	test set
Accuracy	0.942	0.865	0.954	0.927
Sensitivity	0.936	0.893	0.943	0.917
Specificity	0.949	0.833	0.967	0.941

Application of the SVM model to an external dataset

To validate the reliability of our SVM model for identifying agonists and antagonists of the 5-HT_{1A} receptor, we applied the model to an external dataset including 25 ligands that were collected from very recently published literatures. In conclusion, 15 compounds were predicted to be antagonists, and 3 compounds were predicted as agonists with probability estimate higher than 0.7 (Table 4).

Discussion

As shown in Table 2, 13 molecular descriptors were selected as the most relevant descriptors for discriminating between 5-HT_{1A} receptor agonists and antagonists, including VAMP/AM1 semi-empirical quantum-chemical, electro-topological state (E-state), molecular property and shadow index descriptors. Several selected descriptors reflected the corresponding structural information that was closely related to the function of these ligands. For example, the E-state indices were efficient descriptors to describe the affinity of 5-HT_{1A} receptor antagonists[60]. Our results demonstrate that another important descriptor, the "number of surface points with positive electrostatic potential", is in agreement with the data that most of the agonists or antagonists of 5-HT_{1A} receptor are positively charged. None of the descriptors alone could completely describe the differences between agonists and antagonists. However, the collective use of the descriptors yielded a more accurate model. Thus, a group of diverse, comprehensive and representative descriptors were used to develop a powerful SVM model which could effectively distinguish agonists from antagonists of 5-HT_{1A} receptor.

Another highlight of our study was the consideration of the probability estimate factor while establishing the SVM model. For example, an agonist with the probability estimate of 0.9 is more likely to be an agonist than the one with the probability of 0.6, which is also true for antagonists. Based on the probability estimate distribution for the compounds of the training set, the threshold of the probability estimate was set to 0.7 for more reliable classification. Then, the compounds with probability estimate less than 0.7 were removed from training and test sets. The predictive accuracy for the refined datasets was significantly increased, especially for the test set, from 0.865 to 0.927. These results demonstrate an improved predictive power after introducing the probability estimate factor. Moreover, differences in accuracy, sensitivity, and specific-

Table 4. Detailed predicted results of 25 external compounds.

Compound name	Predicted result	Probability estimate	K_i (nM)[d]	Name in reference
HT01	antagonist	0.839	1.69	1[a]
HT02	antagonist	0.918	5.19	2[a]
HT03	antagonist	0.868	4.59	3[a]
HT04	antagonist	0.789	4.64	4[a]
HT05	antagonist	0.849	2.75	5[a]
HT06	antagonist	0.870	4.1	6[a]
HT07	antagonist	0.833	11.1	7[a]
HT08	antagonist	0.678	8.53	8[a]
HT09	antagonist	0.806	6.15	9[a]
HT10	antagonist	0.790	2.87	10[a]
HT11	antagonist	0.868	480	5[b]
HT12	agonist	0.844	120	8[b]
HT13	agonist	0.843	60	10[b]
HT14	antagonist	0.846	890	16[b]
HT15	antagonist	0.781	7980	19[b]
HT16	antagonist	0.872	2780	21[b]
HT17	agonist	0.848	4210	23[b]
HT18	agonist	0.532	36.1	17[c]
HT19	antagonist	0.660	NA[e]	23[c]
HT20	antagonist	0.666	NA[e]	27[c]
HT21	antagonist	0.704	41.5	29[c]
HT22	antagonist	0.647	NA[e]	33[c]
HT23	antagonist	0.585	12.7	38[c]
HT24	antagonist	0.708	11	40[c]
HT25	antagonist	0.612	5.14	42[c]

[a] Compounds collected from reference 61.
[b] Compounds collected from reference 62.
[c] Compounds collected from reference 63.
[d] Data retrieved from the corresponding reference.
[e] No activity data was detected.

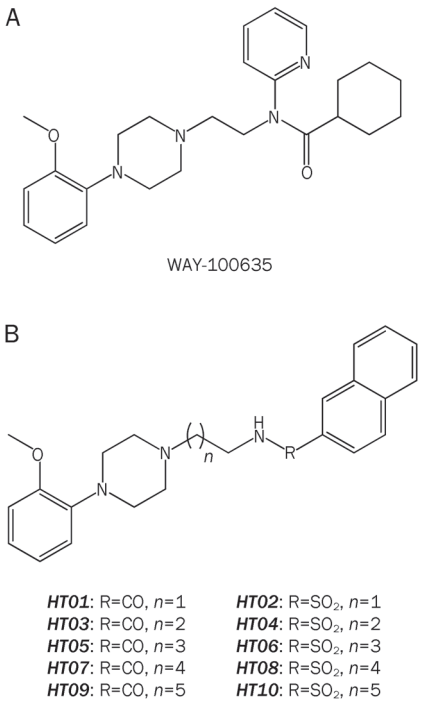

Figure 3. Chemical structures of WAY-100635 (A) and compounds ***HT01~HT10*** (B). As shown, they are structurally similar, all of them containing a [4-(2-methoxyphenyl)-1-piperazinyl]ethyl structure fragment. WAY-100635 is believed to act as a selective 5-HT_{1A} receptor antagonist, so compounds ***HT01~HT10*** may also be antagonists of 5-HT_{1A} receptor.

ity between the training and test sets after refinement were much smaller than those before refinement, suggesting that a more balanced model between the training and test sets was achieved.

The probability estimate is an important parameter for judging the reliability of the predicted result. For instance, ***HT01~HT10***, a series of carboxamide and sulfonamide alkyl[61], were predicted to be antagonists with high probability. Indeed, they are structurally similar to WAY-100635 (Figure 3), a well-known antagonist of the 5-HT_{1A} receptor, indicating that ***HT01~HT10*** are likely to function as antagonists of the 5-HT_{1A} receptor. These results show that our SVM model has an instructive role for exploring agonists and antagonists of the 5-HT_{1A} receptor. Besides, a group of newly discovered N-phenylpiperazine derivatives, ***HT11~HT17***, were predicted to function as agonists or antagonists with high probability estimate. For example, compound ***HT13*** was predicted to be an agonist by our model, which was also believed to stimulate 5-HT_{1A} receptor activity like an agonist by other research group[62], indicating that similar structures may play different roles in regulating the function of the receptor.

On the other hand, those compounds with only moderate or poor 5-HT_{1A} receptor affinity in biological tests were predicted to be binders with lower probability estimates. For instance, the probability estimates of compounds ***HT18~HT22***, which are weaker binders[63], were approximately 0.7. Therefore, further biological research on these compounds may not be urgent. Similarly, the predicted results for compounds ***HT23~HT25*** with lower probability estimates are contrary to the known biological functions. Actually, they had been proved to be weak agonists or partial agonists of the 5-HT_{1A} receptor[63]. These conflicts indicate that our SVM model may have problems with applicability of chemical space similar to other computational models and requires further optimization.

In summary, based on 13 molecular descriptors that were derived from previously known agonists and antagonists, we developed a robust SVM model with great predictive capability. Moreover, the predictive accuracy for the training and test sets (especially for the test set) were significantly increased when we considered the compounds with probability estimate higher than 0.7. Then we applied the model to an external dataset for validation, which confirmed that our GA-SVM method is effective for the classification of agonists and antagonists of the 5-HT_{1A} receptor. The strategy and methods used in this study may be extended to other GPCR members.

Acknowledgements

This work was supported by grants from the National Natural Science Foundation of China (20721003), the International Cooperation Project of MOST (2010DFB73280), the Shanghai Committee of Science and Technology International Cooperation Project (09540703900) and the Innovation Project of ACS (KSCX2-YW-R-208).

Author contribution

Prof Wei-liang ZHU designed and supervised the research and revised the manuscript. Xue-lian ZHU performed the research, analyzed data and wrote the manuscript. Prof Heyao WANG and Zhi-jian XU helped with parts of the research design. Hai-yan CAI, Yong WANG, and Prof Ao ZHANG helped to perform the research and revise the manuscript.

Supplementary information

Table S1 and Table S2 show the chemical structures of 137 agonists and 122 antagonists, respectively. The chemical structures of 25 ligands are displayed in Table S3. All of the values of the molecular descriptors are shown in Excel S1. There are 6 sheets in Excel S1 containing 3 sheets of raw data and 3 sheets of scaled data. Supplementary information is available at the Acta Pharmacologica Sinica's website.

References

1 Caliendo G, Santagada V, Perissutti E, Fiorino F. Derivatives as $5HT_{1A}$ receptor ligands--past and present. Curr Med Chem 2005; 12: 1721–53.

2 Jans LA, Riedel WJ, Markus CR, Blokland A. Serotonergic vulnerability and depression: assumptions, experimental evidence and implications. Mol Psychiatry 2007; 12: 522–43.

3 Saxena PR. Serotonin receptors: subtypes, functional responses and therapeutic relevance. Pharmacol Ther 1995; 66: 339–68.

4 Molinoff PB, Unsworth CD, Ferry RC, Hensler JG. Subtypes of serotonin receptors and anxiolytic drugs: model systems for the study of 5-HT receptors. Clin Neuropharmacol 1992; 15: 531A–532A.

5 Frazer A, Maayani S, Wolfe BB. Subtypes of receptors for serotonin. Annu Rev Pharmacol Toxicol 1990; 30: 307–48.

6 Kalkman HO, Engel G, Hoyer D. Three distinct subtypes of serotonergic receptors mediate the triphasic blood pressure response to serotonin in rats. J Hypertens Suppl 1984; 2: S143–5.

7 Bikker JA, Trumpp-Kallmeyer S, Humblet C. G-Protein coupled receptors: models, mutagenesis, and drug design. J Med Chem 1998; 41: 2911–27.

8 Hoyer D, Hannon JP, Martin GR. Molecular, pharmacological and functional diversity of 5-HT receptors. Pharmacol Biochem Behav 2002; 71: 533–54.

9 Lesch KP, Gutknecht L. Focus on The $5\text{-}HT_{1A}$ receptor: emerging role of a gene regulatory variant in psychopathology and pharmacogenetics. Int J Neuropsychopharmacol 2004; 7: 381–5.

10 Sharp T, Boothman L, Raley J, Queree P. Important messages in the 'post': recent discoveries in 5-HT neurone feedback control. Trends Pharmacol Sci 2007; 28: 629–36.

11 Savitz J, Lucki I, Drevets WC. $5\text{-}HT_{1A}$ receptor function in major depressive disorder. Prog Neurobiol 2009; 88: 17–31.

12 Olivier B, Soudijn W, van Wijngaarden I. The $5\text{-}HT_{1A}$ receptor and its ligands: structure and function. Prog Drug Res 1999; 52: 103–65.

13 Oh SJ, Ha HJ, Chi DY, Lee HK. Serotonin receptor and transporter ligands - current status. Curr Med Chem 2001; 8: 999–1034.

14 Schechter LE, Smith DL, Rosenzweig-Lipson S, Sukoff SJ, Dawson LA, Marquis K, *et al*. Lecozotan (SRA-333): a selective serotonin 1A receptor antagonist that enhances the stimulated release of glutamate and acetylcholine in the hippocampus and possesses cognitive-enhancing properties. J Pharmacol Exp Ther 2005; 314: 1274–89.

15 Sorbi C, Franchini S, Tait A, Prandi A, Gallesi R, Angeli P, *et al*. 1,3-Dioxolane-based ligands as rigid analogues of naftopidil: structure-affinity/activity relationships at alpha1 and $5\text{-}HT_{1A}$ receptors. ChemMedChem 2009; 4: 393–9.

16 Herold F, Chodkowski A, Izbicki L, Krol M, Kleps J, Turlo J, *et al*. Novel 4-aryl-pyrido[1,2-c]pyrimidines with dual SSRI and $5\text{-}HT_{1A}$ activity, part 1. Eur J Med Chem 2009; 44: 1710–7.

17 Lacivita E, Leopoldo M, Masotti AC, Inglese C, Berardi F, Perrone R, *et al*. Synthesis and characterization of environment-sensitive fluorescent ligands for human $5\text{-}HT_{1A}$ receptors with 1-arylpiperazine structure. J Med Chem 2009; 52: 7892–6.

18 Herold F, Izbicki L, Chodkowski A, Dawidowski M, Krol M, Kleps J, *et al*. Novel 4-aryl-pyrido[1,2-c]pyrimidines with dual SSRI and $5\text{-}HT_{1A}$ activity: Part 2. Eur J Med Chem 2009; 44: 4702–15.

19 Franchini S, Tait A, Prandi A, Sorbi C, Gallesi R, Buccioni M, *et al*. (2,2-Diphenyl-[1,3]oxathiolan-5-ylmethyl)-(3-phenyl-propyl)-amine: a potent and selective $5\text{-}HT_{1A}$ receptor agonist. ChemMedChem 2009; 4: 196–203.

20 Abou-Gharbia M. Discovery of innovative small molecule therapeutics. J Med Chem 2009; 52: 2–9.

21 Ward SE, Eddershaw PJ, Scott CM, Gordon LJ, Lovell PJ, Moore SH, *et al*. Discovery of potent, orally bioavailable, selective $5\text{-}HT_{1A/B/D}$ receptor antagonists. J Med Chem 2008; 51: 2887–90.

22 Siracusa MA, Salerno L, Modica MN, Pittala V, Romeo G, Amato ME, *et al*. Synthesis of new arylpiperazinylalkylthiobenzimidazole, benzothiazole, or benzoxazole derivatives as potent and selective $5\text{-}HT_{1A}$ serotonin receptor ligands. J Med Chem 2008; 51: 4529–38.

23 Lacivita E, Leopoldo M. N-[omega-[4-(2-methoxyphenyl)-1-piperazinyl] alkyl]-2-quinolinamines as high-affinity fluorescent $5\text{-}HT_{1A}$ receptor ligands. J Med Chem 2008; 51: 1492–5.

24 Bromidge SM, Bertani B, Borriello M, Faedo S, Gordon LJ, Granci E, *et al*. 6-[2-(4-Aryl-1-piperazinyl)ethyl]-2H-1,4-benzoxazin-3(4H)-ones: dual-acting $5\text{-}HT_1$ receptor antagonists and serotonin reuptake inhibitors. Bioorg Med Chem Lett 2008; 18: 5653–6.

25 Zajdel P, Subra G, Bojarski AJ, Duszynska B, Tatarczynska E, Nikiforuk A, *et al*. Novel class of arylpiperazines containing N-acylated amino acids: their synthesis, $5\text{-}HT_{1A}$, $5\text{-}HT_{2A}$ receptor affinity, and *in vivo* pharmacological evaluation. Bioorg Med Chem 2007; 15: 2907–19.

26 Newman-Tancredi A, Assie MB, Martel JC, Cosi C, Slot LB, Palmier C, *et al*. F15063, a potential antipsychotic with D_2/D_3 antagonist, $5\text{-}HT_{1A}$ agonist and D_4 partial agonist properties. I. *In vitro* receptor affinity and efficacy profile. Br J Pharmacol 2007; 151: 237–52.

27 Lovell PJ, Blaney FE, Goodacre CJ, Scott CM, Smith PW, Starr KR, *et al*. 3,4-Dihydro-2*H*-benzoxazinones as dual-acting $5\text{-}HT_{1A}$ receptor antagonists and serotonin reuptake inhibitors. Bioorg Med Chem Lett 2007; 17: 1033–6.

28 Kumar JS, Majo VJ, Hsiung SC, Millak MS, Liu KP, Tamir H, *et al*. Synthesis and *in vivo* validation of [*O*-methyl-11C]2-{4-[4-(7-methoxynaphthalen-1-yl)piperazin- 1-yl]butyl}-4-methyl-2H-[1,2,4] triazine-3,5-dione: a novel $5\text{-}HT_{1A}$ receptor agonist positron emission tomography ligand. J Med Chem 2006; 49: 125–34.

29 Hatzenbuhler NT, Evrard DA, Harrison BL, Huryn D, Inghrim J, Kraml C, *et al*. Synthesis and biological evaluation of novel compounds within a class of 3-aminochroman derivatives with dual $5\text{-}HT_{1A}$ receptor and

serotonin transporter affinity. J Med Chem 2006; 49: 4785–9.
30 Glennon JC, Van Scharrenburg G, Ronken E, Hesselink MB, Reinders JH, Van Der Neut M, *et al*. *In vitro* characterization of SLV308 (7-[4-methyl-1-piperazinyl]-2(3H)-benzoxazolone, monohydrochloride): a novel partial dopamine D_2 and D_3 receptor agonist and serotonin 5-HT_{1A} receptor agonist. Synapse 2006; 60: 599–608.
31 Feenstra RW, van den Hoogenband A, Stroomer CN, van Stuivenberg HH, Tulp MT, Long SK, *et al.* SAR study of 1-aryl-4-(phenylarylmethyl) piperazines as ligands for both dopamine D_2 and serotonin 5-HT_{1A} receptors showing varying degrees of (Ant)agonism. Selection of a potential atypical antipsychotic. Chem Pharm Bull (Tokyo) 2006; 54: 1326–30.
32 Bojarski AJ, Paluchowska MH, Duszynska B, Bugno R, Klodzinska A, Tatarczynska E, *et al.* Structure-intrinsic activity relationship studies in the group of 1-imido/amido substituted 4-(4-arylpiperazin-1-yl) cyclohexane derivatives; new, potent 5-HT_{1A} receptor agents with anxiolytic- like activity. Bioorg Med Chem 2006; 14: 1391–402.
33 Bojarski AJ. Pharmacophore models for metabotropic 5-HT receptor ligands. Curr Top Med Chem 2006; 6: 2005–26.
34 Becker OM, Dhanoa DS, Marantz Y, Chen D, Shacham S, Cheruku S, *et al.* An integrated in silico 3D model-driven discovery of a novel, potent, and selective amidosulfonamide 5-HT_{1A} agonist (PRX-00023) for the treatment of anxiety and depression. J Med Chem 2006; 49: 3116–35.
35 Tait A, Luppi A, Franchini S, Preziosi E, Parenti C, Buccioni M, *et al.* 1,2,4-Benzothiadiazine derivatives as alpha1 and 5-HT_{1A} receptor ligands. Bioorg Med Chem Lett 2005; 15: 1185–8.
36 Kolaczkowski M, Zajdel P, Fhid O, Duszynska B, Tatarczynska E, Pawlowski M. Synthesis and 5-HT_{1A}/5-HT_{2A} activity of some butyl analogs in the group of phenylpiperazine alkyl pyrimido[2,1-f]theophyllines. Pharmacol Rep 2005; 57: 229–35.
37 Kling A, Lange UE, Mack H, Bakker MH, Drescher KU, Hornberger W, *et al.* Synthesis and SAR of highly potent dual 5-HT_{1A} and 5-HT_{1B} antagonists as potential antidepressant drugs. Bioorg Med Chem Lett 2005; 15: 5567–73.
38 Heightman TD, Gaster LM, Pardoe SL, Pilleux JP, Hadley MS, Middlemiss DN, *et al.* 8-Piperazinyl-2,3-dihydropyrrolo[3,2-g]isoquinolines: potent, selective, orally bioavailable 5-HT_1 receptor ligands. Bioorg Med Chem Lett 2005; 15: 4370–4.
39 Byrtus H, Pawlowski M, Czopek A, Bojarski AJ, Duszynska B, Nowak G, *et al.* Synthesis and 5-HT_{1A}, 5-HT_{2A} receptor activity of new beta-tetralonohydantoins. Eur J Med Chem 2005; 40: 820–9.
40 Bojarski AJ, Paluchowska MH, Duszynska B, Klodzinska A, Tatarczynska E, Chojnacka-Wojcik E. 1-Aryl-4-(4-succinimidobutyl) piperazines and their conformationally constrained analogues: synthesis, binding to serotonin (5-HT_{1A}, 5-HT_{2A}, 5-HT_7), alpha1-adrenergic, and dopaminergic D_2 receptors, and *in vivo* 5-HT_{1A} functional characteristics. Bioorg Med Chem Lett 2005; 13: 2293–303.
41 Atkinson PJ, Bromidge SM, Duxon MS, Gaster LM, Hadley MS, Hammond B, *et al*. 3,4-Dihydro-2H-benzoxazinones are 5-HT_{1A} receptor antagonists with potent 5-HT reuptake inhibitory activity. Bioorg Med Chem Lett 2005; 15: 737–41.
42 Paluchowska MH, Charakchieva-Minol S, Tatarczynska E, Klodzinska A, Stachowicz K, Chojnacka-Wojcik E. New 4-[omega-(diarylmethylamino)alkyl]- and 4-[omega-(diarylmethoxy)alkyl]-1-arylpiperazines as selective 5-HT_{1A}/5-HT_{2A} receptor ligands with differentiated *in vivo* activity. Pol J Pharmacol 2004; 56: 743–54.
43 Jurczyk S, Kolaczkowski M, Maryniak E, Zajdel P, Pawlowski M, Tatarczynska E, *et al.* New arylpiperazine 5-HT_{1A} receptor ligands containing the pyrimido[2,1-f]purine fragment: synthesis, *in vitro*, and *in vivo* pharmacological evaluation. J Med Chem 2004; 47: 2659–66.
44 Heinrich T, Bottcher H, Bartoszyk GD, Greiner HE, Seyfried CA, Van Amsterdam C. Indolebutylamines as selective 5-HT_{1A} agonists. J Med Chem 2004; 47: 4677–83.
45 Lopez-Rodriguez ML, Ayala D, Benhamu B, Morcillo MJ, Viso A. Arylpiperazine derivatives acting at 5-HT_{1A} receptors. Curr Med Chem 2002; 9: 443–69.
46 Kamei K, Maeda N, Ogino R, Koyama M, Nakajima M, Tatsuoka T, *et al*. New 5-HT_{1A} receptor agonists possessing 1,4-benzoxazepine scaffold exhibit highly potent anti-ischemic effects. Bioorg Med Chem Lett 2001; 11: 595–8.
47 Mellin C, Vallgarda J, Nelson DL, Bjork L, Yu H, Anden NE, *et al*. A 3-D model for 5-HT_{1A}-receptor agonists based on stereoselective methyl-substituted and conformationally restricted analogues of 8-hydroxy-2-(dipropylamino)tetralin. J Med Chem 1991; 34: 497–510.
48 SYBYL 6.8, Tripos International, 1699 South Hanley Rd, St Louis, MI, 63144, U S A.
49 Cortes C, Vapnik V. Support-Vector Networks. Mach Learn 1995; 20: 273–97.
50 Chang CC, Lin CJ. LIBSVM: a library for support vector machines. Software available at http://www.csie.ntu.edu.tw/~cjlin/libsvm 2001.
51 Kriegl JM, Arnhold T, Beck B, Fox T. A support vector machine approach to classify human cytochrome P450 3A4 inhibitors. J Comput Aided Mol Des 2005; 19: 189–201.
52 Karelson M, Lobanov VS, Katritzky AR. Quantum-chemical descriptors in QSAR/QSPR studies. Chem Rev 1996; 96: 1027–44.
53 Katritzky AR, Gordeeva EV. Traditional topological indices *vs* electronic, geometrical, and combined molecular descriptors in QSAR/QSPR research. J Chem Inf Comput Sci 1993; 33: 835–57.
54 Accelrys Software Inc. Discovery Studio Modeling Environment, Release 2.1, San Diego: Accelrys Software Inc 2007.
55 Wang Y, Zheng M, Xiao J, Lu Y, Wang F, Lu J, *et al*. Using support vector regression coupled with the genetic algorithm for predicting acute toxicity to the fathead minnow. SAR QSAR Environ Res 2010; 21: 559–70.
56 Hanley JA, McNeil BJ. A method of comparing the areas under receiver operating characteristic curves derived from the same cases. Radiology 1983; 148: 839–43.
57 Zou KH, O'Malley AJ, Mauri L. Receiver-operating characteristic analysis for evaluating diagnostic tests and predictive models. Circulation 2007; 115: 654–7.
58 Matthews BW. Comparison of the predicted and observed secondary structure of T4 phage lysozyme. Biochim Biophys Acta 1975; 405: 442–51.
59 Krueger BA, Weil T, Schneider G. Comparative virtual screening and novelty detection for NMDA-GlycineB antagonists. J Comput Aided Mol Des 2009; 23: 869–81.
60 Debnath B, Samanta S, Naskar SK, Roy K, Jha T. QSAR study on the affinity of some arylpiperazines towards the 5-HT_{1A}/alpha1-adrenergic receptor using the E-state index. Bioorg Med Chem Lett 2003; 13: 2837–42.
61 Resimont M, Liegeois JF. Synthesis and in vitro binding studies of piperazine-alkyl-naphthamides: impact of homology and sulphonamide/carboxamide bioisosteric replacement on the affinity for 5-HT_{1A}, $alpha_{2A}$, $D_{4.2}$, D_3, and D_{2L} receptors. Bioorg Med Chem Lett 2010; 20: 5199–202.
62 Neves G, Menegatti R, Antonio CB, Grazziottin LR, Vieira RO, Rates SM, *et al*. Searching for multi-target antipsychotics: Discovery of orally active heterocyclic *N*-phenylpiperazine ligands of D_2-like and 5-HT_{1A} receptors. Bioorg Med Chem 2010; 18: 1925–35.
63 Venkatesan AM, Dos Santos O, Ellingboe J, Evrard DA, Harrison BL, Smith DL, *et al*. Novel benzofuran derivatives with dual 5-HT_{1A} receptor and serotonin transporter affinity. Bioorg Med Chem Lett 2010; 20: 824–7.